TURBULENT JETS IN A DEFLECTING STREAM

By

Keith Norman Atkinson

Thesis submitted for the degree of
Doctor of Philosophy
in the Faculty of Engineering
University of London
and for the
Diploma of Membership
of Imperial College

Imperial College of Science and Technology
Mechanical Engineering Department

May 1988

To my Mother and Father

ABSTRACT

This thesis presents experimental measurements and numerical calculations of turbulent jets injected at right-angles into a confined uniform stream. The measurements and calculations are intended to be relevant to primary and dilution jets in gas-turbine combustors, and geometric and flow parameters are considered which are typical of this application.

The measurements were obtained for the configurations of a single jet, a single row of jets and two opposed single jets, and include mean velocities and turbulence stresses, obtained by hot-wire anemometry, and concentrations of a passive scalar. The measurements provide information on the trajectory and spreading of the jets which is relevant to combustor design, and offer the detailed coverage of the flow necessary to develop and test a numerical calculation procedure.

The numerical calculations were obtained by solving finite-difference forms of the time-averaged Navier-Stokes equations in conjunction with a two-equation model for the turbulence flux terms. Solutions are presented for a single jet and two opposed single jets which show close agreement with the measured trajectory and spreading and demonstrate the potential of the procedure as a design method. An analysis of numerical truncation errors and careful comparisons of calculation and measurement show that many of the detailed differences between calculation and measurement are due mainly to numerical errors. It is concluded that with due regard for the numerical errors the procedure could be applied to more complex configurations of jets, but that for flows of much greater aerodynamic complexity it would be worthwhile to investigate alternative finite-difference schemes.

ACKNOWLEDGEMENTS

I should like to acknowledge my considerable debt to my supervisor, Professor J H Whitelaw, for his advice, encouragement and friendly criticism during my time at Imperial College. The writing of this thesis was not completed until several years after the completion of the research, and I should like to express my deep gratitude to Professor Whitelaw for his patience and confidence in me during the intervening time.

I should also like to thank Dr J J McGuirk for help and advice on all aspects of the work, particularly the computational aspect.

In addition, I should like to thank Professor M M Ribeiro for advice on the experimental work and instruction in the use of the hot-wire and data processing equipment.

The work reported here is part of a collaborative research effort involving Imperial College, Rolls-Royce PLC and the National Gas Turbine Establishment, and I should like especially to thank Dr Z A Khan and Dr W P Jones of Imperial College, Mr A Sotheran, Mr D C Dryburgh and Dr C H Priddin of Rolls-Royce PLC and Mr J Bullard of NGTE for much help and advice.

I have also benefitted from the help of my colleagues at Imperial College, and I should like to thank in particular Dr A S Green, Dr B Thompson and Dr A M K P Taylor.

The experimental work could not have been undertaken without the assistance of the technical staff, and I should like to acknowledge the help of Mr O Vis, Mr N Frost, Mr J Laker and especially the help of the late Mr R H Church.

I should also like to acknowledge the help of Mrs E Archer of the library and Mr G Tindall of the reprographics department.

For the wonderful presentation and typing of the thesis I should like to thank Mrs E Le'Mon of Surrey University.

Finally, I should like to acknowledge the financial support of the National Gas Turbine Establishment.

CONTENTS

			PAGE NUMBER
ABSTRACT			3
ACKNOWLEDGEMENTS			4
CONTENTS			6
LIST OF TABLES			9
LIST OF FIGURES			10
NOMENCLATURE			18
CHAPTER 1			
INTRODUCTION			
1.1	OBJECTIVES		23
1.2	PREVIOUS WORK		25
	1.2.1	Experimental Work	25
	1.2.2	Computational Work	30
	1.2.3	Assessment	33
1.3	PRESENT WORK		34
	1.3.1	Experimental Work	34
	1.3.2	Computational Work	35
1.4	OUTLINE OF THE THESIS		36
CHAPTER 2			
EXPERIMENTAL MEASUREMENTS			
2.1	INTRODUCTION		37
2.2	EXPERIMENTAL APPARATUS		37
2.3	MEASUREMENT TECHNIQUES		39
	2.3.1	Mean Velocity Measurement	39
	2.3.2	Turbulence Measurement	39
	2.3.3	Scalar Concentration Measurement	42
	2.3.4	Wall Static Pressure Measurement	43

			PAGE NUMBER
2.4	RESULTS		43
	2.4.1	A Single jet in a Deflecting Stream	43
	2.4.2	A Single Row of Jets with a Pitch-to-Diameter Ratio of 4.0	44
	2.4.3	A Single Row of Jets with a Pitch-to-Diameter Ratio of 2.0	46
	2.4.4	Two Opposed Single Jets	47
2.5	CONCLUSIONS AND IMPLICATIONS OF THE EXPERIMENTAL STUDY		48

CHAPTER 3

CALCULATION PROCEDURE

3.1	INTRODUCTION		51
3.2	CONSERVATION EQUATIONS		51.
3.3	TURBULENCE MODEL		52
	3.3.1	Choice of Model	52
	3.3.2	The k - ε Turbulence Model	54
3.4	FINITE-DIFFERENCE SCHEME		56
	3.4.1	Choice of Finite-Difference Scheme	56
	3.4.2	Formulation of the Finite-Difference Equations	59
	3.4.3	Solution of the Equations	60
	3.4.4	Wall Boundary Conditions	61
	3.4.5	Numerical Diffusion	63

CHAPTER 4

CALCULATION OF A SINGLE JET IN A DEFLECTING STREAM

4.1	INTRODUCTION		66
4.2	COMPUTATIONAL DETAILS		66
	4.2.1	Solution Domain	66
	4.2.2	Boundary Conditions	67
	4.2.3	Finite-Difference Grid	71
4.3	ASSESSMENT OF NUMERICAL DIFFUSION		72
4.4	RESULTS		75

PAGE NUMBER

4.5 CONCLUSIONS AND IMPLICATIONS OF THE CALCULATIONS 83

CHAPTER 5

CALCULATION OF TWO OPPOSED SINGLE JETS IN A DEFLECTING STREAM

5.1 INTRODUCTION 86
5.2 COMPUTATIONAL DETAILS 86
5.2.1 Solution Domain 86
5.2.2 Boundary Conditions 87
5.2.3 Finite-Difference Grid 87
5.3 RESULTS 88
5.4 CONCLUSIONS AND IMPLICATIONS OF THE CALCULATIONS 90

CHAPTER 6

CALCULATION OF A CONFINED DISC-STABILIZED TURBULENT DIFFUSION FLAME

6.1 INTRODUCTION 92
6.2 CALCULATION PROCEDURE 93
6.2.1 Transport Equations and Turbulence Model 93
6.2.2 Combustion Model 95
6.2.3 Nitric Oxide 99
6.2.4 Boundary Conditions 100
6.2.5 Finite-Difference Grid 101
6.3 RESULTS 102
6.3.1 Non-Reacting Flow 102
6.3.2 Reacting Flow 103
6.4 CONCLUSIONS 108

CHAPTER 7

CLOSURE

7.1 EXPERIMENTAL WORK 109
7.2 COMPUTATIONAL WORK 110

REFERENCES 113

TABLES 124

FIGURES 129

LIST OF TABLES

CHAPTER 1

TABLE 1.1 Typical Operating Conditions of Gas-Turbine Combustors.

CHAPTER 2

TABLE 2.1 Operating Conditions of the Air-Flow Rigs.

CHAPTER 6

TABLE 6.1 Estimates of Measurement Errors.

6.2 Exchange Coefficient and Source Terms in the Conservation Equations for Combusting Flow.

6.3 Operating Conditions of the Elliman Combustor; Reacting Flow.

LIST OF FIGURES

CHAPTER 2

Figure	Title
2.1	Flow rig for a single row of jets in a deflecting stream.
2.2	Flow rig for two opposed single jets in a deflecting stream.
2.3	Orientation of the crosswire (a) measurement of $\overline{U}$, $\hat{u}$, $\hat{v}$, $\overline{uv}$ (b) measurement of $\overline{U}$, $\hat{u}$, $\hat{w}$, $\overline{uw}$.
2.4	Profiles of measured $\overline{U}$ velocity and mean scalar concentration in the symmetry plane of a single jet (a) V_J/U_∞ = 1.5 (b) V_J/U_∞ = 2.3.
2.5	Contours of measured $\overline{U}$ velocity and mean scalar concentration for a single jet; V_J/U_∞ = 1.5 (a) X/D = 4.0 (b) X/D = 8.0.
2.6	Contours of measured $\overline{U}$ velocity and mean scalar concentration for a single jet; V_J/U_∞ = 2.3 (a) X/D = 4.0 (b) X/D = 8.0.
2.7	Contours of measured wall static pressure coefficient for a single jet (a) V_J/U_∞ = 1.5 (b) V_J/U_∞ = 2.3.
2.8	Contours of measured $\overline{U}$ velocity and mean scalar concentration in the plane X/D = 8.0 for a single row of jets; S/D = 4.0 (a) V_J/U_∞ = 1.5 (b) V_J/U_∞ = 2.3.
2.9	Contours of measured wall static pressure coefficient for a single row of jets; S/D = 4.0 (a) V_J/U_∞ = 1.5 (b) V_J/U_∞ = 2.3.
2.10	Profiles of measured Reynolds stresses in the plane Z/D =

2.0 for a single row of jets; S/D = 4.0; V_J/U_∞ = 2.3.

2.11 Profiles of measured Reynolds stresses in the plane X/D = 8.0 for a single row of jets; S/D = 4.0; V_J/U_∞ = 2.3.

2.12 Profiles of measured $\overline{U}$ velocity and mean scalar concentration in the symmetry plane Z/D = 0 of a single row of jets; S/D = 2.0 (a) V_J/U_∞ = 1.5 (b) V_J/U_∞ = 2.3.

2.13 Contours of measured $\overline{U}$ velocity and mean scalar concentration in the plane X/D = 8.0 for a single row of jets; S/D = 2.0 (a) V_J/U_∞ = 1.5 (b) V_J/U_∞ = 2.3.

2.14 Contours of measured wall static pressure coefficient for a single row of jets; S/D = 2.0 (a) V_J/U_∞ = 1.5 (b) V_J/U_∞ = 2.3.

2.15 Profiles of measured Reynolds stresses in the plane Z/D = 1.0 for a single row of jets; S/D = 2.0; V_J/U_∞ = 2.3.

2.16 Profiles of measured $\overline{U}$ velocity and mean scalar concentration in the symmetry plane Z/D = 0 of two opposed single jets; H/D = 4.0 (a) V_J/U_∞ = 1.0 (b) V_J/U_∞ = 1.8.

2.17 Contours of measured $\overline{U}$ velocity and mean scalar concentration for two opposed single jets; H/D = 4.0; V_J/U_∞ = 1.0.

2.18 Contours of measured $\overline{U}$ velocity and mean scalar concentration for two opposed single jets; H/D = 4.0; V_J/U_∞ = 1.8.

2.19 Profiles of measured Reynolds stresses in the plane X/D = 8.0 for two opposed single jets; H/D = 4.0; V_J/U_∞ = 1.8.

CHAPTER 4

Figure	Title
4.1	Profiles of calculated and measured $\overline{U}$ velocity in the symmetry plane of a single jet; $V_J/U_\infty = 2.3$.
4.2	Calculated velocity vectors in the symmetry plane of a single jet; $V_J/U_\infty = 2.3$.
4.3	Calculated velocity vectors for a single jet; $V_J/U_\infty = 2.3$ (a) Y/D = 1.0 (b) X/D = 2.0.
4.4	Contours of calculated mean scalar concentration in the symmetry plane of a single jet; $V_J/U_\infty = 2.3$.
4.5	Contours of calculated mean scalar concentration for a single jet; $V_J/U_\infty = 2.3$ (a) Y/D = 1.0 (b) X/D = 2.0.
4.6	Balance of terms in the $\overline{U}$ momentum equation in the plane X/D = 0 for a single jet; $V_J/U_\infty = 2.3$.
4.7	Balance of terms in the $\overline{U}$ momentum equation in the plane X/D = 2.0 for a single jet; $V_J/U_\infty = 2.3$.
4.8	Profiles of calculated and measured $\overline{V}$ velocity at Y/D = 0.25, Z/D = 0 for a single jet; $V_J/U_\infty = 2.3$.
4.9	Profiles of calculated and measured $\overline{V}$ velocity at Y/D = 0.25, Z/D = 0.25 for a single jet; $V_J/U_\infty = 2.3$.
4.10	Profiles of calculated and measured $\overline{U}$ velocity at Y/D = 0.25, Z/D = 0 for a single jet; $V_J/U_\infty = 2.3$.
4.11	Profiles of calculated and measured $\overline{U}$ velocity at Y/D = 0.25, Z/D = 0.5 for a single jet; $V_J/U_\infty = 2.3$.

4.12 Profiles of calculated and measured $\overline{V}$ velocity at Y/D = 1.35, Z/D = 0 for a single jet; $V_J/U_\infty = 2.3$.

4.13 Profiles of calculated and measured $\overline{U}$ velocity at Y/D = 1.35, Z/D = 0 for a single jet; $V_J/U_\infty = 2.3$.

4.14 Contours of calculated and measured $\overline{U}$ velocity in the plane X/D = 4.0 for a single jet; $V_J/U_\infty = 2.3$.

4.15 Contours of calculated and measured mean scalar concentration in the plane X/D = 4.0 for a single jet; $V_J/U_\infty = 2.3$.

4.16 Calculated velocity vectors in the plane X/D = 2.0 for a single jet; $V_J/U_\infty = 2.3$.

4.17 Calculated velocity vectors in the plane Y/D = 0.25 for a single jet; $V_J/U_\infty = 2.3$.

4.18 Calculated velocity vectors in the plane X/D = 0.25 for a single jet; $V_J/U_\infty = 2.3$.

4.19 Contours of calculated and measured wall static pressure coefficient for a single jet; $V_J/U_\infty = 2.3$.

4.20 Profiles of calculated and measured $\hat{v}$ normal stress at Y/D = 0.25, Z/D = 0 for a single jet; $V_J/U_\infty = 2.3$.

4.21 Profiles of calculated and measured $\hat{v}$ normal stress at Y/D = 0.25, Z/D = 0.25 for a single jet; $V_J/U_\infty = 2.3$.

4.22 Profiles of calculated and measured $\hat{u}$ normal stress at Y/D = 0.25, Z/D = 0 for a single jet; $V_J/U_\infty = 2.3$.

4.23 Profiles of calculated and measured $\hat{u}$ normal stress at Y/D = 0.25, Z/D = 0.5 for a single jet; $V_J/U_\infty = 2.3$.

4.24 Profiles of calculated and measured $\hat{v}$ normal stress at Y/D = 1.35, Z/D = 0 for a single jet; $V_J/U_\infty = 2.3$.

4.25 Profiles of calculated and measured $\hat{v}$ normal stress at Y/D = 1.35, Z/D = 0.5 for a single jet; $V_J/U_\infty = 2.3$.

4.26 Profiles of calculated and measured $\hat{u}$ normal stress at Y/D = 1.35, Z/D = 0 for a single jet; $V_J/U_\infty = 2.3$.

4.27 Profiles of calculated and measured $\hat{u}$ normal stress at Y/D = 1.35, Z/D = 0.5 for a single jet; $V_J/U_\infty = 2.3$.

4.28 Coarse and fine grid solutions of turbulence energy in the plane X/D = 2.0 for a single jet; $V_J/U_\infty = 2.3$.

CHAPTER 5

FIGURE TITLE

5.1 Contours of calculated and measured $\overline{U}$ velocity for two opposed single jets; H/D = 4.0; $V_J/U_\infty = 1.0$.

5.2 Contours of calculated and measured mean scalar concentration for two opposed single jets; H/D = 4.0; $V_J/U_\infty = 1.0$.

5.3 Contours of calculated and measured $\overline{U}$ velocity for two opposed single jets; H/D = 4.0; $V_J/U_\infty = 1.8$.

5.4 Contours of calculated and measured mean scalar concentration for two opposed single jets; H/D = 4.0; $V_J/U_\infty = 1.8$.

5.5 Profiles of calculated and measured Reynolds normal stresses in the plane X/D = 8.0 for two opposed single jets; H/D = 4.0; $V_J/U_\infty = 1.8$.

5.6 Profiles of calculated and measured Reynolds shear stresses in the plane X/D = 8.0 for two opposed single jets; H/D = 4.0; V_J/U_∞ = 1.8.

CHAPTER 6

FIGURE	TITLE
6.1	Axisymmetric combustor with disc baffle.
6.2	Equilibrium species concentration, temperature and density of methane and air mixtures for initial conditions: $T_{methane} = T_{air}$ = 300K, P = latm.
6.3	Instantaneous formation rate of nitric oxide for methane and air mixtures with initial conditions: $T_{methane} = T_{air}$ = 300K, P = latm.
6.4	Influence of inlet radial velocity on the centreline mean velocity for non-reacting flow; Re = 1.9 x 10^5.
6.5	Influence of inlet turbulence energy on the centreline mean velocity for non-reacting flow; Re = 1.9 x 10^5.
6.6	Influence of grid refinement on the centreline mean velocity for non-reacting flow; Re = 1.9 x 10^5.
6.7	Influence of grid refinement on the radial profiles of axial mean velocity for reacting flow; condition 1.
6.8	Influence of grid refinement on the radial profiles of mean mixture fraction for reacting flow; condition 1.
6.9	Contours of calculated and measured axial and radial mean velocity and non-dimensional stream function for non-reacting flow; Re = 1.9 x 10^5.

6.10 Contours of calculated and measured axial and radial mean velocity and non-dimensional stream function for non-reacting flow; Re = 6.5×10^5.

6.11 Influence of Reynolds number on the centreline mean velocity for non-reacting flow.

6.12 Contours of calculated and measured axial and radial mean velocity and non-dimensional stream function for reacting flow; condition 1.

6.13 Contours of calculated and measured mean equivalence ratio and mean temperature for reacting flow; condition 1.

6.14 Calculated and measured radial profiles of mean temperature for reacting flow; condition 1.

6.15 Influence of the turbulence Prandtl number σ_F on the calculated radial profiles of mean mixture fraction for reacting flow; condition 1.

6.16 Influence of the turbulence Prandtl number σ_F on the calculated radial profiles of mean temperature for reacting flow; condition 1.

6.17 Radial profiles of calculated and measured axial mean velocity for reacting flow; condition 1.

6.18 Contours of calculated and measured mean species concentrations for reacting flow; condition 1.

6.19 Contours of calculated mean quantities for reacting flow; condition 3.

6.20 Radial profiles of calculated and measured mean temperature for reacting flow; condition 3.

6.21 Radial profiles of calculated and measured axial mean velocity for reacting flow; condition 3.

NOMENCLATURE

Symbol	Meaning
A	Area of control volume face
a	Coefficient in finite-difference equations
Cp	Wall static pressure coefficient
C_μ C_1 C_2	Constants in turbulence model
D	Jet diameter
E	Voltage from hot-wire anemometer (Chapter 2)
E	Constant in "law of the wall" (Chapter 3)
F	Weighting factor used in finite-difference equations (Chapter 3)
F	Mixture fraction (Chapter 6)
f	Shedding frequency (Chapter 1)
f	Fluctuation in mixture fraction (Chapter 6)
H	Tunnel height
k	Yaw factor of hot-wire (Chapter 2)
k	Turbulence kinetic energy (Chapter 3)
ℓ	Local length scale
P	Pressure

P_e	Local Peclet number
R	Combustor radius
r	Radial ordinate
Re	Reynolds number
S	Distance between adjacent jet centrelines (Chapter 1)
S	Sensitivity factor of hot-wire (Chapter 2)
$S\Phi$	Source term
S_u, S_p	Linearized source terms
T	Temperature
t	Time
U	Velocity component in x direction
u	Fluctuation in U
V	Velocity component in y (or r) direction
v	Fluctuation in V
W	Velocity component in z direction
w	Fluctuation in W
X,x	Axial ordinate
Y,y	Vertical ordinate

y^+	Characteristic parameter used in "law of wall"
Z,z	Lateral ordinate

Greek Symbol	Meaning
α	Angle between instantaneous velocity vector and plane at right-angles to hot-wire (Chapter 2)
α	Under-relaxation factor (Chapter 4)
Γ	Exchange coefficient
Δx	Increment in axial direction
Δy	Increment in vertical direction
Δz	Increment in lateral direction
δ_{ij}	Kronecker delta
ε	Dissipation rate of turbulence kinetic energy
κ	von Karman constant
μ	Molecular viscosity
μ_T	Isotropic eddy viscosity
ν	Kinematic viscosity
ρ	Density

σ_k, σ_ε, σ_T σ_F, σ_f	Constant turbulent Prandtl/Schmidt numbers
τ	Time
Φ	Dependent variable
ϕ	Fluctuation in Φ (Chapter 3)
ϕ	Equivalence ratio (Chapter 6)

Subscript	Meaning
eff	Effective value
i,j,k	Components in Cartesian tensor notation
J	Jet
N,S,E,W, L,R,P	Nodal positions
u,v,w,p k,ε,	Notation for each variable
w	Wall
∞	Freestream

Superscript	Meaning
$-$	Unweighted time-averaged value
$\sim$	Density-weighted time-averaged value
'	Fluctuation about an unweighted time-averaged value (i.e. $\phi' = \Phi - \overline{\Phi}$)

$''$	Fluctuation about a density-weighted time-averaged value (i.e. $\phi'' = \Phi - \tilde{\Phi}$)
$\hat{}$	rms value

CHAPTER 1

INTRODUCTION

1.1 OBJECTIVES

This thesis is concerned with the trajectory and mixing of turbulent jets injected at right-angles into a confined uniform stream.

The simple configuration of a jet in a deflecting stream is the basis of a wide variety of engineering flows. When the mainstream is confined the flow behaviour may be applied to internal impingement cooling in turbine blades or to primary and dilution jets in gas-turbine combustion chambers. When the mainstream is unconfined the behaviour may be applied to discharges from chimney stacks and cooling towers or to the jets from V/STOL aircraft in transition from vertical to horizontal flight.

The practical application which underlies the present work is the mixing of primary and dilution jets in gas-turbine combustion chambers. In a modern combustion chamber the chamber wall usually contains rows of discrete circular holes through which jets of air are injected. Primary jets are injected through rows of holes located towards the head of the combustor, and secondary (or dilution) jets through rows of holes located towards the rear of the combustor. The primary jets penetrate to the combustor centreline to create a region of recirculation in the head of the combustor which stabilizes the flame and promotes thorough mixing and combustion. The dilution jets mix with the hot combustion products to create a low and uniform temperature acceptable to the turbine components downstream. The mixing characteristics of the jets have a considerable influence on the performance of the combustor, and so a knowledge of these characteristics is essential in combustor design.

A widely adopted approach to combustor design is to conduct experiments on real and model combustors and to build up correlations of the main performance parameters in terms of the combustor design parameters; these correlations are then used in the design of new combustors. The disadvantage of this approach is that the correlations are reliable only

within the range of the measurements, and must be used with extreme caution to design new combustors which depart significantly from previous designs. In addition, the correlations provide no insight into the flow processes, such as the mixing of the primary and dilution jets, which affect combustor performance.

In response to the latter problem, engineers have obtained measurements of local flow properties in real and model combustors, but this approach has proved to be costly and time-consuming. Moreover, because of the complexity and inter-dependence of the various flow processes it has often proved difficult to determine relationships from a limited number of measurements.

Faced with these difficulties, engineers and researchers have attempted to develop other approaches to combustor design. An approach often taken in research is to study individual aspects of the flow in isolation in order to determine relationships which may be applied to the practical situation. In the present work the mixing of the primary and dilution jets is studied experimentally by means of isothermal air-flow rigs containing practical arrangements of turbulent jets in a deflecting stream. These idealized flows, although simpler than practical combustor flows, are sufficiently realistic for the measured flow behaviour to be applied to the practical situation.

Another, more modern approach, is to solve finite-difference forms of the time averaged Navier-Stokes equations in conjunction with a model for the turbulence flux terms. This approach has also been taken here and a procedure developed to calculate the experimental flows. Solutions of the flows are compared with the experimental measurements with the aim first of determining the accuracy and current limitations of the technique, and second of demonstrating the potential of the method as a design technique in combustor engineering.

The objectives of the present work can therefore be summarized as follows:

To obtain experimental measurements of the trajectory and mixing of turbulent jets in a deflecting stream for configurations of jets and parameter values typical of primary and dilution jets.

To develop a finite-difference procedure to calculate the experimental flows, and to assess the accuracy of the procedure by comparing solutions with the measured data.

If the experimental flows are to simulate practical combustor flows then the geometric and flow parameters considered must be similar to those of practical combustors. Crabb (1979) gives representative values of the most important parameters, and these are reproduced for future reference in table 1.1.

The remainder of this chapter is divided into three sections: Section 1.2 describes previous related work and discusses its relevance to the present work, Section 1.3 describes the present work in greater detail, and Section 1.4 presents an outline of each of the remaining chapters of the thesis.

1.2 PREVIOUS WORK

The emphasis of the discussion on previous work will be on configurations of jets and parameter values typical of primary and dilution jets. The previous work may be classified as either experimental or computational.

1.2.1 Experimental Work

Most of the work on jets in a deflecting stream is concerned with the configuration consisting of a single jet. Though less relevant to combustor applications, this simple configuration provides a basis for the understanding of more complex and practical configurations, and should be carefully considered.

A Single Jet in a Deflecting Stream

Measurements of wall static pressure for jet-to-mainstream velocity ratios typical of primary and dilution jets were reported by, for example, Vogler (1963), Bradbury and Wood (1965) and McMahon and Mosher (1969). These measurements were intended specifically for the V/STOL application where designers require a knowledge of the pressure field induced on flying surfaces by the presence of lifting jets. The results in each case were presented as contours of the wall static pressure coefficient, $Cp = (P_w - P_\infty)/\frac{1}{2}\rho U_\infty^2$. Upstream of the jet the coefficient is positive in sign, reaching a maximum value at the edge of the jet. Downstream the coefficient is negative in sign and greater in magnitude, and increases in magnitude with velocity ratio. For a velocity ratio of 2.5, which is typical of primary and dilution jets, Vogler reported maximum and minimum coefficient values of +0.7 and -1.5 respectively. Bradbury and Wood investigated the influence on the pressure distribution of the boundary layer thickness, but after applying a three-fold increase to the momentum thickness for one particular velocity ratio observed only minor local changes in the distribution.

Andreopoulos (1980) measured the velocity distribution in the jet exit plane for velocity ratios between 0.25 and 3.0. This work is particularly relevant to numerical calculations as these require boundary conditions to be specified in the jet exit plane. When the velocity ratio was reduced the velocity distribution in the jet exit plane was distorted by the pressure field set up over the hole. Upstream of the hole centreline the velocities were lower than those of the undisturbed symmetric distribution, whereas downstream they were higher, the mass flow lost in the upstream part of the hole being equal to the mass flow gained in the downstream part.

From observations of jets at very low velocity ratios ($V_J/U_\infty < 1.0$) where the distortion is greater, Bergeles (1976) suggested that the velocities were consistent with a condition of constant total pressure. In calculations of a single row of jets, Khan, McGuirk and Whitelaw (1981) demonstrated that this condition in conjunction with the calculated static pressure field accurately reproduces the jet distortion. An alternative

approach adopted by White (1983), is to perform a calculation of the flow within the hole linked to the calculation of the main flow, but although this method produces accurate predictions of the velocity distributions it involves a considerable increase in computational costs.

The trajectory of the jet has been measured by many workers; for example, Jordinson (1956), Keffer and Baines (1963) and Kamotani and Greber (1972). Much of the available trajectory data was examined by Margason (1968) who discovered differences between data obtained at nominally the same operating conditions. One of the reasons for these differences was that different definitions of the trajectory had been used. A popular trajectory is the velocity trajectory, defined as the locus of maximum velocity in cross-planes of the flow, but a temperature trajectory is also used in heated-jet experiments, defined as the locus of maximum temperature. From experiments on a heated jet, Kamotani and Greber (1972) discovered that the temperature trajectory may be up to 20% lower than the velocity trajectory. The experiments show that the most important flow variable governing the velocity trajectory is the momentum flux ratio $\rho_J V_J^2/\rho_\infty U_\infty^2$; this variable of course reduces to the velocity ratio for uniform density flows. The temperature trajectory is also strongly dependent on the momentum flux ratio, but also has a weak dependence on the density ratio ρ_J/ρ_∞.

Using a hot-wire probe and wave analyser, McMahon, Hester and Palfery (1971) detected vortex shedding downstream of the jet exit. They observed that the Strouhal number, fD/U_∞, was independent of the Reynolds number, $\rho U_\infty D/\mu$, but decreased with increase in velocity ratio, the Reynolds number having been varied from 26,000 to 52,000 and the velocity ratio from 8.0 to 12.0. Moussa, Trischka and Eskinazi (1977) also detected vortex shedding and observed the same influence of Reynolds number and velocity ratio, the Reynolds number in this case having been varied from 30,000 to 160,000 and the velocity ratio from 1.0 to 30.0. In previous numerical calculations of jets in a deflecting stream, it has been assumed that the flow is steady, i.e. that vortex shedding does not occur, and the results suggest that the absence of vortex shedding is not a major cause of error.

A number of detailed hot-wire studies of the mean velocity and turbulence of the jet have been reported (e.g. Kamotani and Greber (1972), Moussa et al (1977) and Andreopoulos and Rodi (1984)). A characteristic feature of a jet in a deflecting stream which is revealed in these measurements is a counter-rotating vortex motion in the cross-section of the jet. This vortex motion has a considerable influence on the mixing of the jet, and gives the cross-sectional distribution of the jet fluid a characteristic kidney shape. This kidney shape can be seen in temperature measurements in cross-planes of the jet by Ramsey and Goldstein (1971) and Kamotani and Greber (1972). The measurements by Kamotani and Greber show that the kidney shape becomes more pronounced at higher velocity ratios ($V_J/U_\infty > 4$) with the temperature peak moving outwards from the symmetry plane and into the vortex centres.

A further detailed study of the flow has been made by Crabb (1979). This study differs from other studies in the use of laser Doppler anemometry to obtain the results. The measurements are thought to be more accurate than other measurements obtained by hot-wire anemometry, as the latter system suffers serious rectification errors in highly turbulent regions of the flow. In the present work these measurements are employed to assess the near-field solution of a single jet. The measurements were obtained for a velocity ratio of 2.3 and include near-field values of $\overline{U}$ and $\overline{V}$ mean velocity components and $\hat{u}$ and $\hat{v}$ turbulence normal stress components. Further details of these measurements are presented in Chapter 4.

A Single Row of Jets

Several authors have reported measurements of a single row of jets, but only a small proportion of the results are relevant to primary and dilution jets; the majority of the results are intended for the film-cooling application where velocity ratios are much lower.

Kamotani and Greber (1974) reported trajectories and mean velocity and mean temperature distributions for a single row of heated jets. The authors were particularly concerned with the influence of the duct height, and found it to cause a lowering of the trajectory when the jets were closely spaced. Mean temperature distributions were also reported by Holdeman,

Walker and Kors (1973) and Walker and Kors (1973), but for a cold jet in a heated mainstream. The results cover a wide range of momentum flux ratio, density ratio, hole diameter and pitch spacing and were used to calculate a cooling efficiency coefficient which weights the results according to the amount of cooling attempted (i.e. the amount of jet fluid injected). The authors observed that the momentum flux ratio was the most important parameter governing the trajectory and mixing. In addition, they observed that the cooling efficiency coefficient increases with momentum flux ratio, despite the increase in jet flow, because the rate of mixing increases. Recently the results were extended by Holdeman, Srinivasan and Berenfeld (1984) to include the effects of a non-uniform mainstream inlet temperature distribution and of an area contraction.

Crabb and Whitelaw (1979) and Khan and Whitelaw (1980a) investigated the influence of small asymmetries in the pitch spacing of a size found typically in gas-turbine combustors. Their results show that even small asymmetries in geometry can produce considerable asymmetries in the downstream flow. In numerical calculations, symmetry conditions are often assumed to exist in order to save computational expense, but as the results show, if small asymmetries are present in the combustor then the solutions obtained may be entirely misleading.

Two Opposed Rows of Jets

Khan and Whitelaw (1980b) reported measurements of mean velocity and mean scalar concentration for two opposed rows of jets. The measurements were obtained for a velocity ratio of 2.25 and a height-to-diameter ratio of 4.0 and a range of pitch-to-diameter ratios and pitch asymmetries. Measurements were also obtained with the rows of jets staggered relative to each other axially and laterally. When the holes were positioned directly opposite each other the jets tended to slip over each other, producing an asymmetric flow from a nominally symmetric arrangement of holes. This behaviour is particularly relevant to the primary region of gas-turbine combustors, where the jets are intended to impinge so as to create a region of recirculation upstream. The behaviour would not be predicted by a numerical procedure with symmetry conditions imposed, and so the measurements are particularly useful in indicating the conditions which

give rise to asymmetry.

Khan (1982) extended the measurements to lower velocity ratios of 1.0 and 1.8 which produced symmetric flow. When the pitch-to-diameter ratio was varied at each velocity ratio, a wide variety of flow behaviour was produced, with the opposed jets either forming two jet cores or bifurcating to form four jet cores or bifurcating and combining to form two mixed jet cores. This range of flow behaviour and the symmetry of the flows make the measurements an ideal basis on which to develop a numerical procedure, and in the present work the measurements are extended to include the simpler case of two opposed single jets. Details of the latter measurements are reported in Chapter 2, and also in the paper by Atkinson, Khan and Whitelaw (1982) where they are combined with the measurements for two opposed rows of jets.

Further, more recent, measurements of opposed jets were reported by Holdeman et al (1984). The measurements extend the results by Holdeman and co-workers for a single row of jets and are particularly relevant to the mixing of dilution jets. Measurements were obtained of mean temperature distributions with the jets positioned opposite each other or staggered laterally for values of velocity ratio, density ratio, hole diameter and pitch spacing similar to those of the earlier measurements.

1.2.2 Computational Work

Numerous attempts have been made to develop procedures to predict the major characteristics of a single jet or a multiple arrangement of jets in a deflecting stream. These procedures may be classified as either correlations, analytical procedures or numerical procedures. The following paragraphs give brief details of the work done in each case.

Correlations and Analytical Procedures

One of the most frequently correlated flow characteristics is the trajectory of a single jet (see, for example, Jordinson (1956), Margason (1968) and Kamotani and Greber (1972)). Kamotani and Greber (1972) gave the following correlation based on their experiments of a jet issuing into

an unconfined mainstream:

$$\frac{Y}{D} = CJ^{0.47} \cdot \left(\frac{X}{D}\right)^{0.36}$$

where J is the momentum flux ratio and C is a constant which is equal to 0.89 if the jet issues from a nozzle or 0.81 if the jet issues from a fully developed turbulent pipe flow.

Correlations of the temperature field downstream of a single row of jets were reported by Cox (1975) and Walker and Eberhardt (1975). Both sets of correlations were based on the data of Holdeman, Walker and Kors (1973) and Walker and Kors (1973), discussed in Subsection 1.2.1, and rely on the assumption that the temperature profiles are self-similar when properly non-dimensionalized. The accuracy of the assumption was demonstrated by Holdeman and Walker (1977), who presented comparisons of correlated and measured profiles over the range of the data.

Several authors have reported analytical procedures for the calculation of a single jet (e.g. Keffer and Baines (1963), Wooler (1969) and Stoy and Ben-Haim (1973)). These procedures involve the solution of integral equations of motion in conjunction with an entrainment function and assumptions relating to the shapes of the velocity profiles and the cross-sectional shape of the jet. Keffer and Baines (1963) were concerned with the trajectory and reported accurate calculations of their own trajectory measurements, while Wooler (1969) was concerned with the pressure field and reported accurate calculations of the wall static pressure data of Bradbury and Wood (1965). The main drawback of correlations and analytical procedures is their limited scope for development due to the many restrictive assumptions which they contain.

Numerical Procedures

Greater scope for development is offered by numerical procedures, which solve finite-difference forms of the time-averaged Navier-Stokes equations in conjunction with a model for the turbulence flux terms.

Several authors have reported numerical calculations of a single jet; for example, Crabb (1979), White (1983), Claus (1983), Patankar, Basu and Alpay (1977) and Jones and McGuirk (1979); calculations of a single row of jets were reported by Khan, McGuirk and Whitelaw (1981).

Crabb (1979) reported calculations and measurements of a single jet for a velocity ratio of 2.3 (the measurements having been described in Subsection 1.2.1). The solutions gave the correct trajectory and spreading of the jet, but contained considerable errors in detail, the most prominent being the presence of two scalar concentration peaks. In addition, the downstream turbulence levels were less than 10% of measured levels (even though, paradoxically, the spreading of the jet was correct). The errors were attributed mainly to lack of grid refinement, there being only 22 x 12 x 12 grid points in the X, Y and Z directions respectively. The problem was exacerbated by the fact that the solution domain boundaries were set according to the dimensions of the flow rig, and enclosed an excessive amount of undisturbed flow.

White (1983) repeated the calculations, but with the solution domain boundaries located in the mainstream surrounding the jet, and with the number of grid points increased to 25 x 20 x 15. These solutions also gave good agreement with the trajectory and spreading, but also gave poor agreement at a more detailed level.

Claus (1983) also repeated the calculations, but using a series of progressively finer grids up to a maximum of 90 x 40 x 22 grid points. These solutions showed a progressive improvement with grid refinement, demonstrating the importance of numerical errors, and gave good quantitative agreement on the finest grid.

The calculations by Patankar, Basu and Alpay (1977) and Jones and McGuirk (1979) were obtained for a range of velocity ratios between 2.0 and 10.0. Patankar et al were mainly concerned with the trajectory, and reported good agreement with the trajectory data of Jordinson (1956), Keffer and Baines (1963) and others. Jones and McGuirk (1979) compared calculated temperature distributions with measurements by Kamotani and Greber (1974), and showed good qualititative agreement. Detailed errors which occurred

were attributed partly to numerical errors and partly to turbulence modelling errors.

Khan, McGuirk and Whitelaw (1981) reported calculations and measurements of a single row of jets for a velocity ratio of 2.3 and a range of pitch-to-diameter ratios and height-to-diameter ratios. Comparisons of calculated and measured mean velocity and mean scalar concentration showed qualitative agreement, but also evidence of numerical errors. In addition, the results for a pitch-to-diameter ratio of 2.0 appeared to be sensitive to the assumed form of the jet exit velocity distribution.

1.2.3 Assessment

The preceding two subsections have reviewed experimental and computational work on turbulent jets in a deflecting stream; this subsection briefly summarizes the work and indicates where further work is required.

Most of the experimental work has been concerned with the configuration of a single jet. This configuration is less relevant to combustor design, but the measurements show evidence of behaviour which is likely to be relevant to more practical configurations. Much less work has been done on multiple-jet configurations, and further work is required in order to increase the range of geometric and flow parameters.

A number of the single-jet studies include detailed information on mean velocity and turbulence and provide a suitable basis on which to assess a numerical calculation procedure. Unfortunately, few such measurements exist for multiple-jet configurations, and if the calculations are to be extended to these configurations then further work must be carried out.

The computational work has also tended to be concerned with the single jet. The numerical procedures appear to offer the greatest potential for development, and have produced good agreement with the measured trajectory and spreading, but poor agreement at a more detailed level. Workers have established a strong link between these errors and numerical errors, but there is a need for further work to investigate the various sources of error and to quantify their influence on the solutions. In addition, there

is a need for calculations of more practical configurations to demonstrate the potential of the method in combustor design.

1.3 PRESENT WORK

The preceding section has reviewed previous work and indicated where further work is required; this section gives details of the present experimental and computational work.

1.3.1 Experimental Work

The experimental work consists of measurements of a single jet, a single row of jets, and two opposed single jets in a deflecting stream.

The measurements of the single jet were obtained for velocity ratios of 1.5 and 2.3, which are typical of primary and dilution jets, and consist of values of mean velocity and mean scalar concentration obtained at and beyond X/D = 4.0. The measurements for the velocity ratio 2.3 were intended to be combined with the near-field measurements by Crabb (1979) to provide data on the whole flow field with which to assess a numerical calculation procedure.

The measurements of the single row of jets and two opposed single jets were intended to extend the information on multiple-jet configurations and to provide much needed information on mean velocity and turbulence. The measurements of the single row of jets were obtained for velocity ratios of 1.5 and 2.3, as in the single-jet study, and for a range of pitch-to-diameter ratios. The measurements include values of mean velocity, mean scalar concentration and turbulence stresses obtained mainly in the far field. The configuration of two opposed single jets represents the limiting case of two opposed rows of jets as $S/D \rightarrow \infty$, and provides a test case more complex than a single jet but less complex than two opposed rows of jets. The measurements were obtained for velocity ratios of 1.0 and 1.8 and a height-to-diameter ratio of 4.0, and consisted of values of mean velocity, mean scalar concentration and turbulence stresses obtained mainly in the far field. The parameter values give two extremes of flow behaviour, one involving weak interaction between the jets, and one

involving strong interaction, and provide a stringent test of the calculation procedure for this configuration.

1.3.2 Computational Work

The computational work consists of calculations of the single jet for velocity ratio 2.3 and of the two opposed single jets. Because of lack of time it was not possible to calculate the single row of jets, but other workers may wish to make use of these measurements.

The main aim of the calculations was to identify the main sources of error and to quantify their influence on the solutions. In addition, the solutions of the two opposed single jets were intended to demonstrate the ability of the method to calculate more practical jet configurations of interest to combustor designers. Previous numerical calculations suggest that many of the differences between calculation and measurement are caused by numerical errors, and for this reason a solution of the single jet was subjected to an analysis devised by McGuirk and Rodi (1978) which provides an estimate of the local size of the numerical truncation terms. By applying this analysis and by carefully comparing calculation and measurement it was possible to estimate the influence of these terms and other sources of error. In the case of the two opposed single jets the comparisons between calculation and measurement were restricted to the far field, but any difficulties in assessing the numerical procedure were easily resolved by reference to the single-jet results.

In addition to the calculations of jets in a deflecting stream, a number of calculations were performed of the flow in a simple model combustor. This work was intended as a further preliminary step to develop a general procedure to calculate practical combustor flows. As in the other computational work the main aim was to assess the models and numerical techniques involved. The procedure was developed to calculate a simple gaseous-fuelled turbulent flame with the fuel and oxidant admitted separately, but one containing some of the complex aerodynamic flow features of practical combustor flows. Details of this work, including a review of previous related work, a description of the procedure, and the presentation and discussion of the results are presented in Chapter 6 of

the thesis.

1.4 OUTLINE OF THE THESIS

The thesis is divided into seven chapters. Chapter 1 has indicated the practical importance of turbulent jets in a deflecting stream, reviewed previous work and stated the objectives of the present work. Chapter 2 is concerned with the experimental study and includes a description of the experimental apparatus and procedure, a statement of measurement errors and the presentation and discussion of results. Chapter 3 is concerned with the numerical calculation procedure and presents the governing partial differential equations and turbulence model, the corresponding finite-difference equations, and a description of the method of their solution. The chapter also considers the accuracy of the numerical procedure and describes a method of estimating the local size of truncation errors in a numerical solution. Chapters 4 and 5 present and discuss the results of calculations of turbulent jets in a deflecting stream, Chapter 4 dealing with a single jet and Chapter 5 with two opposed single jets in a deflecting stream. Chapter 6 is concerned with the calculation of the flow in a simple model combustor, and describes modifications to the numerical procedure necessary to calculate a simple combusting flow, and presents and discusses calculations for both isothermal and combusting flow. Chapter 7 summarizes the results of the thesis, discusses their implications for combustor design and for the development of the numerical procedure, and presents recommendations for future work.

CHAPTER 2

EXPERIMENTAL MEASUREMENTS OF JETS IN A DEFLECTING STREAM

2.1 INTRODUCTION

This chapter describes an experimental study of turbulent jets in a deflecting stream. The objectives of the study were to determine the trajectory and mixing characteristics of the jets for configurations and parameter values typical of gas-turbine combustors, and to acquire sufficient detailed information to develop and test a numerical calculation procedure.

Apart from this introduction the chapter consists of four sections: Section 2.2 describes the experimental apparatus, which consists of two air-flow rigs, one to generate a single jet and a single row of jets, and the other to generate two opposed single jets in a deflecting stream; Section 2.3 describes the measurement techniques and discusses their limitations and accuracy; Section 2.4 presents the results of the measurements; and Section 2.5 summarizes the main conclusions and discusses their implications for the design of gas-turbine combustors and for the development of a numerical calculation procedure.

2.2 EXPERIMENTAL APPARATUS

The experimental apparatus consisted of two air-flow rigs, one to generate a single row of jets (and the limiting case of a single jet), and one to generate two opposed single jets in a deflecting stream. Each rig consisted of an open-circuit wind tunnel to generate the mainstream flow, and a secondary air supply system to generate the jet flow. In the case of the single row of jets the area contraction ratio of the tunnel was 7 to 1, and in the case of the opposed jets 12 to 1. The mainstream air was regulated and filtered at the fans before being passed through screens and honeycomb to the working sections. Both arrangements resulted in a uniform mainstream flow, with a mainstream turbulence intensity ($\hat{u}/U_\infty$) of 0.0055 in the case of the single row of jets and a turbulence intensity of 0.0070 in the case of the opposed jets. To eliminate vibration from the working

sections the fans and wind tunnels were supported on rubber pads and were separated from each other except by cloth strip.

The secondary air was generated by a separate fan and was regulated and filtered at the fan. For the single row of jets the air was passed into a separate settling chamber and then via flexible tubing into a row of straight one-inch diameter steel pipes connected to the floor of the wind tunnel working section. For the two opposed single jets the secondary air was passed into two separate settling chambers and then via flexible tubing into two opposed steel pipes, one in the roof and one in the floor of the working section. Honeycomb was placed in the entrance to the pipes to eliminate swirl, and the pipes were of sufficient length (30D) to produce fully developed turbulent flow.

The relevant dimensions of each rig are given in figures 2.1 and 2.2. The single row of jets was generated from seven holes with a pitch spacing (distance between centrelines) of two diameters; pitch spacings of four and six diameters and the limiting case of a single jet were obtained by blocking off holes. For the two opposed single jets the holes were positioned directly opposite each other, four diameters apart.

Sandpaper trips were fixed to the floor and roof of the working sections to give identical, but opposite, two-dimensional boundary layers. The shapes of the boundary layers were measured at the leading edge of the holes in the absence of the jets and were found to conform to a fully-developed turbulent boundary layer. The boundary layer momentum thickness for each rig is given in table 2.1.

The flow in the exit plane of each hole was measured in the absence of the mainstream and found to conform to fully developed turbulent flow. Velocity profiles were measured in two orthogonal directions to check for symmetry, and after adjustments were made to the flexible tubing the profiles were found to be symmetrical to within 3% of the centreline velocity. The mass flow from the holes could be adjusted by means of steel clips fastened around the flexible tubing. These were adjusted until the flow from each hole was the same to within 1% of the average value.

A traverse mechanism was mounted on the roof of the working section which allowed measurement probes to be moved in all three co-ordinate directions to an accuracy of ±0.05mm. Checks were made on the symmetry of the velocity field in the working section in the presence of the mainstream and the jets and the flow was found to be symmetrical to within 1%.

2.3 MEASUREMENT TECHNIQUES

Measurements were obtained by a variety of techniques; the following subsections discuss each technique and assess its limitations and accuracy.

2.3.1 Mean Velocity Measurement

The mean velocity was measured by a Pitot probe of internal and external diameters 0.6 and 1.1mm respectively. Measurements were obtained at and beyond X/D = 4.0 where the static pressure was close to the atmospheric ambient pressure. The axis of the probe was fixed in the axial direction and so the measurements were subject to an error due to misalignment of the probe and flow direction. However, this error is insignificant unless the misalignment is comparatively large and at the measurement locations could be considered negligible. A further, more significant error, is caused by the high turbulence levels. Ower and Pankhurst (1977) show that at a turbulence intensity of 15%, which is typical of the downstream region, the error in the mean velocity is about 2%. With the output voltage time-averaged for up to 60 seconds the measurements were reproducible to within 1%.

2.3.2 Turbulence Measurement

Measurements of turbulence were obtained by hot-wire anemometry with the voltage signals processed on-line by a mini-computer.

The measurements were obtained by a cross-wire probe (DISA 55P61) connected to two constant temperature anemometers (DISA 55D01). The voltage signals were linearized by linearizers (DISA 55D10) before being passed to an analogue-to-digital converter (DEC A862) where they were sampled by a mini-computer (DEC PDP8E) at a rate of 20kHz.

To determine the linearizer exponent and zero settings the probe was placed in the low-turbulence mainstream of the air-flow rigs. The ratio of the linearized voltage signals to the velocity measured by a Pitot tube (E/U) was determined on-line by the mini-computer for a range of velocities between 5 and 25m/s, and the linearizers were adjusted until the ratio varied by less than 1% over the velocity range.

After linearization the voltage signal (E) from each wire is related to the effective cooling velocity (U_{eff}) by

$$E = SU_{eff} \tag{2.1}$$

where S is the sensitivity constant of the hot-wire. Champagne and Sleicher (1967) suggest that the effective cooling velocity may be related to the instantaneous velocity U by the equation:

$$U_{eff} = \frac{E}{S} = U(\cos^2\alpha + k^2\sin^2\alpha)^{\frac{1}{2}} \tag{2.2}$$

where k is a constant and α is the angle made by the instantaneous velocity and the normal to the wire axis. The values of S and k were determined by the method suggested by Ribeiro and Whitelaw (1975), i.e. by positioning each wire at a pair of angles, $\alpha_1 = 30°$ and $\alpha_2 = 45°$, to the flow and by solving the equations:

$$S^2 = \frac{2E^2(30) - E^2(45)}{U^2} \tag{2.3}$$

$$k^2 = \frac{3E^2(45) - 2E^2(30)}{-E^2(45) + 2E^2(30)} \tag{2.4}$$

Equations 2.3 and 2.4 were solved on-line by the mini-computer for each wire. The amplitude gain of the linearizers was then adjusted so that the value of S was the same for both wires.

Values of the turbulence stresses were determined from the voltage signals by means of the transform equations of Champagne and Sleicher (1967). In

the derivation of these equations it is assumed that the axis of the probe is aligned with the local mean-flow direction. Since the axis of the probe was fixed in the axial direction this assumption meant that measurements were restricted to where $\overline{V}$ and $\overline{W}$ velocity components were small. With the wire and its supports positioned in the X-Y plane (figure 2.3a) the transform equations yield the axial mean velocity $\overline{U}$, the normal stresses $\hat{u}$ and $\hat{v}$ and the shear stress $\overline{uv}$

i.e.

$$\overline{U} = \frac{(\overline{E}_1 + \overline{E}_2)}{\sqrt{2}S\,(1 + \tfrac{1}{2}k^2 - 1/8k^4)} \tag{2.5}$$

$$\frac{\overline{u^2}}{\overline{U}^2} = \frac{1}{4}\left(\frac{\overline{E_1^2}}{\overline{E}_1^2} + \frac{\overline{E_2^2}}{\overline{E}_2^2} + \frac{\overline{2E_1E_2}}{\overline{E}_1\overline{E}_2}\right) - 1 \tag{2.6}$$

$$\frac{\overline{v^2}}{\overline{U}^2} = \frac{1}{4}\left(\frac{1 + k^2}{1 - 3k^2 + 4k^4}\right)\left(\frac{\overline{E_1^2}}{\overline{E}_1^2} + \frac{\overline{E_2^2}}{\overline{E}_2^2} - \frac{\overline{2E_1E_2}}{\overline{E}_1\overline{E}_2}\right) \tag{2.7}$$

$$\frac{\overline{uv}}{\overline{U}^2} = \frac{1}{4}\left(\frac{1 + k^2}{1 - k^2}\right)\left(\frac{\overline{E_1^2}}{\overline{E}_1^2} - \frac{\overline{E_2^2}}{\overline{E}_2^2}\right) \tag{2.8}$$

where the overbars denote time-averaging and the subscripts refer to each wire. With the wire and its supports positioned in the X-Z plane (figure 2.3b) the stresses $\hat{w}$ and $\overline{uw}$ are obtained. Equations 2.5 to 2.8 were solved on-line by the mini-computer with between 20,000 and 100,000 voltage

samples taken depending on the flow characteristics at the measurement location. A limitation of the hot-wire technique is that turbulence intensities should be low (less than around 25%), and the flow coverage was restricted accordingly.

The errors in the turbulence stress measurements arise from the approximations inherent in the transform equations, 2.5 to 2.8, and from the calibration and measurement. Ribeiro (1972) has presented an analysis of the errors associated with the transform equations, and for a turbulence intensity of 15% this analysis gives error limits of around $\overline{U}$ ± 0.8%, $\hat{u}/\overline{U}$ ± 2% and $\overline{uv}/\overline{U}^2$ ± 5%. When errors due to the linearization and calibration are added the limits increase to around: $\overline{U}/U_\infty$ ± 5%; $\hat{u}/U_\infty$, $\hat{v}/U_\infty$, $\hat{w}/U_\infty$ ± 9%; $\overline{uv}/U^2_\infty$, $\overline{uw}/U^2_\infty$ ± 16%. Comparisons were made between the mean velocity obtained from the crosswire and that obtained from the Pitot probe at a downstream distance of X/D = 4.0, and the two were the same to within 2%.

2.3.3 Scalar Concentration Measurement

A trace quantity of helium (1% by volume) was added to the jets upstream of the straight pipes and the local concentration of helium in the working section was measured by sampling with the same Pitot probe used for the velocity measurement. The concentration distribution for the whole flow field was obtained by seeding only one jet and superposing the results; thus for the single row of jets only the central jet was seeded, and for the opposed jets only the lower jet was seeded. The flow samples were drawn into a microkatharometer (Servomex Mk.158) by means of a small vacuum pump. The flow rate through the katharometer was adjusted to give a minimum response time (20 seconds) without affecting the measured results, and over the range of the measurements the response of the katharometer was linear with helium concentration. Further details of the apparatus and technique are given by Crabb (1979) and Khan and Whitelaw (1980a). Outside of recirculation regions the measurements are thought to be accurate to within 2% of the maximum concentration (1%) in the pipe exit.

2.3.4 Wall Static Pressure Measurement

The wall static pressure around the central jet in the single row of jets was measured by static pressure tappings of 0.25mm diameter and a micromanometer accurate to within 0.02mm of water. The tappings were spaced 6mm apart up to a radius of 25mm from the jet centreline and 12mm apart thereafter. The measurements were expressed as values of the wall static pressure coefficient, $Cp = (P_w - P_\infty)/\frac{1}{2}\rho U_\infty^2$, and actual recorded values varied from Cp = -2.2 to + 0.8. The values of Cp were thought to be accurate to within ±0.02 except in the region immediately downstream of the pipe exit where flow unsteadiness caused the limits to increase to ±0.1.

2.4 RESULTS OF MEASUREMENTS

In the following sections measurements are presented for a single jet, a single row of jets for pitch-to-diameter ratios of 2.0 and 4.0, and for two opposed single jets for a height-to-diameter ratio of 4.0. A summary of the experimental conditions for each set of measurements is given in table 2.1.

2.4.1 A Single Jet in a Deflecting Stream

The results for a single jet in a deflecting stream were obtained for velocity ratios of 1.5 and 2.3. Figure 2.4 presents profiles of mean velocity and mean scalar concentration for the symmetry plane Z/D = 0. The scalar concentration profiles indicate the trajectory of the jet, and show that at both velocity ratios the jet is deflected rapidly into the axial direction.

The jet presents a blockage to the mainstream and a wake is formed which rises away from the wall with the jet. The velocity profiles contain two peaks; the one closest to the wall is caused by mainstream fluid which accelerates around the jet and turns into the low pressure region; the one highest from the wall is caused by jet fluid which is deflected into the mainstream direction and thus acquires a large $\overline{U}$ velocity component.

Figures 2.5 and 2.6 present contours of mean velocity and mean scalar concentration for the cross-planes X/D = 4.0 and 8.0. For both velocity ratios the scalar contours display a kidney shape, which is an indication of the strong vortex motion in the jet. This kidney shape is a characteristic feature of a jet in a deflecting stream, and has been observed by many other workers; e.g. Ramsey and Goldstein (1972), Kamotani and Greber (1972).

The velocity contours show that the wake rises away from the wall with the jet, as was indicated by the velocity profiles, and maintains a position below the peak in scalar concentration. The velocity peak caused by the deflection of the jet can be seen as a kidney-shaped region over which the velocity exceeds that of the mainstream. With downstream distance the peak disappears as momentum is entrained from the mainstream and from the wake.

Figure 2.7 presents contours of wall static pressure coefficients for the two velocity ratios. At both velocity ratios the pressure field is extensive and contains a negative coefficient value of -1.4. The negative pressure region changes shape with the velocity ratio, and this change coupled with the change in trajectory is an indication of the role of pressure forces in the development of the jet. Similar changes in the pressure field were reported by Bradbury and Wood (1965), who found that the changes diminish with velocity ratio.

2.4.2 A Single Row of Jets with a Pitch-to-Diameter Ratio of 4.0

The results for a single row of jets were obtained for velocity ratios of 1.5 and 2.3, as in the single-jet investigation.

Figure 2.8 presents contours of mean velocity and mean scalar concentration for the cross-plane X/D = 8.0. As can be seen, at this pitch-to-diameter ratio there is little interaction between the jets, and the mean velocity and mean scalar concentration contours at X/D = 8.0 for both velocity ratios correspond closely to those of a single jet. However, because of the increase in blockage, the jets follow a lower trajectory, and the velocity above the jets is no longer equal to the mainstream inlet value.

Figure 2.9 presents contours of wall static pressure coefficient. As can be seen, the contour shapes are similar to those for the single jet, except for a symmetry condition at Z/D = 2.0, but the area of the pressure field is now larger. This increase in area, coupled with the lowering of the trajectory, is a further indication of the role of pressure forces in the development of the jet.

For the single row of jets, measurements were also obtained of turbulence normal and shear stresses. Figures 2.10 and 2.11 present measurements of these quantities for the symmetry plane Z/D = 2.0 and the cross-plane X/D = 8.0. In both of these planes the $\overline{V}$ and $\overline{W}$ velocity components are small and so the turbulence quantities can be measured accurately with the hot-wire probe.

As the jets spread outwards with downstream distance the turbulence normal stresses in the plane Z/D = 2.0 increase. In the vicinity of the holes the mainstream accelerates, and in the region where the velocity gradient $\partial\overline{U}/\partial y$ is negative, a large positive shear stress develops which persists into the downstream region.

In the cross-plane X/D = 8.0, the normal stresses are of the order 20% when non-dimensionalized with the mainstream inlet velocity. This order of magnitude suggests that the turbulence fluctuations will exert a considerable influence on the development of the jet, particularly its rate of spreading.

The $\hat{u}$ and $\hat{v}$ normal stresses increase towards the centre of the jet, but the $\hat{w}$ normal stress reaches a peak value much closer to the wall. This peak in the $\hat{w}$ stress is probably caused by mainstream fluid dividing around the jet and meeting again in the symmetry plane. There may also be an influence of flow unsteadiness due to vortex shedding, but this was not investigated in the present work.

The shear stresses in the plane X/D = 8.0 appear to be consistent with the mean velocity gradients, except in the centre of the wake, where a region of zero velocity gradient is accompanied by a large negative $\overline{uv}$ shear stress. This result emphasizes the importance of turbulence transport in

the flow, and shows that in certain regions of the flow the turbulence stresses can not be simply related to the local mean velocity gradients. Turbulence models which adopt the assumption that the turbulence stresses are proportional to the local mean velocity gradients would erroneously predict a zero shear stress in the centre of the wake. However, given that the stresses and the mean velocity gradients are, in general, consistent, the level of agreement for the flow as a whole could be expected to be good.

2.4.3 A Single Row of Jets with a Pitch-to-Diameter Ratio of 2.0

As the pitch-to-diameter ratio is reduced from 4.0 to 2.0, the blockage presented by the jets increases even further.

The mean velocity and mean scalar concentration profiles for the symmetry plane Z/D = 0, figure 2.12, show that the deflection now takes place even more rapidly at both velocity ratios. Because of the increase in blockage, a region of recirculation is formed behind the jets which extends beyond X/D = 8.0, and the location of the peak in scalar concentration rises and then falls with downstream distance as jet fluid recirculates upstream. Contours of mean velocity and mean scalar concentration for the cross-plane X/D = 8.0, figure 2.13, show that the region of recirculation extends across the row of jets, and that there is approximately uniform concentration in the Z direction. The only remaining evidence of the individual jets is the velocity peaks associated with the jets.

Distributions of wall static pressure coefficient for the two velocity ratios are presented in figure 2.14. As expected, the distributions are similar to those for the pitch-to-diameter ratio of 4.0, but the extent of the pressure field is increased even further because of the increase in blockage.

Measurements of turbulence stresses were obtained for the symmetry plane Z/D = 1.0, and profiles of these quantities, together with mean velocities, are presented in figure 2.15. As can be seen, a large peak occurs in the velocity profile at X/D = 0, which is caused by the mainstream accelerating between the jets. This peak rapidly diminishes as the mainstream spreads

outwards behind the jets, and the peak in the profiles at and beyond X/D = 2.0 is caused by jet fluid which is deflected into the mainstream direction.

The turbulence normal stresses, when non-dimensionalized with the mainstream velocity, reach values of around 30% by X/D = 2.0, because of the rapid spreading of the jets into the symmetry plane. These stresses would be even higher if the turbulence stresses were non-dimensionalized with the local mean velocity, and they suggest that the turbulence fluctuations will exert a considerable influence on the flow in the downstream region.

2.4.4 Two Opposed Single Jets in a Deflecting Stream

The results for two opposed single jets were obtained for a height-to-diameter ratio of 4.0 and for velocity ratios of 1.0 and 1.8.

The flow is now symmetric about two planes, Z/D = 0 and Y/D = 2.0, and figure 2.16 presents profiles of mean velocity and mean scalar concentration for the symmetry plane Z/D = 0. At the lower velocity ratio, the scalar profiles show that the jets achieve little penetration into the mainstream and do not interact for a considerable distance downstream, until they mix together. At the higher velocity ratio, on the other hand, the jets impinge and interact strongly, so that the peak in scalar concentration occurs in the midplane Y/D = 2.0.

Distributions of mean velocity and mean scalar concentration for the cross-planes X/D = 2.0, 4.0 and 8.0 are presented in figures 2.17 and 2.18. Since the flow is now symmetric about Z/D = 0 and Y/D = 2.0, only a quadrant of the flow is shown. The distributions for the velocity ratio 1.0 confirm that no interaction takes place between the jets up to X/D = 4.0, after which the jets diffuse together. The behaviour of the jets is, therefore, identical to that of a single jet, and, as with the single jet, the scalar contours display a pronounced kidney shape which is caused by the strong vortex motion in the jet.

The scalar concentration contours for the velocity ratio 1.8 show that the

jets bifurcate to give two peaks in scalar concentration located in the midplane Y/D = 2.0 and separated by the symmetry plane Z/D = 0. This behaviour has been seen previously by Kamotani and Greber (1974), but in connection with a jet impinging on a horizontal wall. In both cases the jets bifurcate and carry momentum and scalar concentration in vortex motion away from the symmetry plane Z/D = 0.

For the velocity ratio 1.8, measurements were obtained of turbulence normal and shear stresses in the cross-plane X/D = 8.0, which are presented in figure 2.19. As seen previously, the $\hat{u}$ and $\hat{v}$ normal stresses reach peak values in the region where the jet fluid is concentrated, but the $\hat{w}$ normal stress reaches a peak much nearer to the wall. Again, the peak in the $\hat{w}$ normal stress is probably due to mainstream fluid dividing around the jet and meeting again in the symmetry plane downstream.

The $\overline{uv}$ and $\overline{uw}$ shear stress distributions contain large positive and negative values respectively, which appear to be consistent with the $\partial\overline{U}/\partial y$ and $\partial\overline{U}/\partial z$ mean velocity gradients in the plane X/D = 8.0. Consequently, the shear stress could be assumed to be related to the local mean velocity gradients, at least for the downstream region.

2.5 CONCLUSIONS AND IMPLICATIONS OF THE EXPERIMENTAL STUDY

This chapter has described an experimental study of flows from various configurations of jets in a deflecting stream. This section summarizes the main conclusions of the study, and discusses their implications for the design of gas-turbine combustors, and for the development of a numerical solution procedure. The main conclusions are as follows:

Mean velocity and scalar concentration measurements for a single jet in a deflecting stream were in close agreement with previously reported measurements, as expected.

For a single row of jets with a pitch-to-diameter ratio of 4.0, there was no interaction between the jets for a considerable distance downstream, and the flow characteristics were identical to those of a single jet.

When the pitch-to-diameter ratio was reduced to 2.0, the flow quickly became two-dimensional, and a large recirculation zone was formed which drew jet fluid back upstream.

For the configuration of two opposed single jets with a height-to-diameter ratio of 4.0 and a velocity ratio of 1.0, there was no interaction between the jets for some distance downstream, and the flow was identical to that of a single jet. When the velocity ratio was increased to 1.8, however, the jets impinged and bifurcated to give two cores of jet fluid located in the midplane between the jets.

Although simpler than practical combustor flows, the flows considered here are sufficiently realistic to be applied to gas-turbine combustors. The results of the study give some indication of which configurations could be employed in gas-turbine combustors, and which configurations should be avoided.

The configuration of a row of jets with a pitch-to-diameter ratio of two, for example, gives rise to a uniform distribution of jet fluid such as would be desirable in the dilution region of a combustor. When the pitch-to-diameter ratio is increased beyond 2.0, however, the flow becomes increasingly non-uniform laterally, until areas consisting solely of mainstream fluid occur. In a gas-turbine combustor these areas would be seen as streaks of hot, undiluted combustion products, damaging to the turbine components downstream. A similar result would occur with a row of opposed jets for a height-to-diameter ratio of 4.0 and a velocity ratio of 1.0. However, the uniformity of the flow could be expected to increase if the velocity ratio were increased to around 1.8.

The present study has, of course, considered only a limited number of jet configurations and parameter values, but further results can be found in the papers of, for example, Khan and Whitelaw (1980a) (a single row of jets with and without hole asymmetry), Khan (1982), Holdeman et al (1984) (two opposed rows of jets). These results, combined with the present results, provide an indication of the trajectory and mixing characteristics for a

wide range of practical jet configurations.

As well as attempting to simulate practical combustor flows, the present work aims to provide measurements of sufficient detail for the development and testing of a numerical calculation procedure. An important part of the present work in this context is the provision of turbulence stress measurements. These measurements provide an indication of the characteristics of the turbulence which need to be modelled accurately.

Results for all of the flows show that turbulence production should be modelled accurately; all of the flows generate a great deal of turbulence, and this turbulence is likely to exert a considerable influence on the spreading of the jet. Turbulence transport should also be modelled accurately, because much of the turbulence generated in the near field is transported downstream by the mean flow. The relationship between the turbulence stresses and the mean velocity gradients in the far field suggests that an eddy viscosity model could be employed, while the importance of turbulence production and transport suggests that the more complex "two-equation" form of this model should be used, in which modelled transport equations are solved for two turbulence properties. In certain areas of the near field the measurements show that the eddy viscosity assumption is invalid, but the fact that the flow in these areas is controlled by convection and pressure gradients suggests that any errors in the turbulence here will have little effect on the overall development of the flow.

CHAPTER 3

CALCULATION PROCEDURE

3.1 INTRODUCTION

This chapter describes a numerical procedure developed for the calculation of turbulent jets in a deflecting stream. The approach adopted is to formulate a set of partial differential equations to describe the flow and to approximate the equations as a set of finite difference equations which may be solved by a numerical algorithm. The basic features of the procedure have been described elsewhere (see, for example, Gosman and Pun (1973)), and only a brief descripion will be given here so as to provide a basis for discussion.

3.2 CONSERVATION EQUATIONS

The equations describing an incompressible, constant viscosity flow, when written in Cartesian tensor form, are as follows:

Conservation of Mass

$$\frac{\partial U_i}{\partial x_i} = 0 \qquad (3.1)$$

Conservation of Momentum

$$\frac{\partial U_i}{\partial t} + \frac{\partial U_i U_j}{\partial x_j} = -\frac{1}{\rho}\frac{\partial P}{\partial x_i} + \nu \frac{\partial^2 U_i}{\partial x_j \partial x_j} \qquad (3.2)$$

These equations form a closed set, and for a given set of initial and boundary conditions may in principle be solved for both laminar and turbulent flow. However, turbulent flows are three-dimensional and have length and time scales which cover many orders of magnitude. The computing capacity necessary to resolve all of these scales is far greater than that available on any present or proposed computer, and so the direct solution

of equations 3.1 and 3.2 for turbulent flows is not possible at present and is unlikely to be possible for the foreseeable future.

The approach commonly taken for turbulent flows is to average the equations so as to convert them into equations for mean quantities. The flows considered here are assumed to be stationary and so time-averaging may be used. After time-averaging the equations take the form:

$$\frac{\partial \overline{U}_i}{\partial x_i} = 0 \qquad (3.3)$$

$$\frac{\partial(\overline{U}_i \overline{U}_j)}{\partial x_j} = -\frac{1}{\rho}\frac{\partial \overline{P}}{\partial x_i} - \frac{\partial(\overline{u_i u_j})}{\partial x_j} \qquad (3.4)$$

In the flows considered here the Reynolds number is assumed to be sufficiently high for the effects of viscosity on the mean flow to be negligible, and so in writing equation 3.4 the viscous terms have been omitted. This assumption will not be valid in the vicinity of a solid wall, however, and here some special treatment will be necessary.

Because of the non-linearity of equation 3.2 the averaging process produces a set of equations which are no longer closed. Closure of the equations involves determining the Reynolds stresses $\overline{u_i u_j}$ (i.e. specifying a turbulence model) and this is considered in the next section.

3.3 TURBULENCE MODEL

3.3.1 Choice of Model

Turbulence models are generally of two types: either the eddy-viscosity type or the Reynolds-stress type. (For a comprehensive review of turbulence models, see, for example, Launder and Spalding (1972).)

Eddy-viscosity models are based on the eddy-viscosity concept of Boussinesq (1877), in which the Reynolds stresses are assumed to be linearly related to the local mean rates of strain.

i.e. $$\overline{\rho u_i u_j} = \frac{2}{3}\rho\delta_{ij}k - \mu_T\left(\frac{\partial \bar{U}_i}{\partial x_j} + \frac{\partial \bar{U}_j}{\partial x_i}\right) \qquad (3.5)$$

where μ_T is an isotropic "eddy" or "turbulence" viscosity

k is the turbulence kinetic energy $\left(= \frac{1}{2}\overline{u_i u_i}\right)$, and

δ_{ij} is the Kronecker delta

When this assumption is made the problem of determining the Reynolds stresses becomes a problem of determining the spatial variation of the eddy viscosity μ_T.

A considerable number of models based on the eddy-viscosity concept have been proposed, from the simple algebraic mixing-length models, e.g Prandtl (1925), Taylor (1932), to the more complex one-equation models, e.g. Bradshaw et al (1967), Nee and Kovasznay (1969), and two-equation models, e.g. Harlow and Nakayama (1968), Jones and Launder (1972).

In the mixing-length models μ_T is related to the local mean velocity gradients and to a characteristic length scale of the turbulence (mixing length). The mixing-length models were devised for, and are suitable for, simple turbulent shear flows in which a characteristic length scale can be easily defined.

In more complex turbulent flows the turbulence properties may vary to a greater extent and depend strongly on conditions elsewhere in the flow. These considerations led to the development of one-equation models in which μ_T is determined from an empirically defined length scale and from the turbulence kinetic energy k, with k being determined from a modelled transport equation.

In one-equation models there is still a need to specify a characteristic length scale of the turbulence and this may prove difficult in complex, recirculating flows. In two-equation models this problem is overcome by solving a modelled transport equation for a second turbulence property, usually the dissipation rate of turbulence kinetic energy ε, which may be related to the length scale.

Reynolds stress models do not rely on the eddy-viscosity concept, but solve modelled transport equations for the individual Reynolds stresses. Models of this type have been described by, for example, Hanjalic and Launder (1972) and Launder, Reece and Rodi (1975).

In complex three-dimensional flows, such as those considered here, the use of Reynolds-stress models involves solving transport equations for each of the six Reynolds stresses and the dissipation rate ε. Solving all these equations makes considerable demands on computer storage space, and with the storage available at present, can only be undertaken on very coarse finite-difference grids. As a result, the advantages of using these models are usually cancelled out by numerical errors.

For complex three-dimensional flows the combined effects of modelling and numerical errors are generally a minimum with two-equation eddy-viscosity models. A number of two-equation models have been proposed, but the $k - \varepsilon$ model of Jones and Launder (1972) has been used more widely than any other, and in fact is the most widely used model in previous numerical calculations of turbulent jets in a deflecting stream. Calculated results for jets in a deflecting stream show that the model is able to reproduce the trends in the measured turbulence field (see, for example, Crabb (1979), Claus (1983)), and on the basis of these results the model was adopted for use in the present work.

3.3.2 The $k - \varepsilon$ Turbulence Model

As explained earlier, in eddy-viscosity models the Reynolds stresses are related to the local mean rates of strain by the eddy-viscosity μ_T. The eddy-viscosity is assumed to satisfy the Prandtl-Kolmogorov expression:

$$\mu_T = c_\mu \rho k^{\frac{1}{2}} \ell \tag{3.6}$$

were C_μ is an empirical constant, k is the turbulence kinetic energy and ℓ is a characteristic length scale of the turbulence.

The turbulence energy k is determined from a modelled transport equation. An exact transport equation for k may be derived by beginning from equation 3.2; Rodi (1970) has modelled this equation and gives the following form for high Reynolds number flows:

$$\rho \overline{U}_j \frac{\partial k}{\partial x_j} = \frac{\partial}{\partial x_j} \left(\frac{\mu_T}{\sigma_k} \frac{\partial k}{\partial x_j} \right) + \mu_T \left(\frac{\partial \overline{U}_i}{\partial x_j} + \frac{\partial \overline{U}_j}{\partial x_i} \right) \frac{\partial \overline{U}_i}{\partial x_j} - \rho \varepsilon \tag{3.7}$$

where ε is the dissipation rate of turbulence energy, defined by

$$\varepsilon = \nu \left(\overline{\frac{\partial u_i}{\partial x_j} \cdot \frac{\partial u_j}{\partial x_i}} \right) \tag{3.8}$$

The length scale ℓ may be assumed to be related to ε (Jones (1971)) by

$$\varepsilon = \frac{k^{3/2}}{\ell} \tag{3.9}$$

in which case, equation 3.6 becomes

$$\mu_T = C_\mu \rho \frac{k^2}{\varepsilon} \tag{3.10}$$

The dissipation rate is determined from a modelled transport equation, and Rodi (1970) gives the following modelled equation for high Reynolds number flows:

$$\rho\overline{U}_j \frac{\partial \varepsilon}{\partial x_j} = \frac{\partial}{\partial x_j}\left(\frac{\mu_T}{\sigma_\varepsilon}\frac{\partial \varepsilon}{\partial x_j}\right) + C_1 \frac{\varepsilon}{k}\mu_T \left(\frac{\partial \overline{U}_i}{\partial x_j} + \frac{\partial \overline{U}_j}{\partial x_i}\right)\frac{\partial \overline{U}_i}{\partial x_j} - C_2\rho\frac{\varepsilon^2}{k} \qquad (3.11)$$

Equations 3.6 to 3.11 contain a number of empirical constants. Launder and Spalding (1972) recommend the following values of the constants on the basis of calculations of a wide range of two-dimensional shear flows:

$$C_\mu = 0.09, \quad C_1 = 1.44, \quad C_2 = 1.92, \quad \sigma_k = 1.0, \quad \sigma_\varepsilon = 1.3$$

3.4 FINITE-DIFFERENCE ALGORITHM

3.4.1 Choice of Finite-Difference Scheme

The finite-difference scheme used in the calculation procedure was the hybrid upwind/central difference scheme (see, for example, Spalding (1972)). This scheme is now in wide-spread use for solving steady-state recirculating flows (see, e.g. Coupland and Priddin (1985), Burns and Wilkes (1987), Durst, Schierholz and Wunderlich (1987)).

To approximate the convection terms in the governing partial differential equations the hybrid scheme uses a combination of upwind and central differencing. Thus, central differencing is used to approximate the convection terms, except when the magnitude of the local cell Peclet number (e.g. $Pe_x = \rho\overline{U}\Delta x/\Gamma$) exceeds 2. When the magnitude of the Peclet number is greater than 2 the use of central differencing for the convection terms gives rise to equations which are unstable to iterative solution; thus, for $|Pe| > 2$ the convection terms are approximated by upwind differencing.

The advantage of the hybrid upwind/central difference scheme over other schemes is its simplicity which makes it computationally inexpensive. However, the use of upwind differencing for the convection terms gives rise to a potentially serious first-order truncation term known as "artificial" or "numerical" diffusion. In solutions suffering from numerical diffusion the gradients of the dependent variables tend to be smeared out not only by physical diffusion, but also by numerical diffusion. The errors tend to be

worst in areas of the flow where the velocity vectors are skewed relative to the numerical grid lines and where simultaneously there are strong gradients of the dependent variables normal to the flow direction; in these areas the numerical diffusion may be so serious as to completely dominate the true physical diffusion in the flow. Although numerical diffusion may be reduced by grid refinement, it is often impossible to reduce the error acceptably because of the limitations of computer storage and running time.

In an effort to reduce numerical diffusion without resorting to very fine grids, workers have turned their attention to other finite-difference schemes. Two schemes, the first proposed by Raithby (1976) and the second by Leonard (1977), have received considerable attention. In the scheme by Raithby a form of upwind differencing referred to as skew upwind differencing is used to approximate the convection terms when $|Pe| > 2$. By taking account of the skewing of the velocity vectors when approximating the convection terms, this scheme considerably reduces numerical diffusion. The Leonard scheme, on the other hand, uses a quadratic upstream interpolation to approximate the convection terms (at all values of the Peclet number).

Leschziner (1980) has compared the performances of the Raithby, Leonard and hybrid schemes in a number of simple test cases in which velocity vectors are skewed relative to the numerical grid lines. One such case involves the convective/diffusive transport of a scalar step in a uniform velocity field inclined to a uniformly spaced numerical grid for the conditions $(\theta, Pe_x, Pe_y) = (45°, 60, 60)$ and $(26.5°, 60, 30)$. The values of the Peclet number, although high, are typical of the values found in turbulent-flow problems and the present problem of a turbulent jet in a deflecting stream. Both the Raithby scheme and the Leonard scheme produced solutions in close agreement with the known exact solution of the scalar transport equation, but the hybrid scheme produced solutions which were over-diffusive, clearly as a result of numerical diffusion. On the other hand, the Raithby and Leonard schemes both suffered to a limited extent from unboundedness, with small (unphysical) under and overshoots occurring in the scalar distributions.

In a later paper Demuren (1983) applied the Leonard and hybrid schemes to

the problem of a row of jets in a deflecting stream. In the case considered the jets were spaced three diameters apart and were ejected at a velocity ratio of 1.96. The solutions for both schemes showed grid dependence, although the Leonard scheme solution for a fine grid of 14 x 50 x 37 points was thought to be almost grid independent. The distribution of total pressure obtained by applying each scheme to the fine grid was compared with measured data. The distribution obtained by the Leonard scheme was in close agreement with the data, but that obtained by the hybrid scheme showed very poor agreement and was only as accurate as that obtained by applying the Leonard scheme to a coarse grid of 10 x 10 x 24 points. Thus the Leonard scheme has the advantage over the hybrid scheme of giving generally greater accuracy on a given grid, but has the disadvantage of requiring greater running time, and, in addition, is prone to unboundedness errors.

In adopting the hybrid scheme for the present calculations it was of course recognised that numerical diffusion represented a potential source of error. However, in complex flows the conditions under which the error occurs are often localized, and often a reasonably accurate solution may be obtained by concentrating the grid points where the error terms are expected to be large. This has been the course adopted in most previous calculations of turbulent jets in a deflecting stream, and it has resulted in accurate calculations of the trajectory and spreading of the jets (see, for example, Jones and McGuirk (1979), White (1983)). In solutions containing numerical diffusion the locations where the error terms are large may be difficult to identify because the effects of numerical diffusion are cumulative, like those of true physical diffusion. However, McGuirk and Rodi (1978) have devised an analytical procedure which may be applied to a solution to identify the problem areas. In the present work this procedure was applied to a numerical solution of a single jet to determine the local size of the error term associated with the $\overline{U}$ momentum equation. Further details of the procedure are given in Subsection 3.4.5 of this chapter.

3.4.2 Formulation of the Finite-Difference Equations

The finite-difference equations are derived with reference to a finite-difference grid covering the region of interest. A non-uniform, "staggered" grid arrangement similar to that popularized by Harlow and Welch (1965) was used. The finite-difference equations are formed by integrating the partial differential equations over a series of individual control volumes superimposed on the finite-difference grid. The formulation of the equations can be illustrated by considering a common form of equation for any dependent variable Φ:

$$\frac{\partial \rho \overline{U}_j \Phi}{\partial x_j} = \frac{\partial}{\partial x_j}\left(\Gamma_\Phi \frac{\partial \Phi}{\partial x_j}\right) + S_\Phi \qquad (3.12)$$

where Φ represents a dependent variable, i.e. $\overline{U}$, $\overline{V}$, $\overline{W}$, k, ε or a passive scalar,

Γ_Φ is a diffusion coefficient, and

S_Φ is a source term.

By integrating over a control volume and making some use of the continuity equation, equation 3.12 can be expressed in the form:

$$a_P \Phi_P = a_N \Phi_N + a_S \Phi_S + a_E \Phi_E + a_W \Phi_W + a_R \Phi_R + a_L \Phi_L + S_u^\Phi \qquad (3.13)$$

where

$$a_P = a_N + a_S + a_E + a_W + a_R + a_L - S_p^\Phi \qquad (3.14)$$

and, for example,

$$a_N = A_n \, q_n \, F_n \qquad (3.15)$$

$$a_S = A_s q_s (F_s - 1) \qquad (3.16)$$

where A_n is the area of the north face of the control volume,

q_n is the mass flow through the north face, and

F_n is a weighting factor for the north face.

The source term S_Φ in equation 3.12 is integrated over a control volume and linearized so that it becomes $S_u^\Phi + S_p^\Phi \Phi_p$.

As explained in Subsection 3.4.1, the present formulation employs the hybrid upwind/central difference scheme. Thus central differencing is used except when the magnitude of the local cell Peclet number exceeds 2 when a switch to upwind differencing is made. The weighting factor F_n can therefore take the following values:

$$F_n = \frac{1}{2} + \frac{1}{Pe_n} \quad |Pe_n| \leq 2 \text{ central differencing}$$

$$\left.\begin{aligned} F_n &= 1 \quad Pe_n > 2 \\ F_n &= 0 \quad Pe_n < -2 \end{aligned}\right\} \text{ upwind differencing} \qquad (3.17)$$

and $Pe_n = \frac{q_n \Delta y}{\Gamma_n}$, where Δy represents distance between neighbouring grid points and Γ_n is a mean diffusion coefficient averaged over neighbouring grid points. Similar relationships exist for the other weighting factors.

3.4.3 Solution of the Equations

The finite-difference equations are solved iteratively, and a guess and correct procedure similar to that suggested by Chorin (1968), Amsden and Harlow (1970) and Patankar and Spalding (1972) is used when solving the continuity and momentum equations. In each iteration the momentum equations are solved first by using a guessed pressure field (i.e. the previous iteration step values). The velocities obtained do not, in general, satisfy the local finite-difference form of the continuity equation but give rise to a mass source. The pressure and velocities are

then adjusted by using the solution of a pressure correction equation so that the continuity equation is satisfied. The k and ε equations are then solved to complete the iteration, and the process is repeated until a converged solution is obtained. The actual solution of the equations is by the successive application of a tri-diagonal matrix algorithm, sometimes referred to as the Thomas algorithm, which is described by, for example, Roache (1972). A solution was taken to be converged when the sum of the mass sources in the continuity equation was less than a small fraction (0.1%) of the mass flow into the solution domain. There was also a condition on the local size of the mass source.

To maintain stability when solving coupled non-linear equations it is necessary to apply under-relaxation. This under-relaxation can be expressed by:

$$\Phi = \alpha\Phi_{NEW} + (1-\alpha)\Phi_{OLD} \qquad (3.18)$$

where α is an under-relaxation factor, which is typically equal to 0.5, Φ_{OLD} and Φ_{NEW} are old and new iteration step values respectively, and Φ is the value carried forward to the next iteration.

3.4.4 Wall Boundary Conditions

The flow problem is not fully defined and the finite-difference equations cannot be solved until boundary conditions appropriate to the problem are specified at the boundaries of the solution domain. The conditions specified at inflow, outflow and other types of boundary are dealt with in the next two chapters; this section deals with the conditions specified at a solid wall boundary.

On the wall surface the appropriate conditions are:

$$\overline{U} = \overline{V} = \overline{W} = k = \frac{\partial \varepsilon}{\partial y} = 0 \qquad (3.19)$$

where y is distance normal to the wall. For a passive scalar variable such as the concentration of a trace of helium the appropriate condition is:

$$\frac{\partial \overline{\Phi}}{\partial y} = 0 \qquad (3.20)$$

Earlier it was noted that the partial differential equations on which the numerical procedure is based were formulated to describe high Reynolds number turbulent flows in which the effects of viscosity on the mean flow are negligible. However, it is well known that turbulent flow over a wall is characterized by a thin region over which viscous effects become important and flow properties vary rapidly. It is possible to calculate these conditions by employing a low Reynolds number formulation of the equations and by concentrating grid points in the vicinity of the wall, but the computing costs involved in this method are often prohibitively large, particularly when the main flow is complex. Consequently, in order to link the conditions in the main flow to those on the wall, the numerical procedure resorts to a number of wall functions. These wall functions rely on the fact that the flow in the immediate vicinity of the wall obeys a number of near-universal laws. This approach is now in wide-spread use and a detailed description of the wall functions has been given by, for example, Patankar and Spalding (1970). However, a brief description will be given here for completeness.

For velocity components parallel to the wall, the logarithmic "law of the wall" is used to define a diffusion coefficient which, when inserted into the momentum equations, produces the correct wall diffusion flux. This diffusion coefficient is given by:

$$\Gamma^* = \frac{\kappa \mu y^+}{\ell n(Ey^+)} \qquad (3.21)$$

in which

$$y^+ = \frac{\rho k^{\frac{1}{2}} C_\mu^{1/4} \Delta y}{\mu} \qquad (3.22)$$

where Δy is distance from the wall and κ and E are constants equal to 0.433 and 8.8 respectively.

The source terms in the momentum equations for velocity parallel to the

wall are also modified and these become:

$$S_u^{\Phi} + S_p^{\Phi}\Phi_p - \frac{\Gamma^* A}{\Delta y} \qquad (3.23)$$

where A is the area of the control volume face. The modifications are only valid in the fully turbulent region of the wall flow, which is taken to be between $y^+ = 11.0$ and $y^+ = 400$.

In the turbulence kinetic energy equation the source term S_u^k becomes:

$$S_u^k = \frac{C_\mu^{\frac{1}{2}} \rho k \bar{U}}{\Delta y \ell n(Ey^+)} \qquad (3.24)$$

In order to approximate the variation of ε near the wall, use is made of the fact that the length scale defined by $\ell = k^{3/2}/\varepsilon$ is equal to $C_\mu^{-3/4}\kappa\Delta y$ in the near-wall region, in which case, ε can be seen to satisfy the equation

$$\varepsilon = \frac{C_\mu^{3/4} k^{3/2}}{\kappa \Delta y} \qquad (3.25)$$

In order to ensure that this equation is satisfied when the dissipation rate equation is solved, the terms S_u^ε and S_p^ε are modified to the form:

$$S_u^\varepsilon = \frac{\lambda C_\mu^{3/4} k^{3/2}}{\kappa \Delta y} \qquad (3.26)$$

$$S_p^\varepsilon = -\lambda \qquad (3.27)$$

where λ is a large number, say 10^{30}, chosen to ensure that all other terms in the equation are negligible compared with S_u^ε and $S_p^\varepsilon \varepsilon_p$.

3.4.5 Numerical Diffusion

It was explained earlier that the partial differential equations are approximated by the hybrid upwind/central difference scheme and that

consequently the convection terms in the equations are approximated by central differencing except when $Pe > 2$ when a switch to upwind differencing is made. In addition, it was pointed out that the use of upwind differencing for the convection terms gives rise to a potentially serious first-order truncation error known as numerical diffusion. The numerical diffusion smears the gradients of the dependent variables in a manner similar to true physical diffusion and tends to be worst where the flow is skewed relative to the numerical grid lines and where, simultaneously, there are strong cross-stream gradients. Since these conditions (and the condition that $Pe > 2$) occur extensively in complex three-dimensional turbulent flows, numerical diffusion represents a major source of error when the hybrid scheme is used. This has been confirmed for the case of turbulent jets in a deflecting stream by many workers, for example, Crabb (1979), White (1983) and Claus (1983), who present solutions in which the gradients of velocity and scalar concentration are considerably underpredicted, clearly as a result of numerical diffusion. Such errors are particularly disturbing when the calculations are to be relevant to primary and dilution jets, because then an important result of the calculations is the rate of spreading of the jets.

Numerical diffusion can be reduced by grid refinement, but the present limits on computer time and storage rule out the possiblity of completely eliminating the error for complex three-dimensional turbulent flows. However, the results of previous calculations show that good qualitative accuracy can often be achieved by employing non-uniform grids and concentrating the available grid points where the truncation terms are expected to be large. The problem of identifying where the truncation terms are large is often made difficult because of the cumulative nature of the numerical diffusion. Fortunately, McGuirk and Rodi (1978) have devised a method which may be applied to a numerical solution to estimate the local size of the truncation terms responsible for numerical diffusion.

In McGuirk and Rodi's method, the solution under consideration is used to re-calculate the terms in the finite-difference equations, but by using central differencing throughout. Wherever upwind differencing was used in the solution, the re-calculated terms in the equation in general no longer sum to zero, but give rise to a residual term. This residual term provides

an estimate of the local size of the truncation terms responsible for numerical diffusion.

In the present work the method has been used to estimate the size of the truncation terms associated with the $\overline{U}$ momentum equation for a fine-grid solution of a single jet in a deflecting stream. The method could also have been applied to other equations, but it is argued that areas where the truncation terms are large for the $\overline{U}$ equation are also likely to be areas where they are large for the $\overline{V}$ equation or the $\overline{W}$ equation or both, since numerical diffusion tends to occur where the velocity vectors are skewed relative to the grid lines. It should also be noted that the truncation terms are only important when they are large in comparison with the other terms in the equation. Consequently, in Chapter 4, comparisons are made of local nett convection, pressure gradient, nett physical diffusion and the residual term for the $\overline{U}$ equation. These comparisons establish the importance of numerical diffusion on the development of the flow, and, in addition, they illustrate the importance of each of the various physical influences: convection, pressure gradients and physical diffusion.

CHAPTER 4

CALCULATION OF A SINGLE JET IN A DEFLECTING STREAM

4.1 INTRODUCTION

This chapter presents calculations of a single jet in a deflecting stream for a velocity ratio of 2.3. The aim of these calculations, as stated in Chapter 1, is to identify the major sources of error in the calculation procedure and to assess the level of their influence. Comparisons are made with the near field measurements by Crabb (1979) and the far field measurements presented in Chapter 2. These measurements provide a detailed description of the mean velocity, mean scalar and turbulence fields of the jet and enable a comprehensive assessment of the procedure to be made.

Previous calculations show that much of the disagreement between calculation and measurement is due to numerical errors associated with the discretization of the governing flow equations. To assess the influence of these errors, a solution was subjected to an analysis devised by McGuirk and Rodi (1978) which provides an estimate of the local truncation error in the solution. By applying this analysis and carefully comparing calculation and measurement it was possible to estimate the influence of numerical errors and other forms of error in the solution.

4.2 COMPUTATIONAL DETAILS

4.2.1 Solution Domain

The solution domain consisted of a rectangular volume with boundaries located in the plane of the wall containing the jet discharge, and in the symmetry plane of the jet, Z/D = 0. The other boundaries were located in the mainstream immediately above and to the side of the jet, and in planes normal to the mainstream, upstream and downstream of the hole. The dimensions of the solution domain were identical to those used previously by White (1983); hence, the upstream and downstream boundaries were located at X/D = -2.0 and 5.5 respectively, and the top and side boundaries were located at Y/D = 6.0 and Z/D = 3.0 respectively.

In choosing the locations of the boundaries, White aimed to minimize the volume of the solution domain in order to minimize the grid spacing and the numerical truncation errors, but he ensured that the boundaries were located where the flow conditions could be accurately approximated. White assumed that at the locations of the top and side boundaries the flow conditions were close to mainstream inlet conditions. In addition, he assumed that at the location of the downstream boundary the gradients in the axial direction of all dependent variables were close to zero. These assumptions are generally supported by the measurements by Crabb and the measurements presented in Chapter 2.

4.2.2 Boundary Conditions

The equations being solved were elliptic in form and so boundary conditions were required on all six sides of the solution domain. The dependent variables for which conditions were required were $\overline{U}$, $\overline{V}$, $\overline{W}$, k, ε and $\overline{\Phi}$, $\overline{\Phi}$ representing the concentration of a passive scalar. The static pressure $\overline{P}$ had only to be set at a single point in the solution domain, and to accord with measured conditions it was given a value of zero at a point on the upper boundary of the domain, well away from the hole.

On the upstream boundary the $\overline{U}$ velocity component was set to the measured value of 12m/s, except over a thin region adjacent to the wall where the measured boundary layer profile was specified. The $\overline{V}$ and $\overline{W}$ velocity components and scalar concentration $\overline{\Phi}$ were set to zero, while the turbulence kinetic energy k was set to the measured value of $0.000023U_\infty^2$ and the dissipation rate ε obtained by assuming a length scale equal to the tunnel height.

On the downstream boundary the axial gradients of the dependent variables were assumed to be equal to zero,

i.e.
$$\frac{\partial \overline{U}}{\partial x} = \frac{\partial \overline{V}}{\partial x} = \frac{\partial \overline{W}}{\partial x} = \frac{\partial k}{\partial x} = \frac{\partial \varepsilon}{\partial x} = \frac{\partial \overline{\Phi}}{\partial x} = 0$$

The use of these conditions at a downstream distance of X/D = 5.5 is supported by the measurements presented in Chapter 2. Although some

reduction in the level of approximation involved can be obtained by placing the boundary farther downstream, White has shown that the difference in the solution obtained is negligible.

The boundary conditions specified in the symmetry plane Z/D = 0 were as follows:

$$\overline{W} = 0$$

$$\frac{\partial \overline{U}}{\partial z} = \frac{\partial \overline{V}}{\partial z} = \frac{\partial k}{\partial z} = \frac{\partial \varepsilon}{\partial z} = \frac{\partial \overline{\Phi}}{\partial z} = 0$$

Several sets of conditions were considered for the top and side boundaries. The results of Chapter 2 suggest that the conditions at the boundaries are closely approximated by the mainstream inlet conditions. These conditions were adopted initially and were found to produce a rapidly converged and accurate solution. Nevertheless, the conditions were thought to represent a potential source of error by not allowing mass to flow through the boundaries. By applying these conditions the acceleration of the mainstream is confined within the volume of the solution domain and may cause the $\overline{U}$ velocity components to be overpredicted. In addition, the conditions on the top boundary may influence the rate at which momentum is lost from the jet.

To determine whether these effects were significant or not, a number of calculations were performed using alternative sets of conditions which allowed mass to flow through the boundaries. Some of the conditions tested affected the stability of the numerical procedure, preventing a converged solution from being obtained. The problem was characterized by the build-up of a large pressure difference between the top and side boundaries, causing large quantities of fluid to flow in through one boundary and out through the other. The problem could not be resolved by adjusting the procedure's under-relaxation factors, and was finally resolved by setting the pressure on the top and side boundaries to zero, a condition in keeping with measured flow conditions. By starting from a condition of zero pressure everywhere in the solution domain, the boundary condition was applied simply by neglecting the pressure correction along the top and side boundaries. Failure to apply the pressure correction means that the

continuity equation is not satisfied along the boundaries; to resolve this problem the velocity components normal to the boundary were specified in such a way that the continuity equation was satisfied. For all other variables the gradients normal to the boundaries were set equal to zero. The conditions finally applied at the top and side boundaries can therefore be summarized as follows:

Top Boundary

$$\overline{P} = 0$$

$$\overline{V}_y = \overline{V}_{y-\delta y} - (\frac{\partial \overline{U}}{\partial x} + \frac{\partial \overline{W}}{\partial z})\delta y$$

$$\frac{\partial \overline{U}}{\partial y} = \frac{\partial \overline{W}}{\partial y} = \frac{\partial k}{\partial y} = \frac{\partial \varepsilon}{\partial y} = \frac{\partial \overline{\Phi}}{\partial y} = 0$$

Side Boundary

$$\overline{P} = 0$$

$$\overline{W}_z = \overline{W}_{z-\delta z} - (\frac{\partial \overline{U}}{\partial x} + \frac{\partial \overline{V}}{\partial y})\delta z$$

$$\frac{\partial \overline{U}}{\partial z} = \frac{\partial \overline{V}}{\partial z} = \frac{\partial k}{\partial z} = \frac{\partial \varepsilon}{\partial z} = \frac{\partial \overline{\Phi}}{\partial z} = 0$$

The use of these conditions produced small increases in the $\overline{V}$ velocity components in the jet (up to $0.03V_J$) and small decreases in the $\overline{U}$ velocity components in the mainstream (up to $0.02U_\infty$), together with an increase in the computer run time of about 10%. The changes produced were considered significant enough to warrant the use of the conditions in the calculations to be described later.

At the solid wall boundary the wall functions described in Chapter 3 were specified.

The remaining conditions to be specified were those in the jet exit plane. Apart from some special treatment where the edge of the hole intersects the rectangular grid lines, two sets of conditions were applied. In the first, and simplest, the $\overline{V}$ velocity component was assumed

to be uniform and equal to the area-averaged velocity V_J of the undisturbed jet. However, at low velocity ratios ($V_J/U_\infty < 3.0$) the flow in the jet exit plane is considerably distorted by the strong local pressure gradients, and the constant-velocity condition leads to significant errors.

Closer agreement with measurements can be achieved by applying the second set of conditions, in which the $\overline{V}$ velocity distribution is deduced from an assumption by Bergeles (1976) that the total pressure over the hole remains constant. By starting from a condition of zero static pressure everywhere in the solution domain the total pressure over the hole can be calculated initially from the equation:

$$P_{TOT} = \frac{1}{2} \rho V_J^2$$

In subsequent iterations the static pressure over the hole changes and the velocity is updated to comply with the equation:

$$P_{TOT} = \overline{P}_{STAT} + \frac{1}{2}\rho\overline{V}^2$$

An additional constraint is that the mass flow through the hole must remain constant. The use of this condition produces much closer agreement between calculated and measured $\overline{V}$ velocity distributions, as will be seen in Section 4.4.

Apart from the difference in the $\overline{V}$ velocity condition the two sets of boundary conditions at the hole were identical. The $\overline{U}$ and $\overline{W}$ velocity components were set equal to zero on the basis of measurements by Andreopoulos (1980), which show that these components are small. The turbulence kinetic energy was given the area-averaged value for a fully-developed turbulent pipe flow, and the dissipation rate was obtained by assuming a length scale equal to the pipe diameter. The scalar concentration was given a value of unity so that with the mainstream inlet value set to zero the calculated scalar concentrations could be compared directly with the non-dimensionalized measurements of Chapter 2.

4.2.3 Finite-Difference Grid

As explained in Chapter 2 the solutions are subject to a numerical truncation error known as numerical diffusion. Numerical diffusion occurs where upwind differencing is used to approximate the convection terms in the governing partial differential equations (i.e. where the cell Peclet numbers are greater than 2) and tends to smear the gradients of the dependent variables, producing solutions in which peak values are too low and diffusion rates are too high. The errors tend to be worst in areas of the flow where the velocity vectors are skewed relative to the numerical grid lines. Since cell Peclet numbers of greater than 2 occur extensively on the present grids, and since the deflection of the jet implies skewing of the velocity vectors, numerical diffusion represents a significant source of error.

Numerical diffusion can be reduced by grid refinement, but the limit on computer storage and the need for a reasonably low running time place a limit on the number of grid points that can be used. Thus care must be taken to distribute the available grid points as effectively as possible, by concentrating points where the numerical error terms are expected to be large.

As in previous studies, the policy adopted here was to concentrate the grid points near the semi-circular hole, with the grid spacing expanding in geometric progression away from the hole in all three co-ordinate directions. This ensures, on the one hand, that the profiles in the jet exit plane are accurately defined, and on the other, that there is a reasonable concentration of points in the bending region of the jet.

To assess the influence of numerical diffusion on the solution, two calculations were performed, one for a coarse grid of 20 x 15 x 15 points, and the other for a fine grid of 30 x 22 x 22 points (in the X, Y and Z co-ordinate directions respectively). With the coarse grid there were a total of 21 grid points within the semi-circular hole, and with the fine grid there were a total of 50. In addition, the fine-grid solution was subjected to an analysis devised by McGuirk and Rodi (1978) (described in Chapter 3) for which results are presented in the next section.

Figure 4.1 presents $\overline{U}$ velocity profiles for the symmetry plane Z/D = 0; this figure includes calculated profiles for the coarse grid and for the fine grid, and measured profiles presented by Crabb (1979). As can be seen, the calculated profiles are sensitive to grid refinement, the peaks in the profiles becoming more pronounced with grid refinement - a change symptomatic of a reduction in numerical diffusion. The refinement produces a general improvement in the level of agreement with measurements, and undoubtedly further improvements will occur with greater refinement. Unfortunately, it was not possible to refine the grid beyond 30 x 22 x 22 points, as this represented the maximum number of points allowed by the IBM 360/195 computer. Nevertheless, with the grid points available a good level of agreement has been obtained.

As explained in Chapter 3, a solution was taken to be converged when the sum of the mass sources in the continuity equation was less than 0.001 of the mass flow into the solution domain. The computer run time on the IBM 360/195 computer expressed as time per equation per iteration per node was 0.00022 seconds. For the coarse-grid calculation, approximately 120 iterations were needed to achieve a converged solution, and the total running time was about 14 minutes. For the fine-grid calculation, approximately 400 iterations were needed, and the total running time was about 130 minutes.

4.3 ASSESSMENT OF NUMERICAL DIFFUSION

The procedure described in Chapter 3 was used to assess the local levels of numerical diffusion in the fine-grid solution. The procedure was applied only to the $\overline{U}$ momentum equation, but as explained in Chapter 3 the results are expected to be roughly similar for the $\overline{V}$ and $\overline{W}$ equations.

Before discussing the variation of the error term it is useful to consider first the development of the calculated jet. Figures 4.2 to 4.5 present velocity vectors and scalar concentrations for planes normal to the three co-ordinate axes.

The velocity vectors and scalar concentrations in the symmetry plane (figures 4.2 and 4.4) show that the jet is deflected into the mainstream direction after a short distance and spreads rapidly in the X - Y plane. In the bending region the velocity vectors make a 45° angle to the numerical grid lines, and strong gradients of velocity and scalar concentration occur normal to the flow direction - conditions which give rise to large amounts of numerical diffusion. Similar conditions occur in planes normal to the X and Y axes (figures 4.3 and 4.5).

There is strong evidence of numerical diffusion around the sides of the jet, where the fluid can be seen to be entrained rapidly by the mainstream and follow a very low trajectory. This loss of momentum in the jet combined with the strong vortex motion (figure 4.3b) causes the jet to bifurcate, giving two peaks in scalar concentration, one on each side of the symmetry plane.

Figures 4.6 and 4.7 examine the numerical diffusion in greater detail for the planes X/D = 0 and 2.0. These figures show the balance of terms in the $\overline{U}$ momentum equation - nett convection (given by central differencing), pressure gradient, nett diffusion and the residual error term.

Figure 4.6 shows that the development of the jet is governed initially by the convection and pressure gradient terms, but also significantly by numerical diffusion. In the jet exit plane the dominant convection term is $\overline{V}\partial\overline{U}/\partial y$, which is large and positive and balanced by the pressure gradient term $1/\rho\ \partial\overline{P}/\partial x$. However, to the side of the jet the residual term rises to 70% of the largest term $(1/\rho\ \partial\overline{P}/\partial x)$ in the equation. Thus numerical diffusion around the sides of the jet is considerable, and probably accounts for the rapid loss of momentum from the jet.

As the jet rises away from the wall and is deflected, the residual term increases towards the jet centreline. At the same time, the pressure gradient term diminishes, and the individual convection terms become the dominant terms. $\overline{V}\partial\overline{U}/\partial y$, which was at first large and positive, becomes large and negative away from the wall and is balanced by $\overline{U}\partial\overline{U}/\partial x$. Numerical diffusion increases along the jet centreline and reaches 30% of the largest term.

By Y/D = 2.0 the pressure gradient term is much less significant, and although the term appears to balance the nett convection term, the individual convection terms are in fact up to five times larger.

The numerical diffusion term is undoubtedly a major cause of the loss of momentum in the jet, and is consequently a major cause of the underprediction of the velocity gradients and peak values in the downstream flow, as seen in figure 4.1. The cell Peclet numbers in the bending region are generally greater than 2 and reach values up to 50. Consequently, upwind differencing will be used even when the grid is refined, and numerical diffusion will continue to be present, although its effect will gradually diminish.

With downstream distance the physical diffusion terms play a greater role in the balance of the equation. In the plane X/D = 2.0 (figure 4.7) the highest values of nett diffusion occur between Y/D = 1.0 and 1.5, and the dominant term is $\Gamma \partial^2 \overline{U}/\partial z^2$, which reflects the rapid change in $\overline{U}$ velocity across the wake. Nevertheless, the individual convection terms remain the dominant terms, and give rise to a peaky numerical error profile with high positive and negative values.

The increase in importance of the physical diffusion terms is due to high local values of turbulence energy, which lead to high local values of turbulence viscosity. This turbulence is generated by the strong vorticity in the jet and is convected downstream to X/D = 2.0 with the jet.

The largest values of the error term in the plane X/D = 2.0 occur between Y/D = 1.5 and 2.5, where the velocity vectors make an angle of 45° with the X grid lines, and where there are strong gradients normal to the flow. Although the dominant terms in the plane are the individual convection terms, the pressure gradient term is still significant below Y/D = 1.0, where it convects mainstream fluid into the symmetry plane.

With downstream distance all the terms in the equation decrease in magnitude. Although the diffusion terms have greater relative importance, the convection terms remain the dominant terms (at least up to X/D =

5.5). On the basis of an analysis of the $\overline{U}$ momentum equation, therefore, the calculated flow appears to be governed mainly by inviscid dynamics and numerical diffusion.

However, Crabb (1979) has pointed out that the effect of the numerical diffusion on the mean velocity gradients tends to cause the turbulence production and hence the physical diffusion to be underpredicted. Consequently, on a coarse grid the main mechanism for diffusion tends to be numerical diffusion. However, as the grid is refined the physical diffusion will increase as the numerical diffusion decreases.

So far the discussion has centred on the $\overline{U}$ momentum equation. However, designers of combustors require an accurate knowledge of the temperature field, and hence a knowledge of the effect of numerical diffusion on scalar equations. Although the analysis was not applied to the scalar equation, it is possible to suggest the likely effect of the numerical diffusion.

The conditions under which numerical diffusion occurs in the scalar equation appear to be as wide-spread as, and often coincident with, those for the $\overline{U}$ equation, and it is therefore likely that the effect of numerical diffusion on the scalar field will be roughly similar to that on the $\overline{U}$ velocity field. In addition, the distribution of the scalar is governed strongly by convection, particularly in the near field, and consequently the accuracy of the scalar field can be expected to be no more than that of the velocity field.

4.4 RESULTS

The fine-grid solution was compared in the near-field with measurements by Crabb (1979), and in the far field with measurements presented in Chapter 2. The measurements by Crabb consist of mean velocity components and turbulence normal stress components. These measurements were obtained by laser-Doppler anemometry and are therefore thought to be among the most accurate near-field measurements obtained so far. (Other near-field measurements of mean velocity and turbulence have invariably been obtained by hot-wire anemometry which is much less accurate in this highly turbulent region.) The measurements presented in Chapter 2 consist of $\overline{U}$ velocity

components and scalar concentration measurements obtained at and beyond X/D = 4.0, in addition to wall static pressure measurements. Crabb gives the following error bounds for the near-field measurements: $\overline{U}/U_\infty, \overline{V}/V_J \pm 3\%$; $\hat{u}/U_\infty$, $\hat{v}/V_J \pm 7\%$; and in Chapter 2 the following bounds are given for the far-field measurements: $\overline{U}/U_\infty \pm 2\%$; $\overline{\theta}/\theta_J \pm 2\%$, Cp $\pm$ 0.02. (The measurements of wall static pressure are less accurate immediately downstream of the hole because of flow unsteadiness, and here the bounds Cp $\pm$ 0.1 are more appropriate.)

Mean Velocity and Mean Scalar Fields

Figures 4.8 and 4.9 compare calculated and measured $\overline{V}$ velocity profiles for the near-wall plane Y/D = 0.25. These figures show calculated profiles obtained by applying the constant velocity condition and by applying the constant total pressure condition in the jet exit plane. The flow within the hole is considerably distorted by the strong local pressure gradients, and so the constant velocity condition leads to poor agreement with the measured profiles. The constant total pressure condition, on the other hand, gives much closer agreement, though the distortion is slightly underpredicted. In view of this improvement, all subsequent comparisons of calculation and measurement feature the constant total pressure condition.

Figures 4.10 and 4.11 compare calculated and measured $\overline{U}$ velocity profiles for the same near-wall plane. In the profile for Z/D = 0 the mainstream can be seen to decelerate as it approaches the jet, but the velocity does not reduce to zero because the jet yields to the flow. Downstream of the hole the calculated profile contains negative velocities, representing reverse flow, which are not present in the measured profile. These negative velocities can also be seen in the $\overline{U}$ velocity profiles of figure 4.1, and can be seen to begin at a point immediately adjacent to the wall surface. From figure 4.1 it is not clear where the measured reverse flow region begins because of the lack of measurement points, but the available points suggest that it begins at a point some distance away from the wall. This is confirmed by the absence of any reverse flow region in the horizontal profile of figure 4.10. This difference in the starting point of the reverse flow region is consistent with the calculated and measured wall static pressure distributions and will be discussed in further detail

later.

In figure 4.11 the measured $\overline{U}$ velocity profile for Z/D = 0.5 contains a large peak caused by the mainstream accelerating around the jet. The calculated profile, on the other hand, does not contain a peak, but first falls to a value of about $0.7U_\infty$ before rising to a value only just above the mainstream inlet value. Examination of the calculated flow shows, however, that the expected peak does occur, but at a location away from the edge of the hole at Z/D = 0.7.

This shift in the location of the peak is probably to a large extent due to numerical error. In Section 4.3 it was seen that the residual term in the $\overline{U}$ momentum equation was estimated at 70% of the largest term in the equation, and it seems reasonable to assume that this would cause the observed error in the velocities. Other contributory factors could be measurement error and error in the measurement locations, but if the error bounds given by Crabb are assumed to be correct ($\pm$ 3% for $\overline{U}$ and $\pm$ 0.004D for the measurement locations) then these factors will make a negligible contribution.

Figures 4.12 and 4.13 present comparisons of calculated and measured $\overline{U}$ and $\overline{V}$ velocities for a horizontal plane higher above the wall, Y/D = 1.35. At this height the jet, in both calculation and measurement, has turned through an angle of 33°, and has therefore acquired a $\overline{U}$ velocity component equal to 65% of the $\overline{V}$ component. The centreline velocity of the measured jet has remained unchanged from its jet exit value, but that of the calculated jet has diminished by some 22%, with the result that the peak in the calculated $\overline{U}$ and $\overline{V}$ velocity profiles is considerably underpredicted.

Probably the major cause of the loss of momentum is again numerical diffusion. In Section 4.3 it was seen that the residual term in the $\overline{U}$ momentum equation rises to a value of 30% along the jet centreline, and it seems reasonable to suppose that this level of error and the cumulative nature of the numerical diffusion could account for a 22% error in velocity.

Other contributory factors could be measurement error and error in the turbulence modelling, but these are unlikely to be major contributory factors. The measurement error in $\overline{U}$ and $\overline{V}$ and hence $\sqrt{(\overline{U}^2 + \overline{V}^2)}$ is 3%, which is small in comparison with the observed error. The turbulence stresses, on the other hand, appear to be influenced much more by the numerical diffusion than by modelling errors, and results presented by Crabb and to be presented here show that the high levels of numerical diffusion cause the turbulence stresses to be underpredicted, and thus cause a loss in diffusion rather than an increase.

Figures 4.14 and 4.15 compare calculated and measured contours of $\overline{U}$ velocity and mean scalar concentration for the cross-plane X/D = 4.0. As can be seen, there is close agreement in the spreading of the jet and the overall position of the fluid in the cross-plane. However, there are considerable errors in detail, the most prominent of which is the presence of two scalar concentration peaks. In the calculation the jet bifurcates causing two scalar peaks to form, one on each side of the symmetry plane. The velocity distribution is also in error and likewise it contains two peaks instead of one.

These errors appear to be consistent with the considerable loss of momentum described earlier, and can, therefore, be attributed mainly to numerical diffusion. The bifurcation of the jet and the formation of two scalar peaks is consistent with a high initial loss of momentum from around the periphery of the jet, and the loss of the velocity peak along the jet centreline is also consistent with a loss of momentum. The two peaks that do appear are caused by mainstream fluid accelerating around the jet, and can be traced upstream to locations either side of the hole; one of these peaks was seen previously in the $\overline{U}$ velocity profile for Y/D = 0.25, Z/D = 0.5 (figure 4.11).

Further evidence to suggest that numerical diffusion is the main cause of the errors has been presented by Claus (1983), who reports a series of similar calculations of the present flow, but using finer grids. Plots of calculated scalar concentration for a cross-section of the jet show a clear improvement with grid refinement, until for a grid of 90 x 40 x 22 points there is very close agreement with the present measurements.

Vortex Field

A characteristic feature of a jet in a deflecting stream is a strong counter-rotating vortex motion in the jet cross-section. In the following paragraphs this vortex motion is described with reference to the calculated results.

The vortex motion is illustrated by figure 4.16, which presents a plot of velocity vectors resolved into the cross-plane X/D = 2.0. On the side of the symmetry plane shown the vortex motion is clockwise when viewed facing upstream, and a similar but anticlockwise motion exists on the other side of the symmetry plane. A closer examination of figure 4.16 shows that there are two vortex tubes on each side of the symmetry plane, labelled 1 and 2 in the figure. The two vortex tubes contribute to the vortex motion as a whole, but originate from different parts of the flow. The first tube, labelled 1, can be traced to a point adjacent to the wall immediately downstream of the hole. Vortex motion associated with this tube can be seen in the velocity vector plot for the horizontal plane Y/D = 0.25 presented in figure 4.17. This vortex is consistent with the bound vortex found behind a circular cylinder in a cross-flow at very low Reynolds numbers, and a similar but counter-rotating vortex will be seen on the other side of the symmetry plane. The second tube, labelled 2, can be traced to the side of the hole and can be seen in the velocity vector plot for the cross-plane X/D = 0.25, figure 4.18. This vortex tube is formed in the shear layer between the jet and the horizontal mainstream, and from its position in figure 4.18 it can be traced around the jet and can be seen to form the second vortex tube on the other side of the symmetry plane. There is also a third source of vorticity in the boundary layer of the approaching mainstream flow. Upstream of the jet this vorticity can be seen as vortex lines running in the Z direction. On meeting with the jet these vortex lines are swept around the jet and form a horse-shoe vortex whose rotation when viewed facing upstream is in the opposite sense to that of vortices 1 and 2.

Experimental evidence of the vortex structure described above can be found in a number of papers, e.g. Moussa et al (1977), Andreopoulos and Rodi (1984). Moussa et al (1977) identify a further source of vorticity in the

form of vortex rings in the pipe flow ahead of the jet exit. These vortex rings are tilted and stretched along the jet and so contribute to the counter-rotating vortex motion. In examining the calculation it was not possible to distinguish clearly between this vorticity and the vorticity between the jet and the horizontal mainstream flow, and it is assumed that the vorticity contributes to vortex 2.

A number of workers, e.g. McMahon et al (1971), Moussa et al (1977), have observed in high Reynolds number experiments that the bound vortex (vortex 1) does not remain attached to the jet, but is shed periodically. Although the phenomenon was not investigated thoroughly by Crabb or in the present work, it is likely that in the high eynolds number flow vortex shedding would have occurred. This vortex shedding could possibly lead to a difference in the time-averaged vorticity in the jet, and hence affect the cross-sectional shape of the jet. However, given Claus's results and the evidence presented here this seems unlikely to be a major cause of error in the jet cross-section, and the major cause of error is probably numerical diffusion.

Wall Static Pressure Field

The measurements presented in Chapter 2 include wall static pressure coefficients, and these are compared with the calculated coefficients in figure 4.19. The calculated coefficients can be seen to be consistent with the velocity vectors in figure 4.17, as expected. The calculated pressure distribution contains a lobe of very low pressure over which the flow accelerates, and a region of severe adverse pressure gradient over which the flow reverses. The measured distribution is similar to the calculated distribution, but the adverse pressure gradient is much weaker, and the contours in this region take the form of an additional lobe shape. The lack of flow reversal in this region (figure 4.10) appears to be consistent with the weaker pressure gradient.

One possible contributory factor to these differences is measurement error, but the error bounds ($\pm$ 3% for $\overline{U}$ and $\pm$ 0.1 for Cp) are small in comparison with the observed error, and so this cannot be a major factor. Probably the major factor is the presence of flow unsteadiness. As discussed

earlier, the presence of flow unsteadiness is well documented, but is not taken into account because of the steady-state nature of the calculation.

Turbulence Field

Figures 4.20 to 4.23 compare calculated and measured $\hat{u}$ and $\hat{v}$ normal stress profiles for the plane Y/D = 0.25. The measured profiles are reproduced well by the calculation, but the peaks in the profiles around the edge of the jet are underpredicted. Probably the main cause of this error is the use of a uniform value of turbulence energy in the jet exit plane. The value used was the area-averaged value for a fully-developed turbulent pipe flow, calculated from measurements by Laufer (1954). However, these measurements show that the turbulence energy is non-uniform, rising to a peak near the pipe wall equal to approximately twice the area-averaged value, a difference large enough to account for the errors in the stress profiles. Another contributory factor could be lack of grid refinement. This source of error is suggested by the fact that refinement of the grid caused the turbulence energy around the periphery of the jet to increase by up to 70%, a significant increase in relation to the observed error.

Another feature of figures 4.22 and 4.23 is that the stresses fall off too rapidly immediately downstream of the hole, particularly in the profile for Z/D = 0. As a result, the $\hat{u}$ normal stresses at the location of the downstream boundary amount to only 15 to 20% of measured values. As is explained later, a large proportion of this error is due possibly to the fact that the measured turbulence stresses contain a contribution from flow unsteadiness due to vortex shedding.

A careful examination was made of the turbulence field, which showed that most of the turbulence in the flow is generated by the strong shear layers of the counter-rotating vortices. The peak in the cross-sectional distribution of turbulence energy can be traced upstream along the jet to a point immediately downstream of the jet exit in the centre of vortex 1. Turbulence is generated and transported along the vortex lines and the cross-sectional distribution of turbulence energy, under the influence of the velocity field, acquires a kidney shape with a peak on each side of the symmetry plane which is roughly coincident with the peak in scalar

concentration.

The generation and transport of the turbulence is reflected in the measured and calculated profiles of $\hat{u}$ and $\hat{v}$ normal stress for the plane Y/D = 1.35, figures 4.24 to 4.27, particularly the $\hat{u}$ normal stress profiles. The profiles contain a peak downstream of the jet exit indicating where the trajectory of the turbulent fluid crosses the horizontal plane.

The importance of turbulence generated by the flow is illustrated by the fact that the turbulence energy in the centre of vortex 1 at a point immediately downstream of the hole is an order of magnitude greater than the turbulence energy in the jet exit plane.

In the $\hat{u}$ and $\hat{v}$ normal stress profiles for Y/D = 1.35 the stresses are considerably underpredicted in the downstream region. The peak in the $\hat{u}$ profile for Z/D = 0 is underpredicted by 26%, while the peak in the profile for Z/D = 0.5 is underpredicted by 22%. These differences increase with downstream distance, becoming at the downstream boundary, 60% for Z/D = 0 and 40% for Z/D = 0.5, while in the $\hat{v}$ normal stress profiles they become 70% for Z/D = 0 and 45% for Z/D = 0.5.

Probably the main cause of these errors is again numerical diffusion. The vortex flow in which the turbulence is generated gives rise to a great deal of numerical diffusion, and this numerical diffusion reduces the rate at which turbulence is produced through its effect on the mean velocity gradients. Evidence of the presence of numerical diffusion was seen earlier in figure 4.7, which shows the distribution of the residual term for the cross-plane X/D = 2.0. Close to the centre of the vortex motion the residual term rises to a peak value equal to 26% of the largest term in the $\overline{U}$ momentum equation. The location and size of this term are such that the generation of turbulence is likely to be considerably underpredicted.

With grid refinement the numerical diffusion, and hence the errors in the turbulence field, can be expected to diminish. Evidence of the improvement produced by grid refinement can be seen in figure 4.28, which compares calculated distributions of turbulence energy for the cross-plane X/D = 2.0 for a coarse grid and for a fine grid. At the centre of the vortex motion

the turbulence energy k/U_∞^2 increases from a value of 0.38 to a value of 0.41 with grid refinement, an increase of about 8%, or 4% in $\sqrt{k}/U_\infty$. This compares with an error of about 50% in the $\hat{u}$ and $\hat{v}$ normal stresses at the same location. Although small, the improvement can be expected to increase with further grid refinement, and it is expected that much of the error in the turbulence field could be eliminated given the necessary computing capacity.

Although numerical diffusion is probably the main cause of errors in the plane Y/D = 1.35, where the flow is dominated by the vortex motion, it is unlikely to be the main cause of errors in near-wall planes such as Y/D = 0.25 (figures 4.22 and 4.23). Examination of the calculated results shows that the near-wall flow consists mainly of low-turbulence mainstream drawn into the symmetry plane under the influence of the vortex motion and the pressure field. Grid refinement is, therefore, unlikely to produce any major increase in the turbulence levels in this region.

In this case the main cause of error is possibly a contribution to the measurements from flow unsteadiness due to shedding from the jet. It was suggested earlier that the main cause of differences between the calculated and measured wall static pressures was the presence of vortex shedding, and this is possibly also the case with the turbulence stresses.

4.5 CONCLUSIONS AND IMPLICATIONS OF THE CALCULATIONS

This chapter has described the results of numerical calculations of a single jet in a deflecting stream. This section summarizes the main conclusions of the calculations, and discusses their implications for the development of the procedure. The main conclusions are as follows:

A numerical calculation of a single jet in a deflecting stream for a velocity ratio of 2.3 produced the correct trajectory and spreading of the jet.

An analysis of the solution showed that the calculated flow was influenced to a considerable extent by numerical diffusion. This numerical diffusion is thought to be responsible for the

overprediction of the loss of momentum from the jet and subsequent detailed errors in the velocity and scalar fields downstream. In particular, the scalar distributions contained two peaks, indicating that the jet had bifurcated, while the measurements contained only one peak.

The calculated turbulence stresses fell well below measured levels, and the error was thought to be due to numerical diffusion through its effect on turbulence production. However, the lack of physical diffusion did not appear to affect the spreading of the jet, probably because of the effect of numerical diffusion on the mean flow.

Although the turbulence levels were too low, the trends in the measured stresses were accurately calculated. Thus, the $k - \varepsilon$ model can be recommended for use in further calculations of jets in a deflecting stream.

In relation to the combustor application, the most important results of the calculations are the trajectory and spreading of the jet. These quantities were calculated accurately for the present flow.

Other workers using similar procedures have shown that these quantities can be calculated accurately for velocity ratios other than 2.3. White (1983), for example, presents accurate calculations of the trajectory and spreading for velocity ratios of 0.5, 1.0 and 2.0, and similar results were obtained by Jones and McGuirk (1979) for velocity ratios of 5.7 and 8.5. Calculations of a single row of jets were presented by Khan, McGuirk and Whitelaw (1981), for a velocity ratio of 2.3 and a variety of pitch-to-diameter ratios and height-to-diameter ratios, which also gave the correct trajectory and spreading.

The results of the present work show, however, that the calculations are influenced to a considerable extent by numerical diffusion. This may not be immediately apparent from the accurate calculation of the trajectory and spreading, and so caution must be exercised when applying the procedure to the single jet and to other more complex arrangements. Results by Claus

(1983) show that an accurate calculation of the flow detail in a single jet requires a grid of around 90 x 40 x 22 points. This number is likely to increase considerably in flows of greater aerodynamic complexity, and in the long term it would be worthwhile to investigate alternative finite-difference schemes.

The numerical diffusion appears to have a considerable influence on the levels of turbulence generated by the turbulence model through its effect on turbulence production. More complex models are likely to be affected in the same way, and so there appears to be no advantage in introducing greater complexity into the modelling, particularly as the present model accurately reproduces the trends in the measured turbulence field.

CHAPTER 5

CALCULATION OF TWO OPPOSED SINGLE JETS IN A DEFLECTING STREAM

5.1 INTRODUCTION

This chapter presents calculations of two opposed single jets in a deflecting stream. Velocity ratios of 1.0 and 1.8 and a height-to-diameter ratio of 4.0 were chosen for which measurements were presented in Chapter 2. These measurements are limited to the far field and are therefore less comprehensive than those for the single jet. However, no difficulty arises in assessing the calculations if reference is made to the single-jet results where necessary.

As demonstrated in Chapter 2, the parameters chosen produce two extremes of flow behaviour, one involving weak interaction between the jets, and one involving strong interaction. The measurements therefore provide a stringent test of the calculation procedure.

5.2 COMPUTATIONAL DETAILS

5.2.1 Solution Domain

As in the single-jet calculation the solution domain consisted of a rectangular volume, but with boundaries in two symmetry planes, Z/D = 0 and Y/D = 2.0. The upstream boundary was again located at X/D = -2.0, but the downstream boundary was moved farther downstream to X/D = 8.0 to allow comparison with measurements of mean velocity and mean scalar concentration at this location. The location of the side boundary was different for the two velocity ratios to allow for the difference in the lateral spreading of the jet. The measurements of Chapter 2 indicate a return to mainstream conditions by Z/D = 3.0 at the lower velocity ratio, but not until Z/D = 4.0 at the higher velocity ratio, and the boundary locations were chosen accordingly.

5.2.2 Boundary Conditions

As in the single-jet calculation, the $\overline{U}$ velocity component on the upstream boundary was set to the measured freestream value, in this case 11.1m/s, and the measured boundary layer profile was specified near the wall. The $\overline{V}$ and $\overline{W}$ velocity components and scalar concentration $\overline{\Phi}$ were given a value of zero, and the turbulence energy k was set to the measured freestream value, in this case $0.000037U_\infty^2$, while the dissipation rate was obtained by assuming that the turbulence length scale was equal to the tunnel height (H = 4D).

On the downstream boundary the axial gradients of all the dependent variables were assumed to be equal to zero.

Symmetry conditions were specified on the top boundary and on the boundary Z/D = 0.

In order to allow mass to flow through the side boundary, Z/D = 3.0 (or 4.0), the conditions developed for the single jet were again specified (see Chapter 4, Section 4.2).

On the solid wall boundary the wall functions described in Chapter 3 were specified. The constant total pressure condition was again used to calculate the $\overline{V}$ velocity components in the exit plane of the hole, in view of the satisfactory results obtained for the single jet. The $\overline{U}$ and $\overline{W}$ components in the exit plane of the hole were again set equal to zero, and the scalar concentration $\overline{\Phi}$ was set equal to 1.0. The turbulence energy k was given the area-averaged value for a fully-developed turbulent pipe flow, and the dissipation rate ε was obtained by assuming that the turbulence length scale was equal to the diameter of the hole.

5.2.3 Finite Difference Grid

One calculation was carried out for each velocity ratio using the maximum number of grid points. As in the single-jet calculation there were 30 x 22 x 22 points in the X, Y and Z directions respectively. The grid spacing was non-uniform in the X and Z directions, and increased in geometric

progression away from the hole, as in the single-jet calculation. In the Y direction a uniform spacing was used, which gave spacings comparable with the smallest spacings in the X and Z directions.

As in the single-jet calculation the solutions were taken to be converged when the sum of the mass sources in the continuity equation was less than 0.001 of the mass flow into the solution domain. The computer run time on the IBM 360/195 computer, expressed as time per equation per iteration per node, was 0.00022 seconds. The calculation for the velocity ratio 1.8 was begun with uniform conditions in the solution domain and required approximately 400 iterations to achieve convergence and a total run time of about 150 minutes. To reduce the number of iterations and run time, the calculation for the velocity ratio 1.0 was started from the solution for velocity ratio 1.8; this calculation required only 150 iterations and 56 minutes of run time.

5.3 RESULTS

The measurements for the two opposed single jets consisted of $\overline{U}$ mean velocity components (obtained by Pitot tube) and mean scalar concentrations. The mean velocity components were obtained at and beyond X/D = 4.0, and the scalar concentrations at and beyond X/D = 2.0. The measurements for the velocity ratio 1.8 also included turbulence normal and shear stresses in the cross-plane X/D = 8.0.

Figures 5.1 and 5.2 compare calculated and measured $\overline{U}$ velocity components and scalar concentrations for the velocity ratio 1.0. The scalar concentrations show that in both calculation and measurement the jets achieve little penetration into the mainstream and do not interact until far downstream. As can be seen, the calculated trajectory and rate of spreading are in close agreement with measurement. However, there are significant errors in the velocity deficit in the wake and in the location of the peak scalar concentration. As in the single-jet calculation, the jets bifurcate, and peaks in scalar concentration appear on each side of the symmetry plane Z/D = 0. As before the error is probably caused by numerical diffusion due to lack of grid refinement.

Figures 5.3 and 5.4 compare calculated and measured $\overline{U}$ velocities and scalar concentrations for the velocity ratio 1.8. In this case the jets penetrate to the mid-plane Y/D = 2.0 and interact strongly. In both calculation and measurement the jets bifurcate about Z/D = 0, but in the calculation the jets do not combine sufficiently, and the resulting flow contains four peaks in concentration instead of two. Examination of the calculated results shows that the jets lose momentum rapidly over the initial part of their trajectory; the rate of loss of momentum is probably too rapid and the major cause of the lack of interaction. It may be recalled that in the single-jet calculation the jet also lost momentum too rapidly because of numerical diffusion, and the locations of the two scalar peaks were too low as a result. Notwithstanding this error, the flow appears to have been calculated particularly well, with the spreading of the jet accurately reproduced.

Figures 5.5 and 5.6 compare calculated and measured turbulence stresses for the cross-plane X/D = 8.0. The calculated and measured normal stresses, $\hat{u}$, $\hat{v}$ and $\hat{w}$, are in close agreement except at Z/D = 0. At Z/D = 0, Y/D = 2.0, for example, the $\hat{u}$ and $\hat{v}$ stresses are too high, while at Z/D = 0.0, Y/D = 0.0 all the stresses are too low, especially the $\hat{w}$ stress. The overprediction of the $\hat{u}$ and $\hat{v}$ stresses at Z/D = 0, Y/D = 2.0 is probably due to the higher velocity gradient $\partial\overline{U}/\partial y$ in the calculation (see figure 5.3). The error at Z/D = 0, Y/D = 0, on the other hand, is probably due to the fact that the calculation does not model accurately the interaction of the two fluid streams meeting in the low pressure region behind the jet. It is also possible that the measured flow contains some unsteadiness due to vortex shedding which, of course, is not represented in the calculation.

Figure 5.6 compares calculated and measured shear stresses. This figure also reveals errors, particularly in the $\overline{uv}$ stress. These errors appear to be due to the differences in the velocity field seen in figure 5.3. In the calculation the $\overline{uv}$ stress field contains a region of high stress running downwards from Z/D = 0, Y/D = 1.75 to Z/D = 0.8, Y/D = 0.8 and then upwards to Z/D = 1.6, Y/D = 1.2. This corresponds to a region of high velocity gradient, $\partial\overline{U}/\partial y$, in the mean velocity field. In the measurements the velocity gradient $\partial\overline{U}/\partial y$ is much lower, and the peaks in the $\overline{uv}$ shear stress distribution are much less pronounced.

The calculated and measured $\overline{uw}$ stresses agree more closely except at Z/D = 0.8. At Z/D = 0.8, Y/D = 1.5 the measured $\overline{uw}$ stress is large and negative, whereas the calculated stress is close to zero. This difference is due to the difference in the position of the wake (or wakes) in each case. In the calculation the wake bifurcates and the two wakes that result are centred at Y/D = 1.5, Z/D = 0.8 and Y/D = 1.5, Z/D = -0.8 respectively. Hence, the velocity gradient $\partial\overline{U}/\partial z$ and the shear stress $\overline{uw}$ at these two locations are close to zero. In the measurements the wake does not bifurcate, and the single wake is centred at Y/D = 2.0, Z/D = 0. Hence, the velocity gradient $\partial\overline{U}/\partial z$ at Y/D = 1.5, Z/D = 0.8 is large and positive while the shear stress $\overline{uw}$ is large and negative.

5.4 CONCLUSIONS AND IMPLICATIONS OF THE CALCULATIONS

This chapter has presented the results of calculations of two opposed single jets in a deflecting stream. This section summarizes the conclusions arising from the calculations, and discusses their implications for the development of the numerical procedure. The main conclusions are as follows:

Numerical calculations of two opposed single jets in a deflecting stream for a height-to-diameter ratio of 4.0 and velocity ratios of 1.0 and 1.8 produced the correct trajectory and overall rate of spreading of the jets.

At both velocity ratios the jets bifurcated, with each jet producing two peaks in scalar concentration. At the lower velocity ratio the bifurcation was inconsistent with measured flow behaviour, and was attributed to numerical diffusion. At the higher velocity ratio the bifurcation was consistent with measured flow behaviour, but the calculation underpredicted the interaction of the jets, and the resulting flow contained a total of four peaks in scalar concentration instead of two; this error was also attributed to numerical diffusion.

The trends in the measured turbulence stresses were accurately

calculated. Errors that did occur were attributable to differences in the mean velocity field which, again, were attributable to numerical diffusion.

As pointed out in Chapter 4, the most important results of the calculations in relation to the combustor application are the trajectory and spreading of the jets. The results of the present calculations indicate that these quantities were calculated accurately. As in the single-jet calculation the solutions were affected to a certain extent by numerical diffusion, but the resulting errors tended to be detailed in nature. However, if the procedure is to be developed to deal with much greater aerodynamic complexity, then it would be worthwhile to investigate alternative finite-difference schemes.

For the present, however, the calculations could be extended with caution to more complex jet configurations. The next step in complexity would appear to be two opposed rows of jets, and measurements for this configuration have been reported by Khan and Whitelaw (1980b) and Khan (1982). The measurements by Khan and Whitelaw were obtained for a combination of a high velocity ratio and a low height-to-diameter ratio, which caused the jets to impinge and slip over each other, so that an asymmetric flow was produced from a nominally symmetric arrangement of holes. Such an arrangement would produce a symmetric solution in a numerical calculation, and so the measurements are not suitable for the present purpose.

However, Khan (1982) repeated the measurements with lower velocity ratios which gave symmetric flow. By varying the velocity ratio and pitch-to-diameter ratio, Khan produced a variety of flow behaviour, with the opposed jets either forming two jet cores, or bifurcating to form four jet cores, or bifurcating and combining to form two mixed jet cores. Thus, the measurements represent an ideal basis on which to develop the procedure. Details of these measurements may also be found in the paper by Atkinson, Khan and Whitelaw (1982), where they are combined with the present measurements of two opposed single jets.

CHAPTER 6

CALCULATIONS OF A CONFINED DISC-STABILIZED DIFFUSION FLAME

6.1 INTRODUCTION

This chapter describes a numerical procedure for the calculation of local flow properties in a simple model combustor, and compares calculated results with the measurements by Elliman (1977). The procedure was developed for the calculation of a simple gaseous-fuelled flame with the fuel and oxidant injected separately, and for a combustor having a simple geometry. The work is intended as a further preliminary step in the development of a more general procedure for the calculation of complex flows in practical combustors.

Two essential components of a procedure for the calculation of turbulent combusting flows are a turbulence model and a combustion model. The main aim of the present work was to assess the performances of these two components. In order to eliminate numerical errors so that the models could be assessed accurately, the procedure was developed for a simple model combustor, either two-dimensional or axisymmetric in form, but one containing some of the complex aerodynamic flow features of a practical combustor.

The calculations were compared with a previously reported set of measurements, and there were several sets of measurements from which to choose. Baker et al (1974) reported measurements of U mean velocity components and turbulence normal stresses in an axisymmetric combustor. The measurements were obtained in an isothermal air flow and in a flame of air and natural gas with swirl numbers of 0 and 0.52 in each case. Owen et al (1976) reported measurements of mean velocity components, mean temperature and mean species concentrations for a flame of air and natural gas in an axisymmetric combustor. The measurements were obtained only in the combusting flow for different values of pressure, fuel/air ratio and swirl number. Elliman (1977) presented measurements of a disc-stabilized methane/air flame in an axisymmetric combustor. Measurements of U and V mean velocity components, mean temperature and local mean equivalence ratio

were obtained in the combusting flow for different values of Reynolds number and overall equivalence ratio. In addition, measurements of U and V mean velocity components were obtained in an isothermal air flow at two Reynolds number values.

Any of the measurements described above could be selected as the basis on which to assess the calculations. However, only the measurements by Elliman offer detailed coverage of both isothermal and combusting flow; this is an important advantage in the present context as it enables the turbulence model to be assessed independently of the combustion model. In addition, the recirculation zone in the Elliman combustor is a feature of the primary zone of practical gas-turbine combustors. Hence, the measurements by Elliman were selected as the experimental data.

The Elliman combustor is shown in figure 6.1 and consisted of a cylinder of 150mm diameter and 400mm length with a centrally located 125mm diameter baffle whose circumference had been machined to an angle of 45°. Air was admitted through the annulus between the baffle and cylinder and methane through a 10.5mm diameter hole in the centre of the baffle. Measurements of mean velocity and mean temperature were made with a 7-hole spherical impact probe and an exposed bead thermocouple probe respectively, and the local mean equivalence ratio was determined from gas samples taken from an uncooled sampling probe. The method of gas analysis was described by Elliman (1977), and was suitable for the measurement of gas samples with an equivalence ratio of not greater than 1.5. Elliman provided estimates of the errors in the measurements and these are reproduced in table 6.1.

6.2 CALCULATION PROCEDURE

6.2.1 Transport Equations and Turbulence Model

The set of equations describing the flow in the combustor were expressed in cylindrical polar co-ordinates with the independent variables defined as axial distance from the baffle and radius from the combustor centreline. For variable density flows two types of averaging may be used: either unweighted averaging as employed in Chapter 3 or density-weighted averaging as proposed by Favre (1969). Density-weighted averaging can be represented

by the equations:

$$\rho U = \overline{\rho U} + \rho u'' = \overline{\rho \tilde{U}} + \rho u''; \quad \rho \Phi = \overline{\rho \Phi} + \rho \phi'' = \overline{\rho \tilde{\Phi}} + \rho \phi''$$

$$\text{where } \overline{\rho U} = \lim_{\tau \to \infty} \frac{1}{\tau} \int_{t_o}^{t_o + \tau} \rho U dt \qquad \text{and } \overline{\rho u''} = 0 \qquad \text{but } \overline{u''} \neq 0$$

The solution of the density-weighted equations yields density-weighted mean values of the velocity components and scalars. In the present work the solution of the density-weighted equations is more appropriate since the quantities measured by the Pitot and sampling probes are close to density-weighted mean quantities. In addition, correlations involving the fluctuating density $\overline{\rho' u'_i}$ and $\overline{\rho' \phi'}$ which are present in the unweighted equations are absent from the density-weighted equations, and the use of the latter equations avoids the need to model these terms. Density-weighted mean values are, however, not appropriate for all of the measured quantities: the quantity measured by the thermocouple probe is thought to be close to an unweighted mean temperature, and in order to solve for this quantity it is necessary either to calculate the correlation $\overline{\rho' \phi'}$ from modelling assumptions or to provide some other equivalent information. In the present model, information is provided in the form of a probability density function.

For high Reynolds number flows the general form of the density-weighted averaged equations is given by:

$$\frac{\partial(\overline{\rho}\tilde{U}\tilde{\Phi})}{\partial x} + \frac{1}{r}\frac{\partial}{\partial r}(r\overline{\rho}\tilde{V}\tilde{\Phi}) = \frac{\partial}{\partial x}\left(a \frac{\partial \tilde{\Phi}}{\partial x}\right) + \frac{1}{r}\frac{\partial}{\partial r}\left(r\, a \frac{\partial \tilde{\Phi}}{\partial r}\right) + S$$

for which corresponding values of a and S are given in table 6.2. The formulation of the equation implies the use of the density-weighted form of the $k - \varepsilon$ turbulence model, which is given by:

$$\widetilde{\overline{\rho u''^2}} = \frac{2}{3}\overline{\rho} k - 2\mu_T \frac{\partial \tilde{U}}{\partial x} \qquad \widetilde{\overline{\rho v''^2}} = \frac{2}{3}\overline{\rho} k - 2\mu_T \frac{\partial \tilde{V}}{\partial r}$$

$$\widetilde{\overline{\rho w''^2}} = \frac{2}{3}\overline{\rho}k - 2\mu_T\frac{\tilde{V}}{r} \qquad \widetilde{\overline{\rho u''v''}} = \mu_T\left(\frac{\partial\tilde{U}}{\partial r} + \frac{\partial\tilde{V}}{\partial x}\right),$$

the turbulence viscosity μ_T being defined by:

$$\mu_T = C_\mu\frac{\overline{\rho}k^2}{\varepsilon}$$

where k and ε are the turbulence kinetic energy and dissipation rate respectively. In scalar transport equations the following density-weighted equations are used:

$$\widetilde{\overline{\rho u''\phi''}} = \frac{\mu_T}{\sigma_T}\frac{\partial\tilde{\Phi}}{\partial x} \qquad \widetilde{\overline{\rho v''\phi''}} = \frac{\mu_T}{\sigma_T}\frac{\partial\tilde{\Phi}}{\partial r}$$

where σ_T is a constant Prandtl/Schmidt number.

The turbulence kinetic energy and dissipation rate were determined from density-weighted modelled transport equations as given in table 6.2. The k and ε equations as written are similar in form to their constant-density counterparts, but other terms may be added arising from the density variations. In particular, terms involving the expression $\overline{\rho' u''_i}\,\partial\overline{P}/\partial x_i$ may be added to both equations. In the past the tendency has been to omit these terms so as to avoid the problem of specifying and solving modelled equations for the correlation $\overline{\rho' u''_i}$. In free-jet diffusion flames, terms involving $\overline{\rho' u''_i}\,\partial\overline{P}/\partial x_i$ are likely to be unimportant, the pressure gradients being very small, but in combustor flows, where pressure gradients are often large, they may be more important. Nevertheless, good results have been obtained by, for example, Khalil et al (1975), without their use, and for this reason, and to avoid specifying and solving further equations, they are omitted here.

6.2.2 Combustion Model

The modelling of the combustor flow follows closely that of gaseous-fuelled turbulent jet diffusion flames. The modelling of combustion processes in these flames has been described by, for example, Jones (1979), and involves

a number of assumptions, the most important of which may be summarized as follows. First, only simple gaseous hydrocarbon flames are considered, for which reaction rates are sufficiently fast that equilibrium products can be assumed to be formed instantaneously. Second, the diffusion coefficients of all species and enthalpy are assumed to be equal (a reasonable assumption in turbulent flows), and third, the heat lost to the surroundings is assumed to be negligible compared with the heat released.

Under these assumptions the instantaneous gas composition, temperature and density correspond to equilibrium conditions and are functions of a single strictly conserved (i.e. zero source) scalar variable. As all of the relevant strictly conserved scalar variables are linearly related, any one may be chosen, and one that is often used is the mixture fraction F, which is defined as the mass fraction of fuel both burnt and unburnt. In figure 6.2 curves of CO, CO_2, CH_4 mole fraction, temperature and density are presented as functions of the mixture fraction for atmospheric inlet conditions.

In a turbulent flow the mixture strength at a point fluctuates with time, and under the instantaneous equilibrium assumption the chemical species, temperature and density will fluctuate with the mixture strength in accordance with the relationships of figure 6.2. If no account is taken of the fluctuations then the calculated flame will tend to acquire a laminar flame like appearance with a thin reaction zone which contrasts with the diffuse reaction zone of a turbulent flame. Thus, to achieve a realistic solution of the flow, some account must be taken of the fluctuations. Since the relationships between the species and the mixture fraction are non-linear, a knowledge of the mean mixture fraction is insufficient to determine the mean species, and it is therefore necessary to specify a probability density function (p.d.f.) for F or some other equivalent information.

The p.d.f. must satisfy the conditions

$$p(F) \geq 0 \qquad 0 \leq F \leq 1$$
$$p(F) = 0 \qquad F < 0 \quad F > 1$$

Following a number of workers, the approach adopted here is to specify a two-parameter p.d.f. in terms of the mean mixture fraction $\tilde{F}$ and its variance $\widetilde{f''^2}$, the values of $\tilde{F}$ and $\widetilde{f''^2}$ being obtained from their respective modelled transport equations as given in table 6.2. The p.d.f. is a density-weighted function, and so values of the density-weighted mean species may be obtained from the equation:

$$\tilde{\Phi} = \int_0^1 \Phi(F)p(F)dF,$$

in which $\Phi(F)$ represents a curve-fit to the equilibrium data of figure 6.2. High-order polynomial curve-fits were used as these were inexpensive in computer time and provided an accurate representation of the curves after careful selection of the polynomial coefficients.

Values of the unweighted mean temperature may be obtained from the equation:

$$\overline{T} = \overline{\rho} \int_0^1 \frac{T(F)p(F)dF}{\rho(F)},$$

and the mean density, which is required in the convection terms of all the transport equations, from the equation:

$$\overline{\rho} = \left(\int_0^1 \frac{p(F)dF}{\rho(F)} \right)^{-1}$$

Several p.d.f. shapes have been proposed in the literature. Spalding (1971), for example, assumes that the fluctuations in F with time follow a square wave pattern, and thus the p.d.f. consists of two delta functions located at F^+ and F^- with

$$p(F) = a\delta (F - F^-) + (1 - a)\, \delta (F - F^+)$$

where a, F^+ and F^- are determined from the values of $\tilde{F}$ and $\widetilde{f''^2}$. A more realistic shape is the "clipped" Gaussian distribution proposed by Lockwood and Naguib (1975), so called because the distribution is clipped where it falls outside the permitted range $0 \leq F \leq 1$. Equally realistic, if not more so, is the β p.d.f. proposed by Richardson, Howard and Smith (1953) which takes the form.

$$p(F) = \frac{F^{a-1}(1-F)^{b-1}}{\int_0^1 F^{a-1}(1-F)^{b-1}\,dF} \qquad 0 \leq F \leq 1$$

where

$$a = \tilde{F}\left(\frac{\tilde{F}(1-\tilde{F})}{\widetilde{f''^2}} - 1\right)$$

and

$$b = \frac{(1-\tilde{F})a}{\tilde{F}}$$

Jones (1977) has compared the performances of all three of the above-mentioned distributions in calculations of a hydrogen round-jet diffusion flame. A suitable basis on which to assess the p.d.f.s is the level of agreement between calculated and measured mean temperature at near stoichiometric conditions, as the relationship between the instantaneous temperature and the mixture fraction at these conditions is highly non-linear. Jones found that the mean temperatures obtained by using the β p.d.f were in good agreement with the measurements, while those obtained by using the clipped Gaussian p.d.f were slightly less accurate and those by using the double delta p.d.f much less accurate. The results, therefore, tended to favour the β p.d.f . Jones and Pope (1977) provide further support for the use of the β p.d.f in calculations of diffusion flames, and on this basis the β p.d.f was chosen for the present calculations.

6.2.3 Nitric Oxide

The assumption of instantaneous chemical reaction is not appropriate for all of the chemical reactions taking place in the combustor. For example, CO formed in fuel-rich areas of the combustor will, when oxidized, form CO_2 at a finite rate comparable with the turbulent mixing rate. The formation of nitric oxide in near-stoichiometric regions of the combustor also proceeds at a rate comparable with the turbulent mixing rate. The instantaneous reaction assumption is therefore invalid for the oxidation of CO to CO_2 and for the formation of NO, and consequently each of the species CO_2 and NO must be determined from its own transport equation with an appropriate source term. Unfortunately, no measurements are available of either CO_2 or NO, but to illustrate the technique, calculations are performed for one of the two species. Since the modelling of NO formation is more straightforward than that of CO_2 (see, for example, Jones (1979)), the calculation of NO is considered.

Nitric oxide is formed in high temperature regions of the flow in concentrations which are small and which have a negligible effect on the thermodynamic properties of the flow (e.g. density). Following Jones (1979), the instantaneous formation rate of nitric oxide is modelled using the extended Zeldovich mechanism and an equilibrium oxygen atom assumption. The instantaneous formation rate is then solely a function of equilibrium quantities, and hence a function of the instantaneous mixture fraction only,

ie

$$r_{NO} = 4.0917 \times 10^{13} T^{-0.0675} \mathrm{Exp}(-67915/T) M_{NO} \rho^{\frac{1}{2}} n_{O_2}^{\frac{1}{2}} n_{N_2}$$

(mass fraction/sec)

where M_{NO} is the molecular weight of nitric oxide and n_α represents moles of species per unit mass. The instantaneous formation rate given by the above equation for the conditions in the combustor is plotted as a function of instantaneous mixture fraction in figure 6.3. The mean formation rate at any point in the flow can then be obtained from the equation:

$$S_{NO} = {}_0\int^1 r_{NO}(F)p(F)dF$$

6.2.4 Boundary Conditions

The mean axial velocities at the combustor inlets were determined from the mass flow rates specified in table 6.3, under the assumption that the inlet profiles were plug-shaped. During the measurement of non-reacting flows the methane inlet was sealed and the mean axial velocity at the air inlet was determined from the combustor Reynolds number, which was based on the diameter of the disc-baffle and the mean axial velocity in the combustor.

The profile of radial velocity at the air inlet had been measured with the seven-hole impact probe and an area-averaged value deduced from the results. Since the tip of the impact probe was comparable in size with the annular gap, the resulting average velocity was subject to error, and it was thought advisable to assess the sensitivity of the solution to any error in the radial velocity boundary condition. The results of this investigation are presented in figure 6.4, and show that even a comparatively large error has a negligible effect on the flow solution. The insensitivity of the solution to the radial velocity is probably in this case due to the proximity of the baffle tip to the combustor wall.

No measurements were available of the turbulence kinetic energy or dissipation rate at the methane and air inlets, and the values used in the calculations were deduced from the equations:

$$k = 0.005U_{IN}^2$$

and

$$\varepsilon = \frac{k^{3/2}}{\ell_{IN}}$$

where ℓ_{IN} was either the diameter of the baffle hole or the width of the

annular gap. The values of k and ε are only approximate, but the solutions are not sensitive to the values used, as may be seen from figure 6.5.

At the air inlet the mean mixture fraction $\tilde{F}$ was set equal to zero, and at the methane inlet it was set equal to 1.0, while the mean square fluctuation in mixture fraction $\widetilde{f''^2}$ was set equal to zero at both inlets.

On the baffle and combustor wall the values of $\tilde{U}$, $\tilde{V}$, k and ε were obtained via the wall functions described in Chapter 3, while the gradients of the quantities $\tilde{F}$ and $\widetilde{f''^2}$ normal to the baffle or wall were set equal to zero.

At the combustor outlet the axial gradients of all quantities were set equal to zero.

6.2.5 Finite-Difference Grid

The grid was arranged so that there were equal numbers of grid points in each co-ordinate direction. The grid spacing in the axial direction was increased in geometric progression with distance from the baffle. The most complex part of the flow occurred immediately next to the disc-baffle, and thus coincided with the smallest grid spacings. In the radial direction, points were concentrated across the methane and air inlets so as to ensure that the inlet profiles were accurately defined. The spacing across the baffle was uniform and comparable with the smallest spacings in the axial direction.

Grid refinement was carried out on an overall basis so that, for example, in the axial direction, geometric progression was preserved, but with smaller grid spacings. The grid was refined in this way (for both non-reacting and reacting flows) until the solutions appeared to be sensibly grid independent. Figures 6.6, 6.7 and 6.8 show the effect of grid refinement on the mean axial velocity and the mean mixture fraction. For both non-reacting and reacting flows the solutions appeared to be sensibly grid independent with 40 x 40 grid points.

A solution was taken to be converged when the sum of the mass sources in

the continuity equation was less than 10^{-3} of the mass flow into the combustor. The computer run time per equation per iteration per node was 0.00044 seconds for non-reacting flows and 0.0010 for reacting flows on a CDC 6600 computer. For a typical non-reacting flow calculation, approximately 430 iterations were needed to achieve convergence, and the total run time was about 25 minutes. For a reacting flow calculation approximately 560 iterations were needed, and the total run time was about 120 minutes.

6.3 RESULTS

6.3.1 Non-Reacting Flow

Elliman provided extensive measurements of the non-reacting flow for Reynolds numbers of 1.9×10^5 and 6.3×10^5. Contours of measured and calculated mean velocity components and non-dimensional stream function for each Reynolds number are presented in figures 6.9 and 6.10. Elliman states that outside the recirculation zone, the measurement errors were within 10%, but that inside the recirculation zone they were very much higher, rising to as high as 50% towards the combustor centreline. This increase in error was due to interference from the probe stem, which was pivoted about a point on the combustor centreline towards the rear of the combustor.

The calculations can be seen to be in close agreement with the measurements, except that the length of the recirculation zone appears to have been underpredicted by about 5% at both Reynolds numbers. Given the measurement error however, it cannot be said for certain that the error is due entirely (or even partly) to the calculation. The consistent misalignment of the measured and calculated $\overline{U}$ mean velocity contours in the recirculation region suggests a calculation error, but the error could also be accounted for by a systematic measurement error.

However, if as seems likely the error is at least partly due to the calculation, then it is necessary to identify possible sources of error in the numerical procedure. Figures 6.4 to 6.6 show that small errors occur due to the inlet conditions and numerical truncation terms. These errors

when combined could account for all of the error in the recirculation zone length. In addition, errors associated with the turbulence model and with the wall boundary conditions could be considered.

Durão and Whitelaw (1978) have carried out measurements in the near wake of an unconfined baffle flow, and shown that the turbulence is strongly anisotropic, and that locations of zero shear stress do not in general coincide with locations of zero velocity gradient. Thus, the assumption that the Reynolds stresses can be determined locally from mean velocity gradients can be expected to be in error. In addition, the underprediction of recirculation zone length has been noted in many other calculations of free and confined separated flows, and has been attributed to deficiencies in the modelling of the sources terms in the dissipation rate equation (see, for example, Pope and Whitelaw (1976)).

The functions describing the wall flow were originally formulated for two-dimensional boundary layers with zero pressure gradient. The functions do not accurately describe the wall flow when strong pressure gradients and recirculation are present in the main, high Reynolds number flow, and if used in such circumstances give rise to erroneous wall diffusion coefficients and erroneous near-wall velocity gradients.

Any of the error sources mentioned above could contribute to the 5% discrepancy in the recirculation zone length. However, it is clear from the level of agreement between calculation and measurement that the calculation procedure has performed well for this particular flow.

Figure 6.11 indicates the influence of the Reynolds number on the calculated recirculation zone length. As anticipated, the recirculation zone length for the high Reynolds numbers used is determined only by flow geometry and is sensibly independent of Reynolds number.

6.3.2 Reacting Flow

Elliman reported measurements of reacting flow for three operating conditions defined in table 6.3. The calculated results for operating condition 1 are presented in figures 6.12 to 6.18. The contour diagrams of

non-dimensional stream function and mean temperature indicate the main features of the flow, which consist of a recirculation zone of hot gases adjacent to the baffle, and a diffuse reaction zone resulting from the mixing of the fuel and air streams.

The calculated results are in good general agreement with the measurements, but there are some significant errors, particularly in the temperature distribution. In the calculation the highest temperature in the combustor occurs on the surface of the baffle, but in the measurements the highest temperature occurs some distance downstream, and the baffle surface is relatively cool. In addition, the width of the high temperature reaction zone is underpredicted, and the peak temperature in the reaction zone is overpredicted.

There are several possible contributory factors to the difference in temperature adjacent to the baffle. Probably the main factor is that the baffle was cooled, allowing a considerable amount of heat transfer to take place between the flow and the baffle. This heat transfer cannot of course be taken into account by the present combustion model, which assumes adiabatic conditions. The surface temperature of the baffle was reported to be around 80°C, which implies a large temperature gradient and a great deal of heat transfer.

Other contributory factors could be measurement error and the use of the unweighted temperature in the calculation. The measurement errors associated with thermocouple probes can be large, especially in high temperature areas of the flow, and Elliman reports errors of several hundreds of degrees in these areas, making it necessary to apply a complex correction procedure. The level of accuracy after correction was put at 15%, but it is possible that this limit was exceeded in high temperature areas. However, if the measurement error were wholly to account for the difference in temperature at the surface of the baffle, it would have to be many times greater than 15%, and so it cannot be considered a major contributory factor.

The quantity measured by the thermocouple probe was thought to be close to an unweighted temperature, and so an unweighted quantity was calculated in

the procedure. However, the possibility remains that the measured temperature was closer to some other quantity, say the density-weighted temperature $\tilde{T}$. However, the difference in calculated $\overline{T}$ and $\tilde{T}$ at the hottest part of the baffle is only 40K, and is therefore insignificant. Moreover, even if the measured quantity were not close to either $\overline{T}$ or $\tilde{T}$, but to some other, similar, quantity, then the difference would probably remain insignificant.

However, it should be stated that the difference between $\overline{T}$ and $\tilde{T}$ at the baffle would increase if the mean square fluctuation $\widetilde{f''^2}$ were increased. (At present the difference is very small partly because the value of $\widetilde{f''^2}$ at the baffle is very small.) In addition, an increase in $\widetilde{f''^2}$ would cause both quantities to fall in value: an order of magnitude increase in $\widetilde{f''^2}$ from its present value of 0.00037 would cause the difference between $\overline{T}$ and $\tilde{T}$ to increase to 250K, and the value of each to fall by 370K and 580K respectively. Thus, the possibility arises that the underprediction of $\widetilde{f''^2}$ is also a contributory factor to the temperature error at the baffle. Given the change required in $\widetilde{f''^2}$, however, it seems unlikely that the underprediction of $\widetilde{f''^2}$ is a major factor, and probably the major factor is that the baffle was cooled.

The mean temperature and mean equivalence ratio contours indicate that the width of the high-temperature reaction zone was underpredicted. The width of the reaction zone is strongly dependent on the distribution of mean mixture fraction, and it is likely that the error occurred because the diffusion of mean mixture fraction was underpredicted.

Because of the error, the high temperature region does not spread far enough towards the centreline and the combustor wall. This error in the temperature distribution can be seen in the radial profiles of mean temperature in figure 6.14, which also indicate that the peak temperature is overpredicted. The shapes of the temperature profiles are strongly influenced by the distribution of mean mixture fraction, and the low temperatures at the centreline and combustor wall are consistent with the underprediction of the mean mixture fraction. The diffusion can be increased by reducing the turbulent Prandtl number σ_F in the mean mixture fraction equation, and figures 6.15 and 6.16 show the influence on the mean

mixture fraction and the mean temperature of reducing σ_F from the recommended value of 0.9 to a value of 0.5. As can be seen, the reduction in σ_F increases the spreading of the mean mixture fraction and mean temperature; however, it does not appear to reduce the calculated temperature peak, which remains too high.

The size of the temperature peak depends strongly on the size of the fluctuations and the shape of the probability density function at stoichiometric conditions, and is particularly sensitive to the size of the fluctuations. It is, therefore, possible that the mean square fluctuation was also underpredicted. A doubling of the rms fluctuation at the location of the peak for X = 250mm from its present value of 0.069 would cause the temperature peak to fall by 200K. This is a significant reduction in relation to the temperature error, and it follows that the underprediction of the mean square fluctuation could be a major contributory factor to the error.

However, a number of other contributory factors could be considered. For example, the 15% measurement error represents 190K at the location of the peak for X = 250mm. In addition, the density-weighted temperature is now less than the calculated temperature $\overline{T}$ by 180K (partly because the fluctuations at this location are large). If these two factors were combined they could account for almost all of the error in the temperature peak. However, it seems unlikely that the error is due entirely to measurement error and to the choice of the calculated temperature, and probably a large proportion of the error is due to the underprediction of the mean square fluctuation. At the combustor wall the measurement error and the choice of calculated temperature can account for only a small proportion of the temperature difference, and the major factor is probably that the diffusion of mean mixture fraction was underpredicted.

The errors in $\tilde{F}$ and $\widetilde{f''^2}$ not only affect the mean temperature, but also affect the mean density, and hence the mean velocity. The radial profiles of mean axial velocity presented in figure 6.17 show that the calculated profiles are similar in shape to the measured profiles, but that the peak values are too low, particularly near the combustor wall and in the downstream region. These errors are consistent with the errors in the mean

temperature profiles when it is assumed that the errors arise from the suggested errors in $\tilde{F}$ and $\widetilde{f''^2}$. The errors in the velocity profiles are greatest near the combustor wall and reach values of 45%. These errors cannot be entirely attributed to the measurement error and to the choice of density-weighting for the mean velocity, and are probably due mainly to the underprediction of the diffusion of mean mixture fraction.

Figure 6.18 presents calculations of selected species and nitric oxide. Unfortunately, no measurements were available for comparison with the calculated species, and the figure is intended only as an approximate guide to the concentration levels of species in the combustor. Although errors will be present in the concentration levels, some important observations can be made. For example, the finite-rate formation of nitric oxide is clearly demonstrated by the presence of concentration levels very much below equilibrium everywhere in the combustor.

The measurements at operating conditions 2 and 3 consisted of profiles of mean axial velocity and mean temperature, and were intended to demonstrate the influence on the flow of Reynolds number and overall equivalence ratio. The calculated distributions of mean temperature, equivalence ratio and species at condition 2 were virtually identical to those at condition 1, the flow being essentially independent of Reynolds number, and are not presented.

To obtain condition 3 the overall equivalence ratio was increased from 0.9 to 1.6. As expected, the richer fuel-air mixture gave rise to lower mean temperatures and nitric oxide concentrations, as can be seen from figure 6.19. The shapes of the temperature contours differed slightly from those at condition 1, but the high temperature at the baffle remained. The calculated radial profiles of mean temperature (figure 6.20) and mean velocity (figure 6.21) contained similar errors to those at condition 1, and the probable sources of error are as discussed above.

6.4 CONCLUSIONS

In the present combustor the turbulence and combustion models produced calculations in good general agreement with measurements. In reacting flows the calculated temperature at the surface of the baffle was too high, and the most probable cause was thought to be the failure to account for heat transfer to the baffle.

The calculated reaction zone was too thin, and the mean temperature was in general too high in the reaction zone and too low in other areas of the flow. The error in the reaction zone width and the underprediction of the mean temperature were thought to be due mainly to the underprediction of the diffusion of mean mixture fraction, while the overprediction of the peak temperature in the reaction zone was thought to be due at least partly to the underprediction of the mean square fluctuation in mixture fraction.

The errors in $\tilde{F}$ and $\widetilde{f''^2}$ appeared to have a strong effect on the mean velocity through their effect on the mean density, and the underprediction of the mean axial velocity near the combustor wall and in the downstream region was thought to be due mainly to the errors in $\tilde{F}$ and $\widetilde{f''^2}$ described above.

The results of grid refinement for both non-reacting and reacting flow suggested that errors due to numerical diffusion were negligible. However, it may be added that further refinement of the grid with a corresponding reduction in numerical diffusion would probably reduce the calculated diffusion of mean quantities, such as the mean mixture fraction, even further and add support to the conclusion that the diffusion of mean mixture fraction was underpredicted.

CHAPTER 7

CLOSURE

The previous chapters have presented and discussed experiments and computations of turbulent jets in a deflecting stream, as well as computations of a simple combusting flow. This chapter briefly discusses the work in relation to the design of gas turbine combustors and to the development of a practical calculation procedure, and presents recommendations for future work.

7.1 EXPERIMENTAL WORK

The experimental work was intended to provide data on the trajectory and mixing of turbulent jets in a deflecting stream for geometric and flow parameters relevant to gas-turbine combustors.

The results are assumed to be directly relevant to gas-turbine combustors, and to provide an indication of the most suitable configurations for combustor design. The results show, for example, that a single row of jets with a pitch-to-diameter ratio of 2.0 would provide the conditions of a low and uniform temperature desirable in the dilution region of the combustor. If the pitch-to-diameter ratio were increased, however, the flow would become increasingly non-uniform laterally, and would eventually lead to dangerous hot streaks. A low and uniform temperature could also be achieved by two opposed rows of jets for a height-to-diameter ratio of 4.0 and a velocity ratio of 1.8.

The total number of configurations tested was small, but the data could be easily supplemented by results from a number of other experimental studies. Khan and Whitelaw (1980b), Khan (1982) and Holdeman et al (1984), for example, provide results for two opposed rows of jets for a range of relevant parameters, including velocity ratio, height-to-diameter ratio, pitch-to-diameter ratio and hole asymmetry. This work, combined with the present work, provides an indication of the trajectory and mixing of the jets for a wide range of parameter values.

Of course, if the data is to be applicable to practical combustors, the influence of the additional variables in practical combustors must be small. These variables include density differences between the jet and mainstream, non-uniformities in the mainstream flow properties, and increased geometric complexity. Other workers have investigated these variables to a limited extent; Kamotani and Greber (1972), for example, performed experiments on a heated jet to determine the influence of density differences between the jet and mainstream. According to their results the main flow parameter affecting the trajectory and mixing is the momentum flux ratio $\rho V_J^2/\rho U_\infty^2$, and density differences have negligible independent effect; this is also likely to be the case in practical combustors.

Crabb and Whitelaw (1979) and Khan and Whitelaw (1980a) investigated the effect of small asymmetries in the spacing of the holes for values of asymmetry typical of gas-turbine combustors. Their results indicate that even small geometric asymmetries can cause considerable asymmetries in the velocity and scalar fields and may in practice lead to damaging hot streaks.

The influence of non-uniformities in the mainstream velocity and turbulence and of additional geometric variables ought also to be investigated. Non-uniformities in the turbulence, for example, and additional geometric complexities could possibly affect the trajectory and mixing, and ought, therefore, to be investigated, at least to a limited extent, in future measurements.

7.2 COMPUTATIONAL WORK

A numerical calculation procedure was described and solutions were presented for a single jet and for two opposed single jets. The main aim of the calculations was to identify the major sources of error in the procedure and to assess the level of their influence. The calculations of the two opposed single jets were, in addition, intended to demonstrate the procedure's potential to calculate more complex jet configurations of interest to combustor designers.

The solutions for both configurations demonstrated that the correct

trajectory and spreading could be achieved. An analysis of numerical errors and careful comparisons of calculation and measurement showed that many of the detailed differences between calculation and measurement were due to numerical errors. With due regard for these errors it is anticipated that the procedure could be applied successfully to other jet configurations of interest to designers. Khan (1982) and Holdeman et al (1984) have presented comprehensive mean-flow measurements of two opposed rows of jets which demonstrate a wide variety of flow behaviour of interest to designers and represent an ideal basis on which to develop the procedure further. However, for flows of much greater aerodynamic complexity it would be worthwhile to investigate alternative, more accurate finite-difference schemes.

In the long term the procedure has much greater potential than to calculate the behaviour of primary and dilution jets, and could, it is believed, be developed to calculate a practical combustor flow, giving details of velocity, temperature, species concentrations and turbulence. A great deal of work will be needed to achieve this objective, and considerable effort is being made by researchers on individual aspects of the problem.

If a realistic combustor geometry is to be represented then a more complex grid arrangement will be required based on boundary-fitted co-ordinates. Much work has been done on techniques to generate boundary-fitted grids (see, e.g. Thompson (1982)), and recent examples of calculations for isothermal turbulent flows have been presented by Peric (1985), Nakayama (1985), and others.

Following the work of Raithby (1976) and Leonard (1977), a number of investigations have been made into alternative finite-difference schemes. Initially, the testing of these schemes tended to be limited to simple geometries and laminar flow, but they are being applied increasingly to turbulent flows in practical geometries (e.g. Leschziner and Rodi (1981), Azzola et al (1986), Kadja (1987)). As these schemes are developed it will become feasible to apply higher-order turbulence models to practical flow problems, and, already, calculations of axisymmetric recirculating flows have been presented involving the Leonard scheme and a second-order turbulence closure (e.g. Jones and Marquis (1985), Huang (1986), Fu et al

(1987)).

Developments are also being made in the modelling of combustion, and in the modelling of turbulence in combusting flows (for an introduction and review, see, for example, Kuo (1986)). The procedure described in Chapter 6 was developed to calculate a simple turbulent flame in a model combustor, but more recently a series of calculations was presented of local flow properties in a production gas turbine combustor (Coupland and Priddin (1985)).

The developments in the various computational techniques should of course be accompanied by a programme of experimental work so that the new models and numerical techniques may be given adequate testing. These developments when combined should, it is hoped, lead to a calculation procedure which is not only accurate and versatile, but also considerably more cost-effective than other design methods.

References

Amsden, A A and Harlow, F M (1970)
The SMAC method
Low Alamos Sci Lab Rep LA-4370

Andreopoulos, J (1980)
Measurements in a pipe flow issuing perpendicularly into a cross-stream
ASME paper 80-WA/HT-24

Andreopoulos, J and Rodi, W (1984)
Experimental investigation of jets in a crossflow
J Fluid Mech 138, 93

Atkinson, K N, Khan, Z A and Whitelaw, J H (1982)
Experimental investigation of opposed jets discharging normally into a cross-stream
J Fluid Mech 115, 493

Azzola, J, Humphrey, J A C, Iacovides, H and Launder, B E (1986)
Developing turbulent flow in a U-bend of circular cross-section: measurement and computation
ASME J Fluids Eng 108, 214

Baker, R J, Hutchinson, P, Khalil, E E and Whitelaw, J H (1974)
Measurements of three velocity components in a model furnace with and without combustion
Proc 15th Int Symposium on Combustion, 553

Bergeles, G (1976)
Three-dimensional discrete hole cooling processes: an experimental and theoretical study
PhD Thesis, University of London

Boussinesq, J (1877)
Theorie de l'ecoulement tourbillant
Mem Pres Acad Sci 23, 46

Bradbury, L J S and Wood, M N (1965)
The static pressure distribution around a circular jet exhausting normally from a plane wall into an airstream.
ARC CP 822

Bradshaw, P, Ferriss, D H and Atwell, N P (1967)
Calculation of boundary-layer development using the turbulent energy equation
J Fluid Mech 28 pt 3, 593

Burns, A D and Wilkes, N S (1987)
A finite difference method for the computation of fluid flows in complex three dimensional geometries
UK Atomic Energy Authority Rep AERE R 12342

Champagne, F H and Sleicher, C A (1967)
Turbulence measurements with inclined hot wires
J Fluid Mech 56, 177

Chorin, A J (1968)
Numerical solution of the Navier-Stokes equations.
Math Comp 22, 745

Claus, R W (1983)
Analytical calculation of a single jet in a crossflow and comparison with experiment
NASA TN 83027

Coupland, J, and Priddin, C H (1985)
Modelling the flow and combustion in a production gas turbine combustor
Proc 5th Symposium on Turbulent Shear Flows

Cox, G B (1975)
Multiple jet correlations for gas turbine engine combustor design
ASME Paper 75-GT-45

Crabb, D (1979)
Jets in crossflow
PhD Thesis, University of London

Crabb, D and Whitelaw, J H (1979)
The influence of geometric asymmetry on the flow downstream of rows of jets discharging normally into a free stream.
ASME J Heat Transfer 101, 183

Demuren, A O (1983)
Numerical calculations of steady three-dimensional turbulent jets in cross flow
Comp Meths Appl Mech Eng 37, 309

Durão, D F G and Whitelaw, J H (1978)
Velocity characteristics of the flow in the near-wake of a flat disc
J Fluid Mech 85, 368

Durst, F, Schierholz, W F and Wunderlich, A M (1987)
Experimental and numerical investigations of plane duct flows with sudden contraction
ASME J Fluids Eng 109, 376

Elliman, D G (1977)
Experimental and numerical studies of an axisymmetric combustor
PhD Thesis, University of Nottingham

Favre, A (1969)
Statistical equations of turbulent gases
Problems of hydrodynamics and continuium mechanics
SIAM, Philadelphia

Fu, S, Launder, B E, and Leschziner, M A (1987)
Modelling strongly swirling recirculating jet flow with Reynolds-stress transport closures
Proc 6th Symposium on Turbulent Shear Flows

Gosman, A D and Pun, W M (1973)
Lecture notes for a course entitled: Calculation of Recirculating Flows
Imperial College, London

Hanjalic, K and Launder, B E (1972)
A Reynolds stress model of turbulence and its application to thin shear flows
J Fluid Mech 52, 609

Harlow, F H and Nakayama, P (1968)
Transport of turbulence energy decay rate
Los Alamos Sci Lab Rep LA-3854

Harlow, F H and Welch, J E (1965)
Numerical calculation of time dependent viscous incompressible flow of fluid with free surface
Phys Fluids 8, 2182

Holdeman, J D, Srinivasan, R and Berenfield, A (1984)
Experiments in dilution jet mixing
AIAA Journal, 22, 1436

Holdeman, J D and Walker, R E (1977)
Mixing of a row of jets with a confined crossflow
AIAA Journal 15, 243

Holdeman, J D, Walker R E and Kors, D L (1973)
Mixing of multiple dilution jets with a hot primary airstream for gas turbine combustors
NASA TM X-71426

Huang, P G (1986)
The computation of elliptic turbulent flows with second moment closure models
PhD Thesis, University of Manchester

Jones W P (1971)
Laminarisation in strongly accelerated boundary layers
PhD Thesis, University of London

Jones, W P (1977)
Workshop on p.d.f. methods for turbulent flows
Technische Hochschule, Aachen

Jones, W P (1979)
Prediction methods for turbulent flows: models for turbulent flows with variable density and combustion
VKI Lecture Series 1979-2

Jones, W P and Launder, B E (1972)
The prediction of laminarisation with a two-equation model of turbulence
Int J Heat Mass Transfer 15, 301

Jones, W P and Marquis, A J (1985)
Calculation of axisymmetric recirculating flows with a second order turbulence model
Proc 5th Symposium on Turbulent Shear Flows

Jones, W P and McGuirk, J J (1979)
Computation of a round turbulent jet discharging into a confined crossflow
Proc 2nd Symposium on Turbulent Shear Flows, London, 233

Jones, W P and Pope, S B (1977)
Properties of turbulent flames and their calculation: lecture notes for a course held in the Chemical Engineering Department, Imperial College, London

Jordinson, R (1956)
Flow in a jet directed normal to the wind
ARC R&M 3074

Kadja, M (1987)
Computation of recirculating flow in complex geometries with algebraic second-moment closures
PhD Thesis, University of Manchester

Kamotani, Y and Greber, I (1972)
Experiments on a turbulent jet in a crossflow
AIAA Journal 10, 1425

Kamotani, Y and Greber, I (1974)
Experiments on confined turbulent jets in crossflow
NASA CR-2392

Keffer, J F and Baines, W D (1963)
The round turbulent jet in a cross-wind
J Fluid Mech 15, 481

Khalil, E E, Spalding, D B and Whitelaw, J H (1975)
The calculation of local flow properties in two-dimensional furnaces
Int J Heat Mass Transfer 18, 775

Khan, Z A (1982)
Opposed jets in crossflow
PhD Thesis, University of London

Khan, Z A, McGuirk, J J and Whitelaw, J H (1981)
A row of jets in a crossflow
AGARD CP 308, Paper 10

Khan, Z A and Whitelaw, J H (1980a)
Mean velocity and concentration characteristics downstream of rows of jets in a crossflow
ASME J Heat Transfer 102, 391

Khan, Z A and Whitelaw, J H (1980b)
Vector and scalar characteristics of opposing jets discharging normally into a cross stream.

Int J Heat Mass Transfer 23, 1673

Kuo, K K (1986)
Principles of Combustion
John Wiley and Sons

Laufer, J (1954)
The structure of turbulence in fully developed pipe flow
NACA Rep 1174

Launder, B E , Reece, G J and Rodi, W (1975)
Progress in the development of a Reynolds-stress turbulence closure
J Fluid Mech 68, 537

Launder, B E and Spalding, D B (1972)
Mathematical Models of Turbulence
Academic Press, London

Leonard, B P (1977)
News Flash: upstream parabolic interpolation
Proc 2nd GAMM conference on numerical methods in fluid mechanics, Koln, 97

Leschziner, M A (1980)
Practical evaluation of three finite difference schemes for the computation of steady-state recirculating flows
Comp Meths Appl Mech Eng 23, 293

Leschziner, M A and Rodi W (1981)
Calculation of annular and twin parallel jets using various discretization schemes and turbulence model variations
ASME J Fluids Eng 103, 352

Lockwood, F C and Naguib, A S (1975)
The prediction of the fluctuations in the properties of free, round-jet, turbulent diffusion flames
Combust Flame 24, 104

Margason, R J (1968)
The path of a jet directed at large angles to a subsonic free stream
NASA TN D-4919

McGuirk, J J and Rodi, W (1978)
A depth-averaged mathematical model for the near field of side discharges into open channel flow
J Fluid Mech 86, 761

McMahon, H M, Hester, D D and Palfery, J G (1971)
Vortex shedding from a turbulent jet in a cross-wind
J Fluid Mech 48, 73

McMahon, H M and Mosher, D K (1969)
Experimental investigation of pressure induced on a flat plate by a jet issuing into a subsonic crosswind
NASA SP 218

Moussa, Z M, Trischka, J W and Eskinazi, S (1977)
The near field in the mixing of a round jet with a cross-stream
J Fluid Mech 80, 49

Nakayama, A (1985)
A numerical method for solving momentum equations in generalised co-ordinates (its application to three-dimensional separated flows)
ASME J Fluids Eng 107, 49

Nee, V W and Kovasznay, L S G (1969)
Simple phenomenological theory of turbulent shear flows
Phys Fluids 12, 473

Owen, F K, Spadaccini, L J and Bowman, C T (1976)
Pollutant formation and energy release in confined turbulent diffusion flames
Proc 16th Int Symposium on Combustion, 105

Ower, E and Pankhurst, R C (1977)
The Measurement of Air Flow
Pergamon Press, 5th Edn, Oxford

Patankar, S V, Basu, D K and Alpay, S A (1977)
Prediction of the three-dimensional velocity field of a deflected turbulent jet
ASME J Fluids Eng 99, 758

Patankar, S V and Spalding, D B (1970)
Heat and Mass Transfer in Boundary Layers
Intertext Books, 2nd Edn, London

Patankar, S V and Spalding, D B (1972)
A calculation procedure for heat, mass and momentum transfer in three-dimensional parabolic flows
Int J Heat Mass Transfer 15, 1787

Peric, M (1985)
A finite volume method for the prediction of three-dimensional fluid flow in complex ducts
PhD Thesis, University of London

Pope, S B and Whitelaw, J H (1976)
The calculation of near-wake flows
J Fluid Mech 73, 9

Prandtl, L (1925)
Uber die ausgebildete turbulenz
ZAMM 5, 136

Raithby, G D (1976)
Skew upwind differencing schemes for problems involving fluid flow
Comp Meths Appl Mech Eng 9, 153

Ramsey, J W and Goldstein, R J (1971)
Interaction of a heated jet with a deflecting stream
ASME J Heat Transfer 93, 385

Ribeiro, M M (1972)
Turbulent mixing of co-axial jets
MSc Thesis, University of London

Ribeiro, M M and Whitelaw, J H (1975)
Statistical characteristics of a turbulent jet
J Fluid Mech 70, 1

Richardson, J H, Howard, H C and Smith, R W (1953)
The relation between sampling-tube measurements and concentration fluctuations in a turbulent gas jet
Proc 4th Int Symposium on Combustion, 814

Roache, D J (1972)
Computational Fluid Dynamics
Hermosa Publishers, New Mexico

Rodi, W (1970)
Basic equations for turbulent flows in Cartesian and cylindrical co-ordinates
Imperial College, Mech Eng Dept Rep BL/TN/A/36

Spalding, D B (1971)
Concentration fluctuations in a round free jet
Chem Eng Sci 26, 95

Spalding, D B (1972)
A novel finite difference formulation for differential expressions involving both first and second derivatives
Int J Num Meths Eng 4, 551

Stoy, R L and Ben-Haim, Y (1973)
Turbulent jets in a confined crossflow
ASME J Fluids Eng 95, 551

Taylor, G I (1932)
The transport of vorticity and heat through fluids in turbulent motion
Proc Roy Soc London, A135, 685

Thompson, J F (Ed) (1982)
Numerical Grid Generation
North Holland

Vogler, R D (1963)
Surface pressure distributions induced on a flat plate by a cold air jet issuing perpendicularly from the plate and normal to a low speed free-stream flow
NASA TN D-1629

Walker, R E and Eberhardt, R G (1975)
Multiple jet study data correlations
NASA CR 134795

Walker, R E and Kors, D L (1973)
Multiple jet study
NASA CR 121217

White, A J (1983)
Film cooling of gas turbine blades
PhD Thesis, University of London

Wooler, P T (1969)
Development of an analytical model for the flow of a jet into a subsonic crosswind
NASA SP 218

Jet	
V_J(m/s)	10 - 160
ρ_J(kg/m³)	4 - 9
μ_J(kg/ms)	3 - 7 x 10^{-5}
D_J(mm)	12 - 46
S (pitch spacing) (mm)	29 - 134
Mainstream	
U_∞(m/s)	10 - 70
ρ_∞(kg/m³)	1.5 - 6.0
μ_∞(kg/ms)	3 - 6 x 10^{-5}
D_∞ (hydraulic diameter) (mm)	80 - 200
Dimensionless	
ρ_J/ρ_∞	1.5 - 3.0
V_J/U_∞	0.3 - 1.5
$\rho_J V_J^2/\rho_\infty U_\infty^2$	0.3 - 165
S/D_J	1.5 - 6.0
D_∞/D_J	4.0 - 15.0
$Re_J(\frac{\rho_J V_J D_J}{\mu_J})$	0.2 - 90 x 10^5
$Re_\infty(\frac{\rho_\infty U_\infty D_\infty}{\mu_\infty})$	1 - 6 x 10^5

Table 1.1 Typical Operating Conditions of Gas-Turbine Combustors.

	Single Row of Jets	Two Opposed Single Jets
D(mm)	25.4	25.4
U_∞(m/s)	12.0	11.1
V_J/U_∞	1.5, 2.3	1.0, 1.8
S/D	2, 4, ∞	∞
H/D	12.0	4.0
k_∞/U^2_∞	0.000023	0.000037
θ(mm)	0.68	1.18

Tabel 2.1 Operating Conditions of the Air-Flow Rigs.

Mean velocity (outside recirculation zone)	10%
Mean temperature	15%
Mean equivalence ratio (<1.5)	10%
Lack of axisymmetry	5%

Table 6.1 Estimates of Measurement Errors.

Conserved Quantity	Φ	a	s
Mass	1	0	0
Axial Momentum	$\tilde{U}$	μ_T	$\frac{\partial}{\partial x}\left(\mu_T \frac{\partial \tilde{U}}{\partial x}\right) + \frac{1}{r}\frac{\partial}{\partial r}\left(\mu_T\, r\, \frac{\partial \tilde{V}}{\partial x}\right) - \frac{\partial \bar{P}}{\partial x}$
Radial Momentum	$\tilde{V}$	μ_T	$\frac{\partial}{\partial x}\left(\mu_T \frac{\partial \tilde{U}}{\partial r}\right) + \frac{1}{r}\frac{\partial}{\partial r}\left(\mu_T\, r\, \frac{\partial \tilde{V}}{\partial r}\right) - 2\mu_T \frac{\tilde{V}}{r^2} - \frac{\partial \bar{P}}{\partial r}$
Turbulence Kinetic Energy	k	$\frac{\mu_T}{\sigma_k}$	$G_k - \bar{\rho}\varepsilon$
Dissipation Rate	ε	$\frac{\mu_T}{\sigma_\varepsilon}$	$\frac{\varepsilon}{k}\left(C_{\varepsilon_1} G_k - C_{\varepsilon_2} \bar{\rho}\varepsilon\right)$
Mean Mixture Fraction	$\tilde{F}$	$\frac{\mu_T}{\sigma_F}$	0
Mean Square Fluctuation	$\widetilde{f''^2}$	$\frac{\mu_T}{\sigma_f}$	$\frac{2\mu_T}{\sigma_f}\left(\left(\frac{\partial \widetilde{F}}{\partial x}\right)^2 + \left(\frac{\partial \widetilde{F}}{\partial r}\right)^2\right) - C_f \bar{\rho}\frac{\varepsilon}{k}\widetilde{f''^2}$

$$G_k = \mu_T \left(2\left(\left(\frac{\partial \tilde{U}}{\partial x}\right)^2 + \left(\frac{\partial \tilde{V}}{\partial r}\right)^2 + \left(\frac{\tilde{V}}{r}\right)^2\right) + \left(\frac{\partial \tilde{U}}{\partial r} + \frac{\partial \tilde{V}}{\partial x}\right)^2\right)$$

$C_\mu = 0.09$, $C_{\varepsilon_1} = 1.44$, $C_{\varepsilon_2} = 1.92$, $\sigma_k = 1.0$, $\sigma_\varepsilon = 1.3$, $\sigma_F = \sigma_f = 0.9$, $C_f = 2.0$

Table 6.2 Exchange Coefficient and Source Terms in the Conservation Equations for Combusting Flow.

Condition	Re	ø	Mass Flow Rates (kg/s) Methane	Air
1	5.0×10^4	0.9	0.0050	0.10
2	8.0×10^4	0.9	0.0086	0.17
3	5.0×10^4	1.6	0.0096	0.10

Table 6.3 Operating Conditions of the Elliman Combustor; reacting flow.

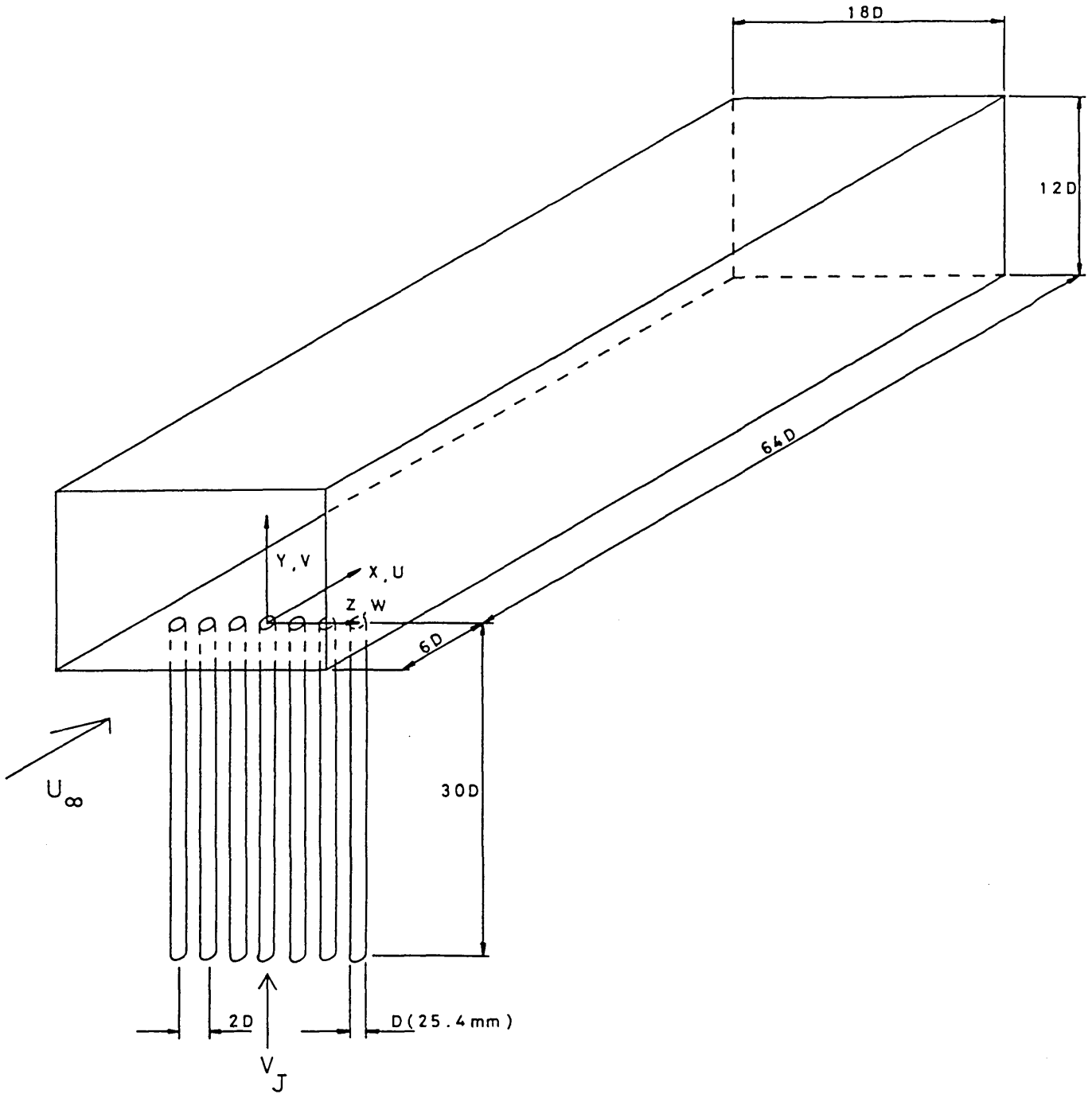


Figure 2.1 Flow rig for a single row of jets in a deflecting stream.

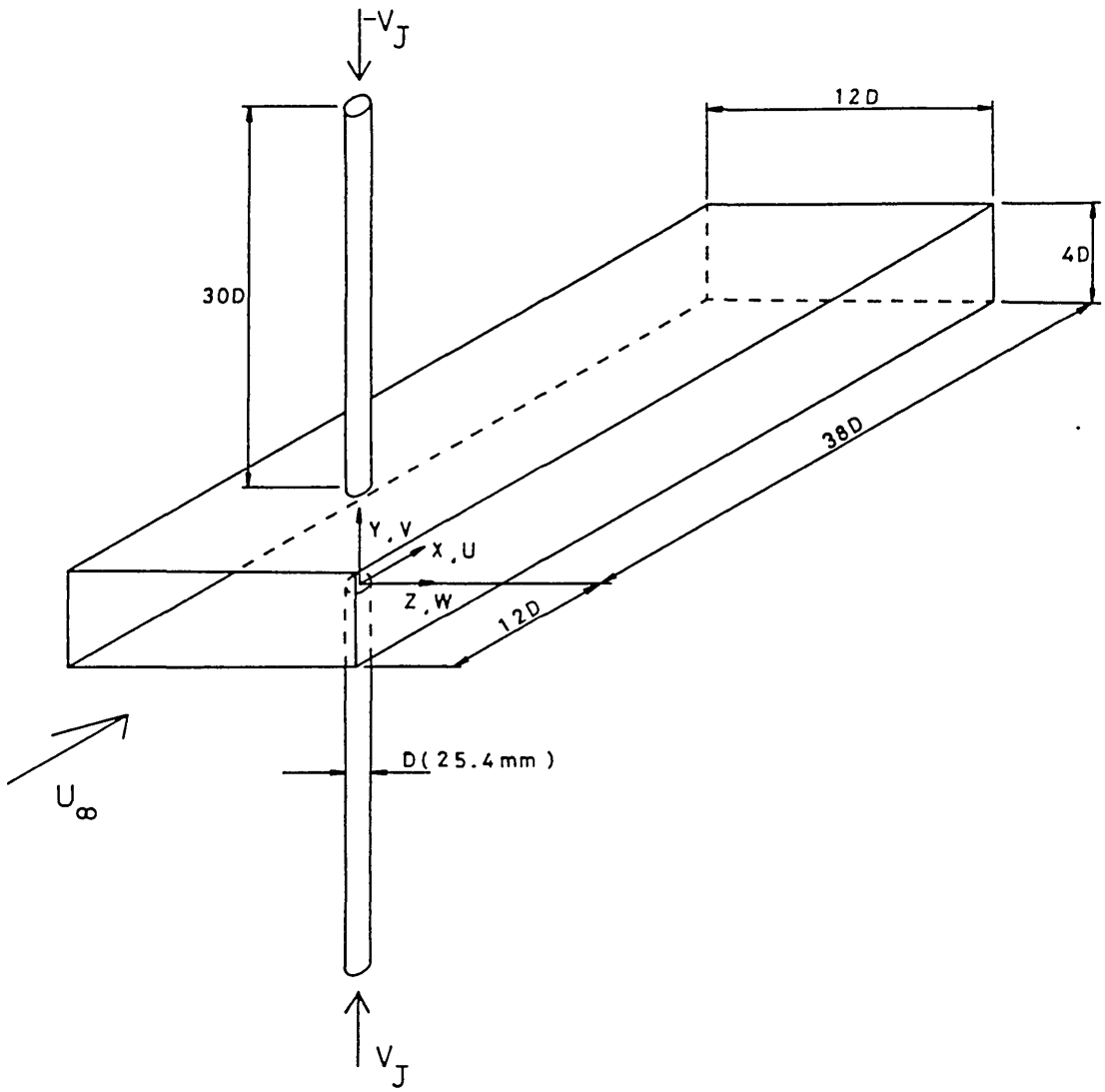
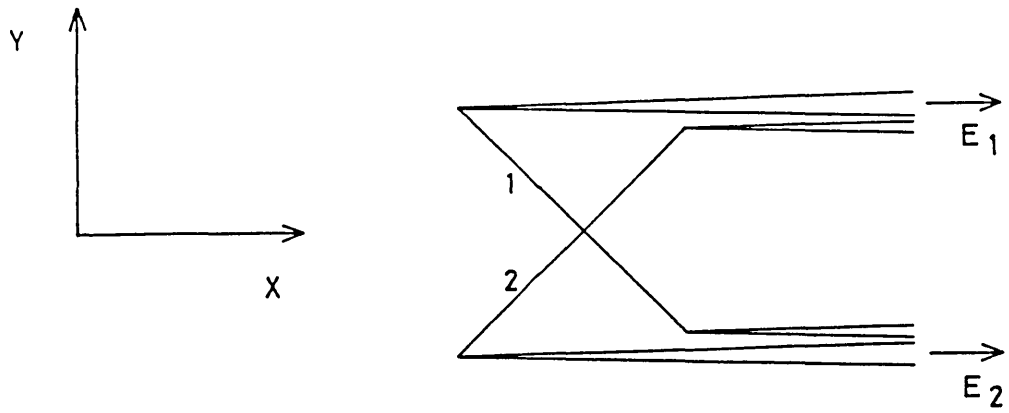
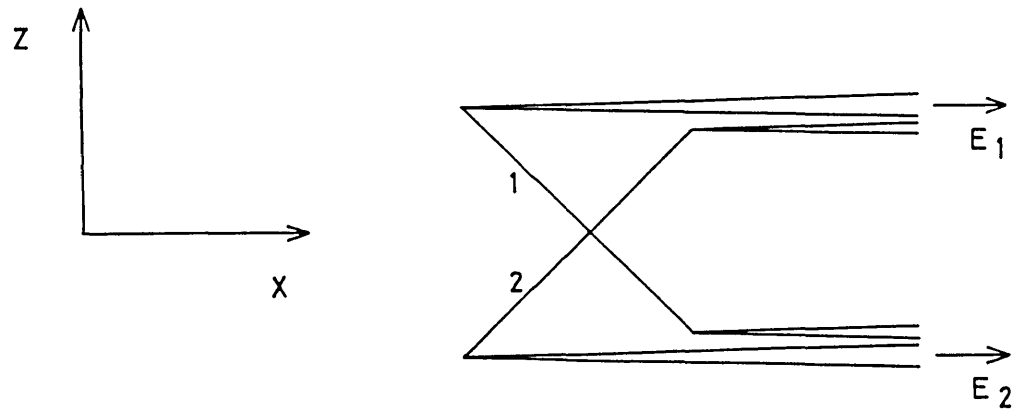


Figure 2.2 Flow rig for two opposed single jets in a deflecting stream.

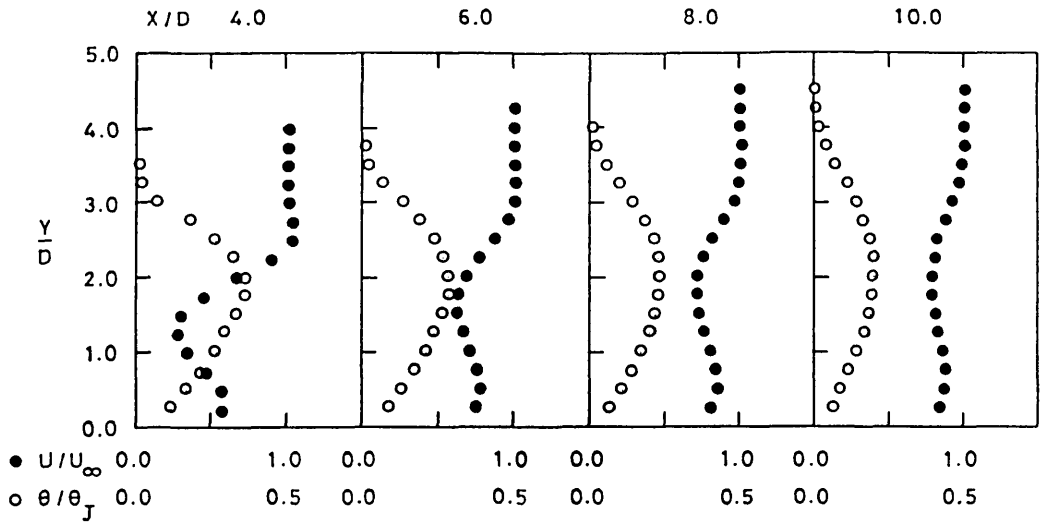


(a)

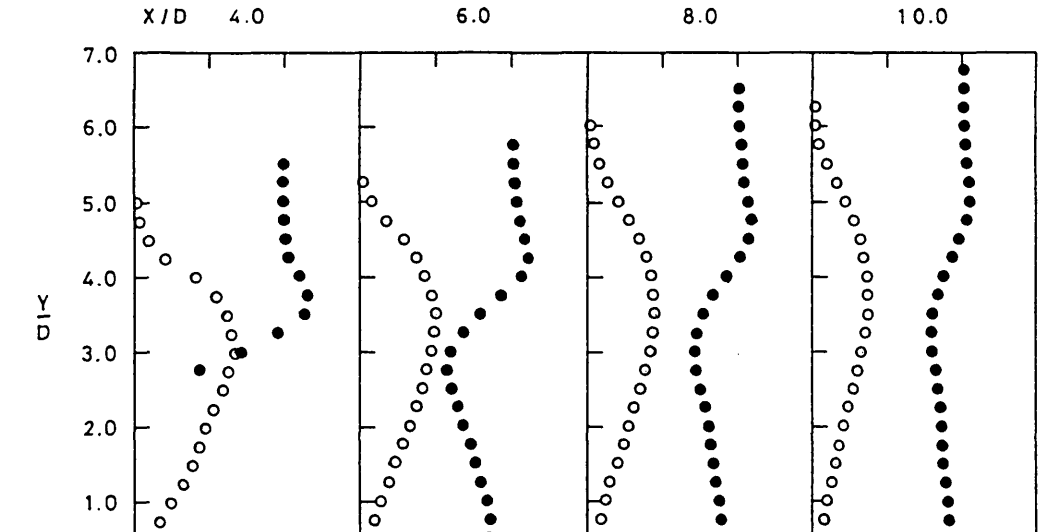


(b)

Figure 2.3 Orientation of the crosswire (a) measurement of $\overline{U}$, $\hat{u}$, $\hat{v}$, $\overline{uv}$ (b) measurement of $\overline{U}$, $\hat{u}$, $\hat{w}$, $\overline{uw}$.



(a)



(b)

Figure 2.4 Profiles of measured $\overline{U}$ velocity and mean scalar concentration in the symmetry plane of a single jet (a) $V_J/U_\infty = 1.5$ (b) $V_J/U_\infty = 2.3$.

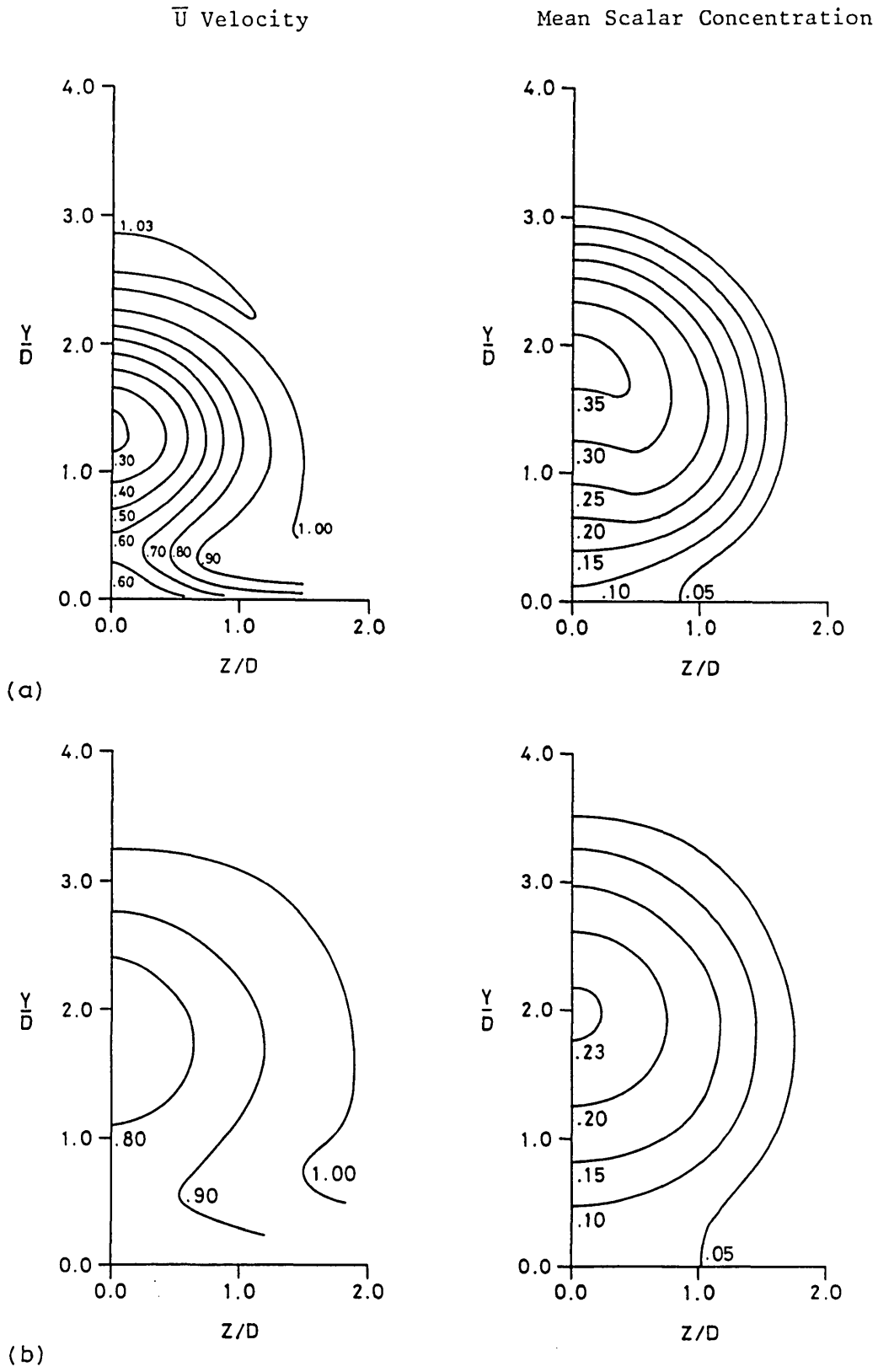
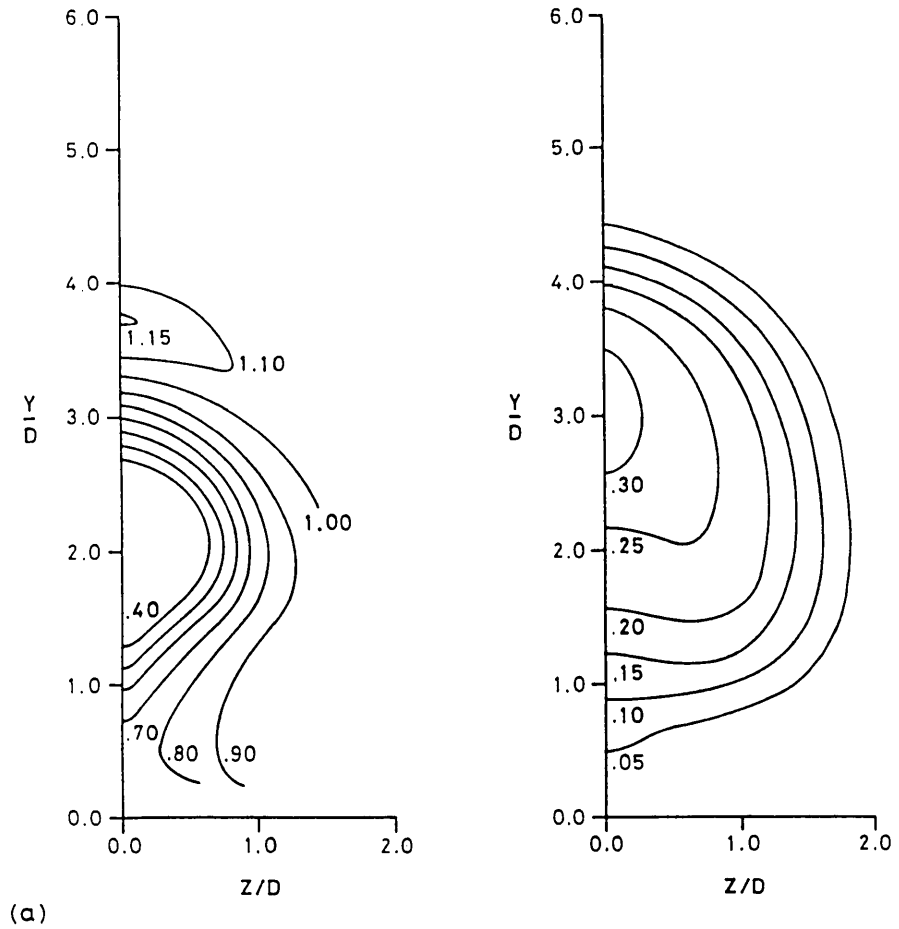
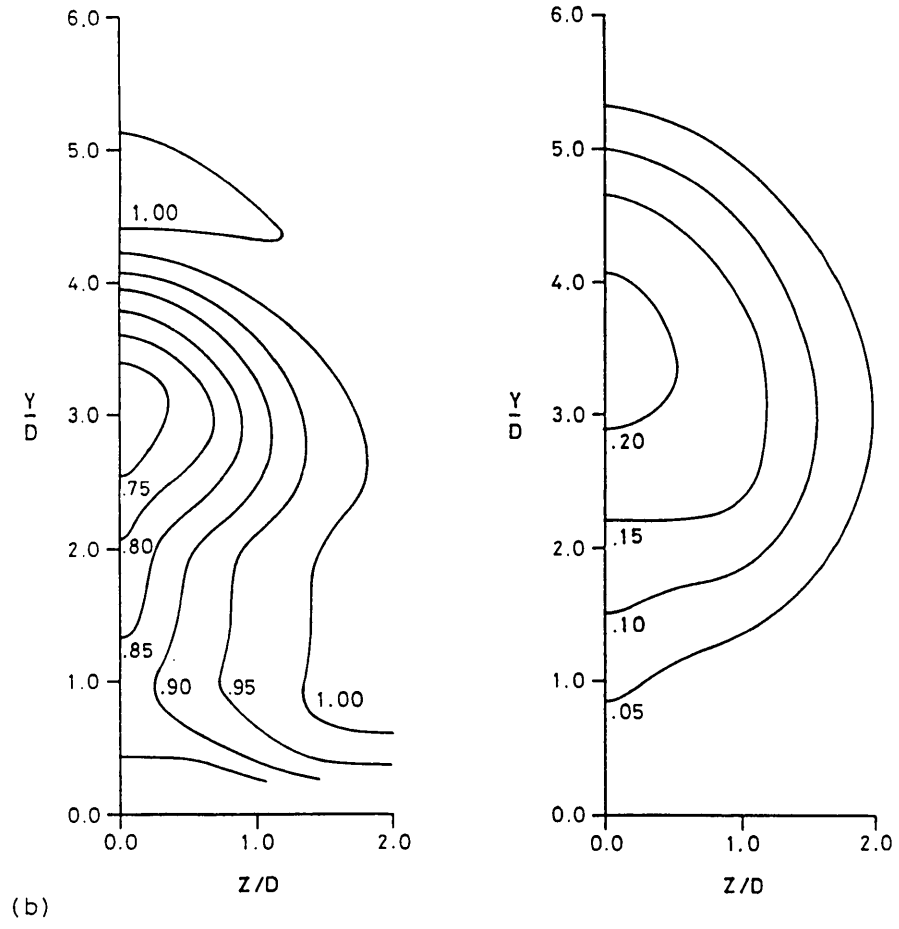


Figure 2.5 Contours of measured $\overline{U}$ velocity and mean scalar concentration for a single jet; V_J/U_∞ = 1.5 (a) X/D = 4.0 (b) X/D = 8.0.



(a)



(b)

Figure 2.6 Contours of measured $\overline{U}$ velocity and mean scalar concentration for a single jet; V_J/U_∞ = 2.3 (a) X/D = 4.0 (b) X/D = 8.0.

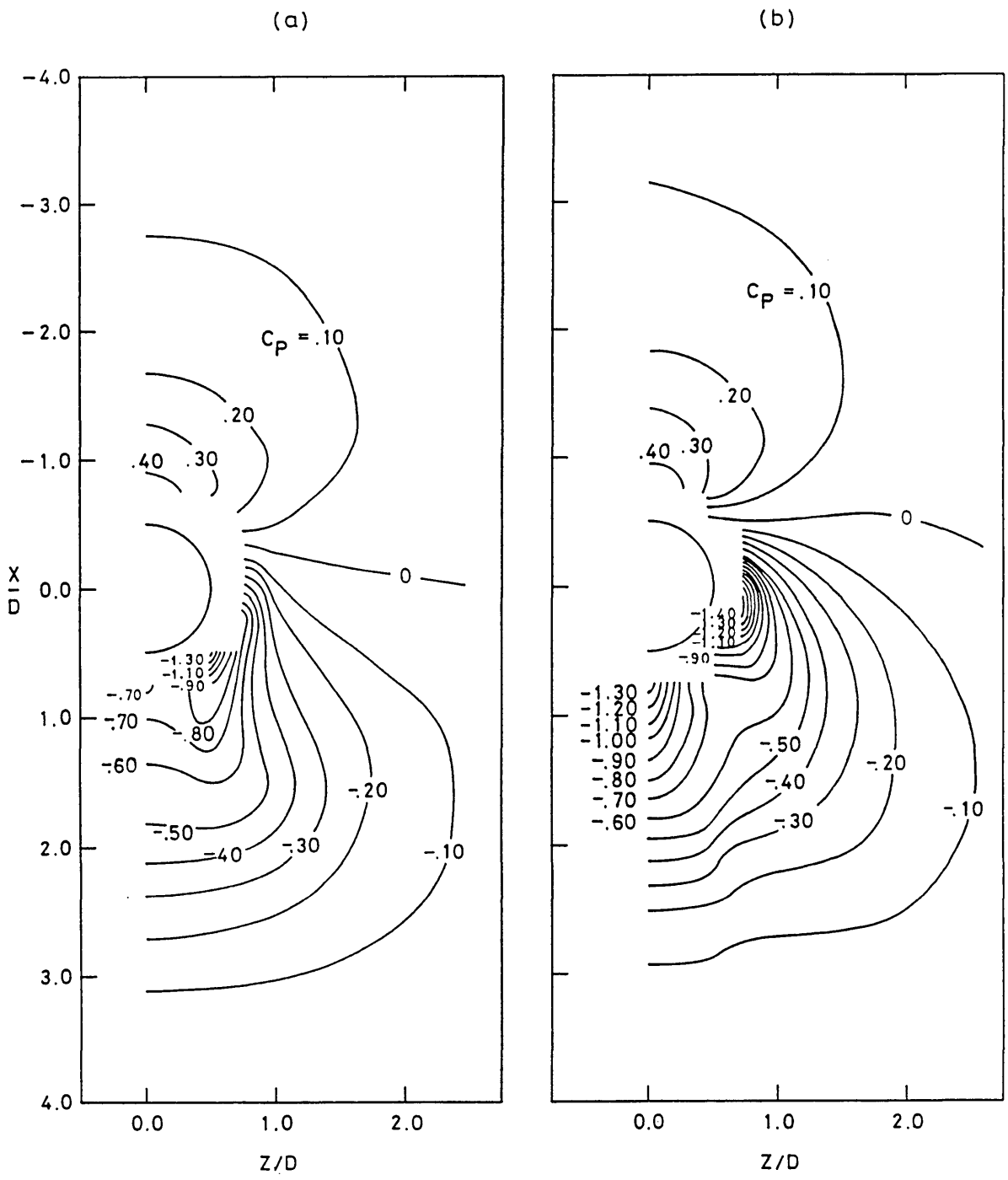
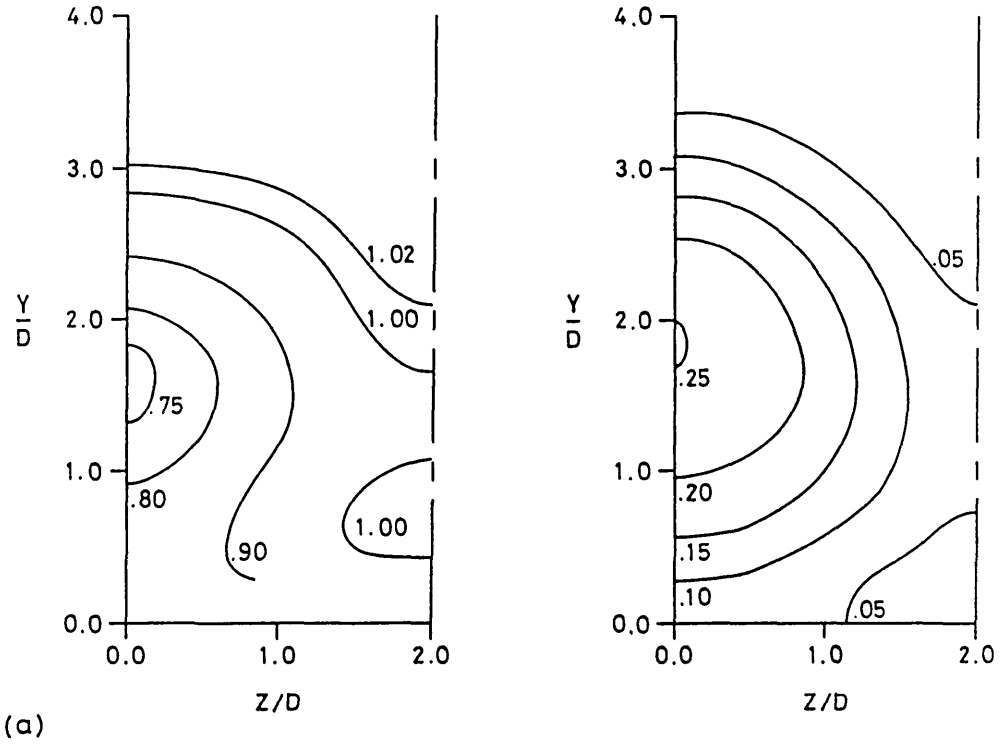
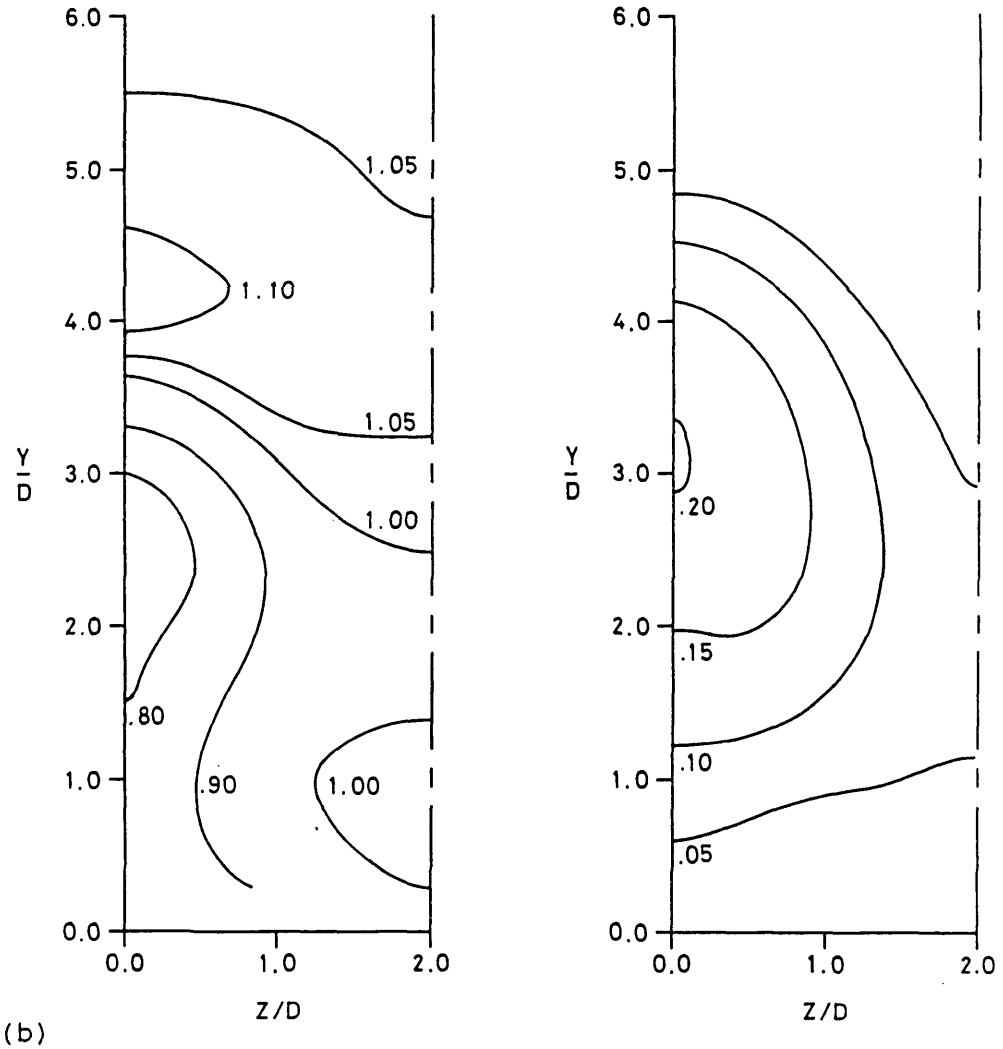


Figure 2.7 Contours of measured wall static pressure coefficient for a single jet (a) V_J/U_∞ = 1.5 (b) V_J/U_∞ = 2.3.



(a)



(b)

Figure 2.8 Contours of measured $\overline{U}$ velocity and mean scalar concentration in the plane X/D = 8.0 for a single row of jets; S/D = 4.0 (a) V_J/U_∞ = 1.5 (b) V_J/U_∞ = 2.3.

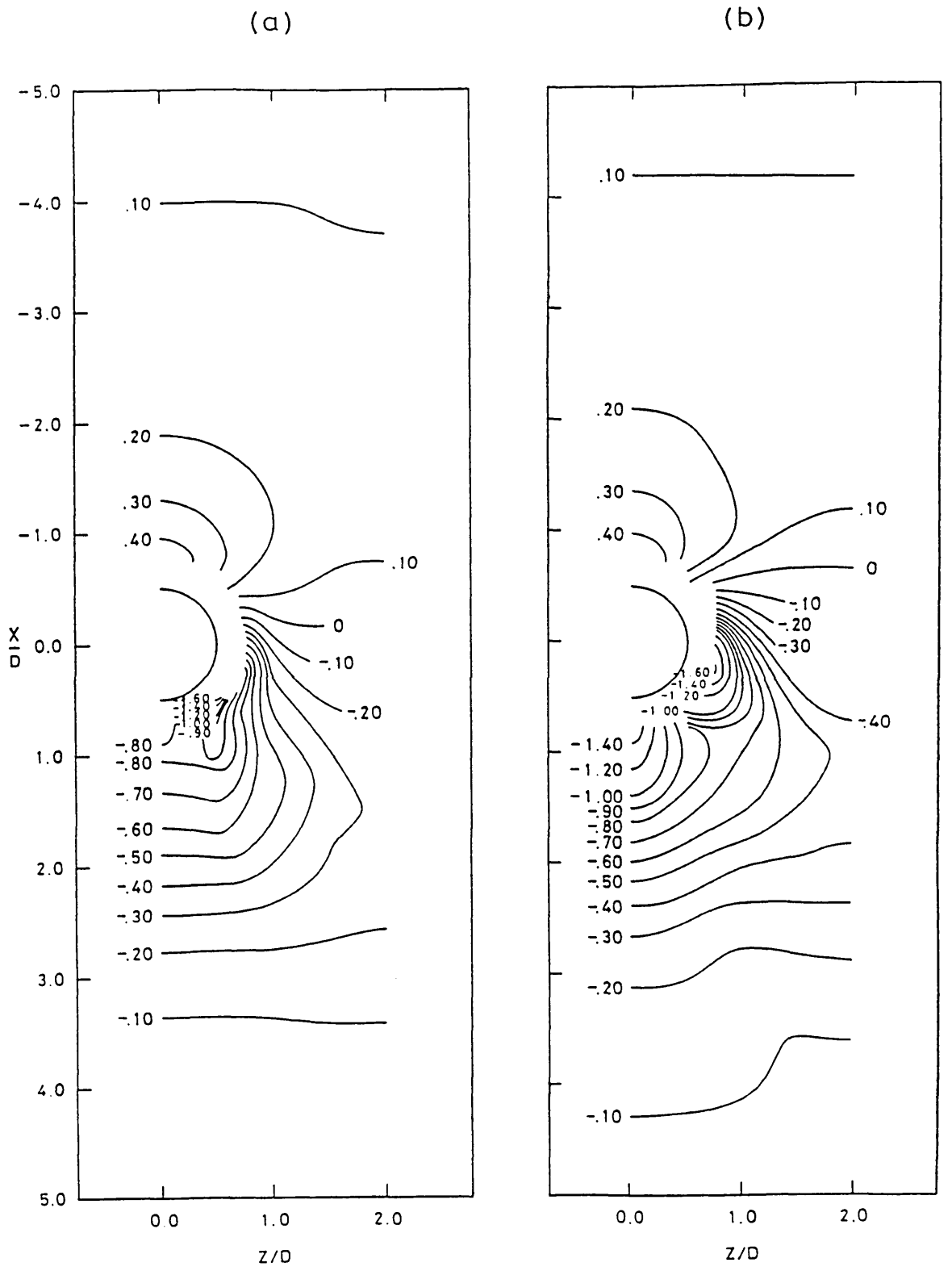


Figure 2.9 Contours of measured wall static pressure coefficient for a single row of jets; S/D = 4.0 (a) V_J/U_∞ = 1.5 (b) V_J/U_∞ = 2.3.

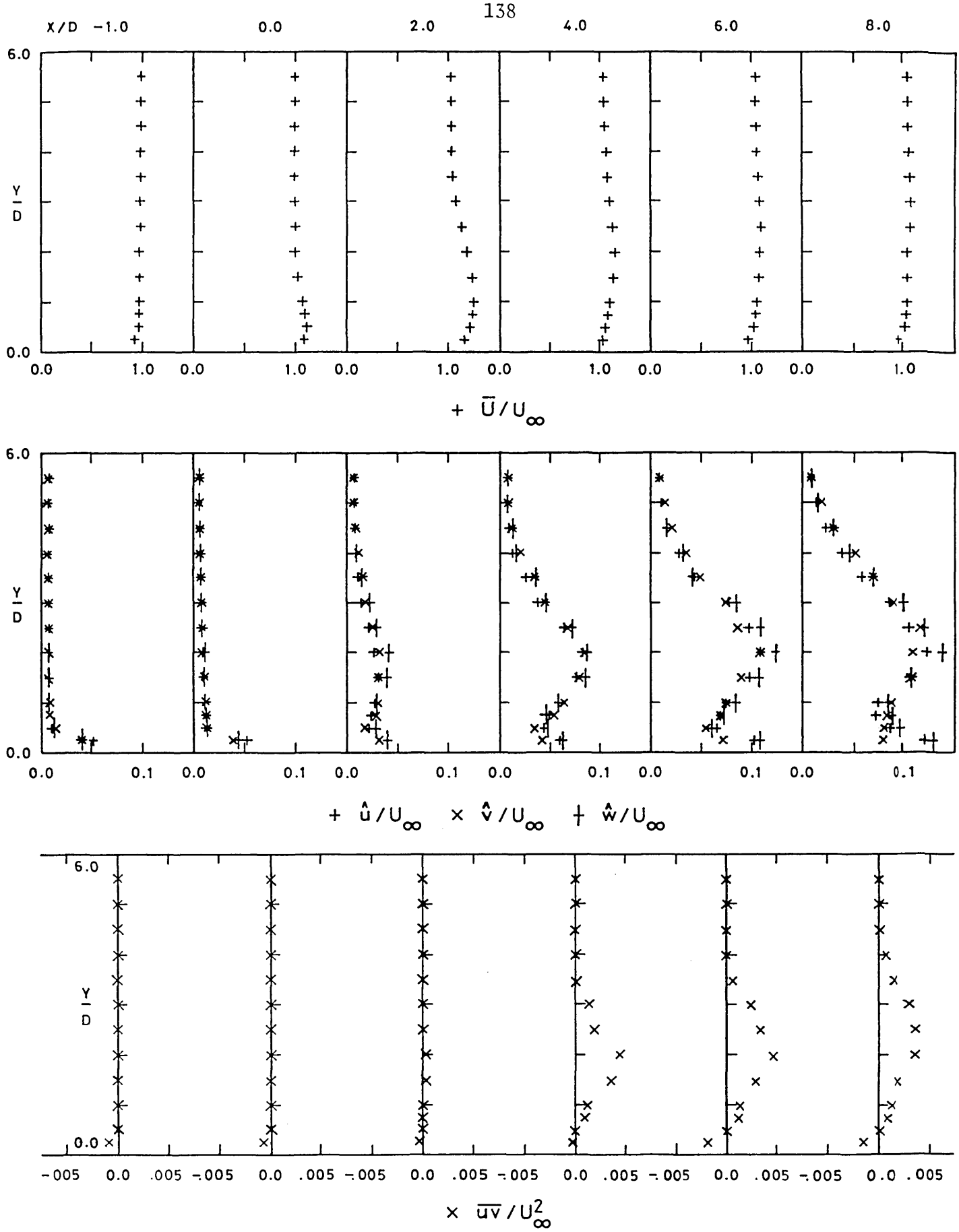


Figure 2.10 Profiles of measured Reynolds stresses in the plane Z/D = 2.0 for a single row of jets; S/D = 4.0; V_J/U_∞ = 2.3.

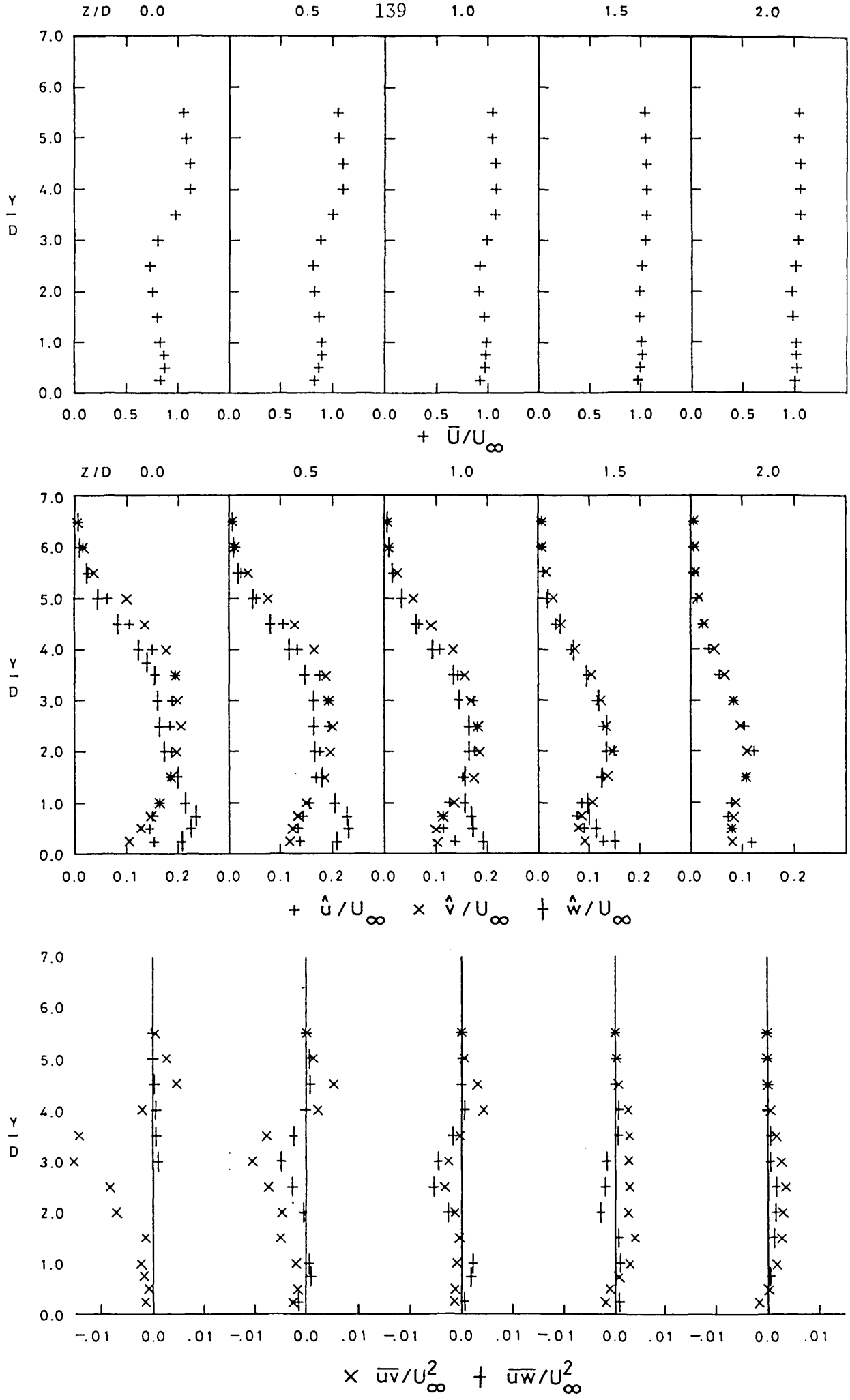
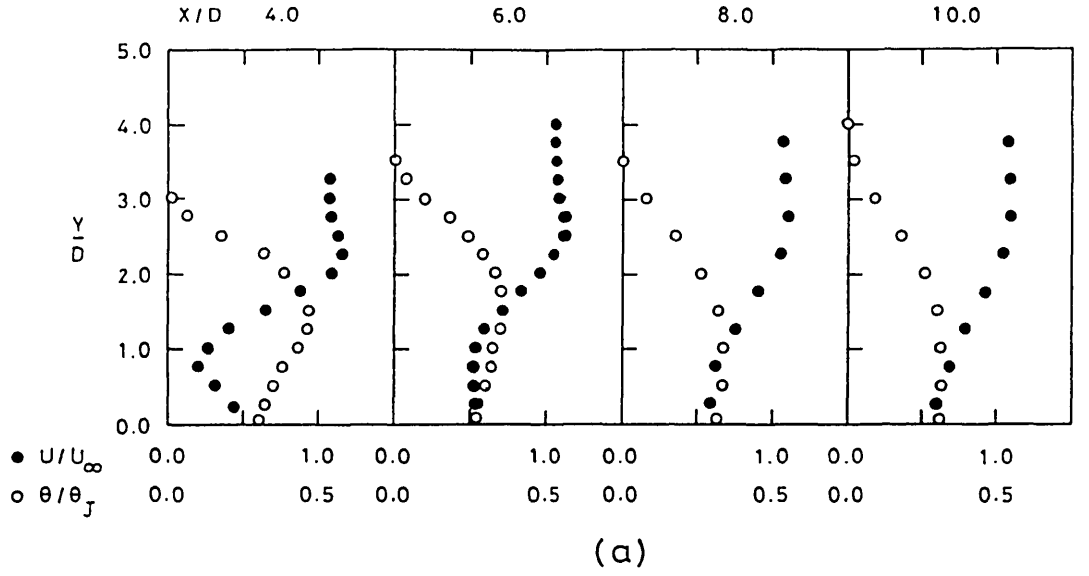
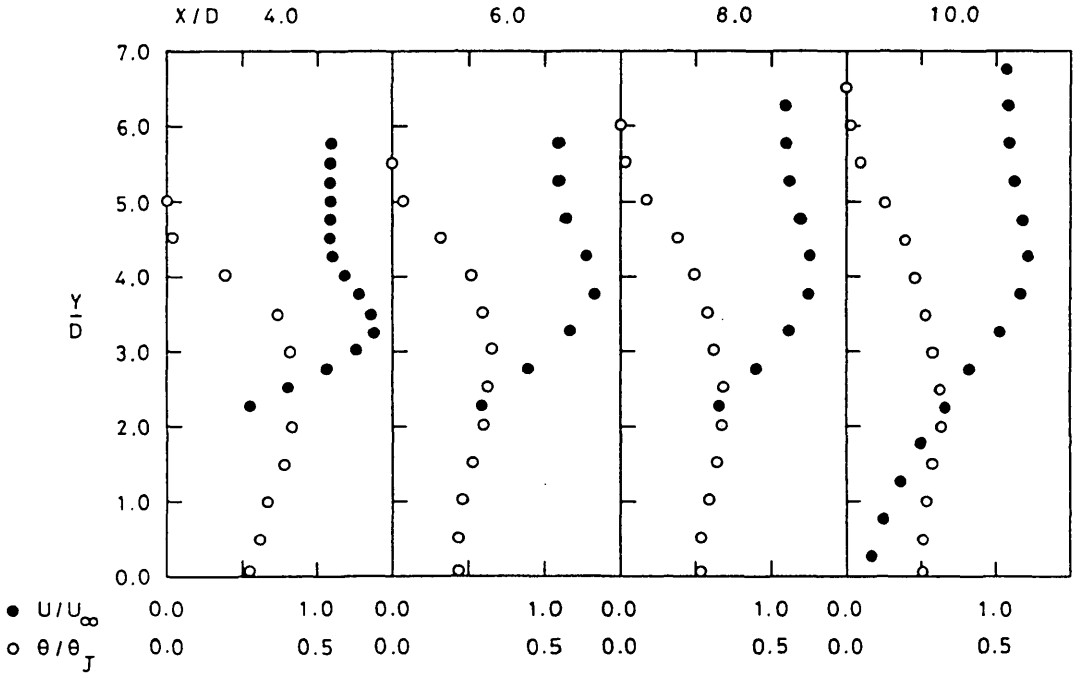


Figure 2.11 Profiles of measured Reynolds stresses in the plane X/D = 8.0 for a single row of jets; S/D = 4.0; V_J/U_∞ = 2.3.

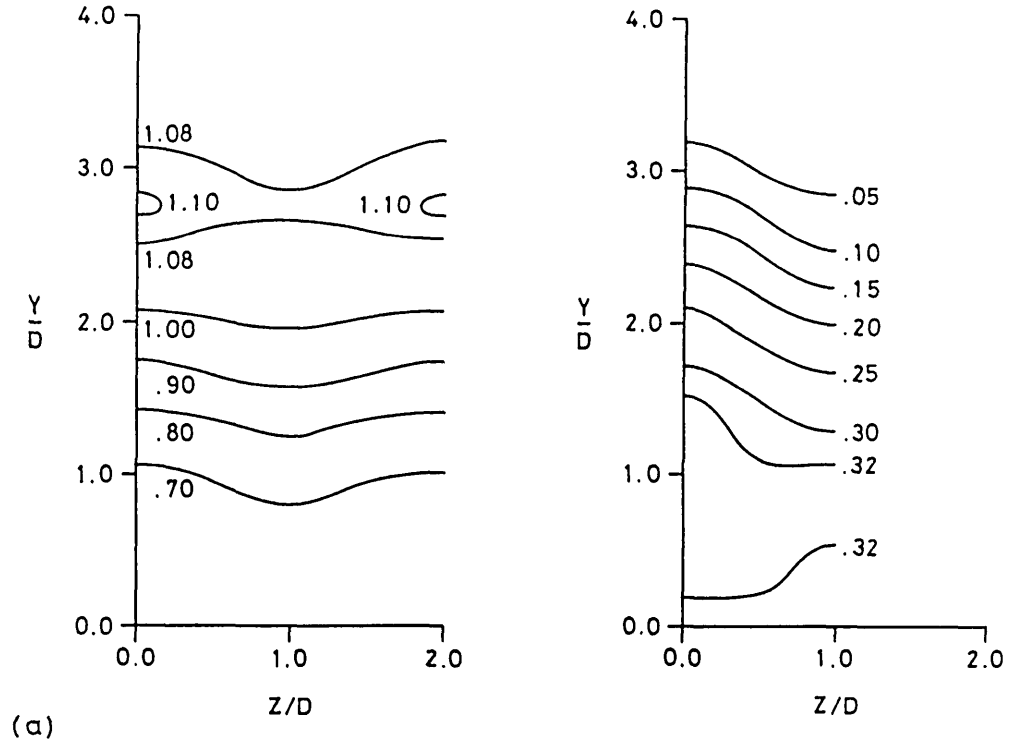


(a)

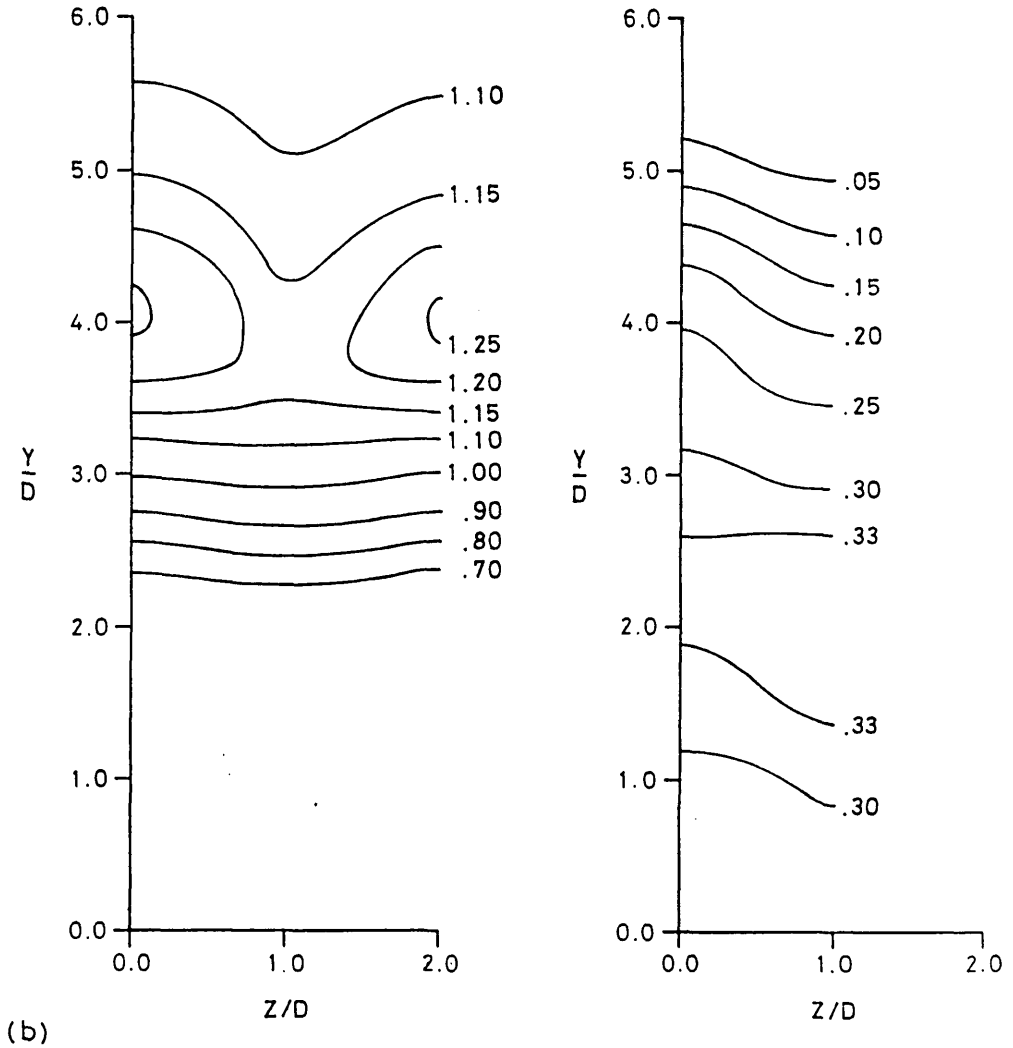


(b)

Figure 2.12 Profiles of measured $\overline{U}$ velocity and mean scalar concentration in the symmetry plane Z/D = 0 of a single row of jets; S/D = 2.0 (a) V_J/U_∞ = 1.5 (b) V_J/U_∞ = 2.3.



(a)



(b)

Figure 2.13 Contours of measured $\overline{U}$ velocity and mean scalar concentration in the plane X/D = 8.0 for a single row of jets; S/D = 2.0 (a) V_J/U_∞ = 1.5 (b) V_J/U_∞ = 2.3.

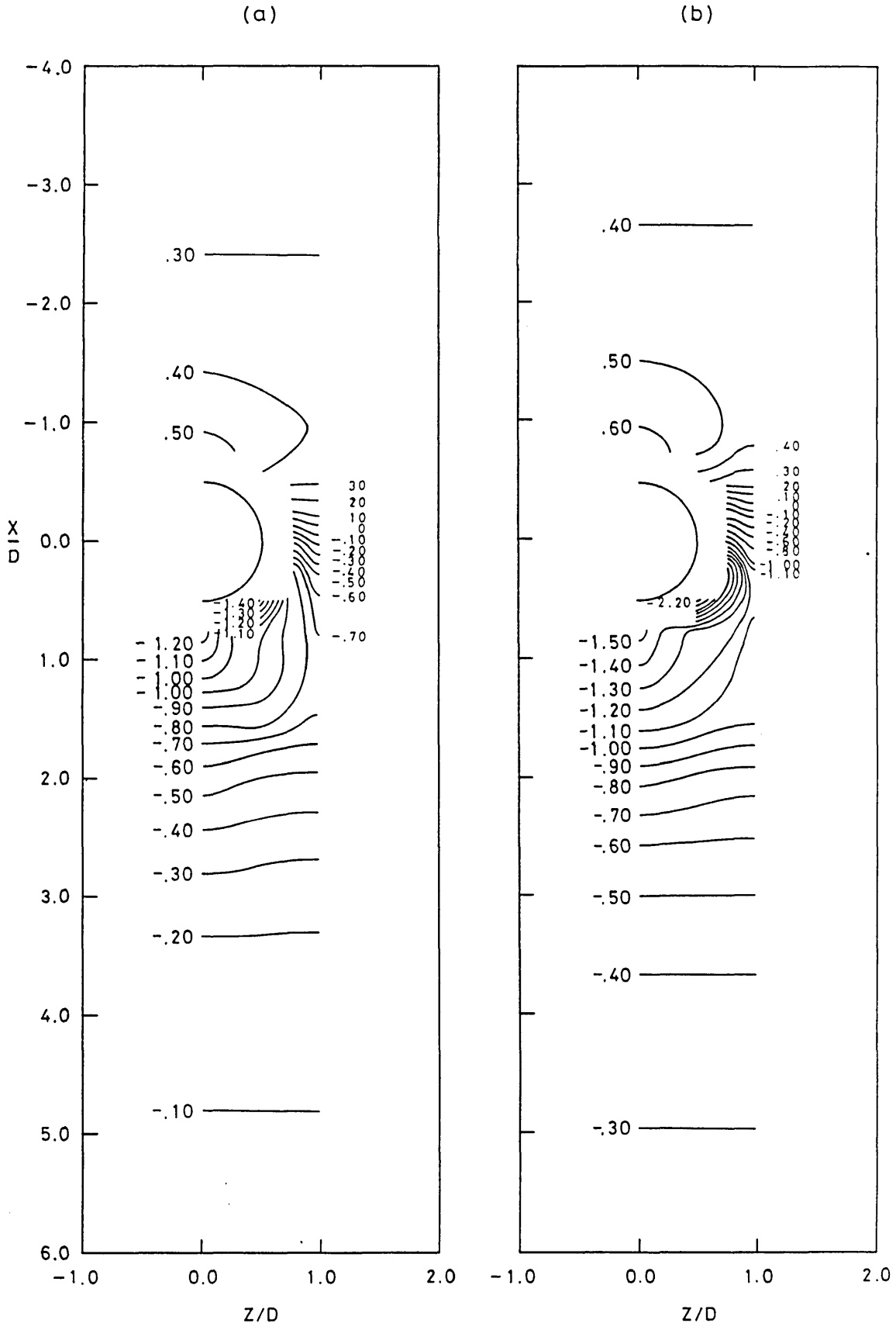


Figure 2.14 Contours of measured wall static pressure coefficient for a single row of jets; S/D = 2.0 (a) V_J/U_∞ = 1.5 (b) V_J/U_∞ = 2.3.

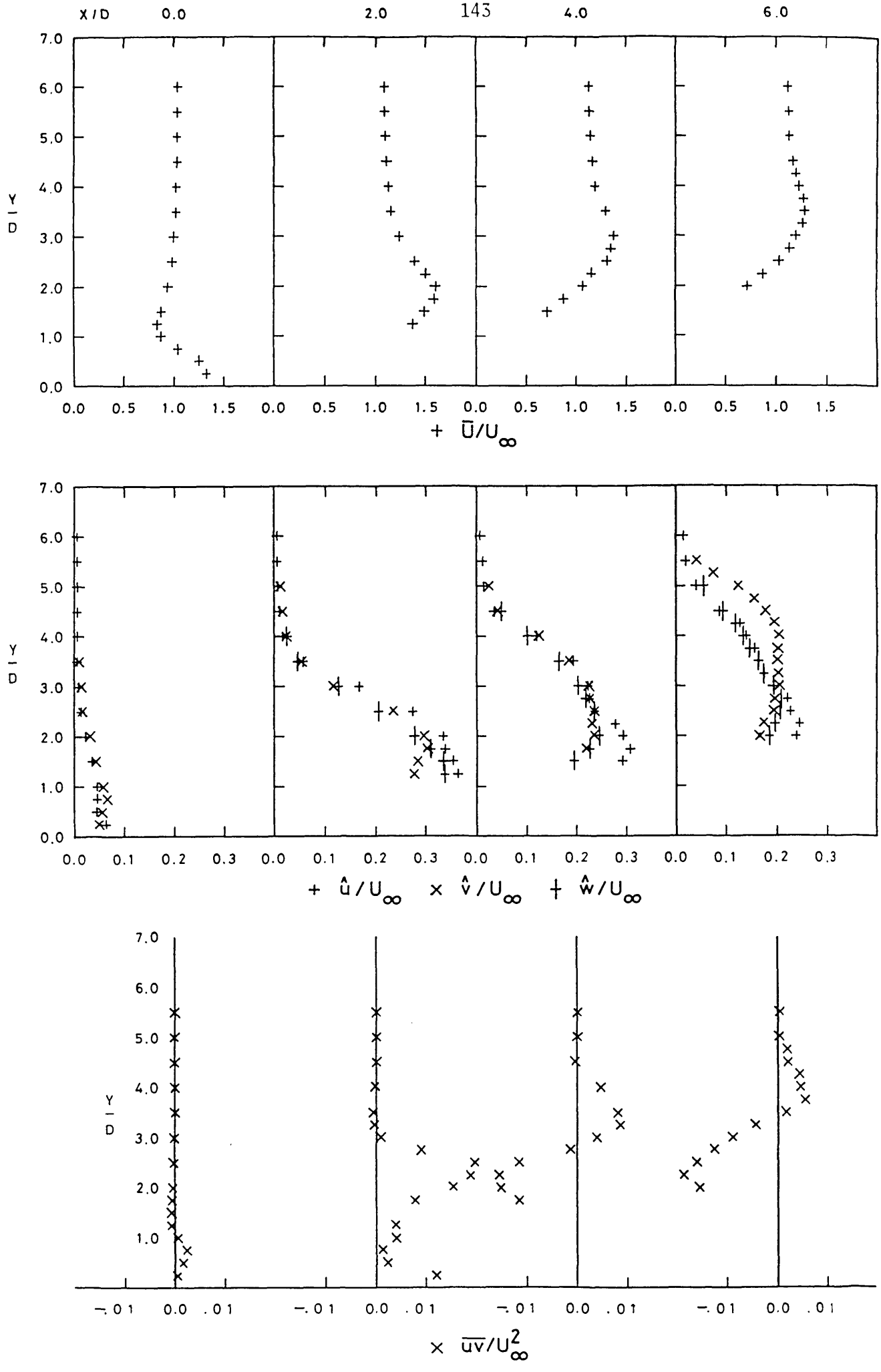
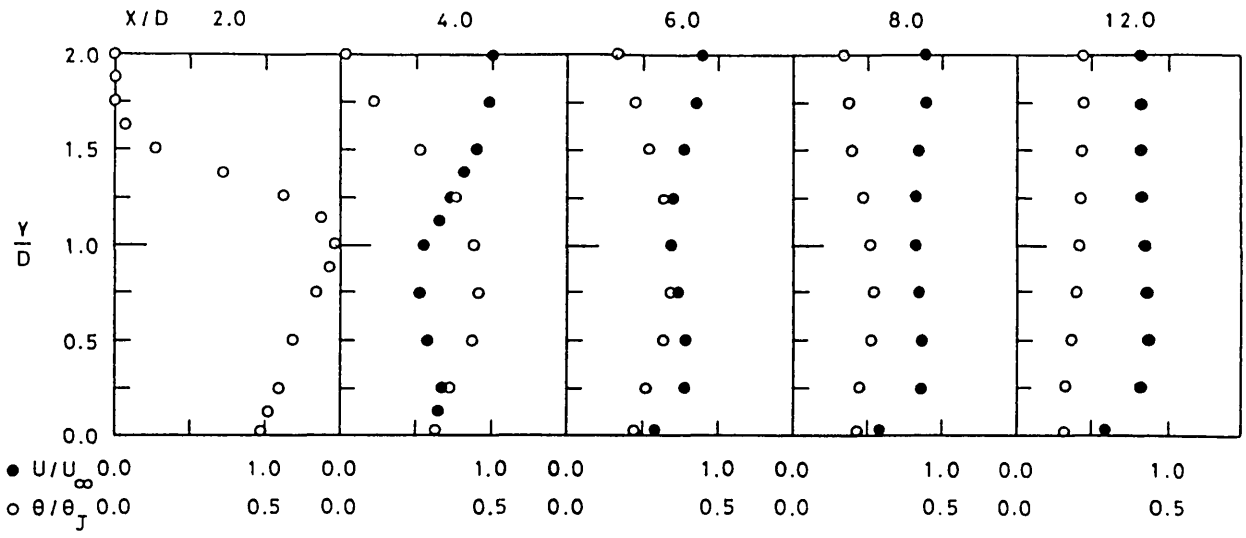


Figure 2.15 Profiles of measured Reynolds stresses in the plane Z/D = 1.0 for a single row of jets; S/D = 2.0; V_J/U_∞ = 2.3.



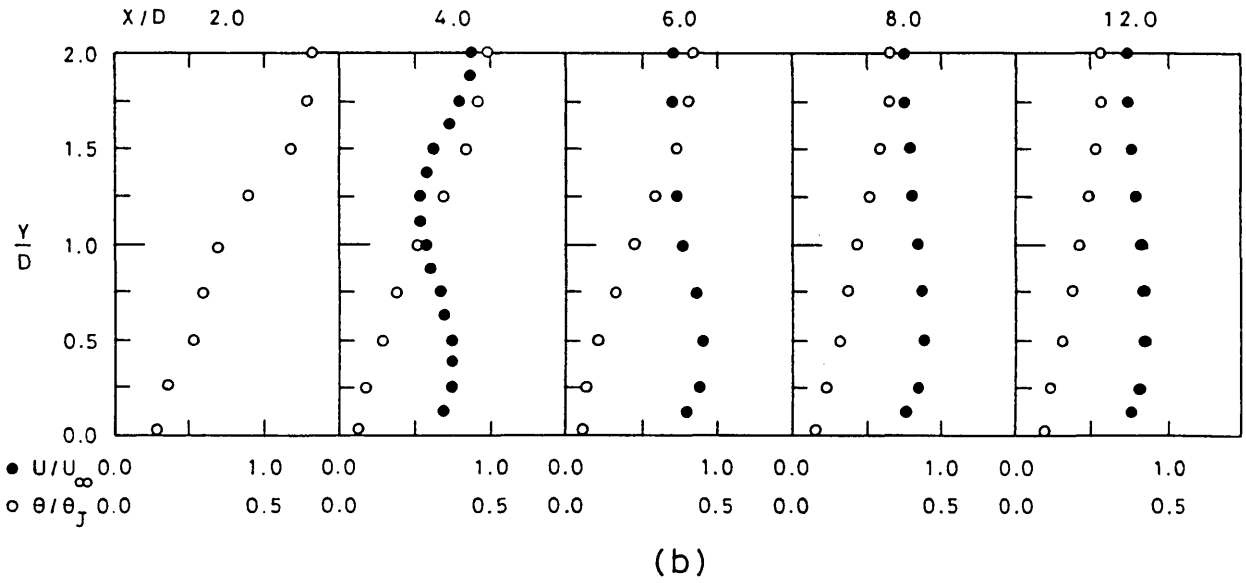


Figure 2.16 Profiles of measured $\overline{U}$ velocity and mean scalar concentration in the symmetry plane Z/D = 0 of two opposed single jets; H/D = 4.0 (a) V_J/U_∞ = 1.0 (b) V_J/U_∞ = 1.8.

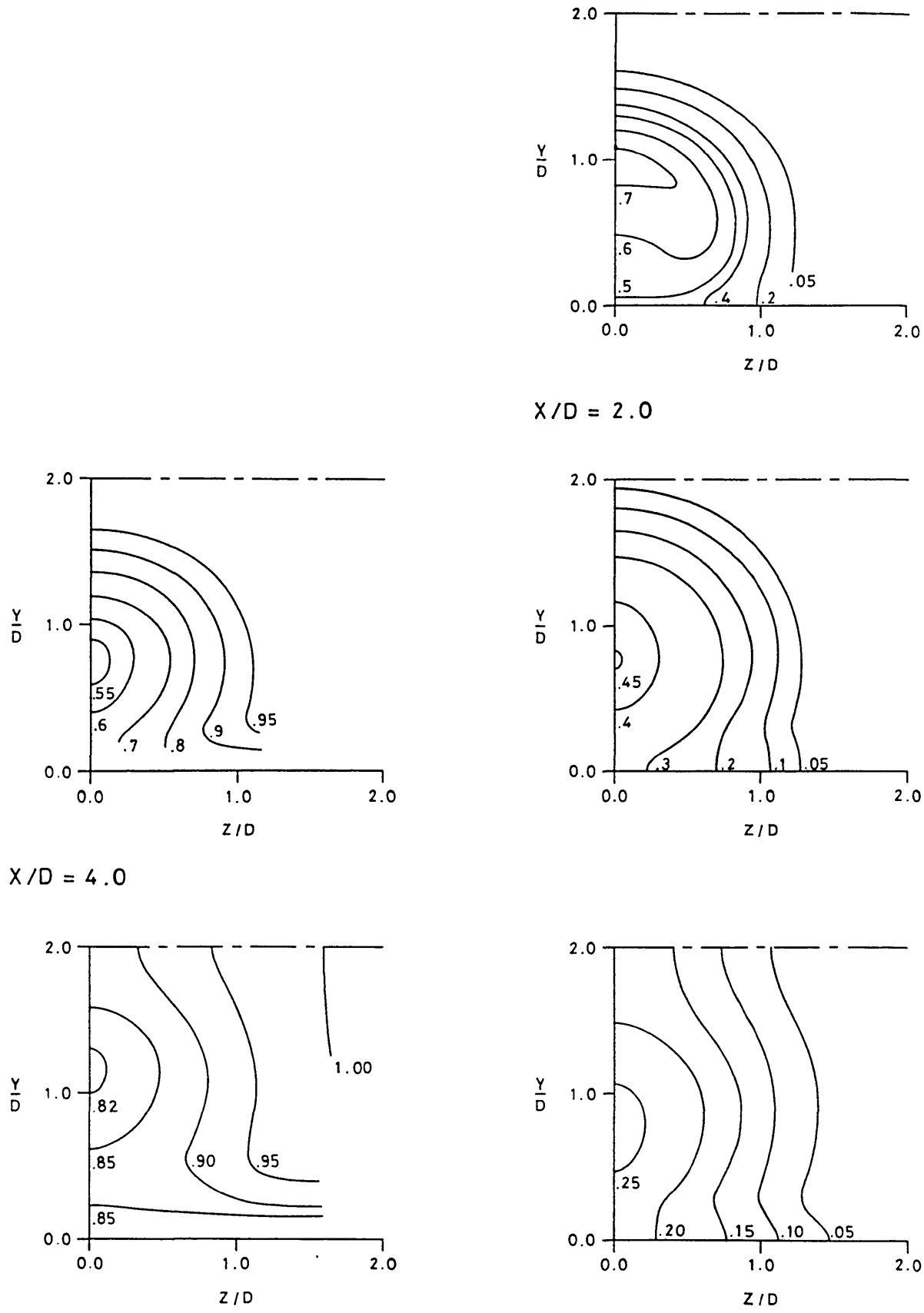
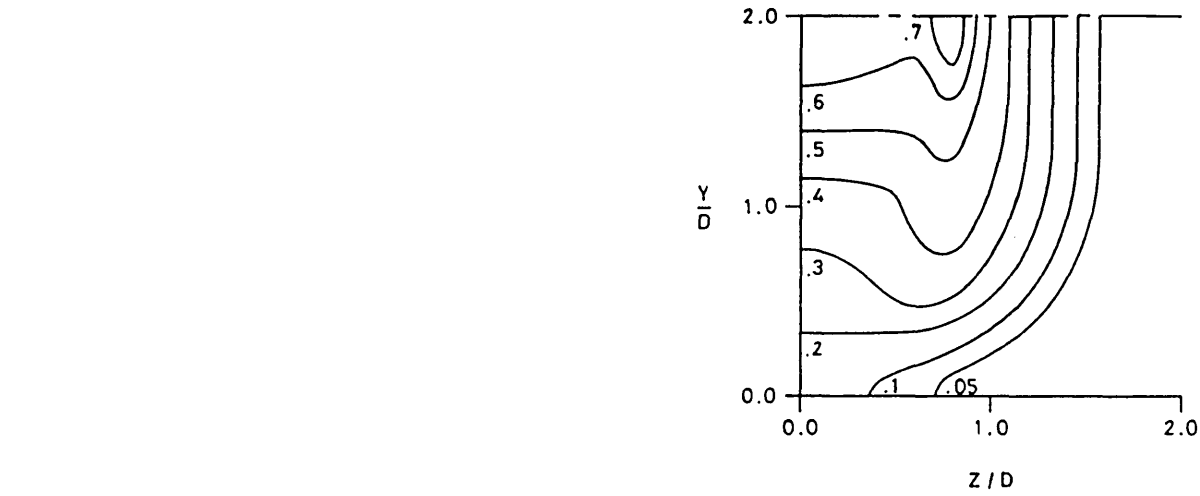
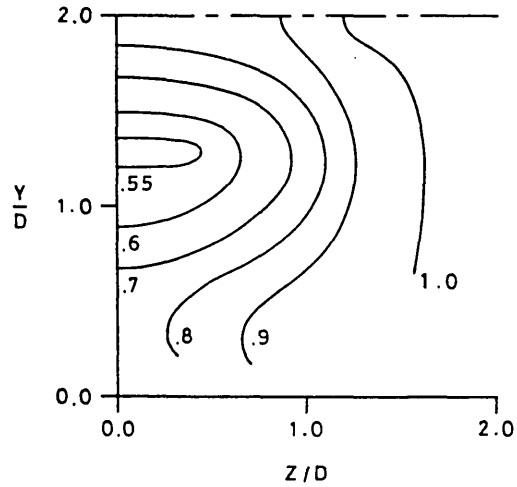
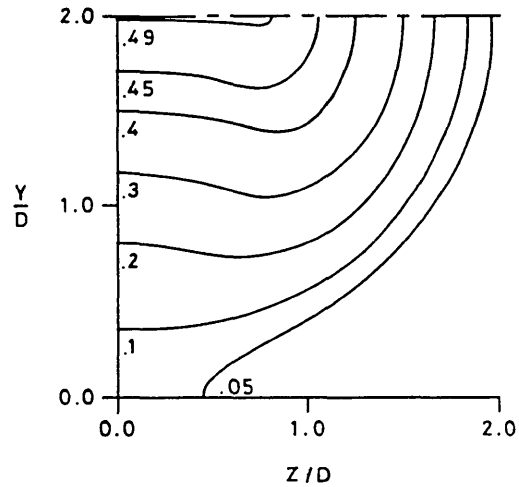


Figure 2.17 Contours of measured $\overline{U}$ velocity and mean scalar concentration for two opposed single jets; H/D = 4.0; V_J/U_∞ = 1.0.

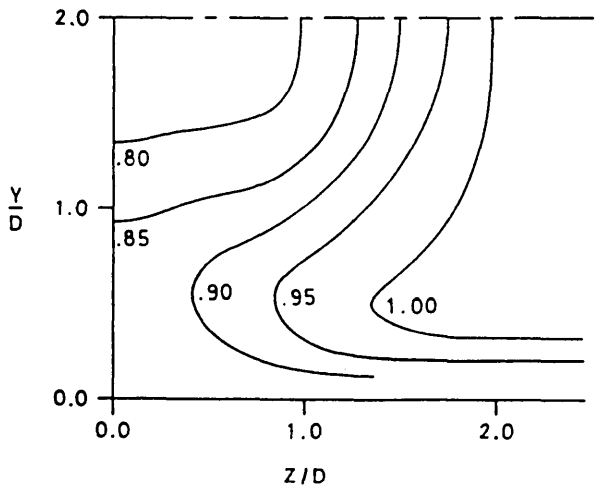


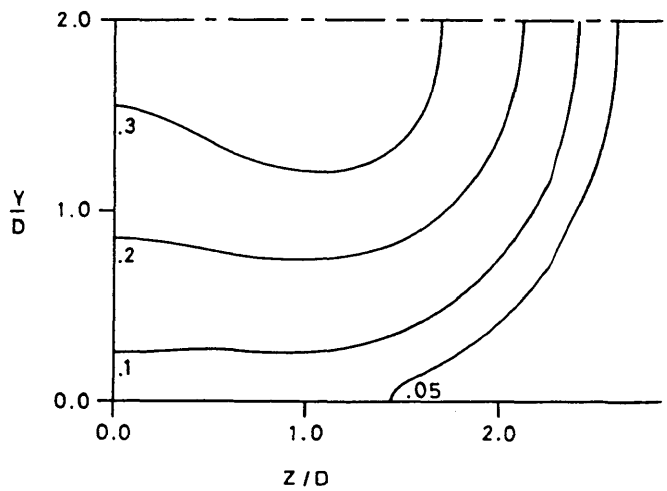
X/D = 2.0





X/D = 4.0





X/D = 8.0

Figure 2.18 Contours of measured $\overline{U}$ velocity and mean scalar concentration for two opposed single jets; H/D = 4.0; V_J/U_∞ = 1.8.

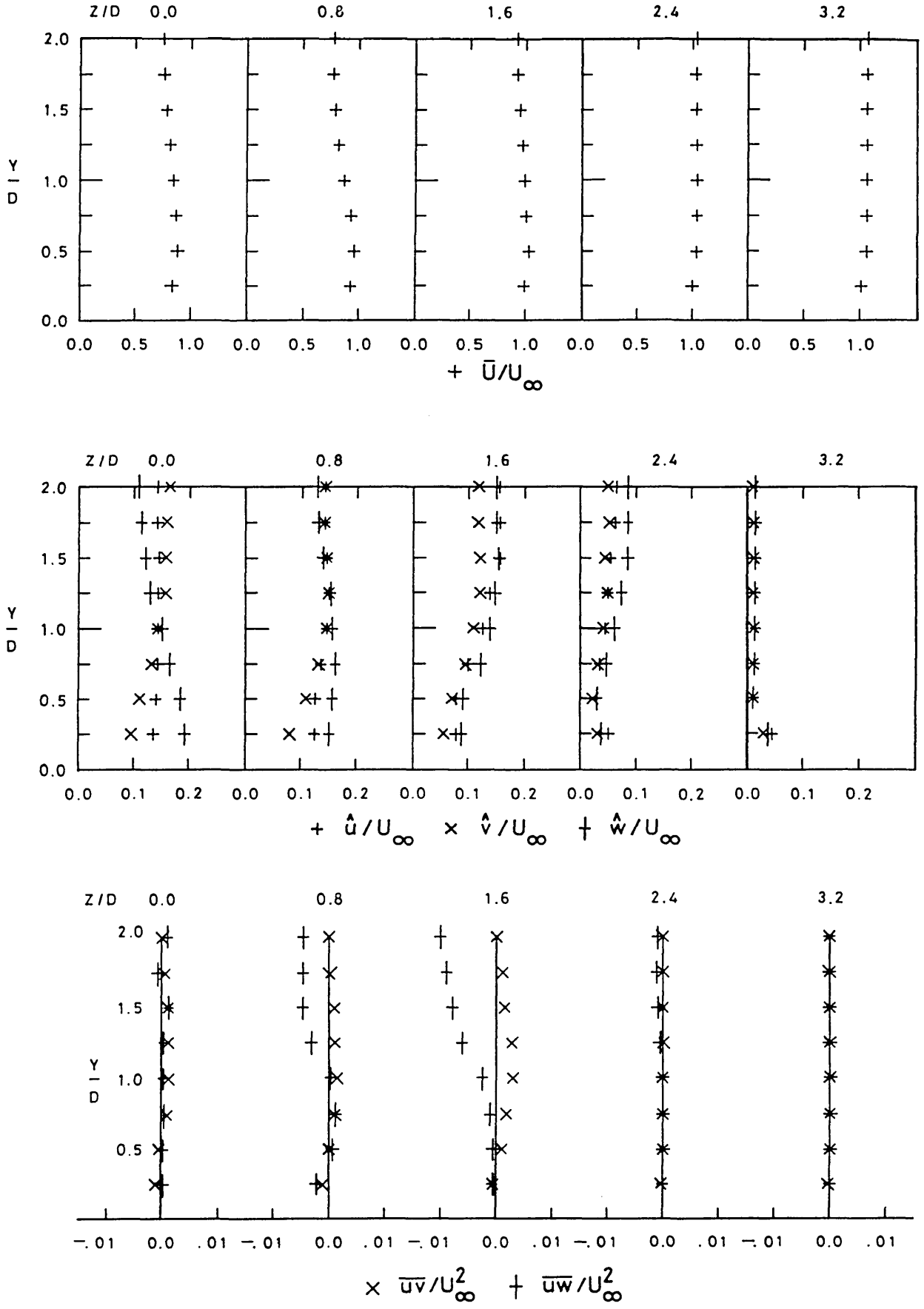


Figure 2.19 Profiles of measured Reynolds stresses in the plane X/D = 8.0 for two opposed single jets; H/D = 4.0; V_J/U_∞ = 1.8.

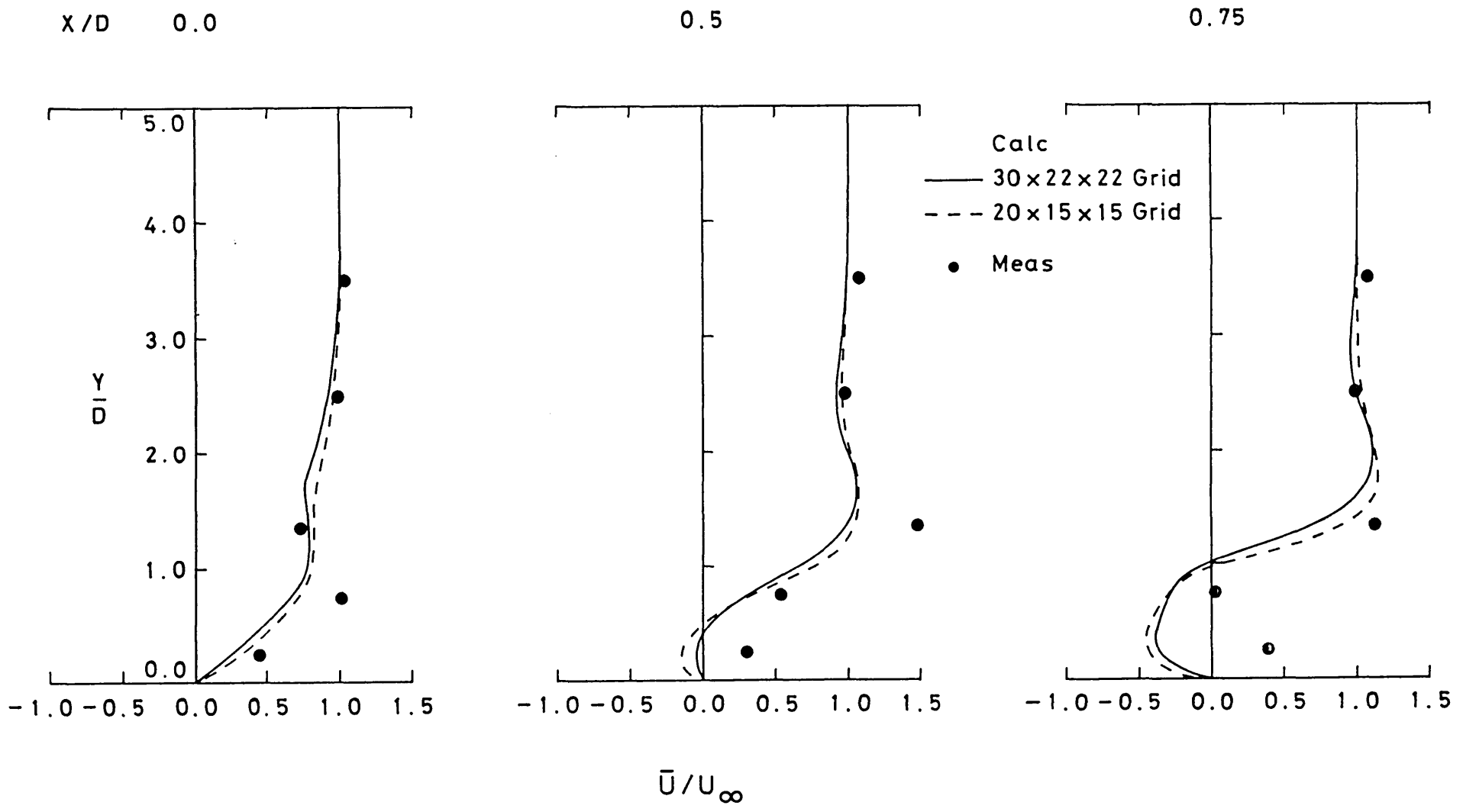


Figure 4.1 Profiles of calculated and measured $\bar{U}$ velocity in the symmetry plane of a single jet; $V_J/U_\infty = 2.3$.

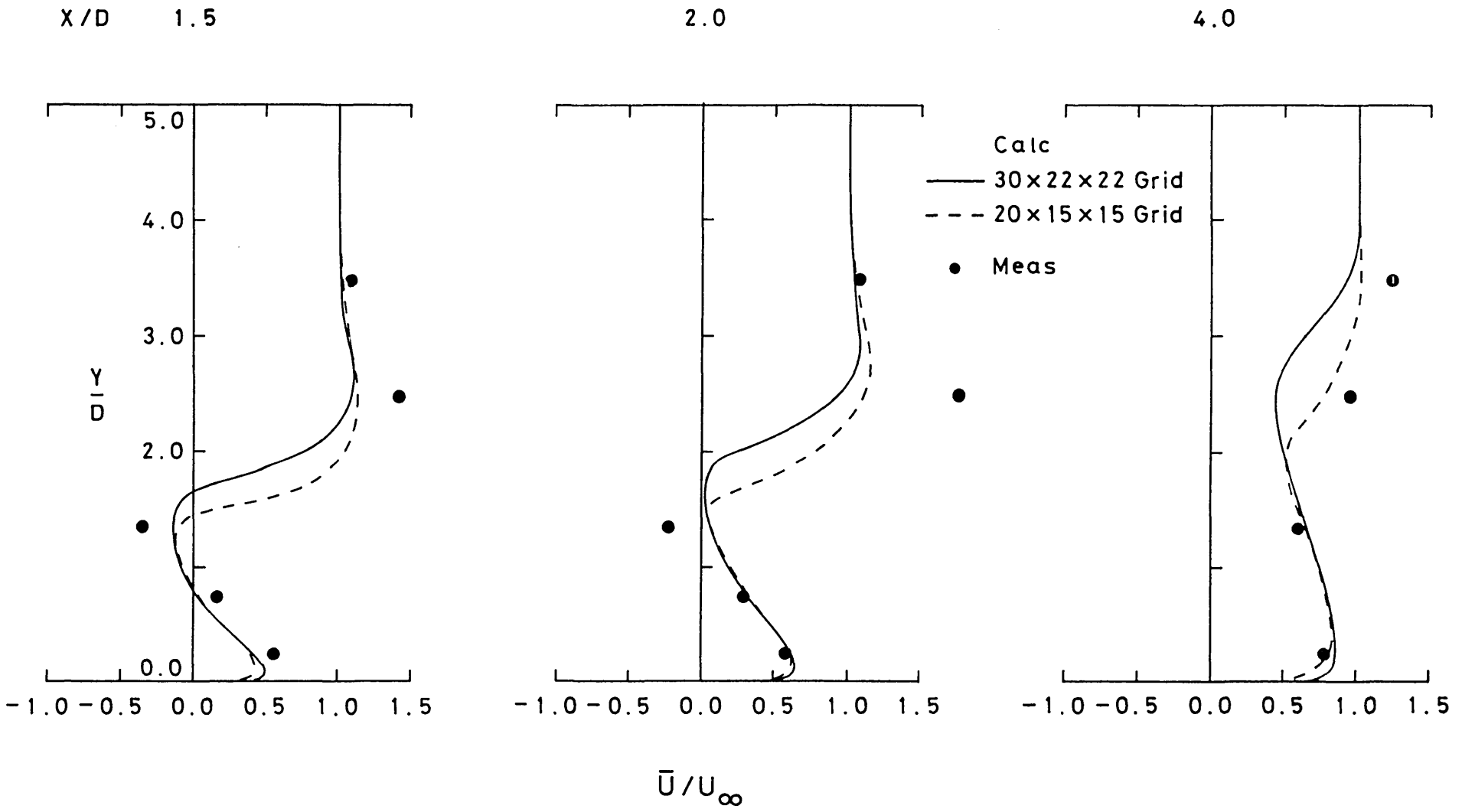


Figure 4.1 continued

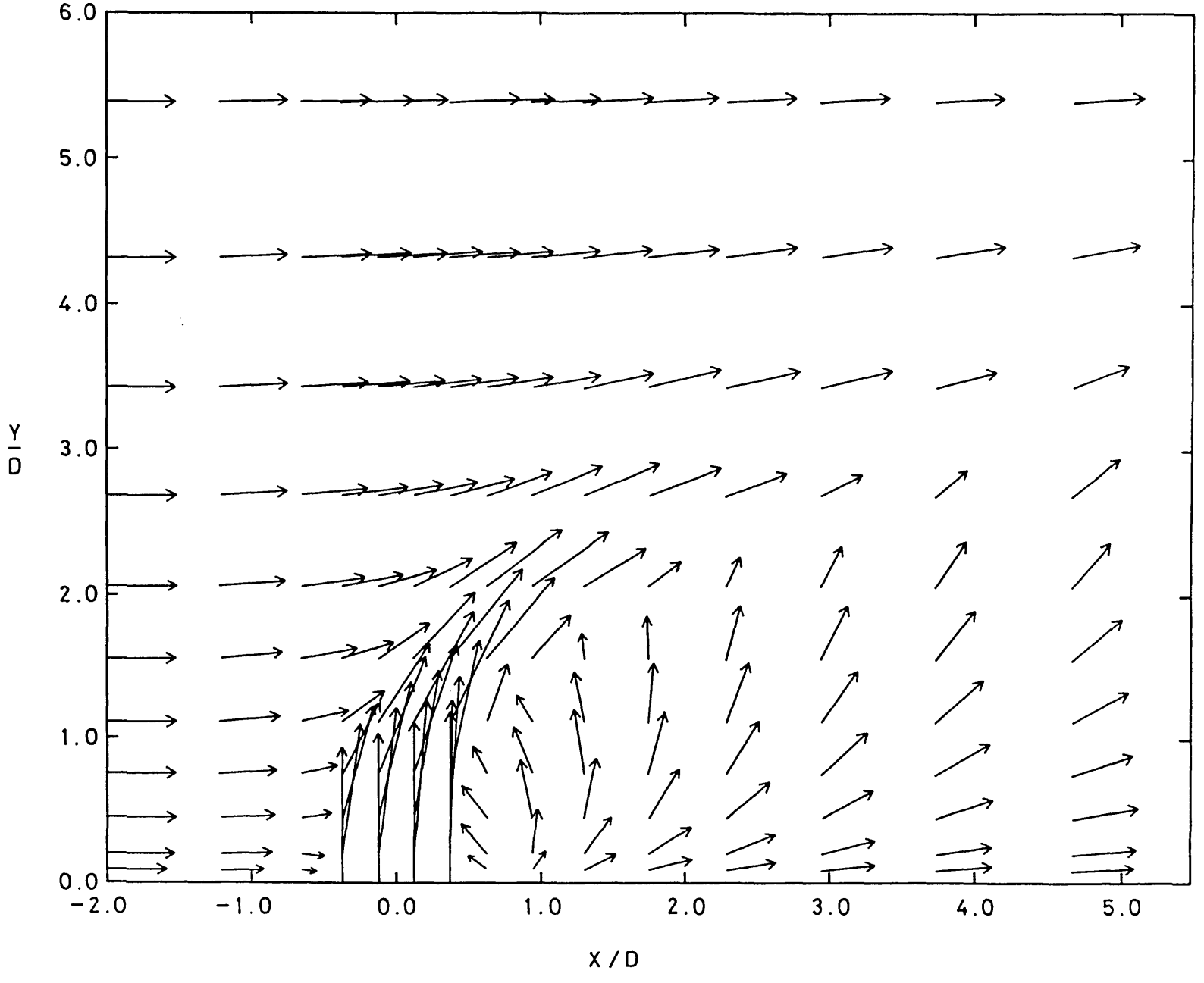


Figure 4.2 Calculated velocity vectors in the symmetry plane of a single jet; $V_J/U_\infty = 2.3$.

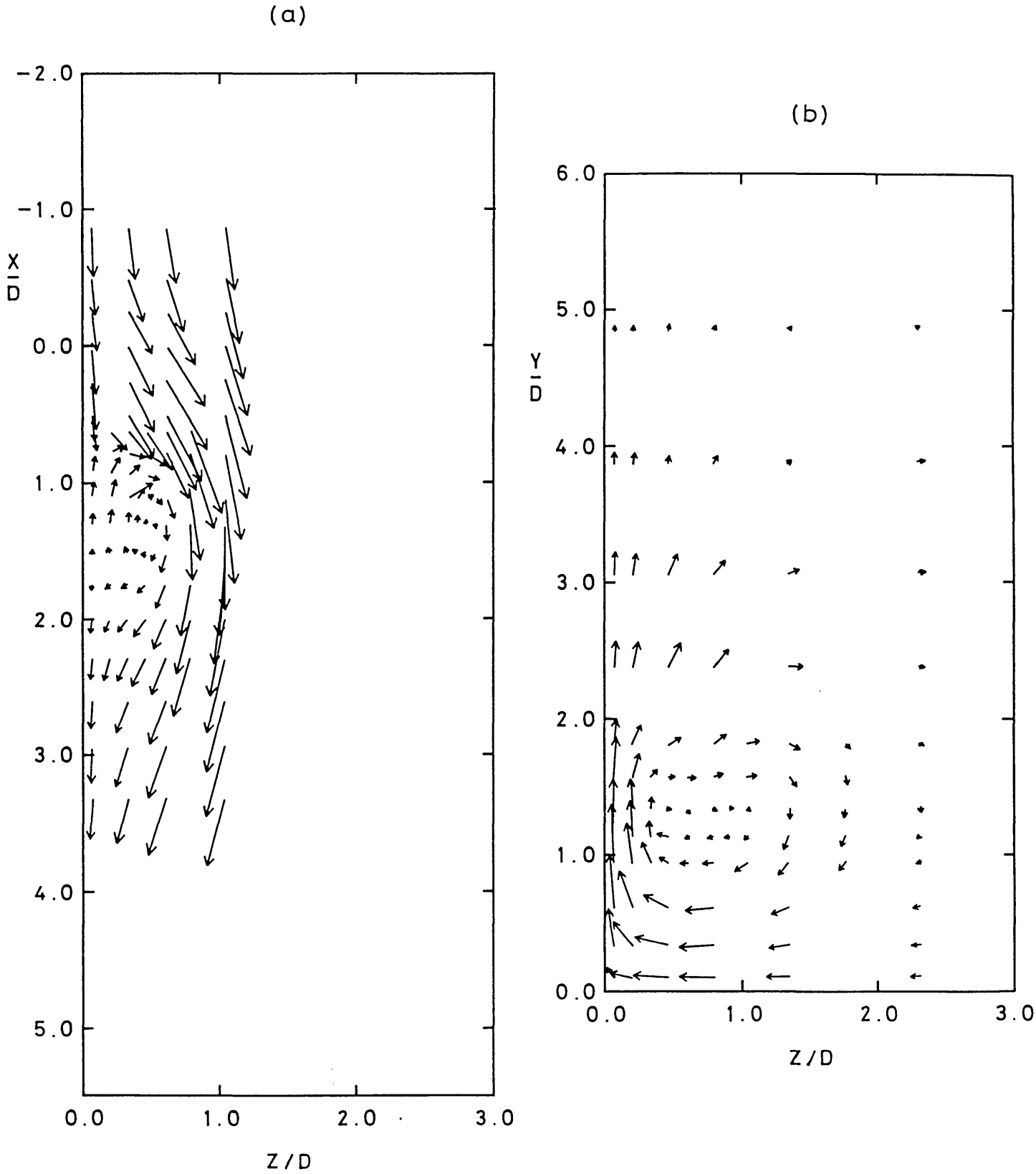


Figure 4.3 Calculated velocity vectors for a single jet; V_J/U_∞ = 2.3 (a) Y/D = 1.0 (b) X/D = 2.0.

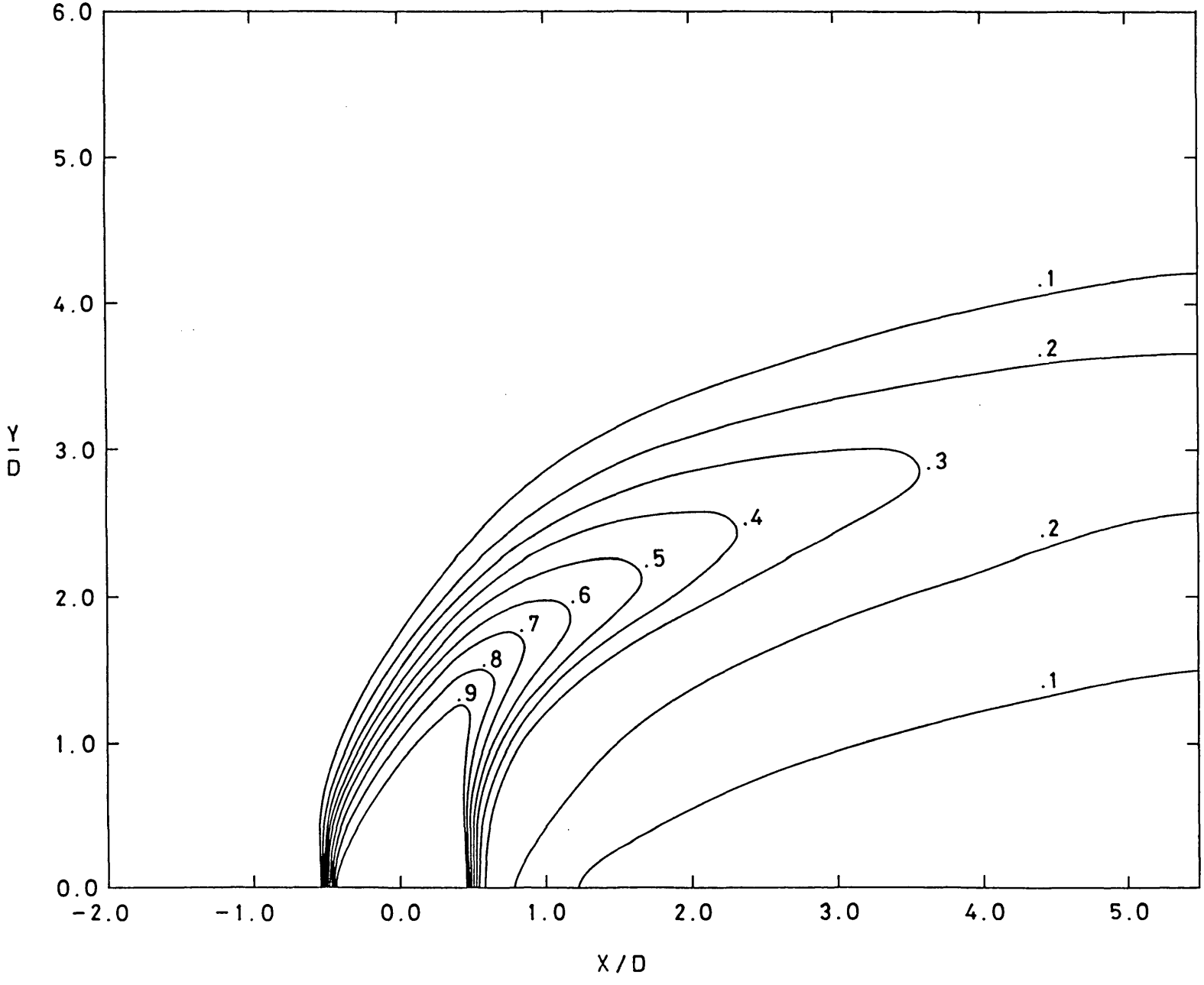


Figure 4.4 Contours of calculated mean scalar concentration in the symmetry plane of a single jet; $V_J/U_\infty = 2.3$.

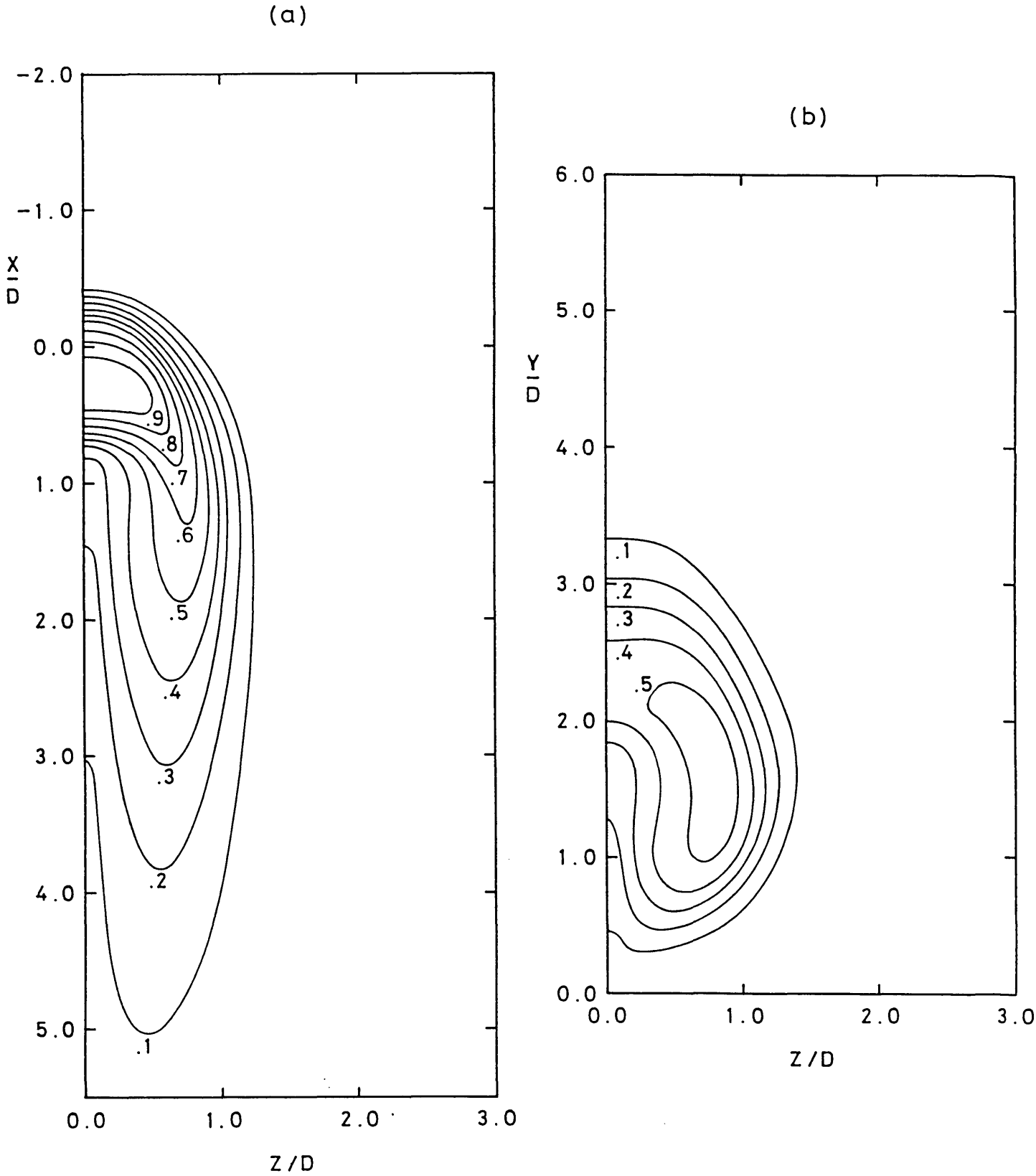


Figure 4.5 Contours of calculated mean scalar concentration for a single jet; V_J/U_∞ = 2.3 (a) Y/D = 1.0 (b) X/D = 2.0.

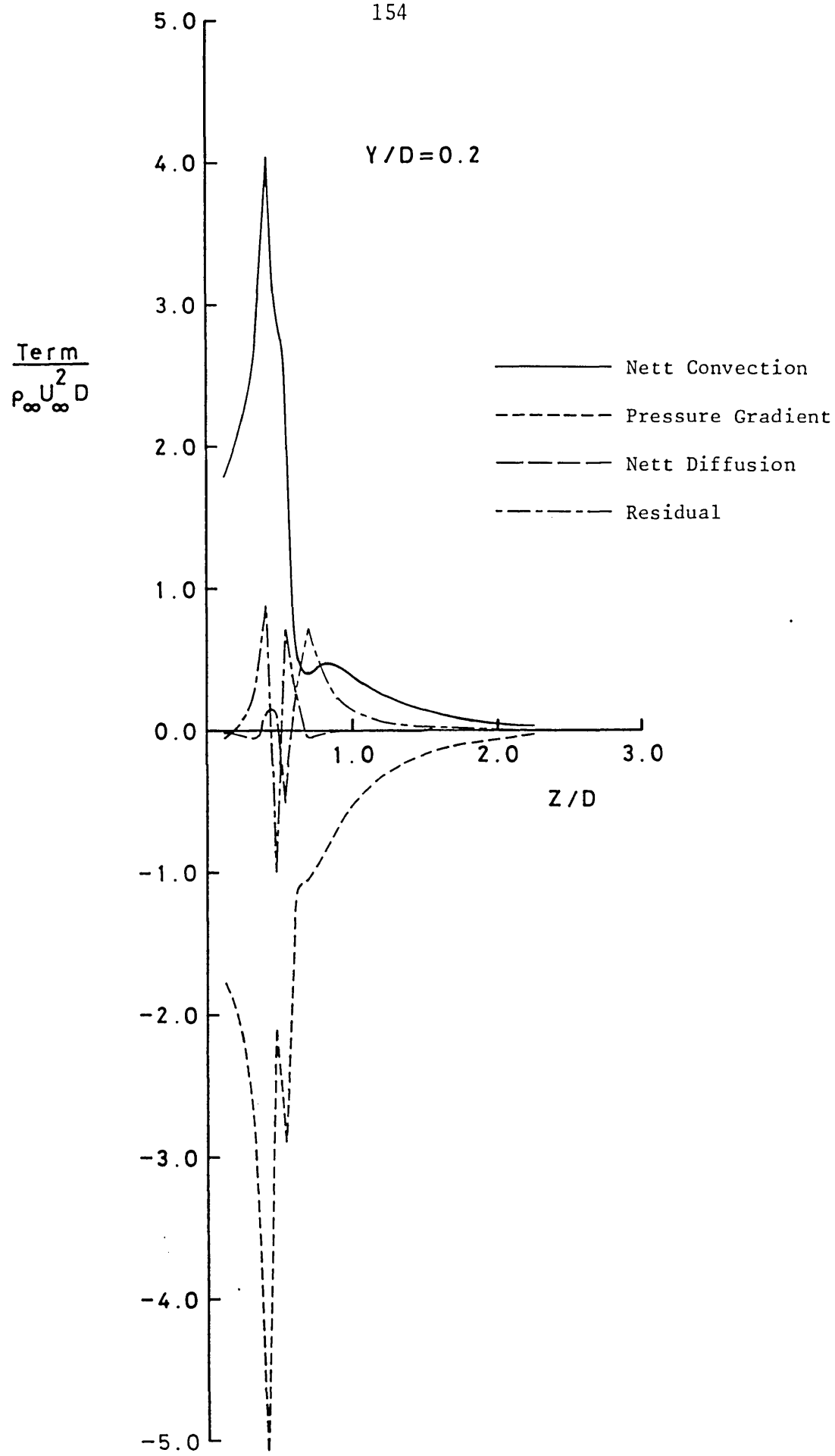


Figure 4.6 Balance of terms in the $\overline{U}$ momentum equation in the plane X/D = 0 for a single jet; V_J/U_∞ = 2.3.

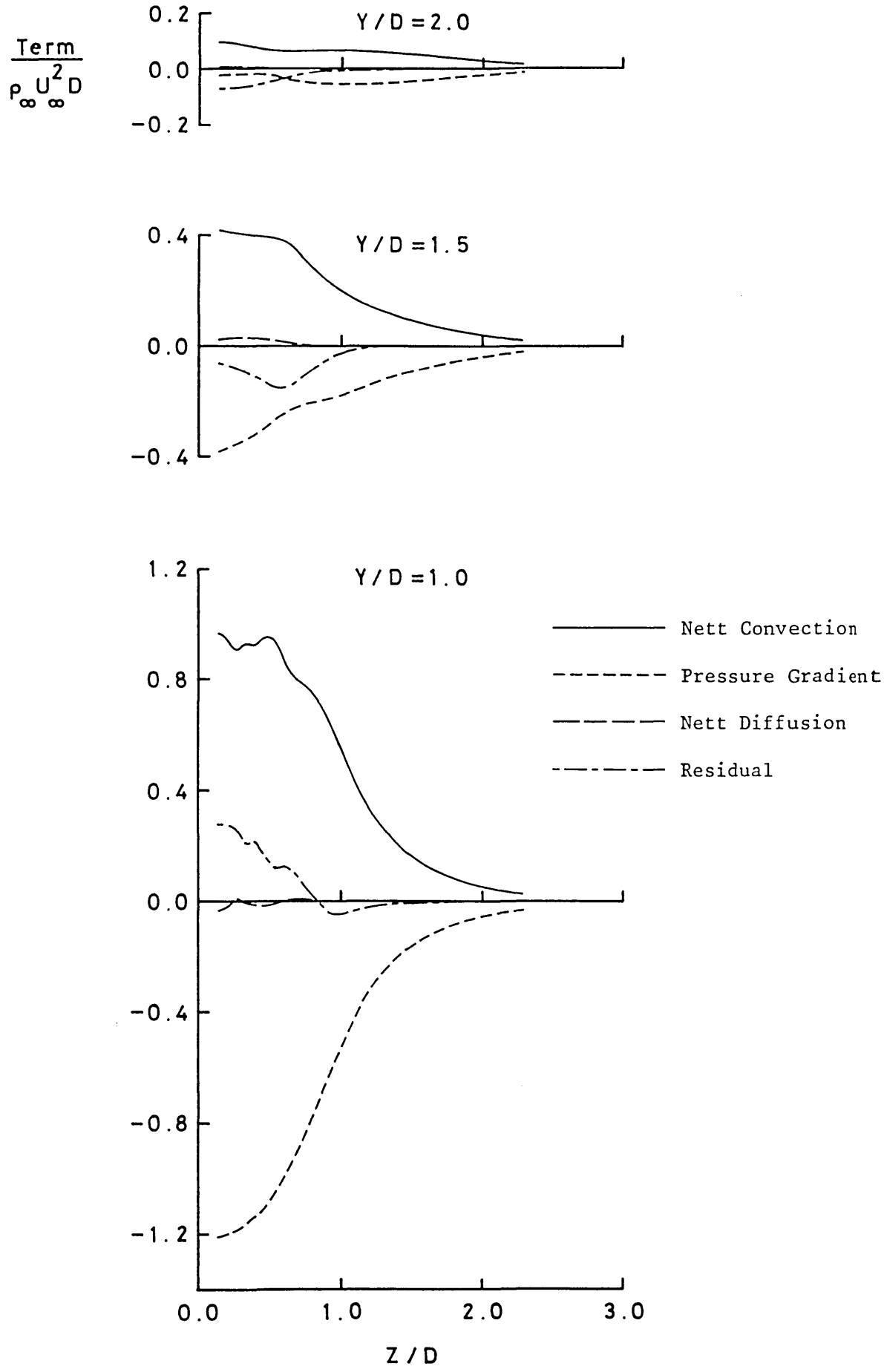


Figure 4.6 continued

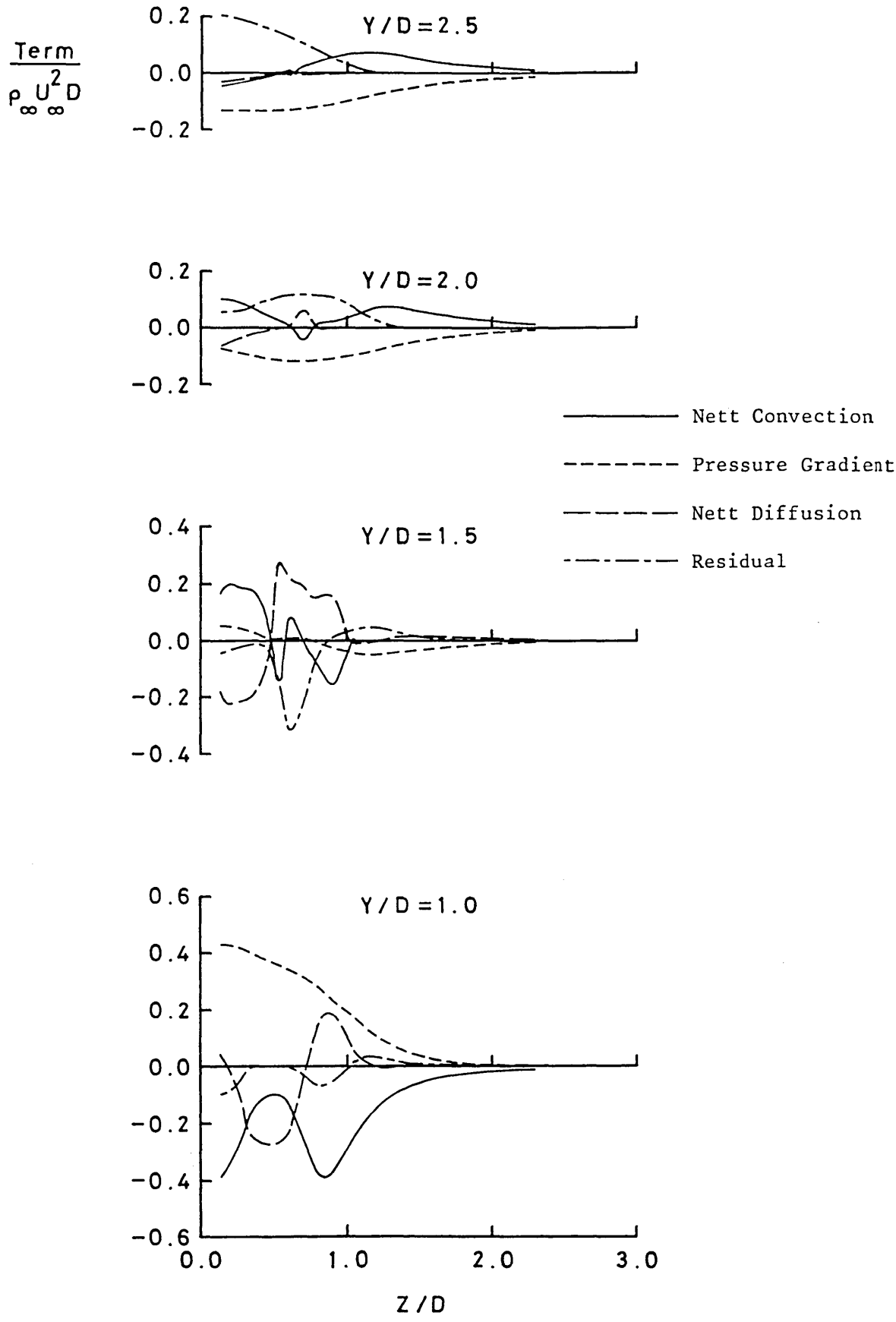


Figure 4.7 Balance of terms in the $\overline{U}$ momentum equation in the plane X/D = 2.0 for a single jet; V_J/U_∞ = 2.3.

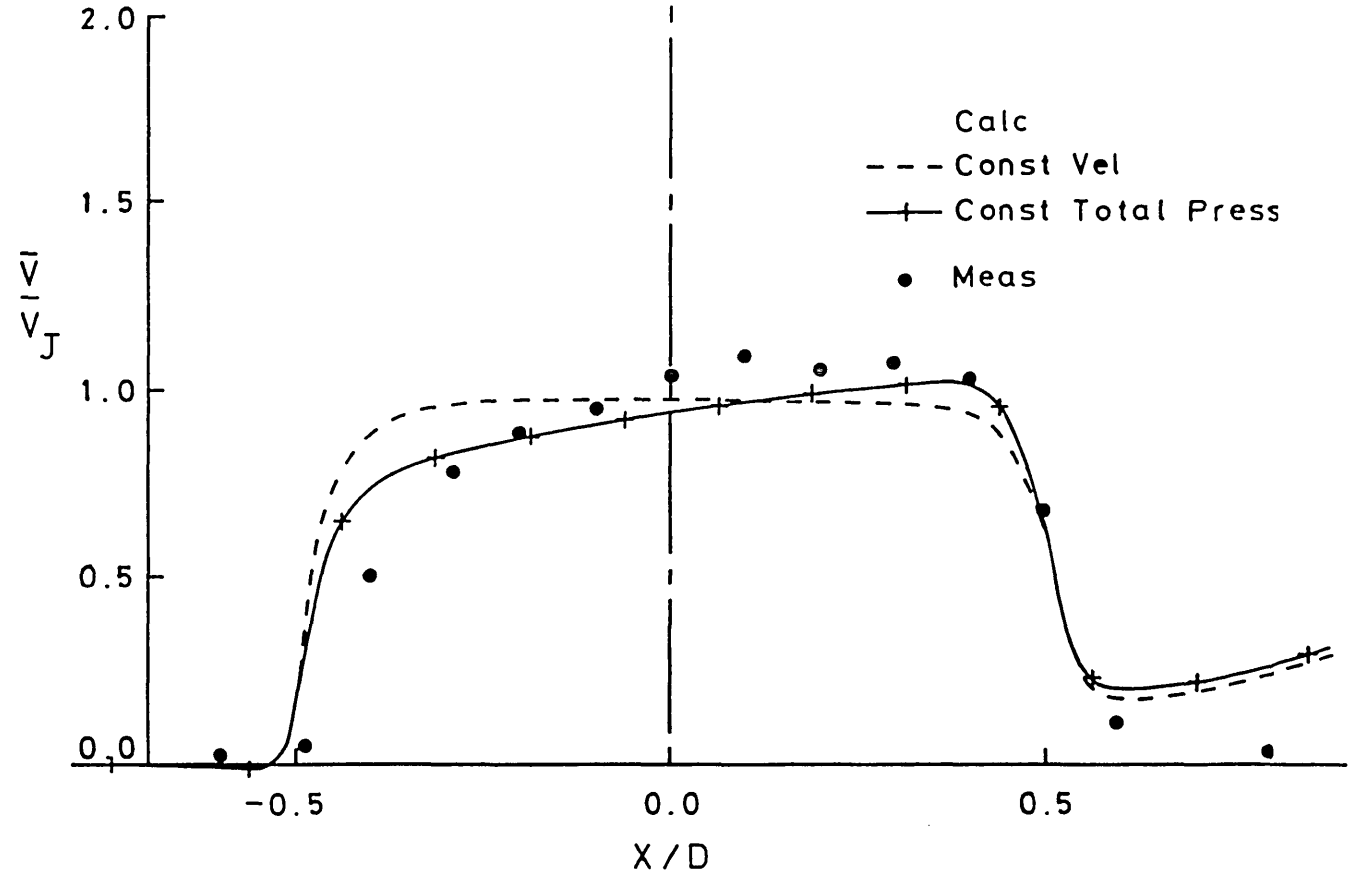


Figure 4.8 Profiles of calculated and measured $\bar{V}$ velocity at Y/D = 0.25, Z/D = 0 for a single jet; $V_J/U_\infty = 2.3$.

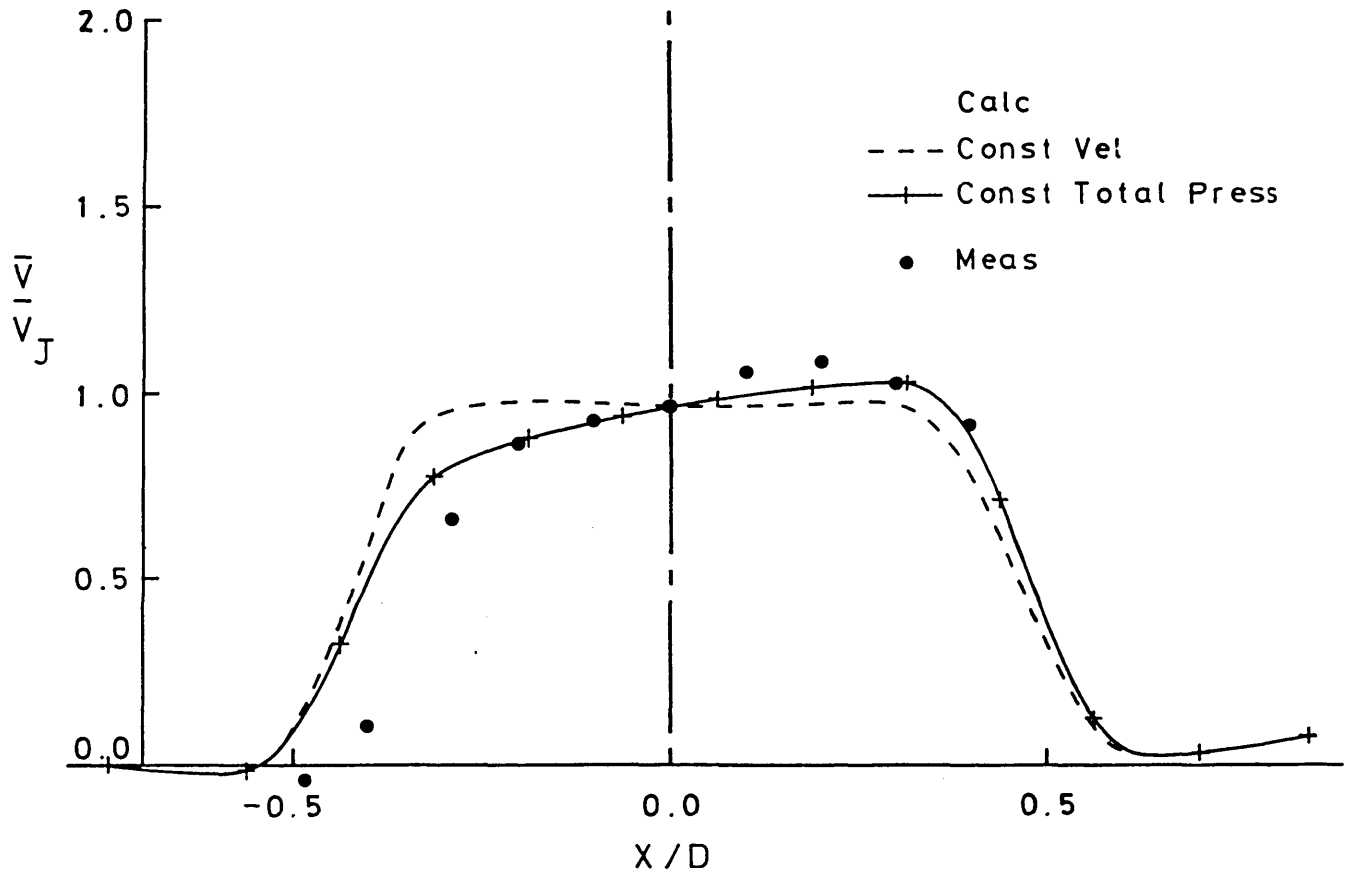


Figure 4.9 Profiles of calculated and measured $\bar{V}$ velocity at Y/D = 0.25, Z/D = 0.25 for a single jet; $V_J/U_\infty = 2.3$.

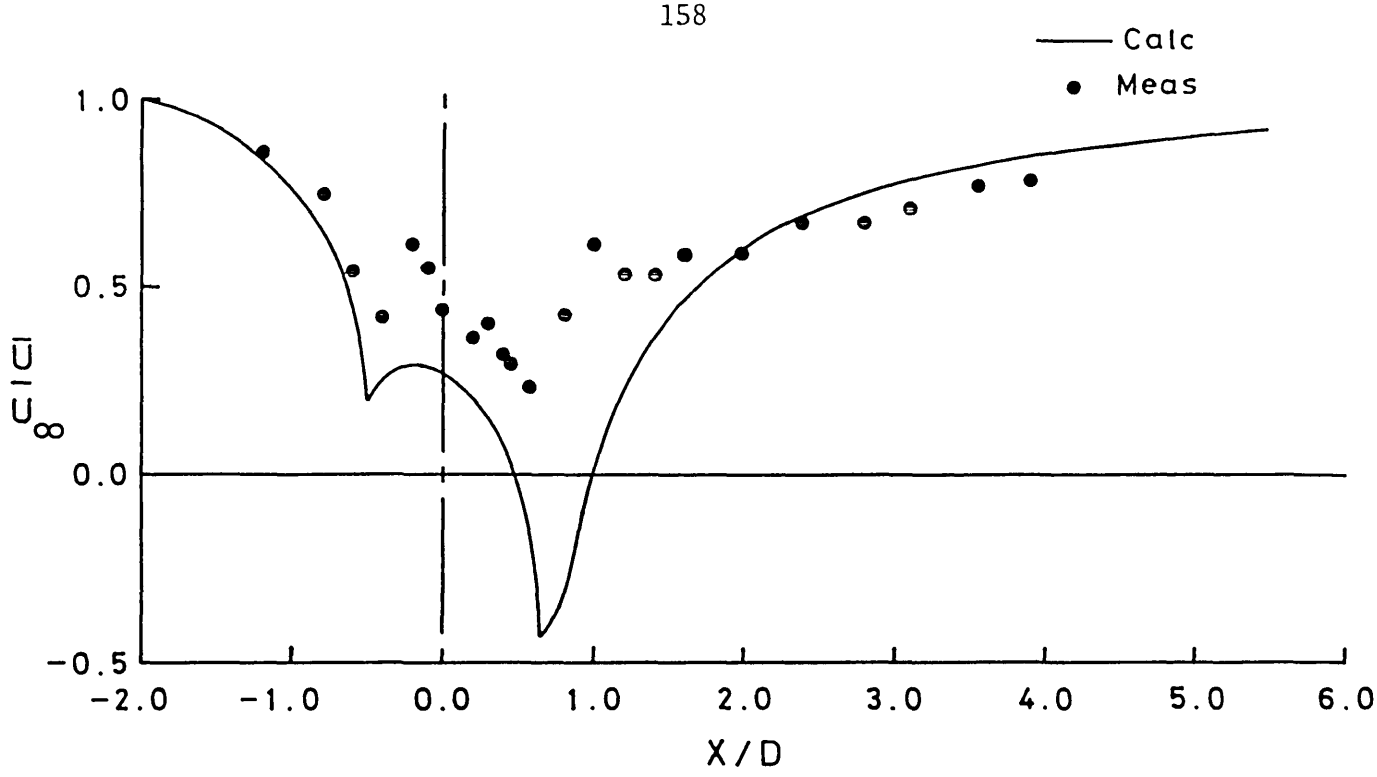


Figure 4.10 Profiles of calculated and measured $\overline{U}$ velocity at Y/D = 0.25, Z/D = 0 for a single jet; $V_J/U_\infty = 2.3$.

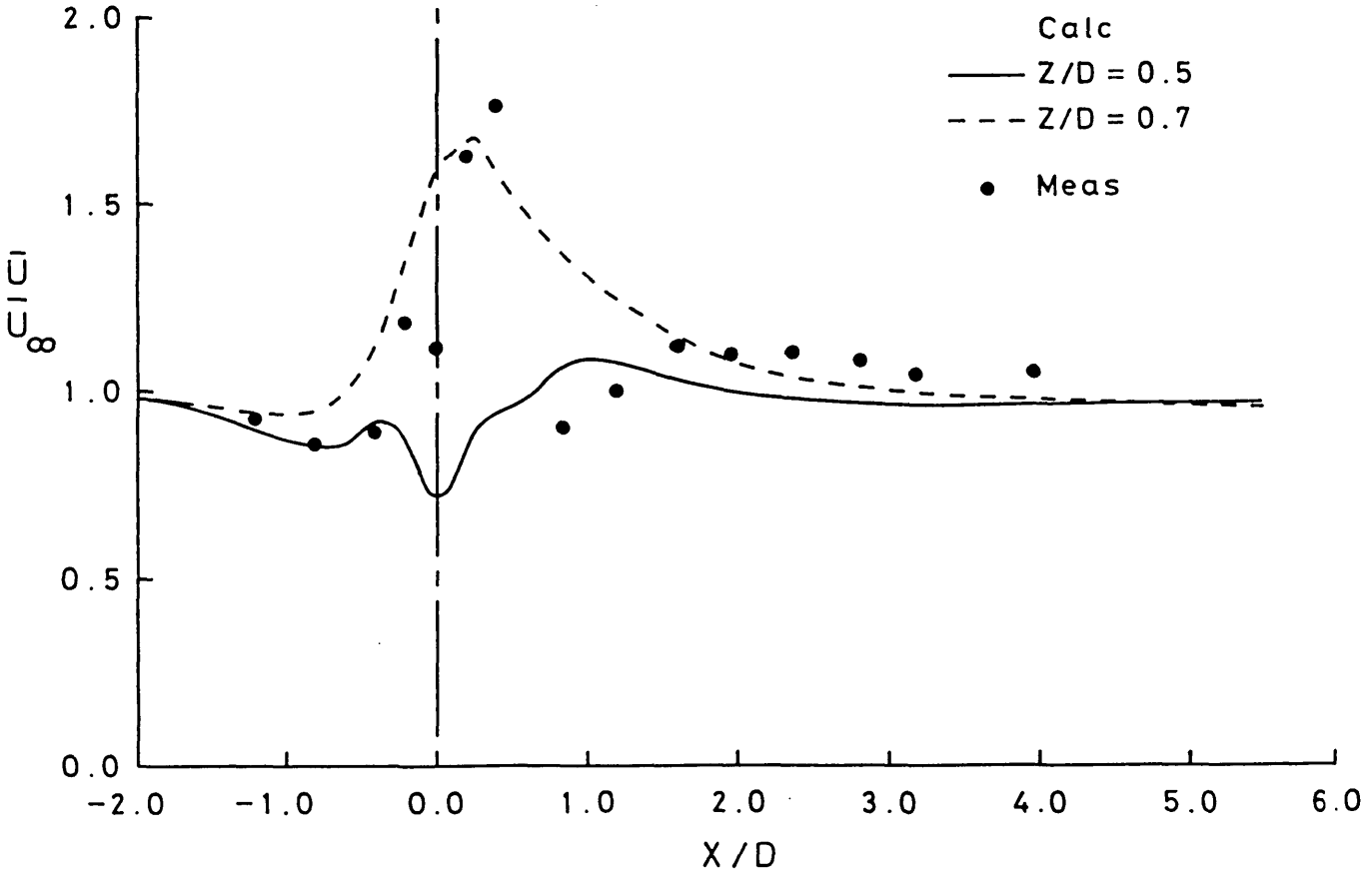


Figure 4.11 Profiles of calculated and measured $\overline{U}$ velocity at Y/D = 0.25, Z/D = 0.5 for a single jet; $V_J/U_\infty = 2.3$.

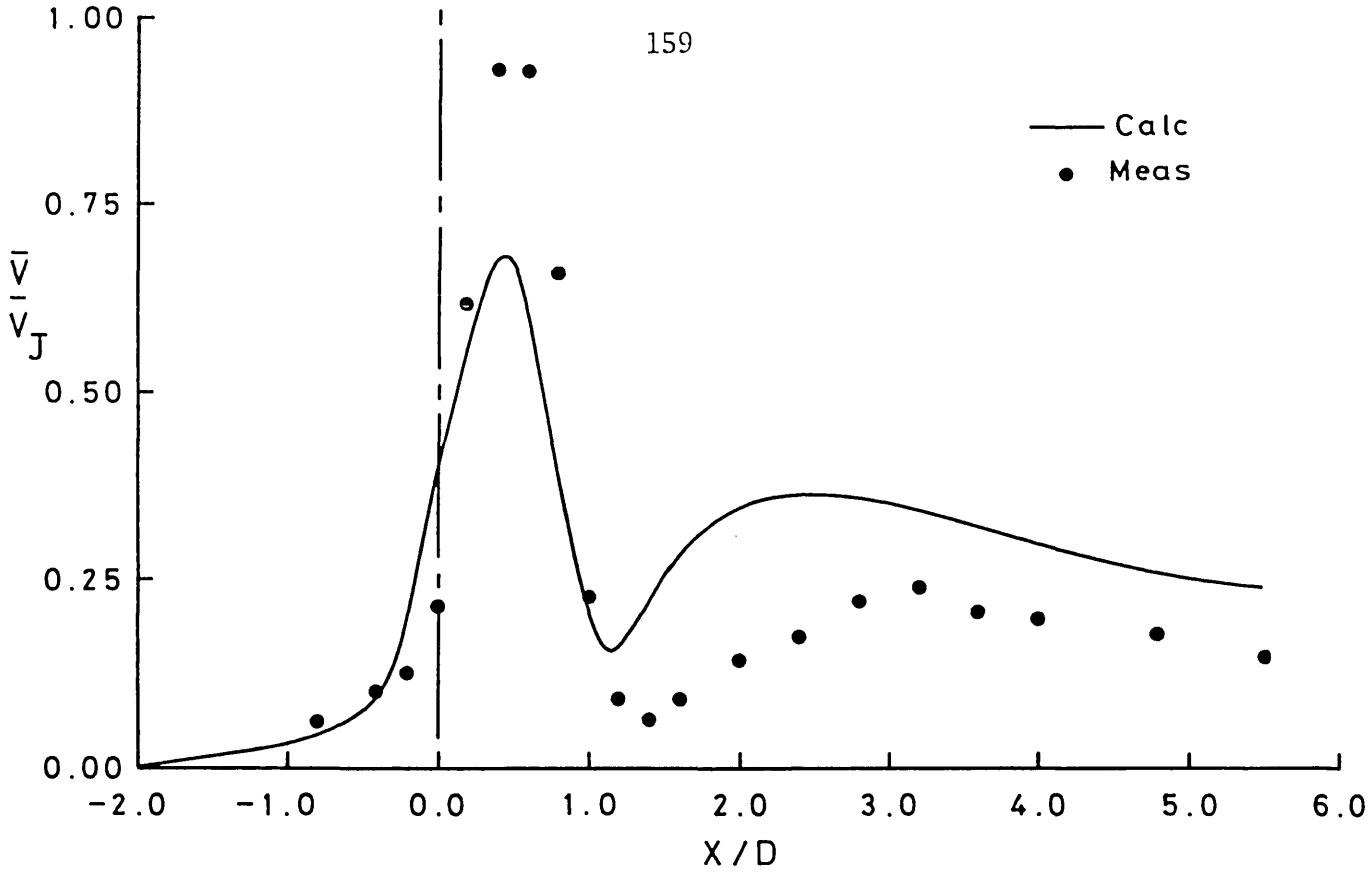


Figure 4.12 Profiles of calculated and measured $\bar{V}$ velocity at Y/D = 1.35, Z/D = 0 for a single jet; $V_J/U_\infty = 2.3$.

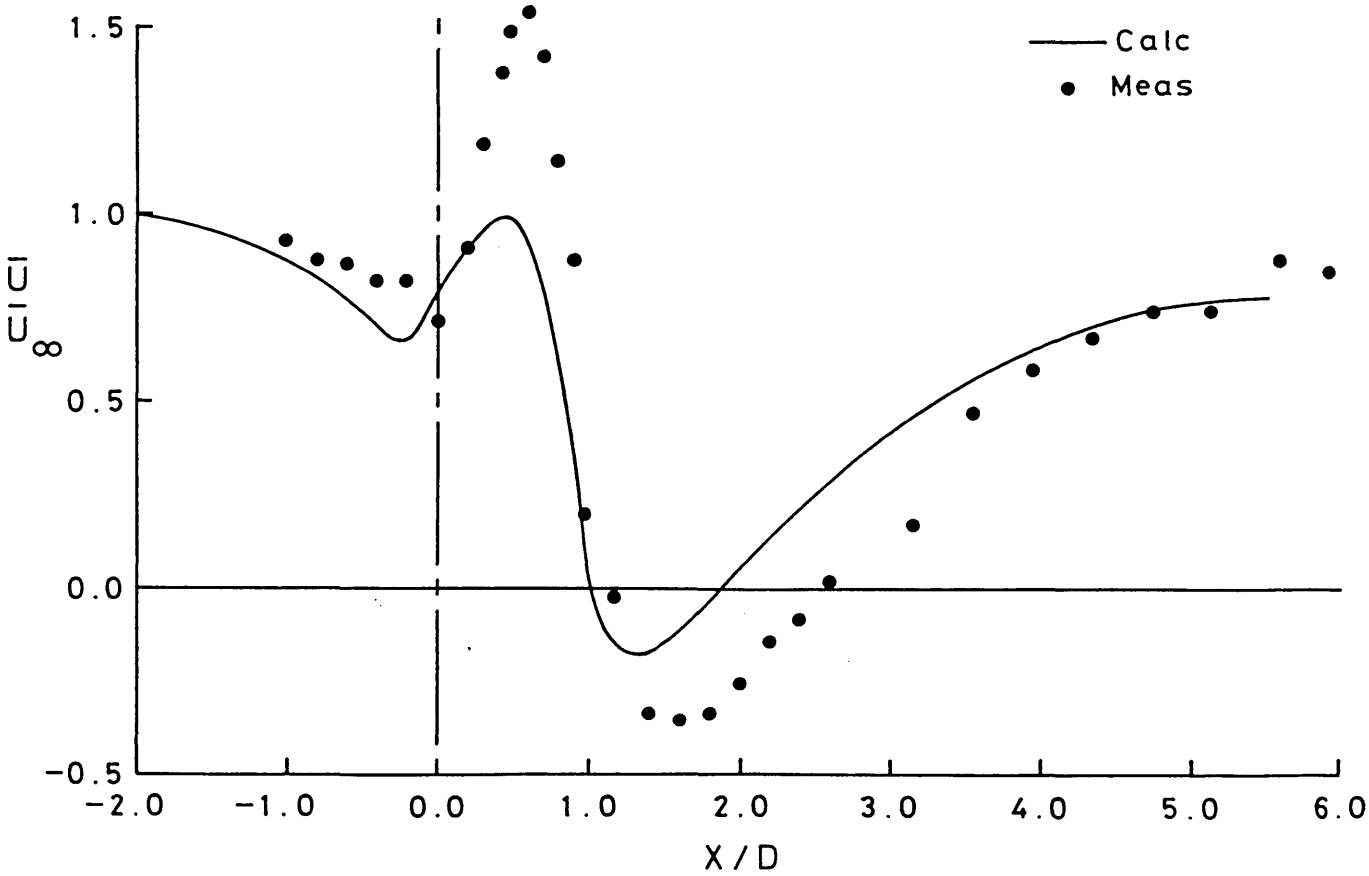


Figure 4.13 Profiles of calculated and measured $\bar{U}$ velocity at Y/D = 1.35, Z/D = 0 for a single jet; $V_J/U_\infty = 2.3$.

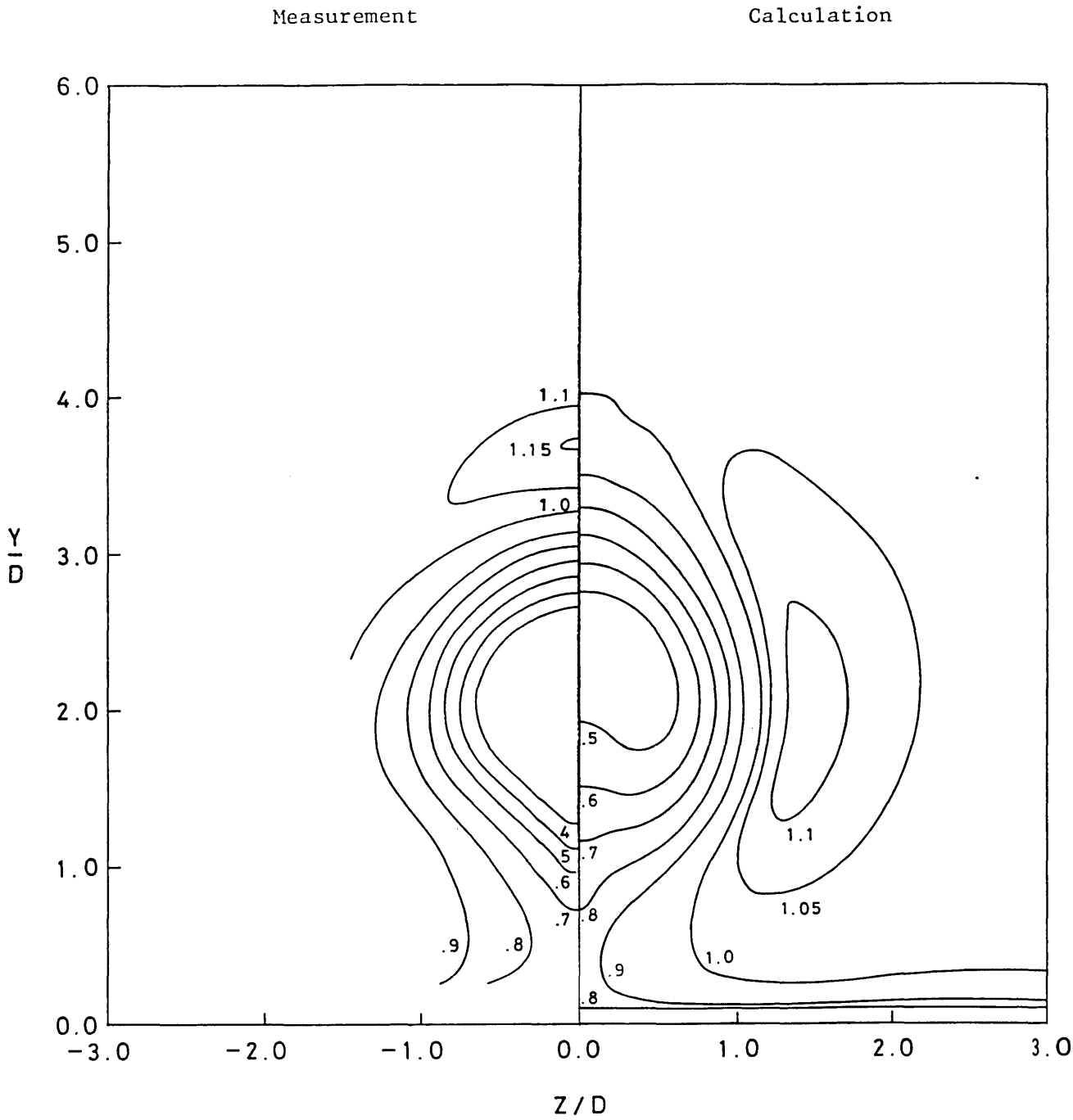


Figure 4.14 Contours of calculated and measured $\overline{U}$ velocity in the plane X/D = 4.0 for a single jet; V_J/U_∞ = 2.3.

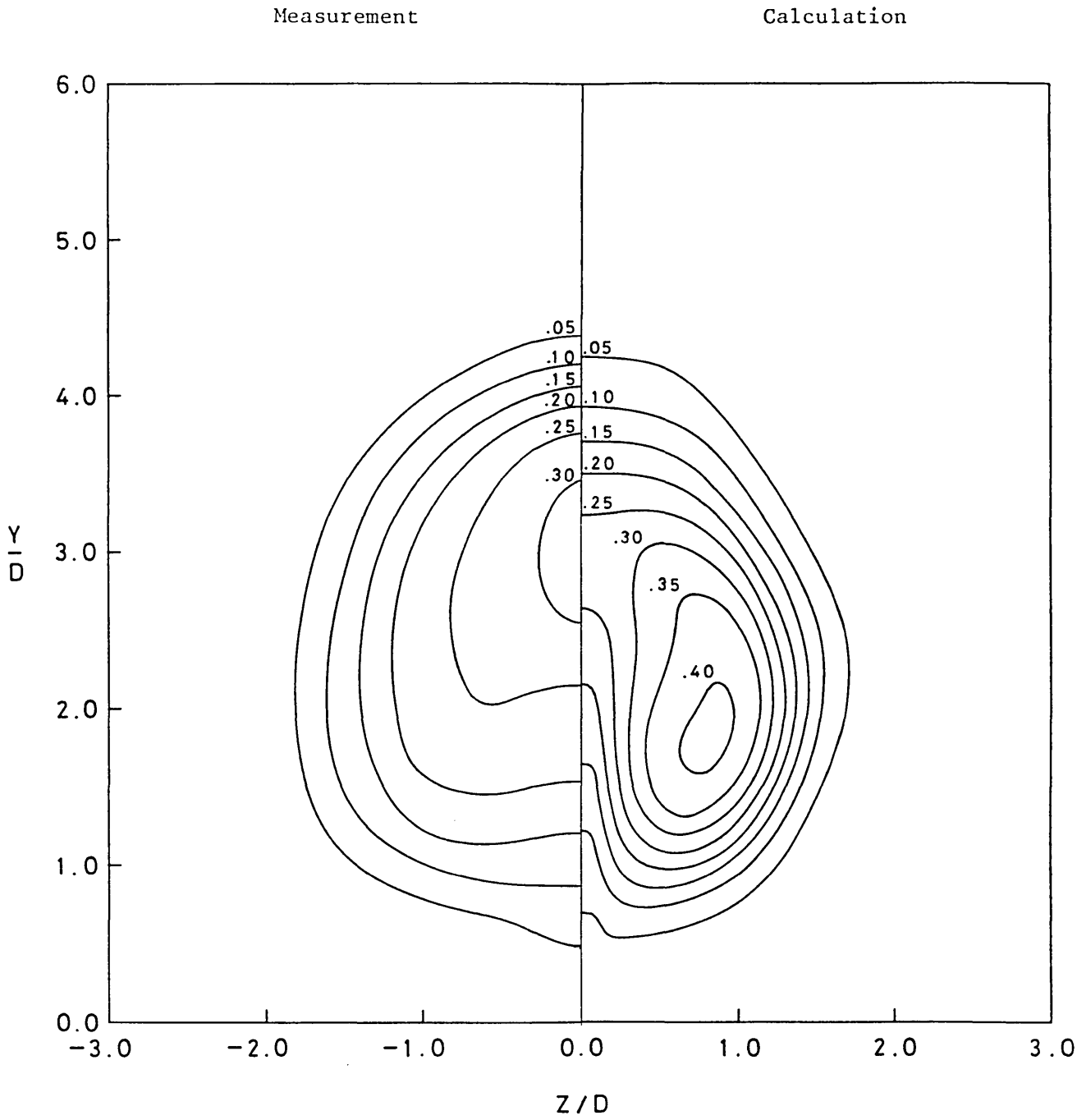


Figure 4.15 Contours of calculated and measured mean scalar concentration in the plane X/D = 4.0 for a single jet; V_J/U_∞ = 2.3.

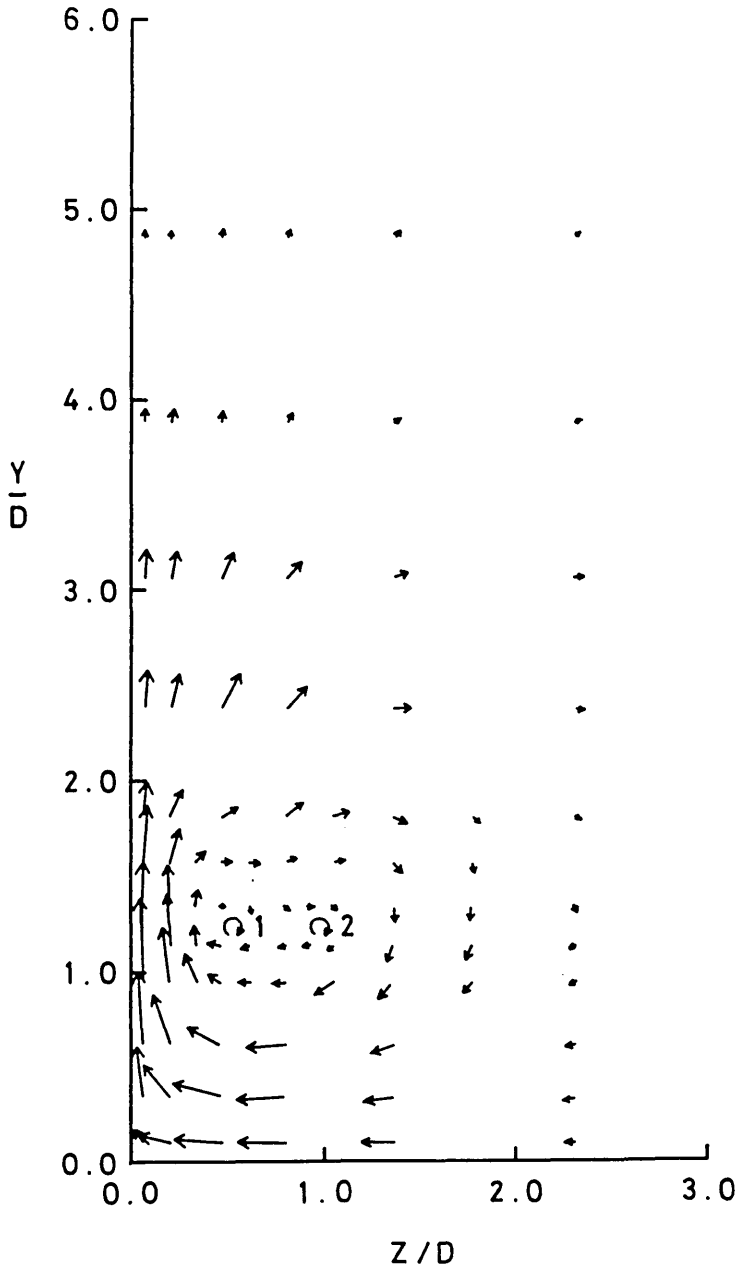


Figure 4.16 Calculated velocity vectors in the plane X/D = 2.0 for a single jet; $V_J/U_\infty = 2.3$.

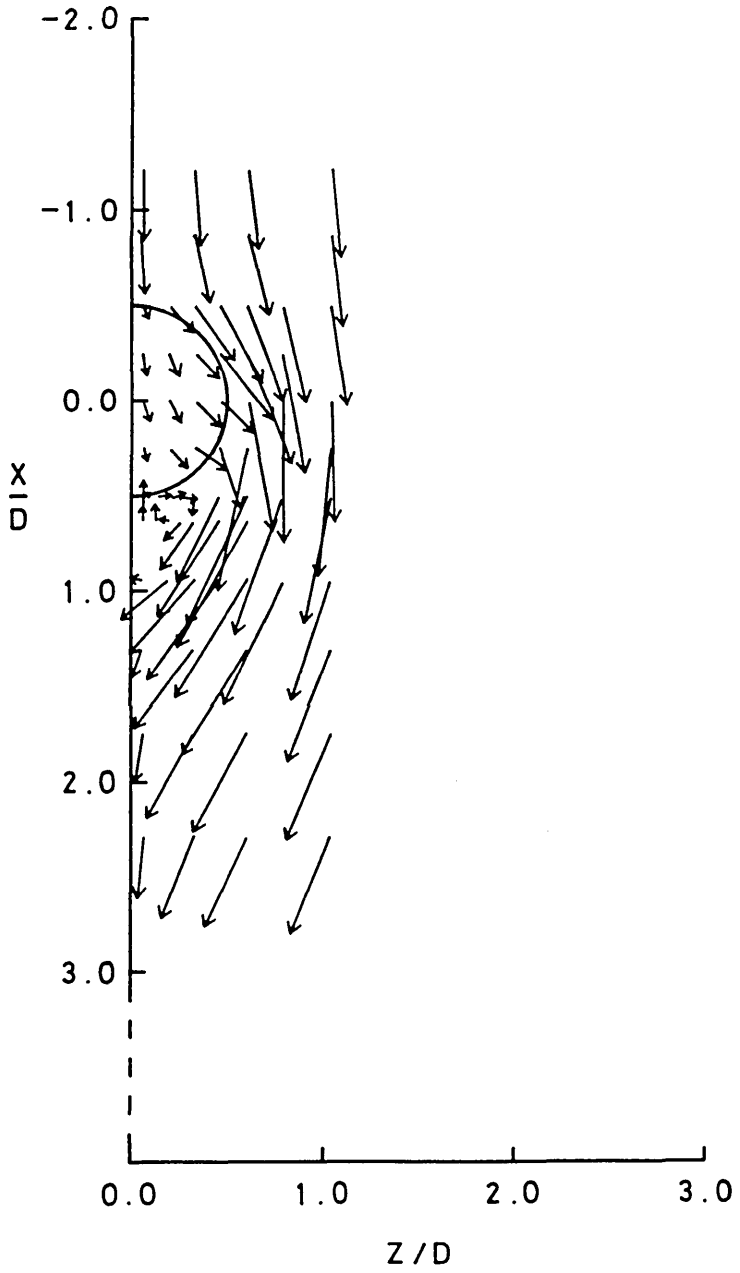


Figure 4.17 Calculated velocity vectors in the plane Y/D = 0.25 for a single jet; $V_J/U_\infty = 2.3$.

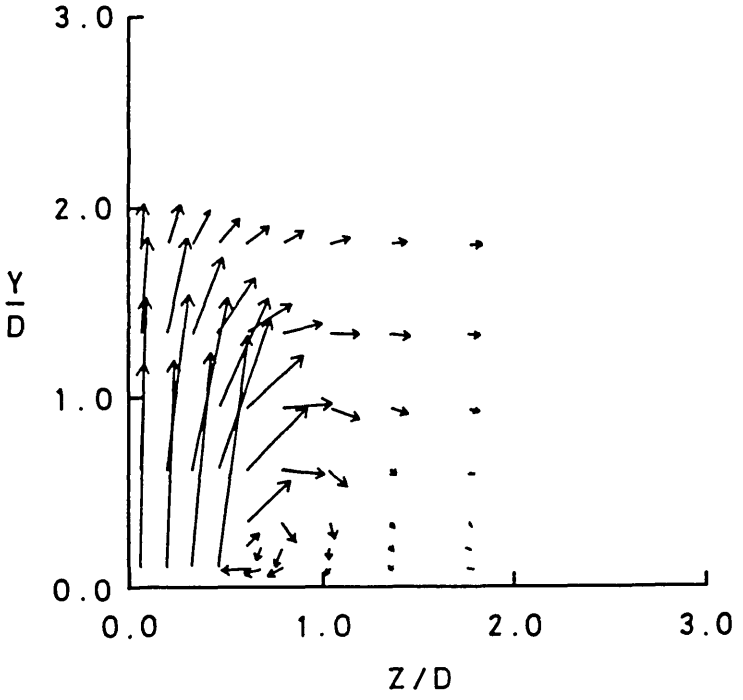


Figure 4.18 Calculated velocity vectors in the plane X/D = 0.25 for a single jet; $V_J/U_\infty = 2.3$.

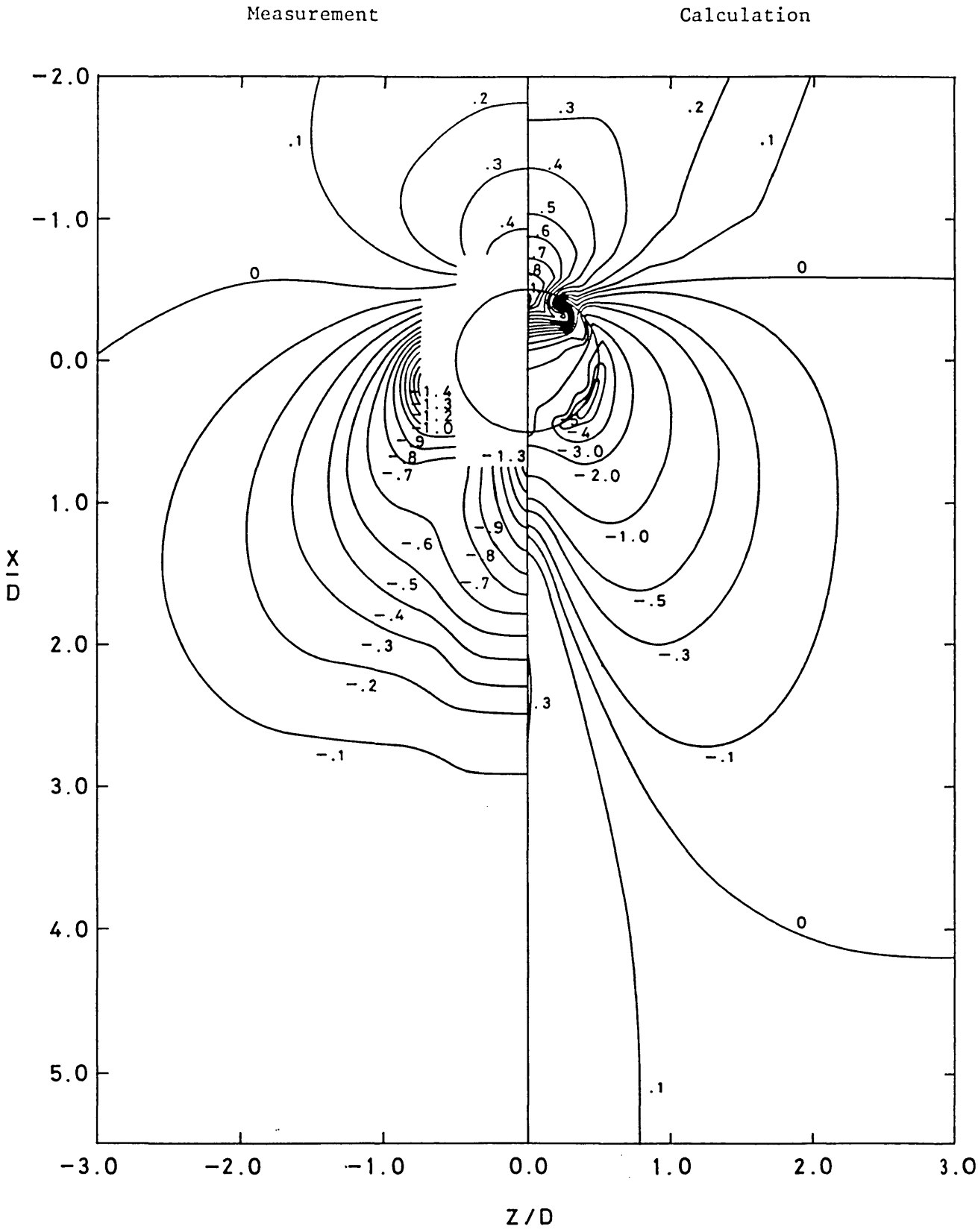


Figure 4.19 Contours of calculated and measured wall static pressure coefficient for a single jet; $V_J/U_\infty = 2.3$.

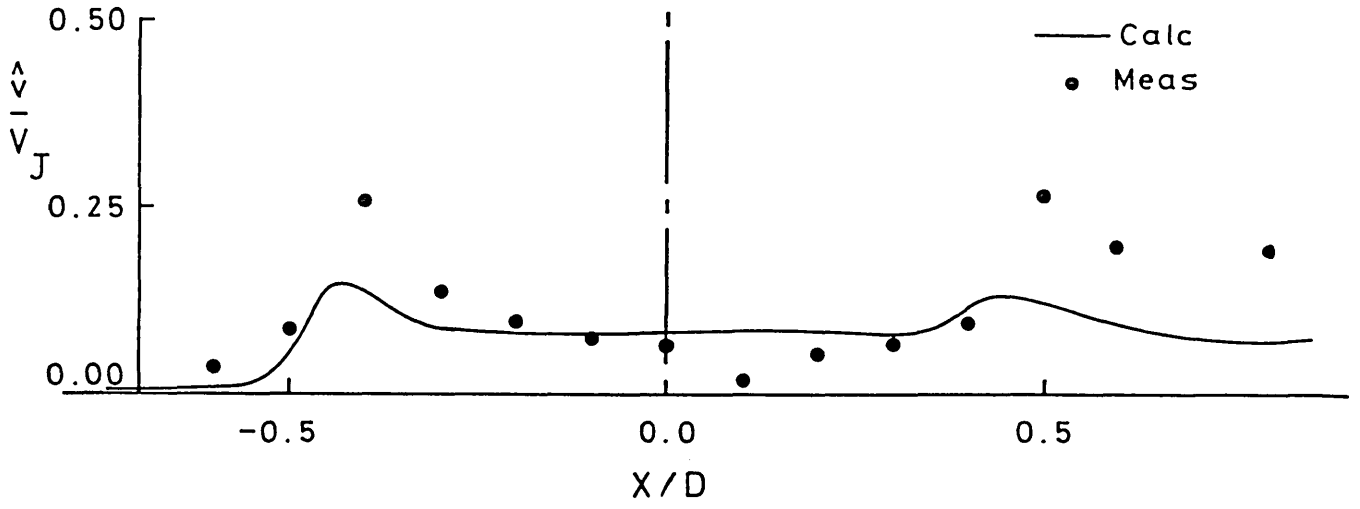


Figure 4.20 Profiles of calculated and measured $\hat{v}$ normal stress at Y/D = 0.25, Z/D = 0 for a single jet; $V_J/U_\infty = 2.3$.

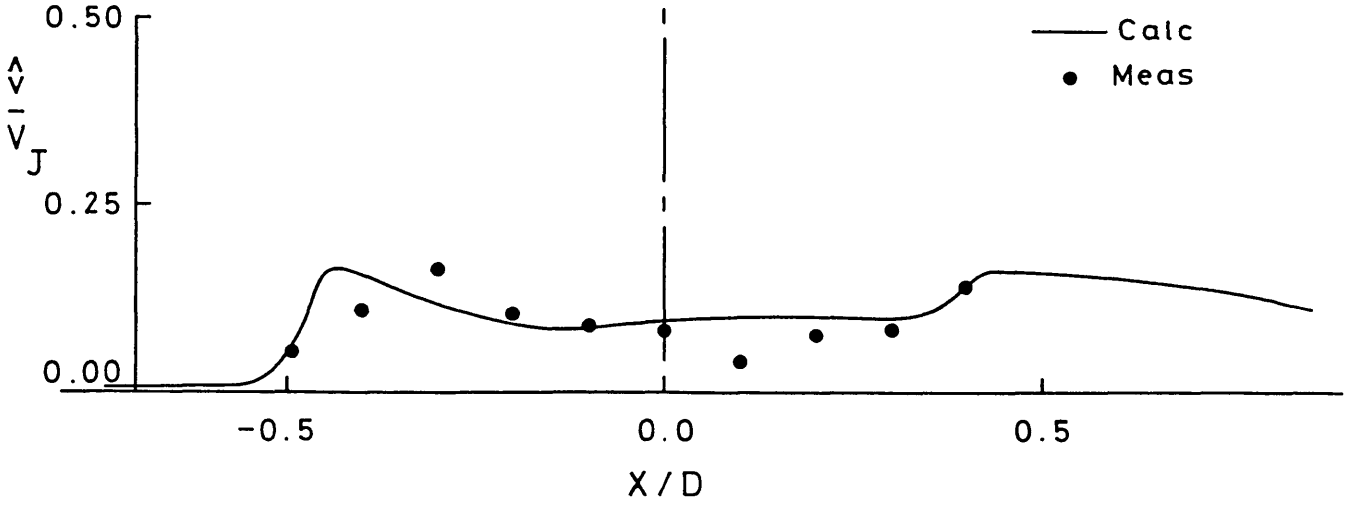


Figure 4.21 Profiles of calculated and measured $\hat{v}$ normal stress at Y/D = 0.25, Z/D = 0.25 for a single jet; $V_J/U_\infty = 2.3$.

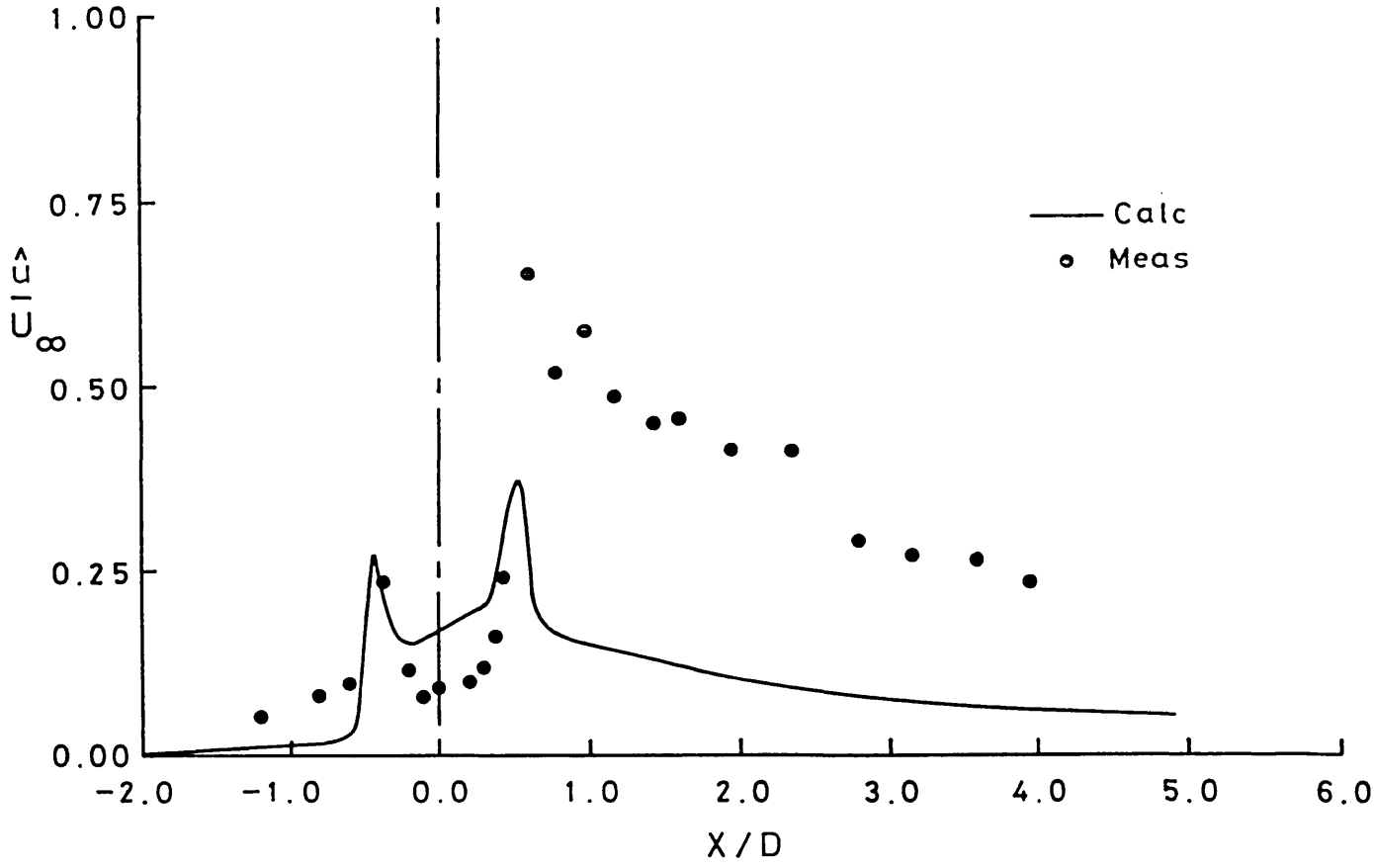


Figure 4.22 Profiles of calculated and measured $\hat{u}$ normal stress at Y/D = 0.25, Z/D = 0 for a single jet; V_J/U_∞ = 2.3.

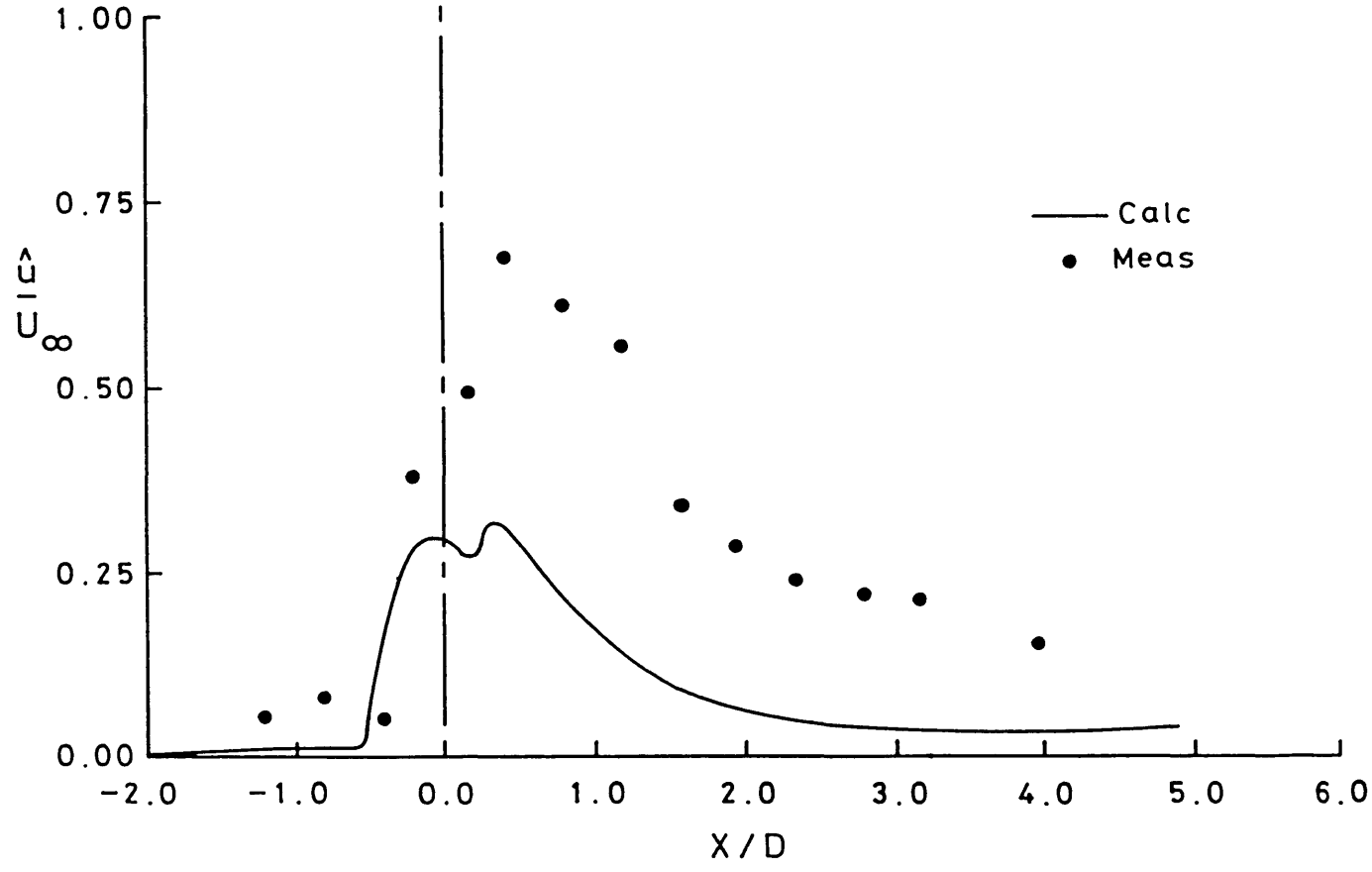


Figure 4.23 Profiles of calculated and measured $\hat{u}$ normal stress at Y/D = 0.25, Z/D = 0.5 for a single jet; V_J/U_∞ = 2.3.

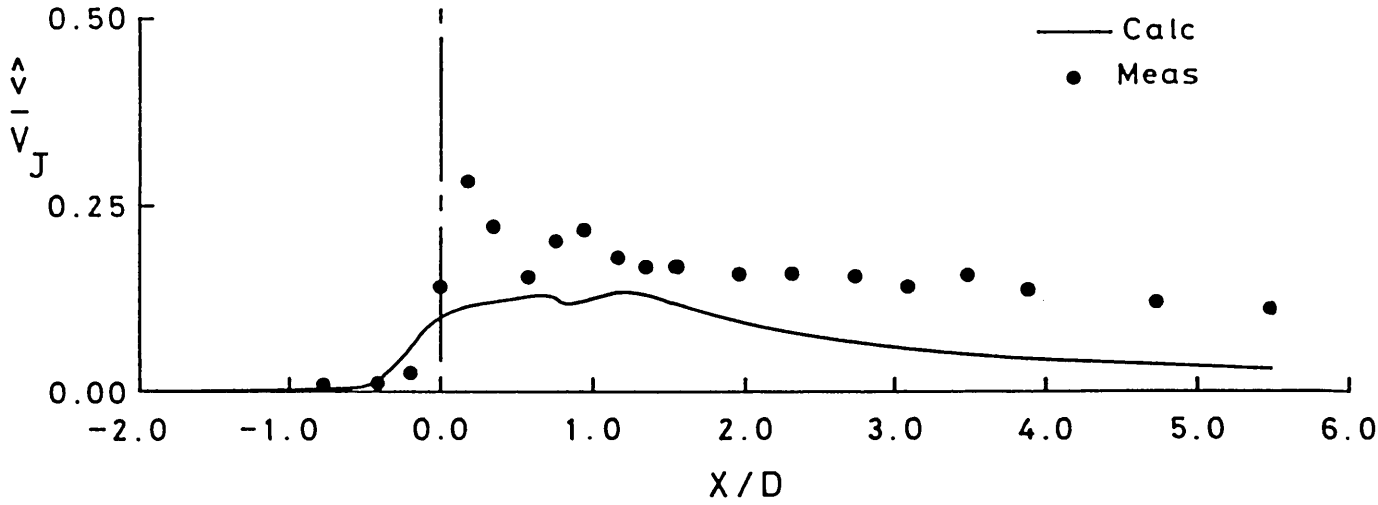


Figure 4.24 Profiles of calculated and measured $\hat{v}$ normal stress at Y/D = 1.35, Z/D = 0 for a single jet; $V_J/U_\infty = 2.3$.

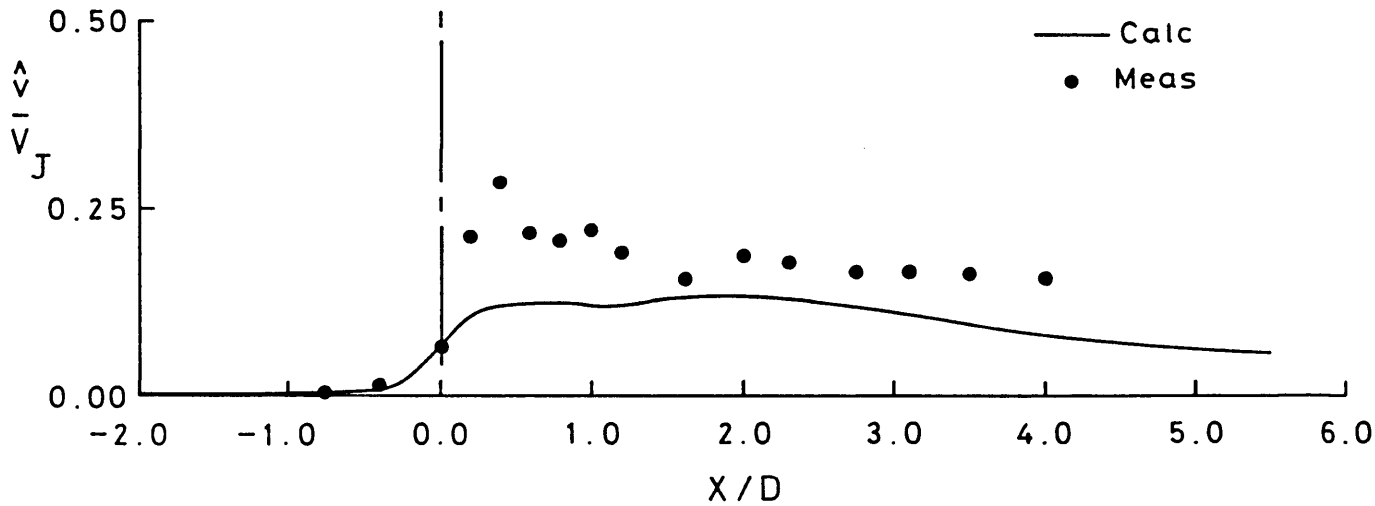


Figure 4.25 Profiles of calculated and measured $\hat{v}$ normal stress at Y/D = 1.35, Z/D = 0.5 for a single jet; $V_J/U_\infty = 2.3$.

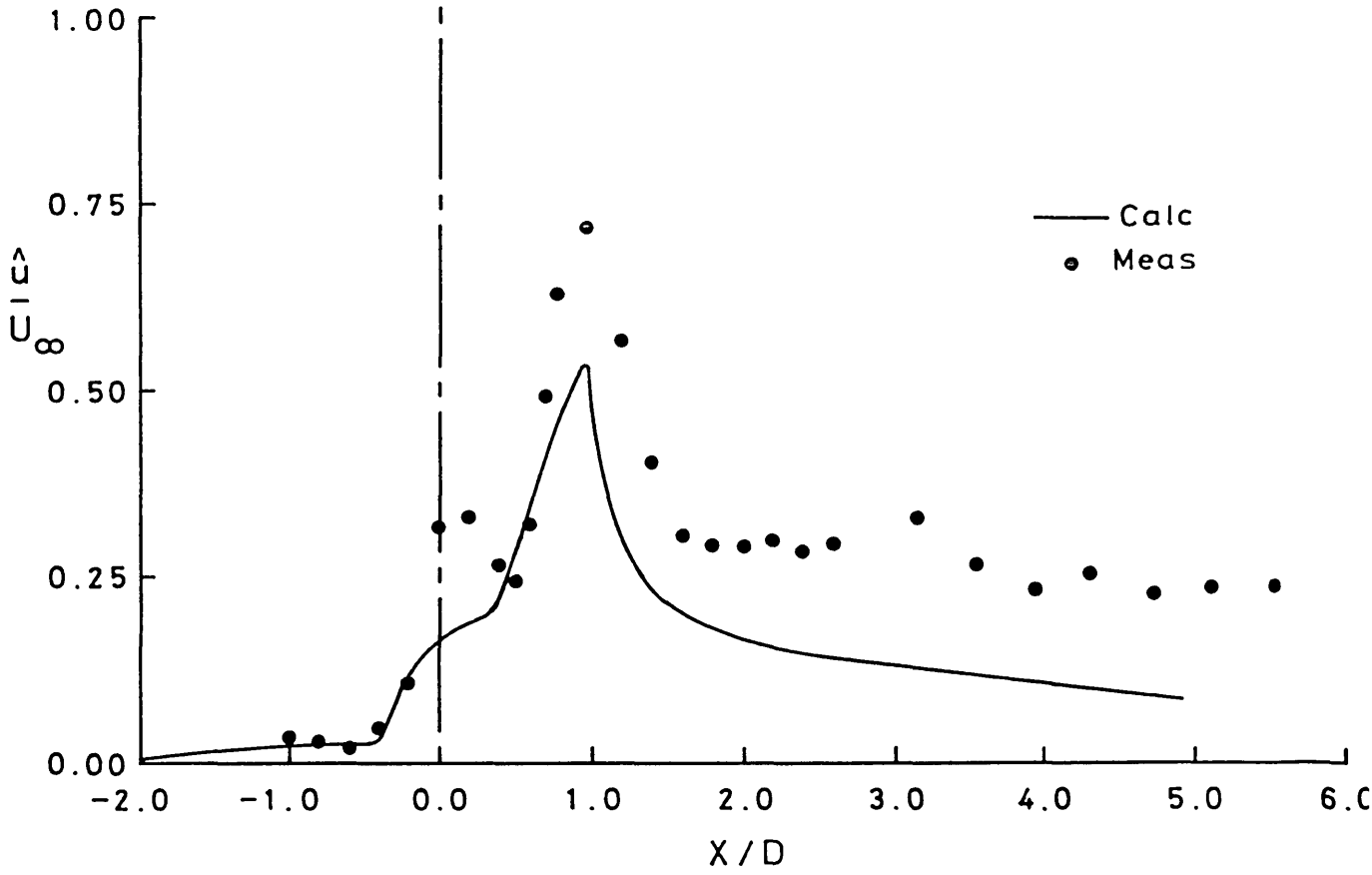


Figure 4.26 Profiles of calculated and measured $\hat{u}$ normal stress at Y/D = 1.35, Z/D = 0 for a single jet; V_J/U_∞ = 2.3.

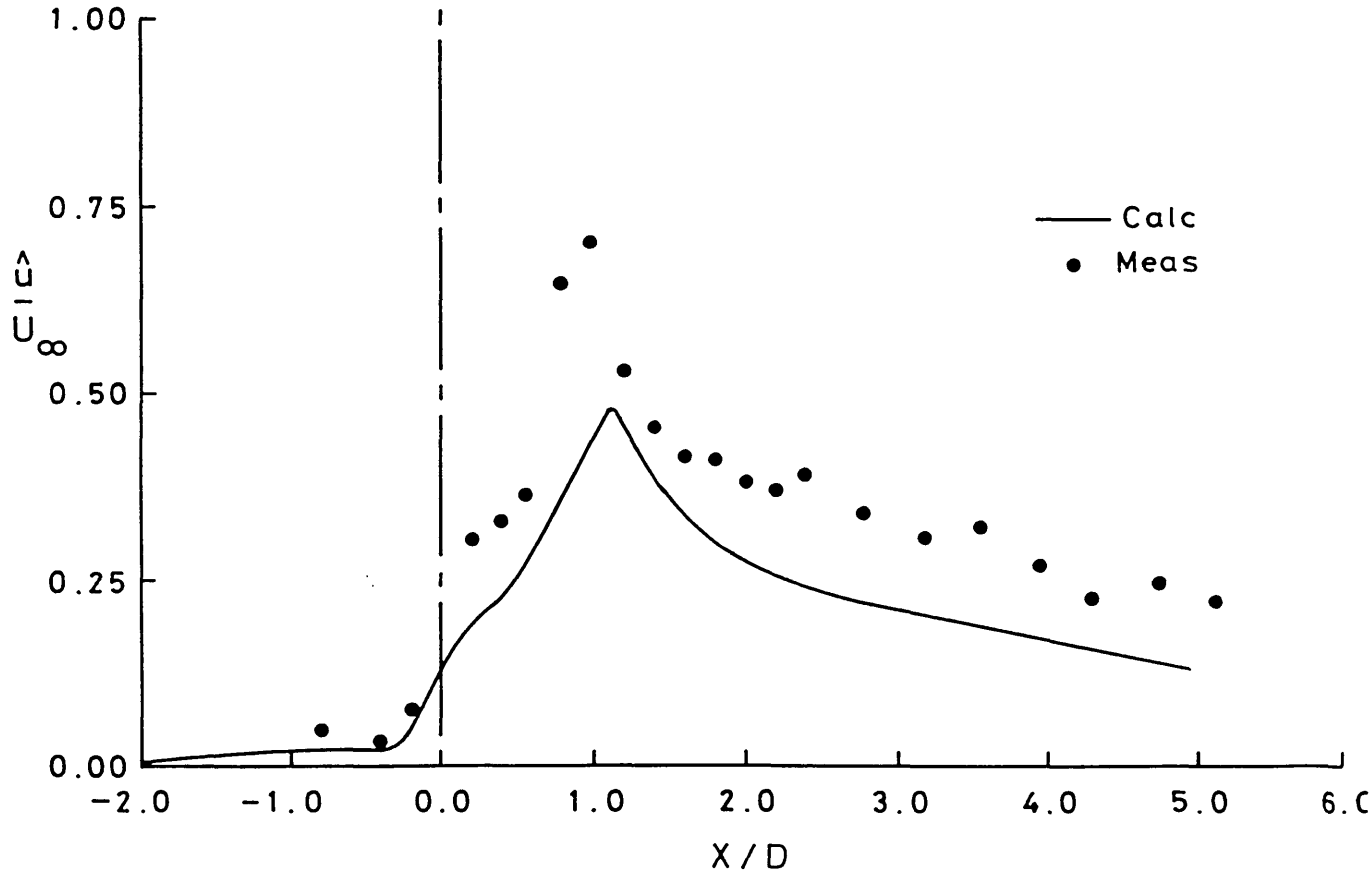


Figure 4.27 Profiles of calculated and measured $\hat{u}$ normal stress at Y/D = 1.35, Z/D = 0.5 for a single jet; V_J/U_∞ = 2.3.

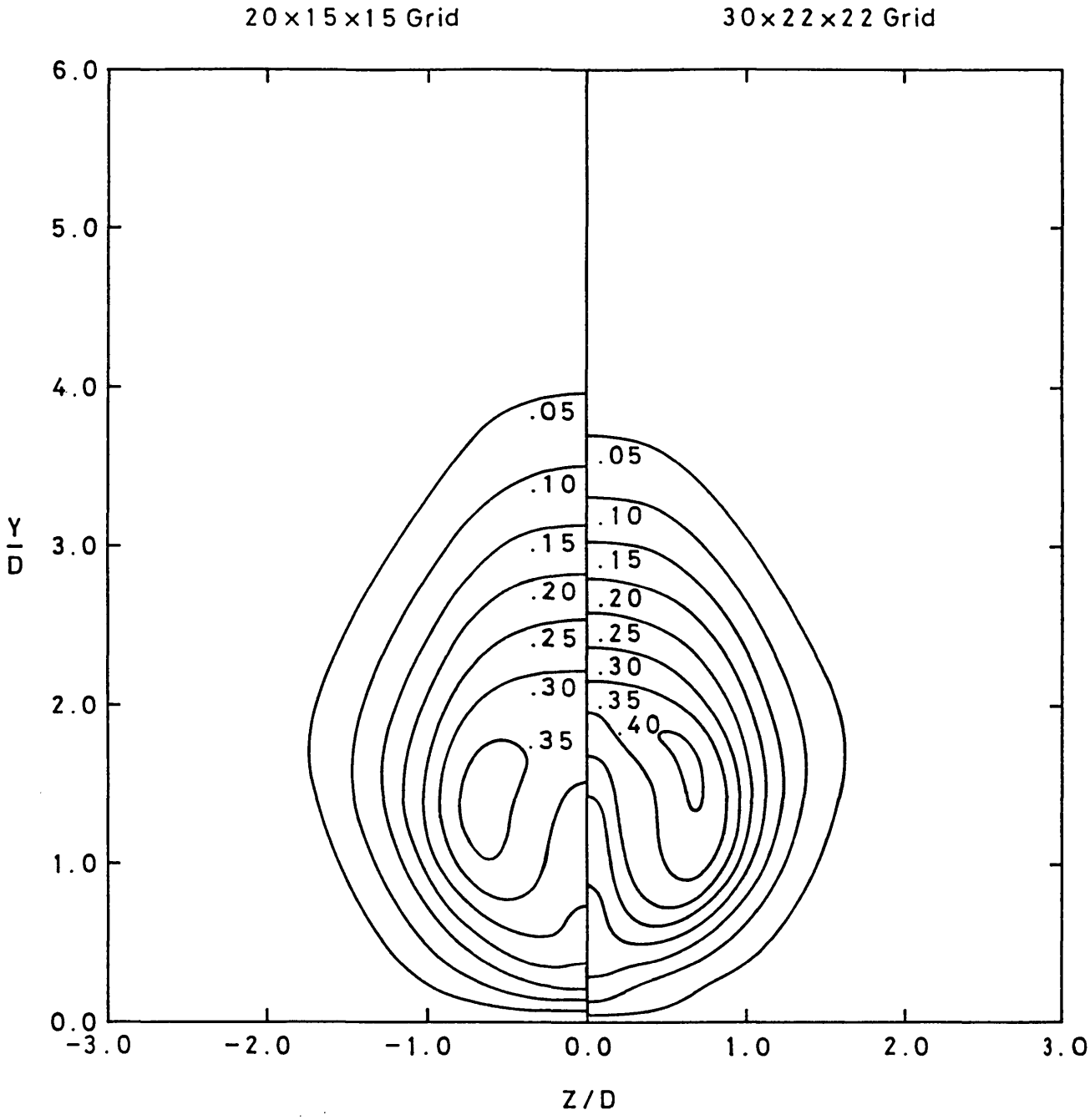


Figure 4.28 Coarse and fine grid solutions of turbulence energy in the plane X/D = 2.0 for a single jet; V_J/U_∞ = 2.3.

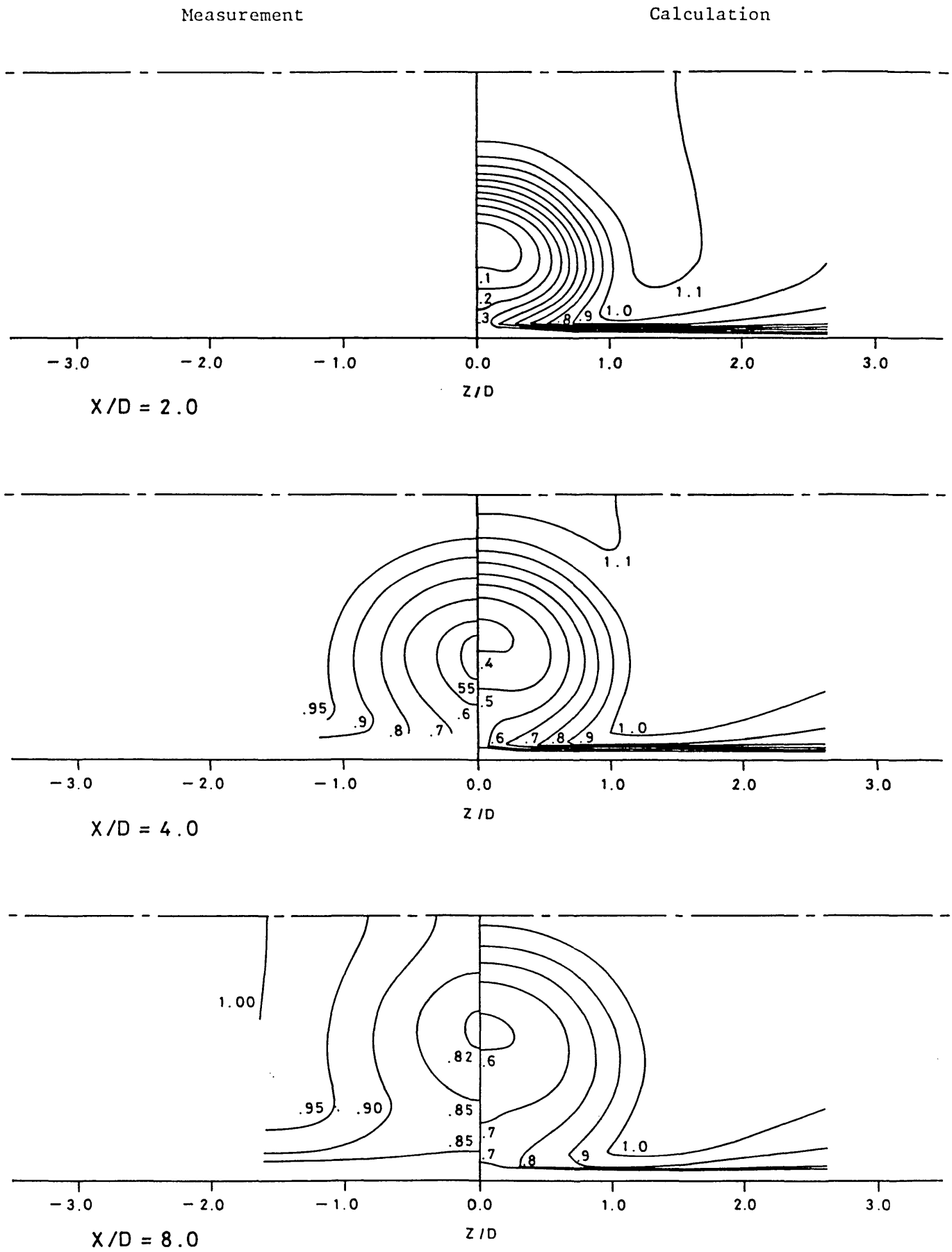


Figure 5.1 Contours of calculated and measured $\overline{U}$ velocity for two opposed single jets; H/D = 4.0; V_J/U_∞ = 1.0.

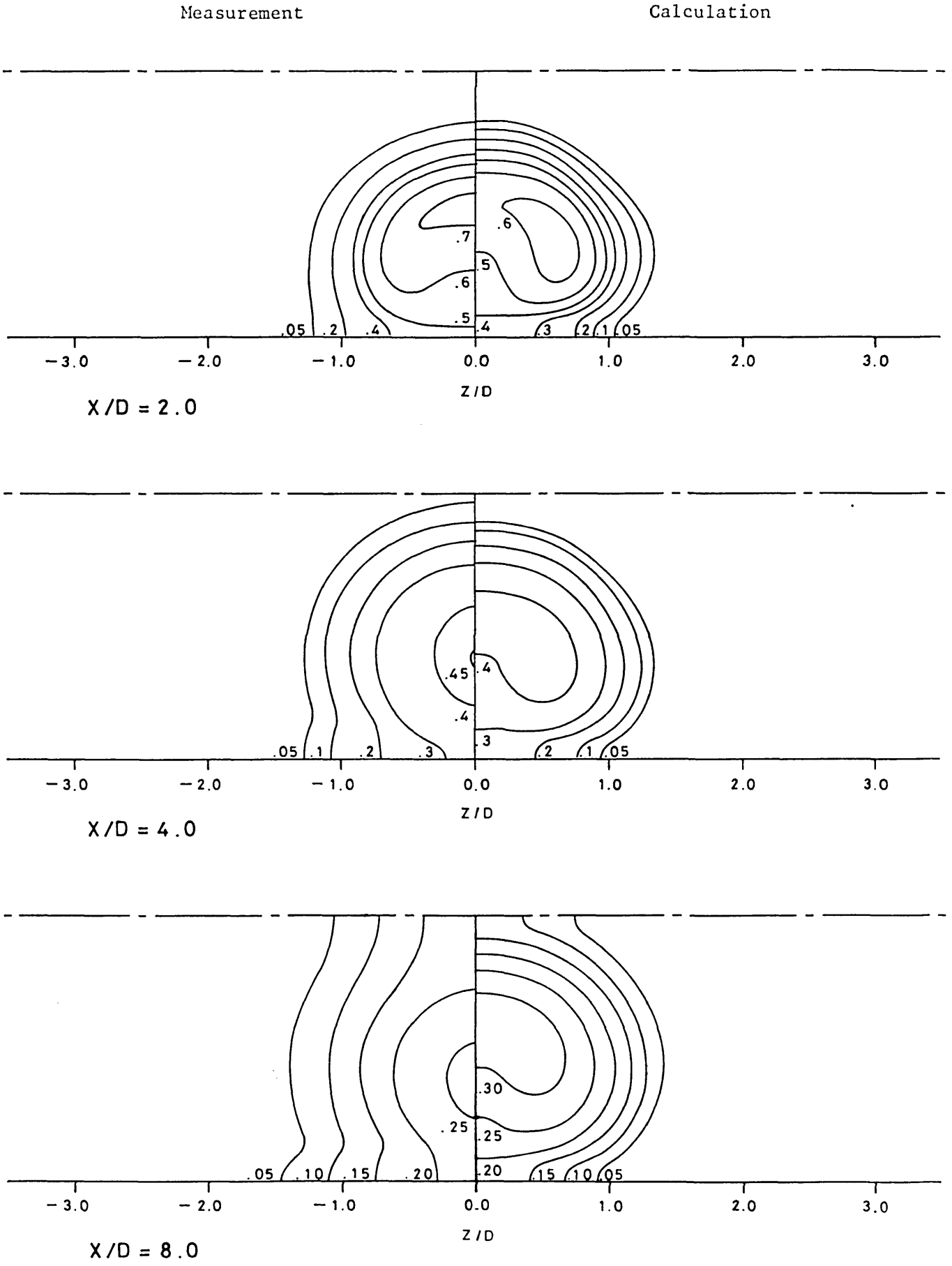


Figure 5.2 Contours of calculated and measured mean scalar concentration for two opposed single jets; H/D = 4.0; V_J/U_∞ = 1.0.

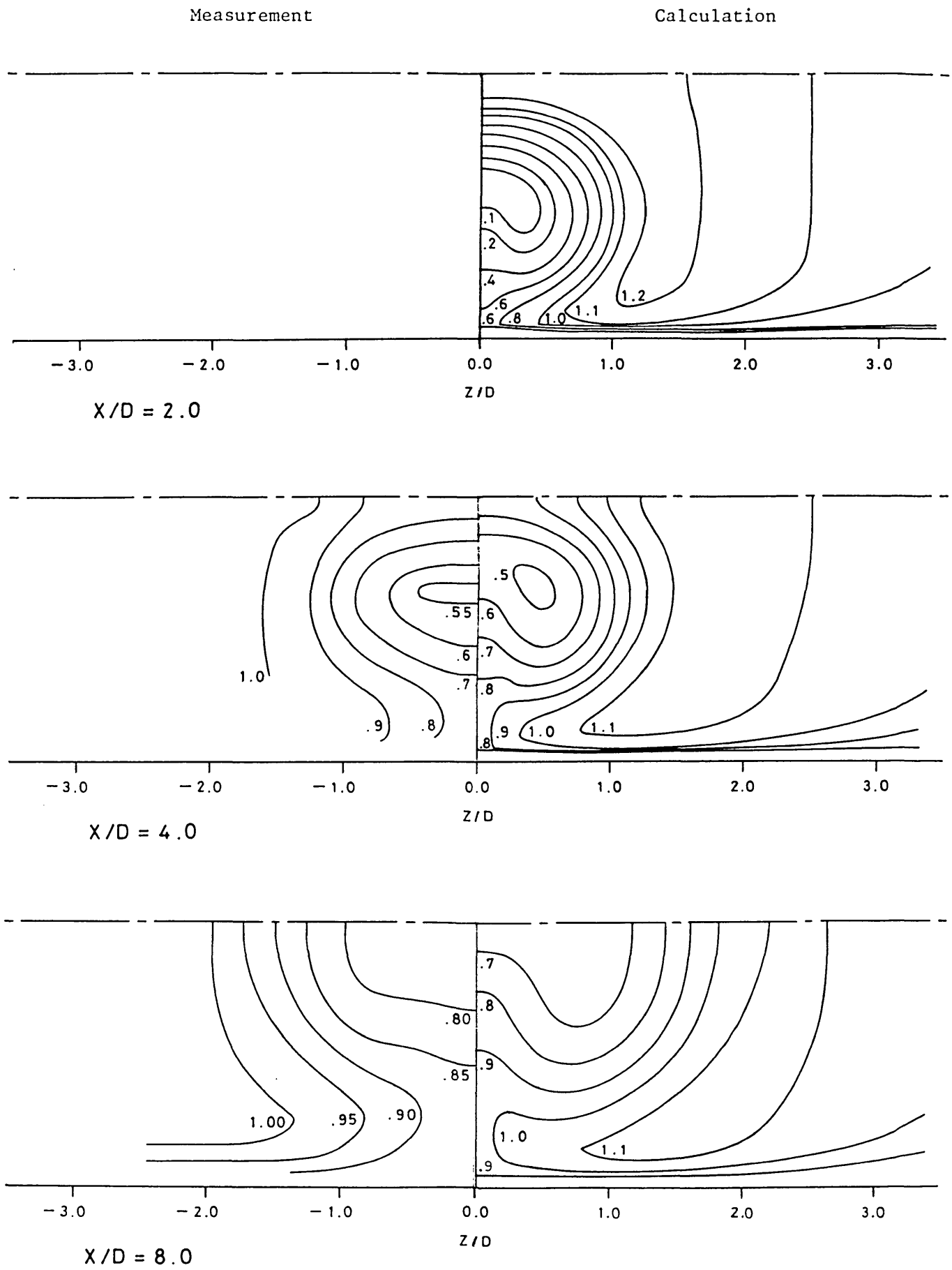


Figure 5.3 Contours of calculated and measured $\overline{U}$ velocity for two opposed single jets; H/D = 4.0; V_J/U_∞ = 1.8.

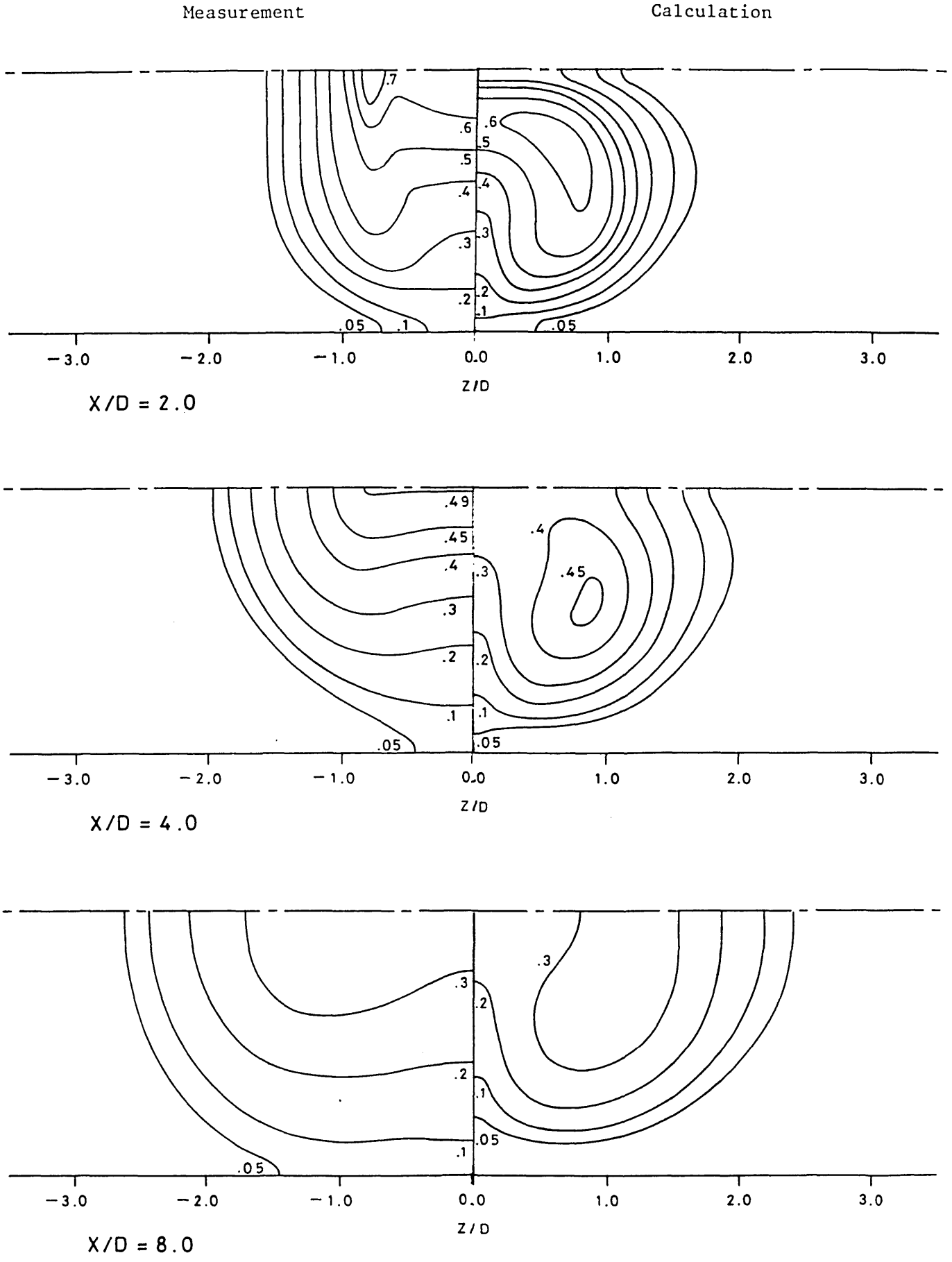


Figure 5.4 Contours of calculated and measured mean scalar concentration for two opposed single jets; H/D = 4.0; V_J/U_∞ = 1.8.

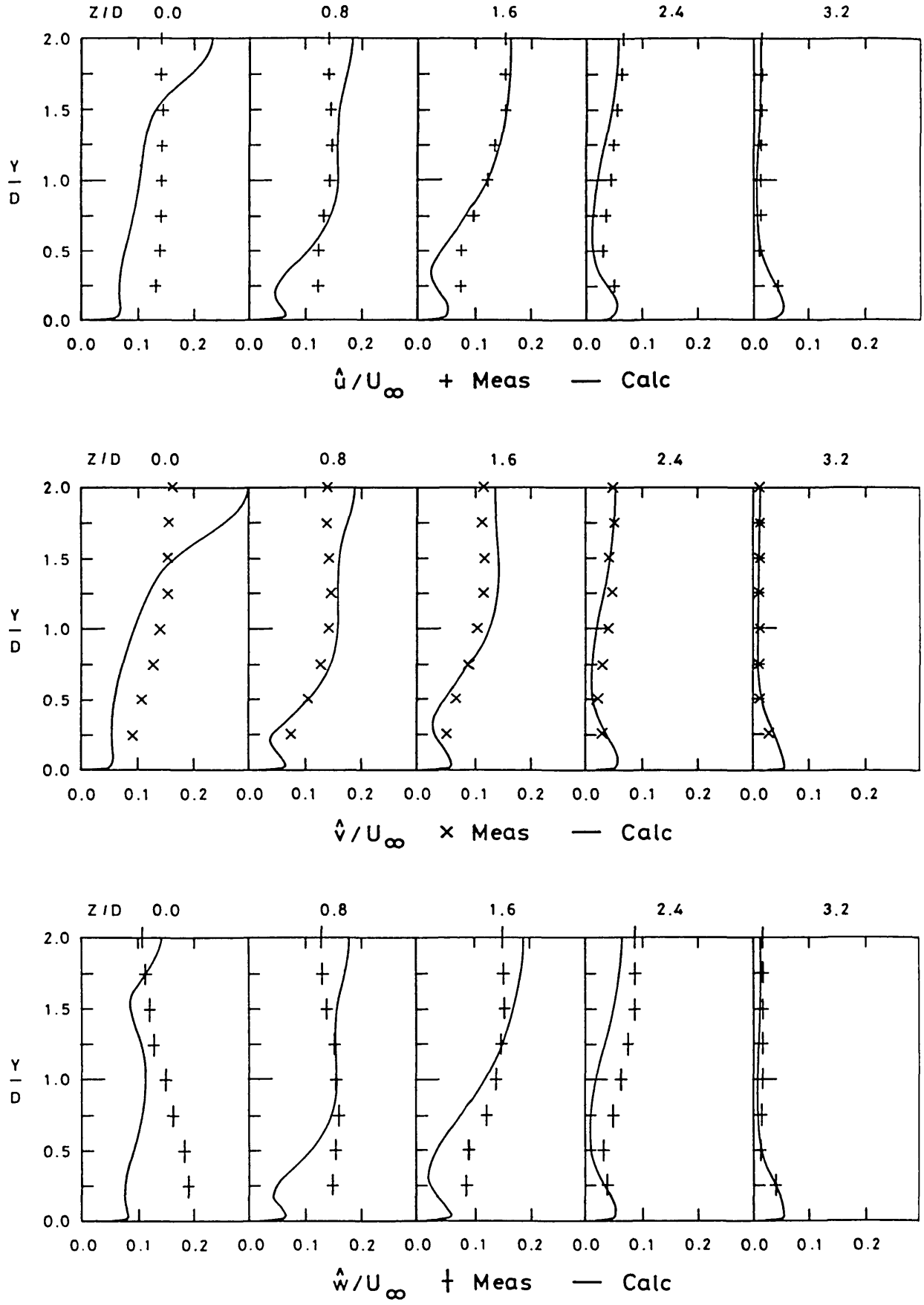


Figure 5.5 Profiles of calculated and measured Reynolds normal stresses in the plane X/D = 8.0 for two opposed single jets; H/D = 4.0; V_J/U_∞ = 1.8.

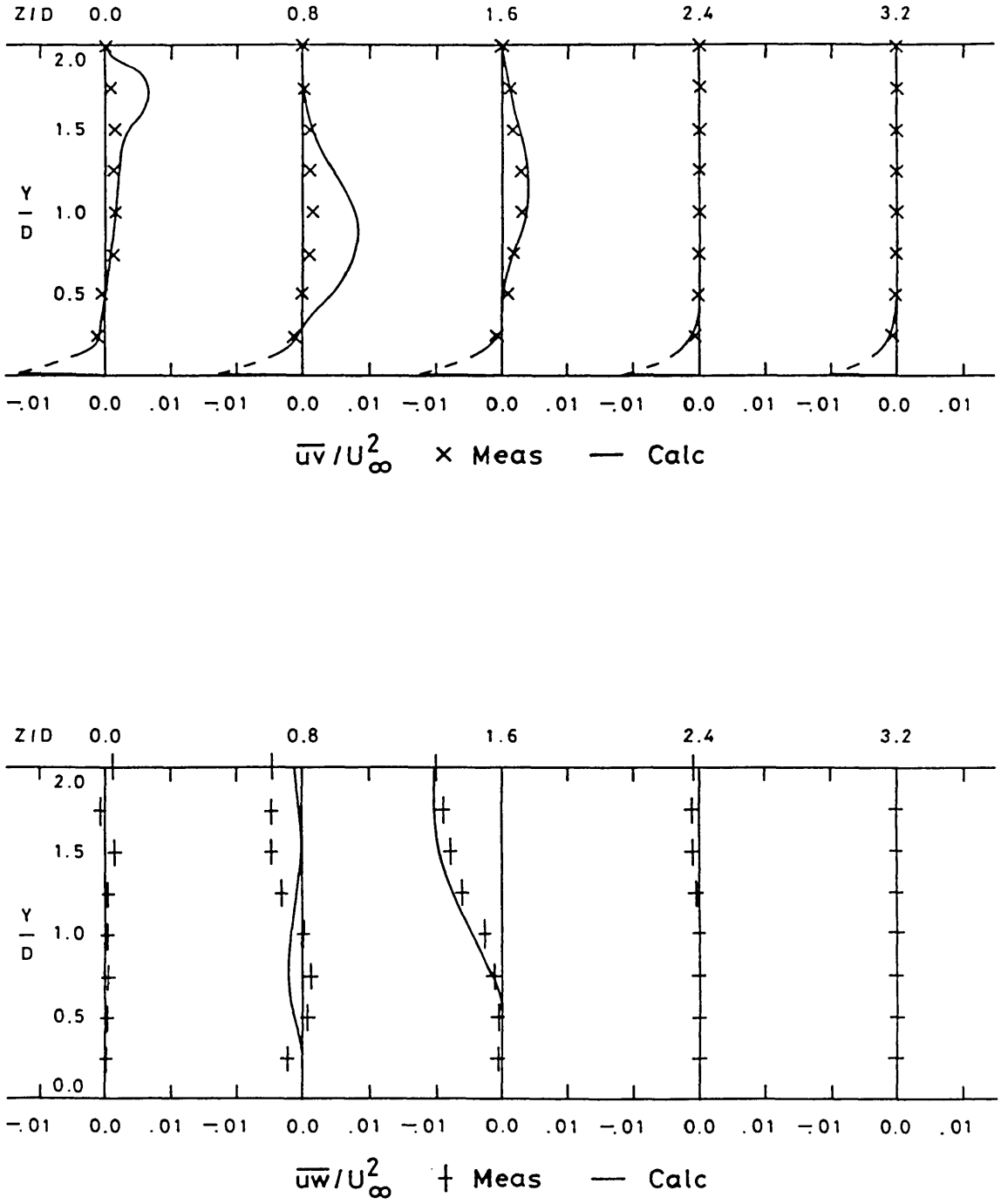


Figure 5.6 Profiles of calculated and measured Reynolds shear stresses in the plane X/D = 8.0 for two opposed single jets; H/D = 4.0; V_J/U_∞ = 1.8.

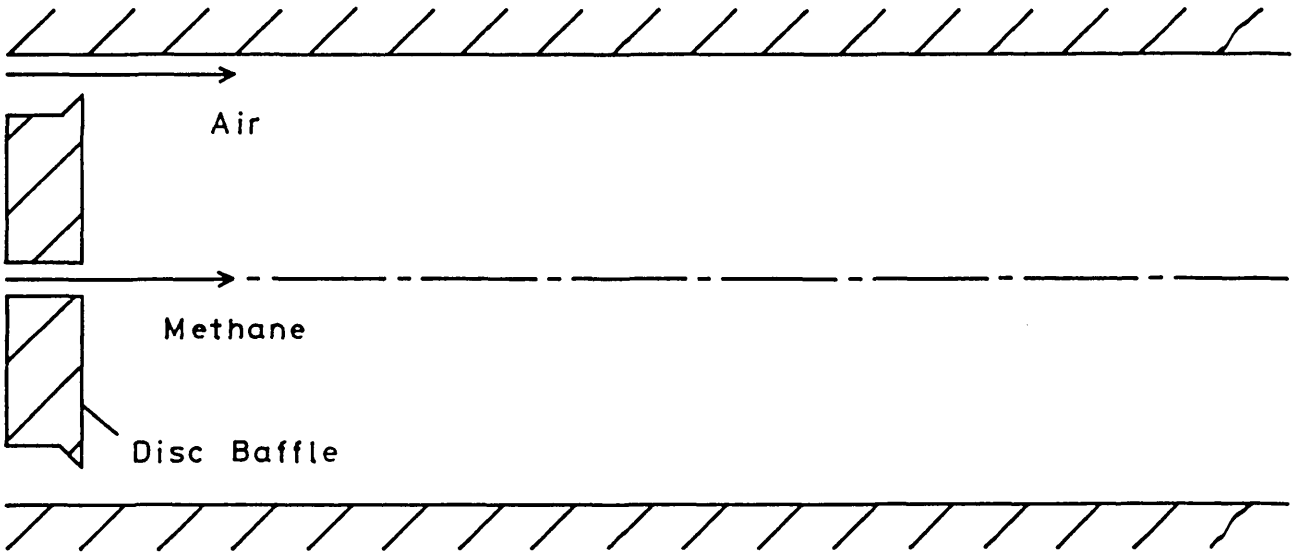


Figure 6.1 Axisymmetric combustor with disc baffle.

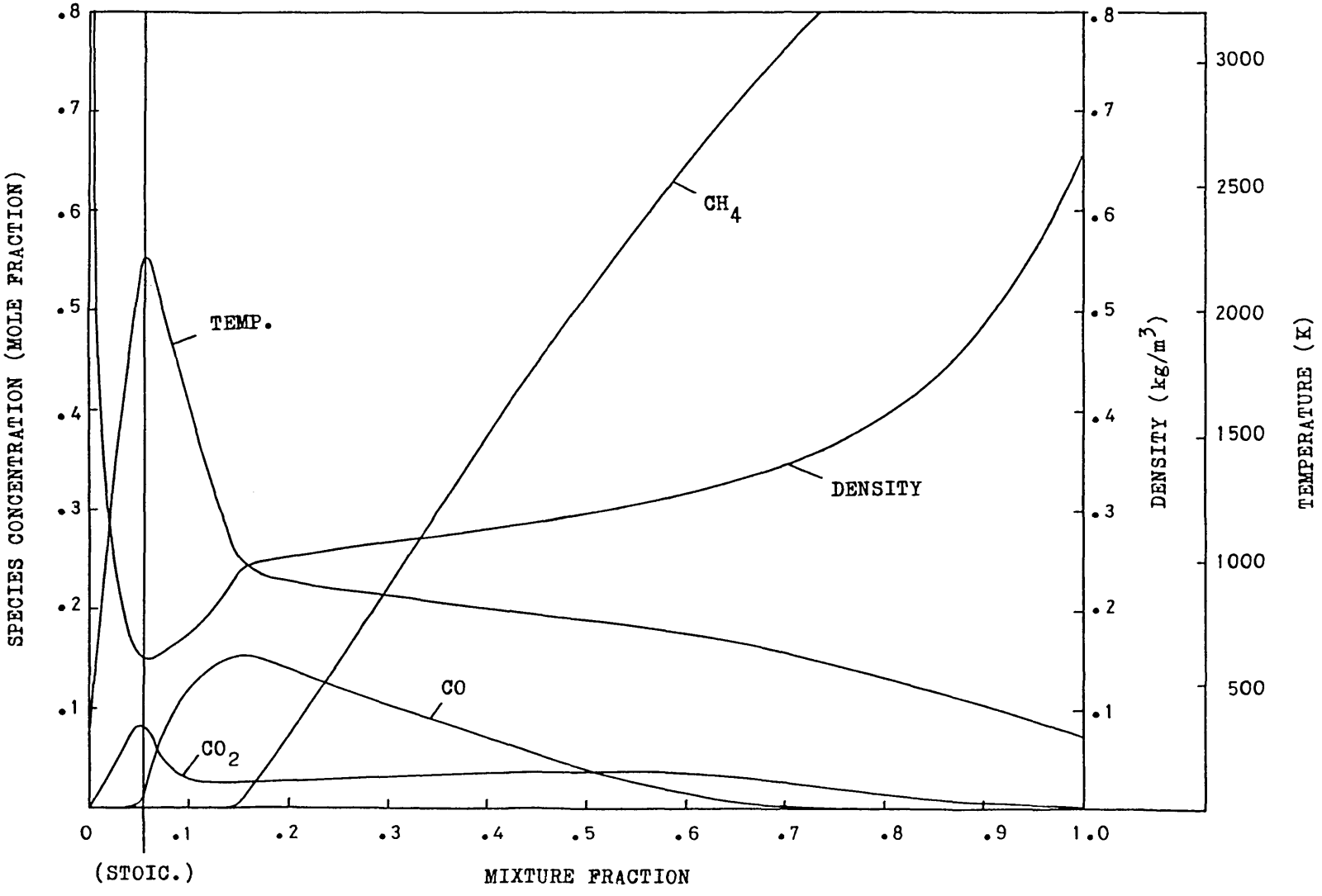


Figure 6.2 Equilibrium species concentration, temperature and density of methane and air mixtures for initial conditions: $T_{methane} = T_{air} = 300K$, P = latm.

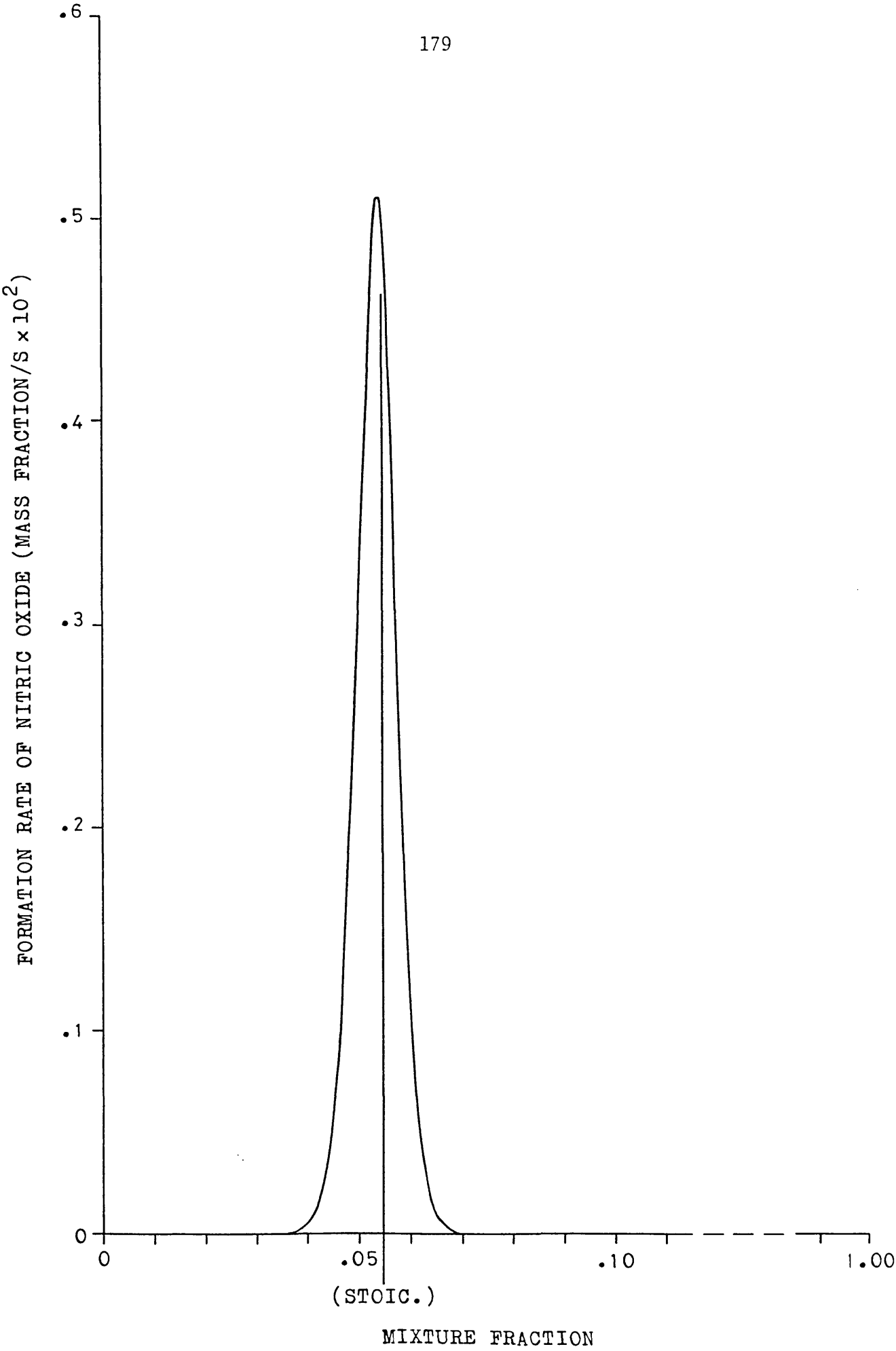


Figure 6.3 Instantaneous formation rate of nitric oxide for methane and air mixtures with initial conditions:
$T_{methane} = T_{air} = 300K$, P = latm.

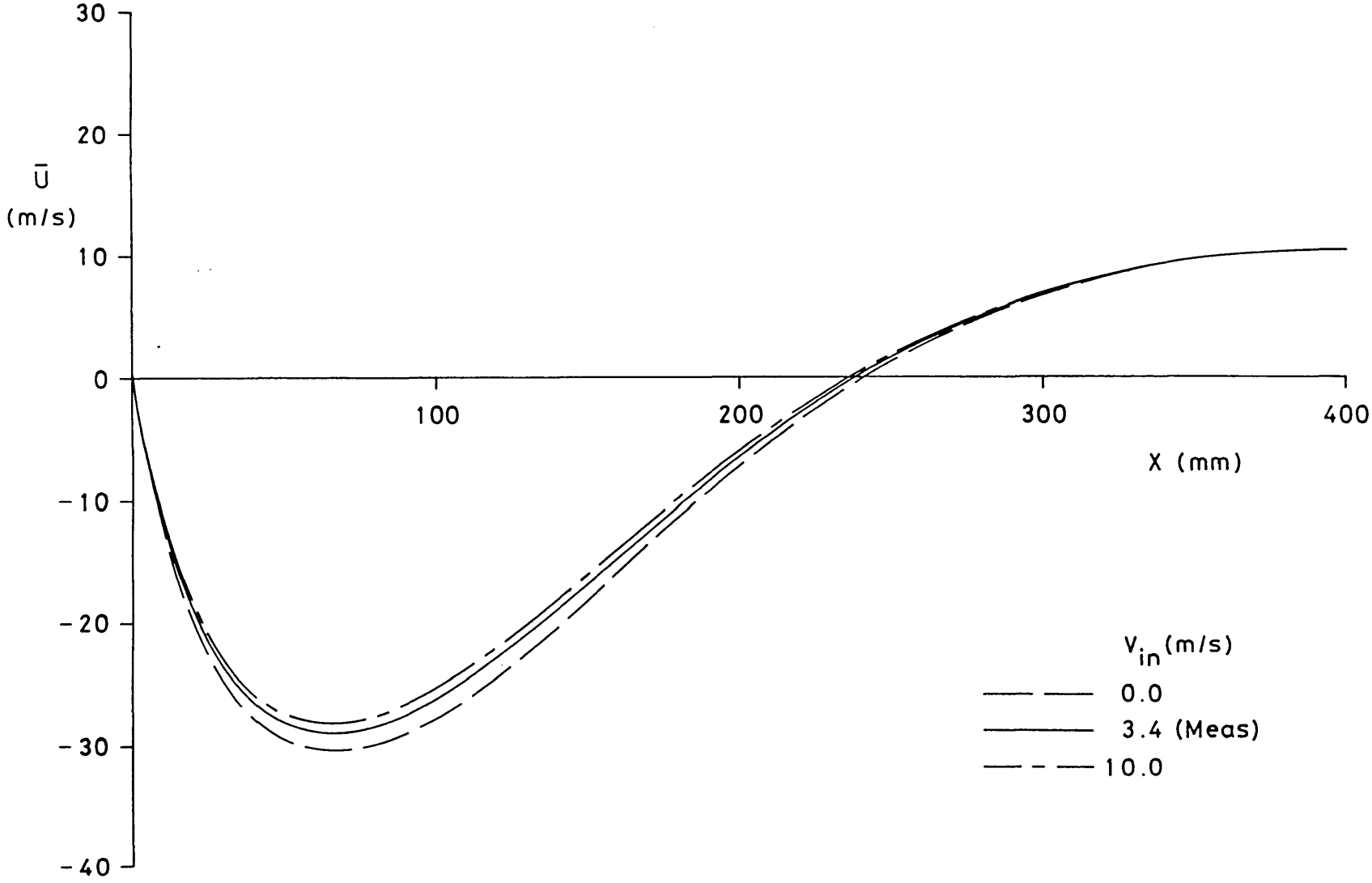


Figure 6.4 Influence of inlet radial velocity on the centreline mean velocity for non-reacting flow; Re = 1.9×10^5.

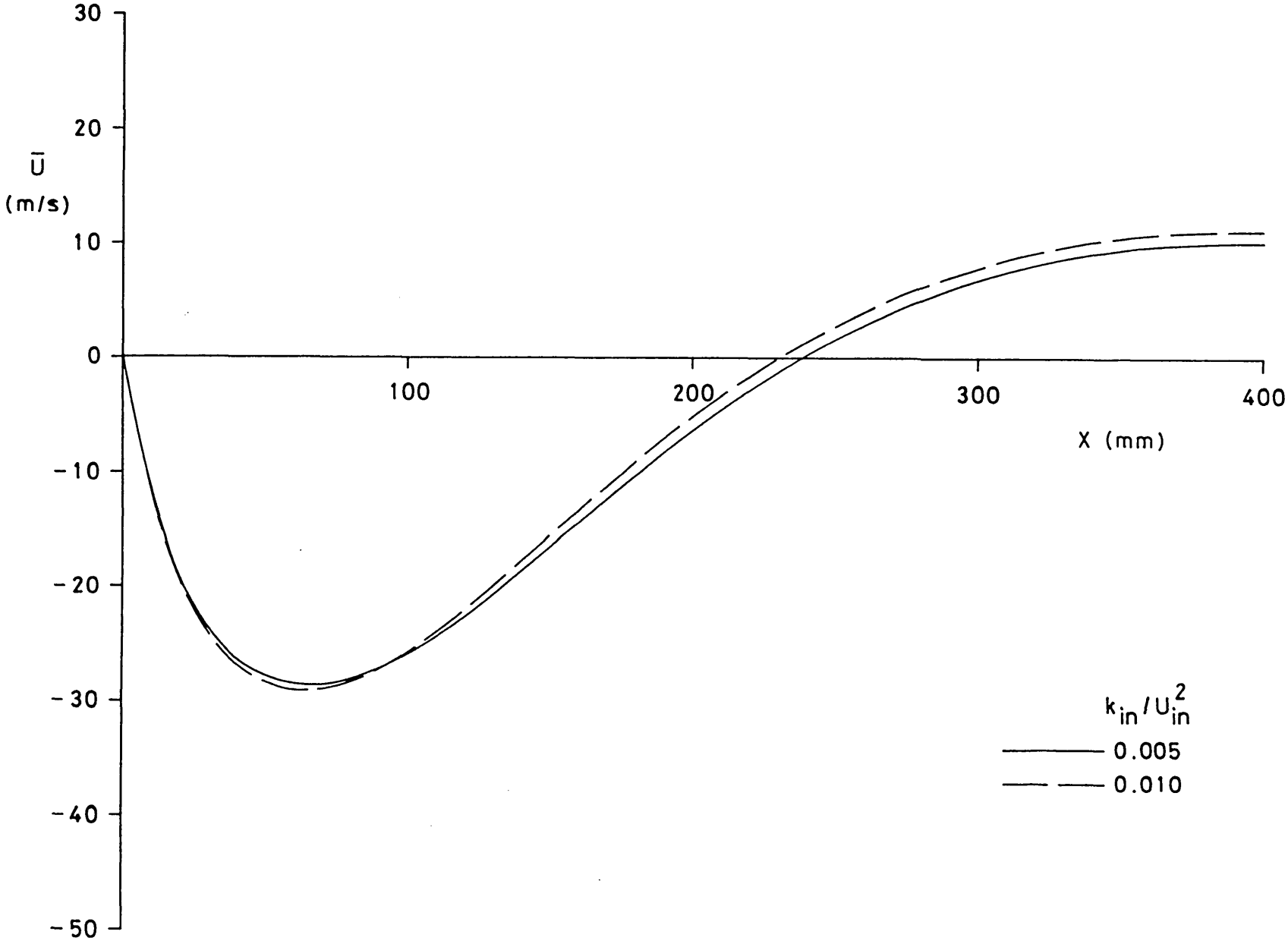


Figure 6.5 Influence of inlet turbulence energy on the centreline mean velocity for non-reacting flow; Re = 1.9×10^5.

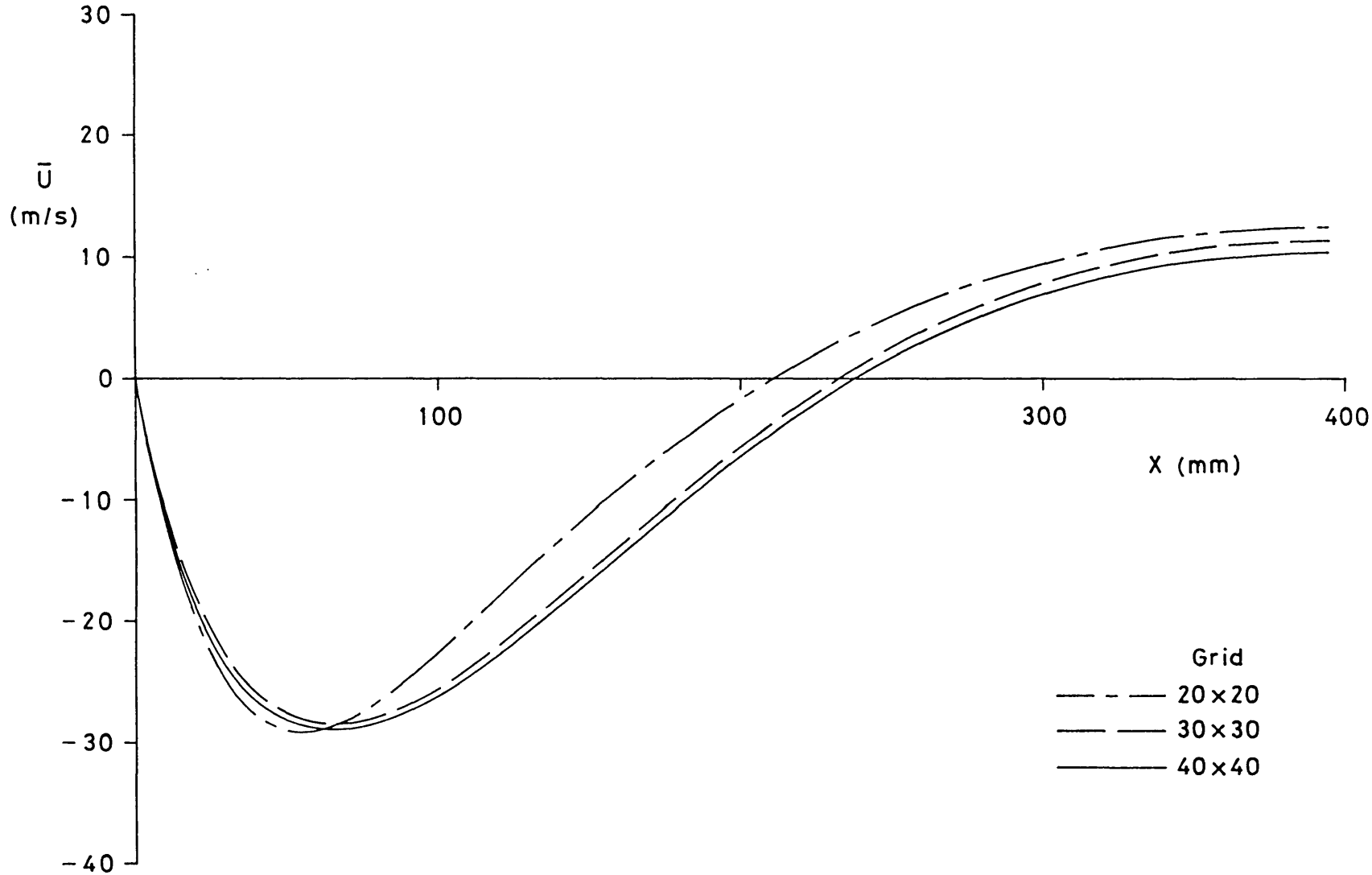
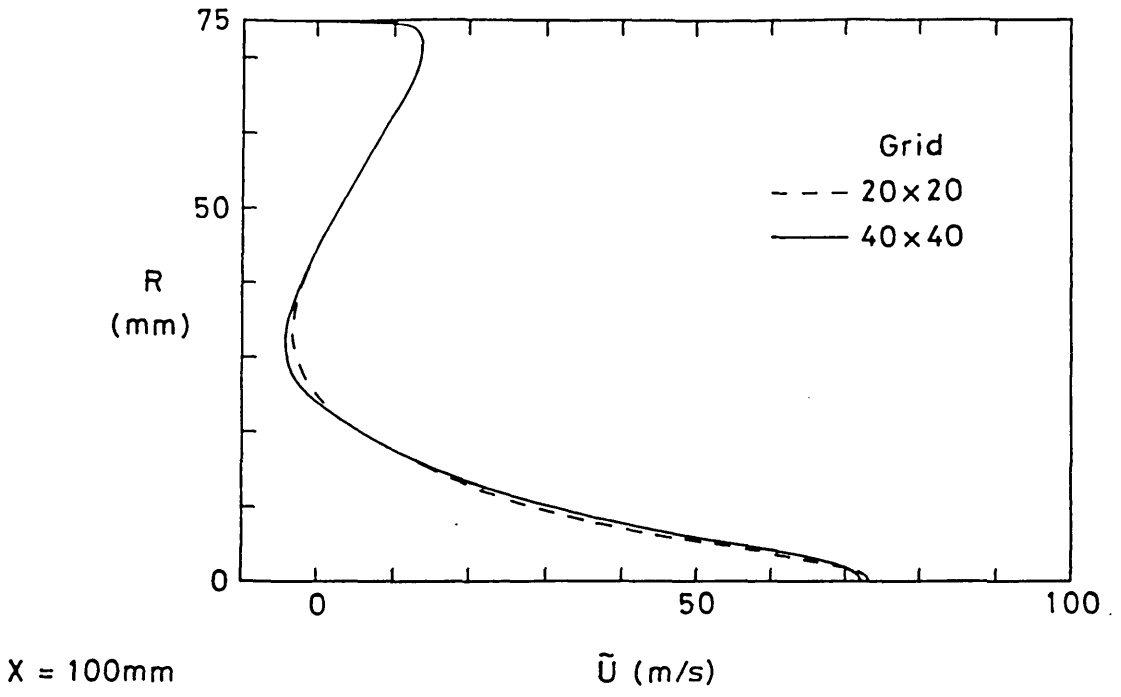


Figure 6.6 Influence of grid refinement on the centreline mean velocity for non-reacting flow; Re = 1.0×10^5.



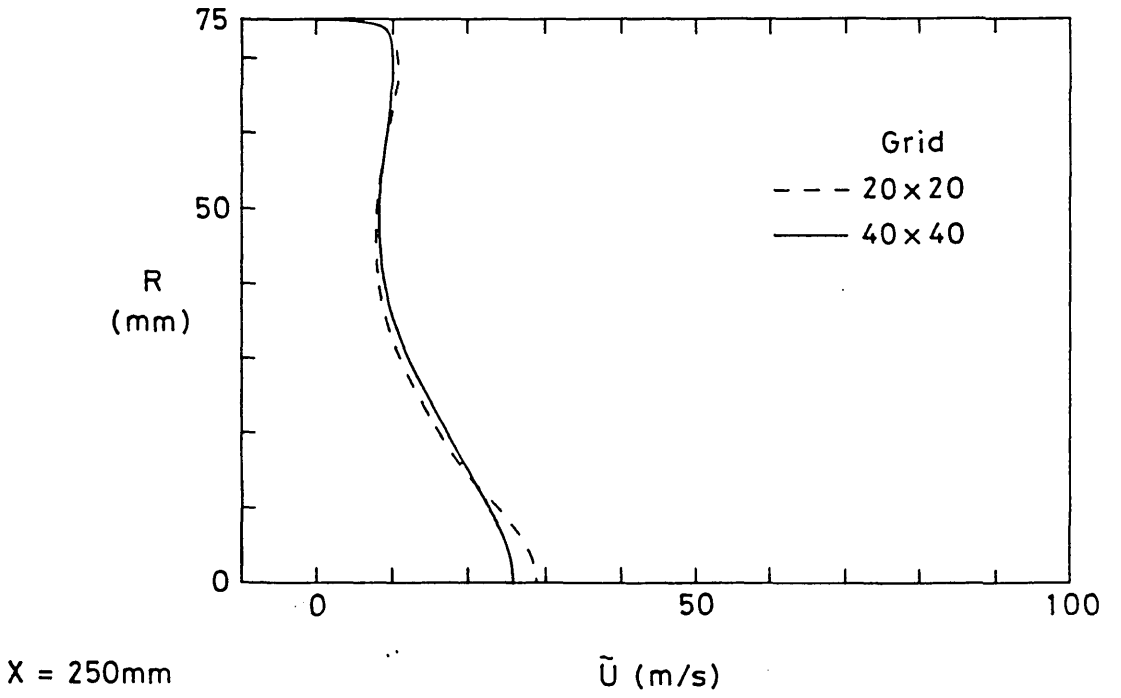


Figure 6.7 Influence of grid refinement on the radial profiles of axial mean velocity for reacting flow; condition 1.

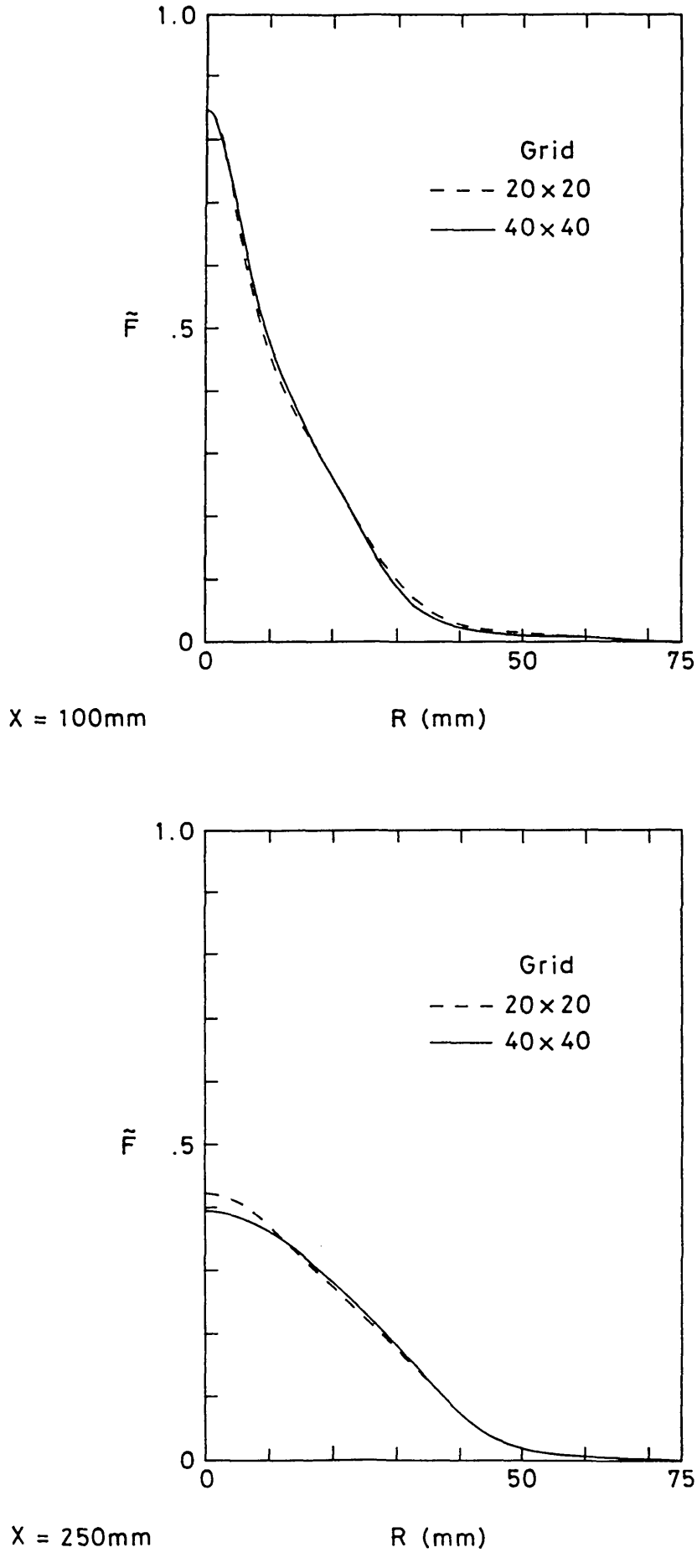
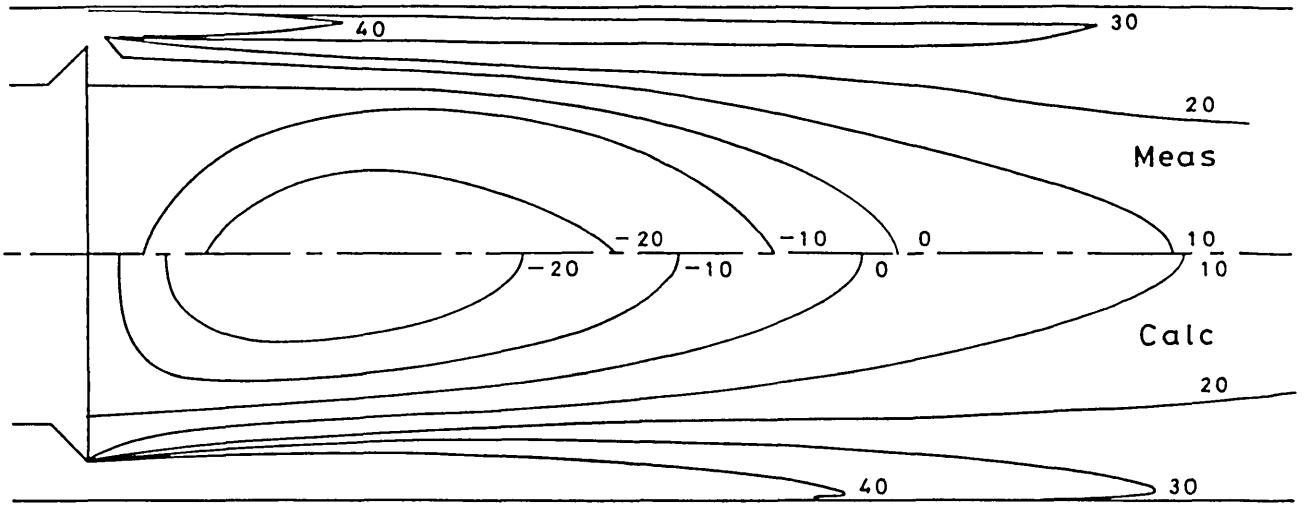
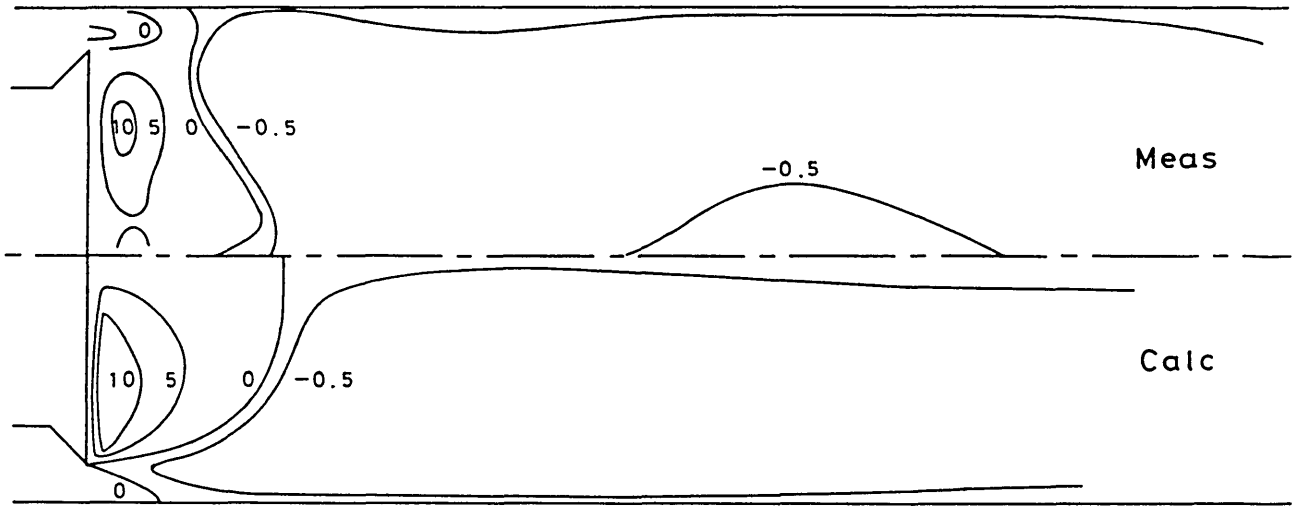


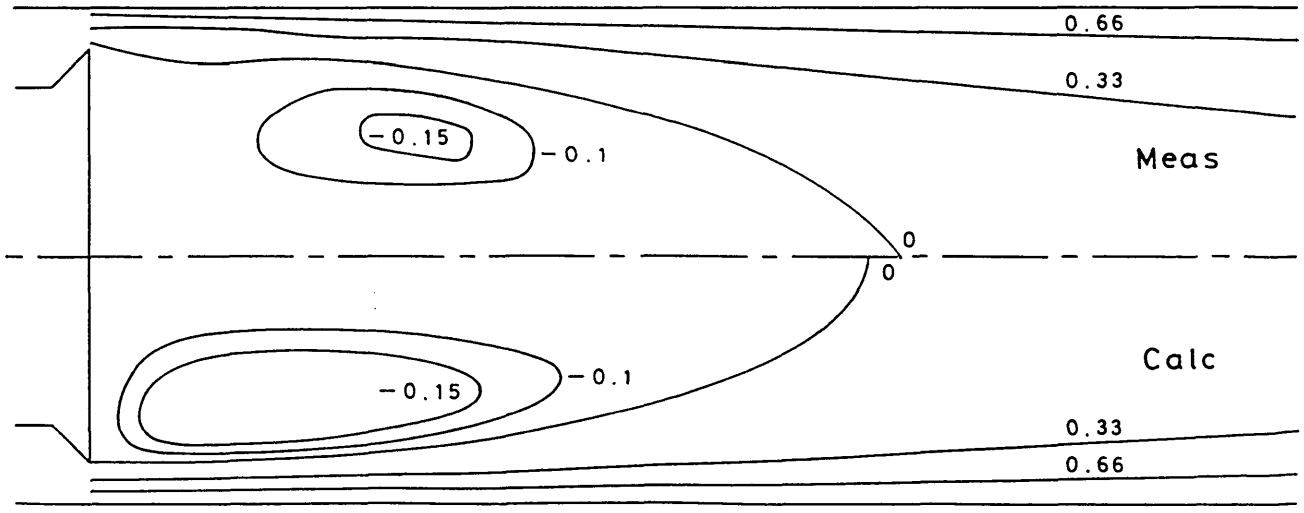
Figure 6.8 Influence of grid refinement on the radial profiles of mean mixture fraction for reacting flow; condition 1.



$\tilde{U}$ (m/s)

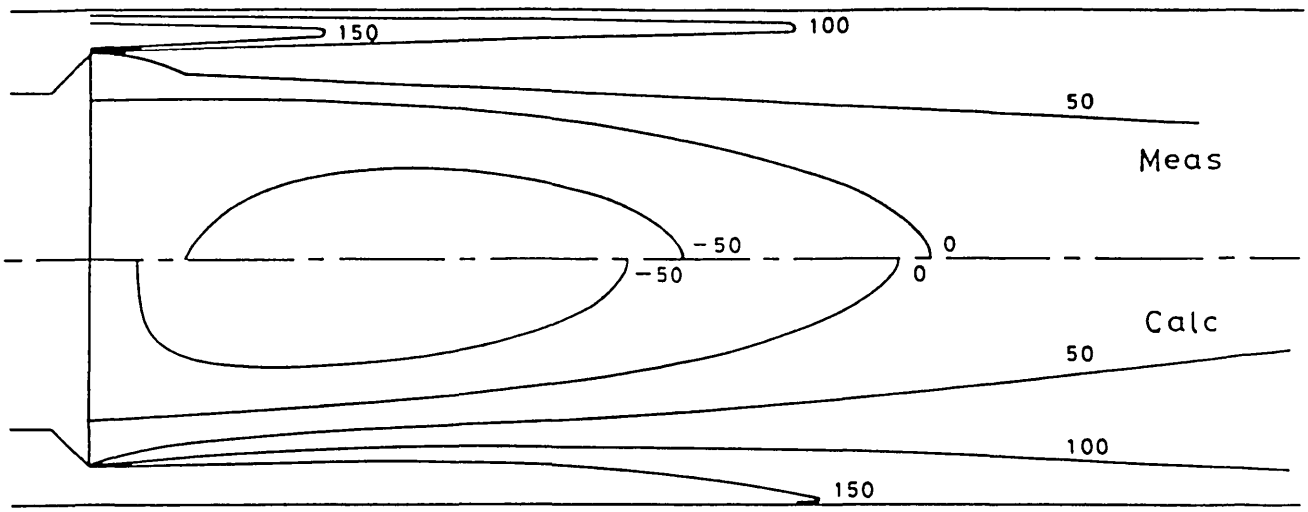


$\tilde{V}$ (m/s)

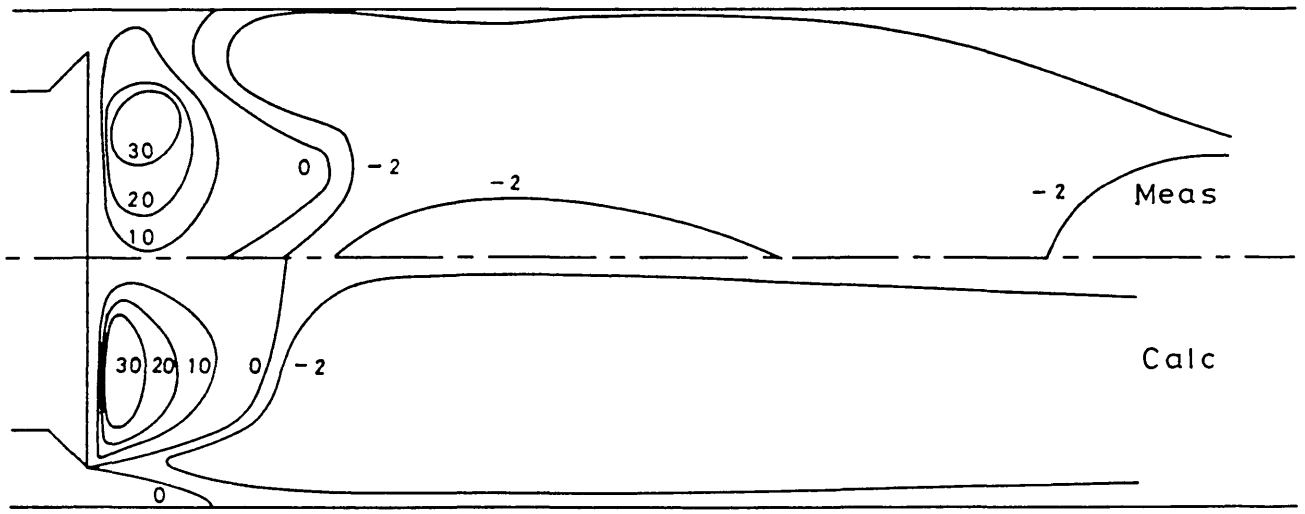


Non-dimensional Stream Function

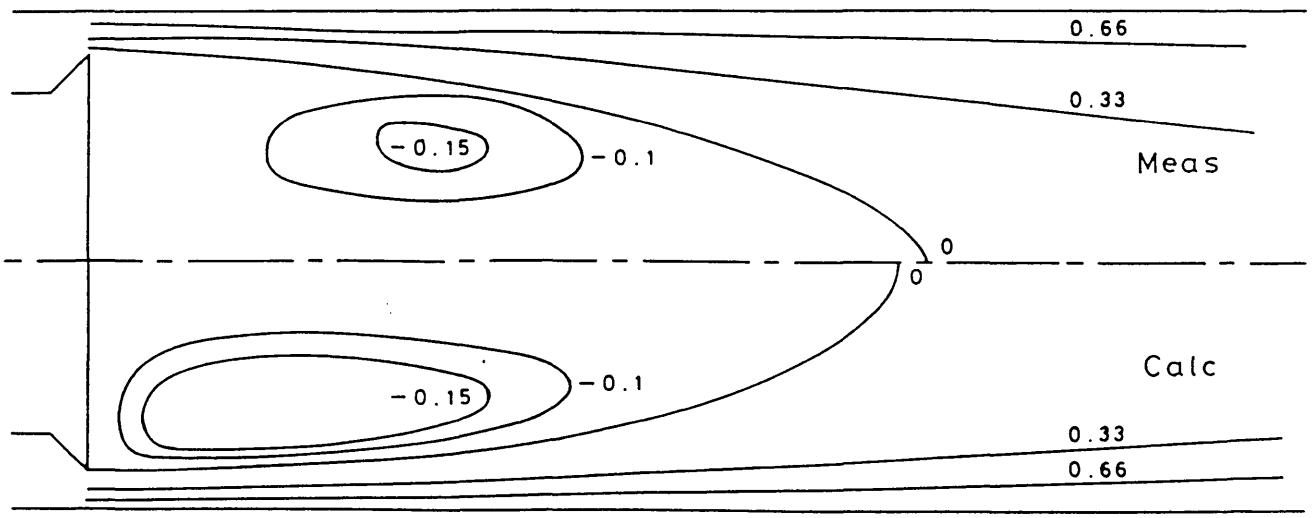
Figure 6.9 Contours of calculated and measured axial and radial mean velocity and non-dimensional stream function for non-reacting flow; Re = 1.9×10^5.



$\tilde{U}$ (m/s)



$\tilde{V}$ (m/s)



Non-dimensional Stream Function

Figure 6.10 Contours of calculated and measured axial and radial mean velocity and non-dimensional stream function for non-reacting flow; Re = 6.5×10^5.

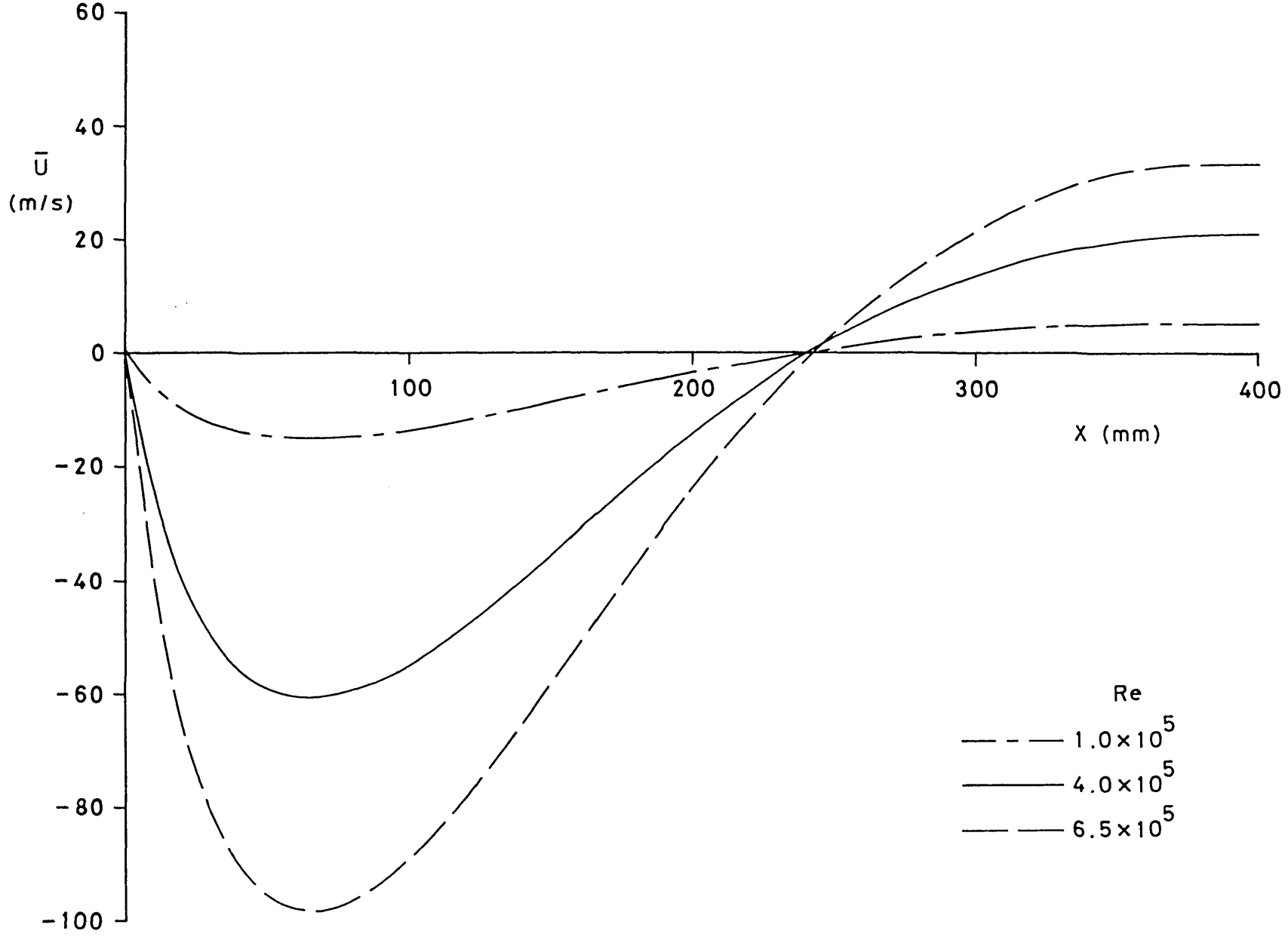
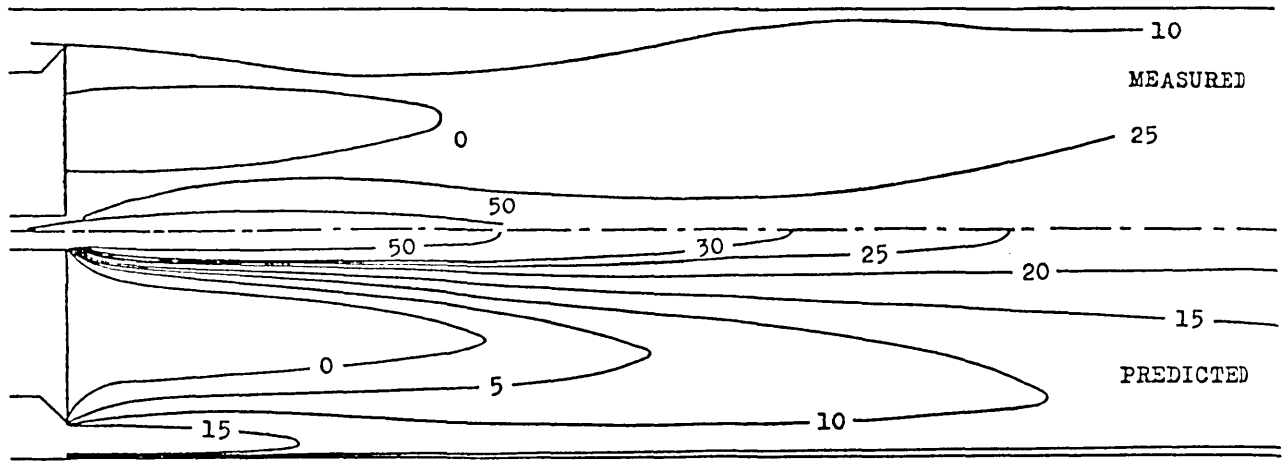
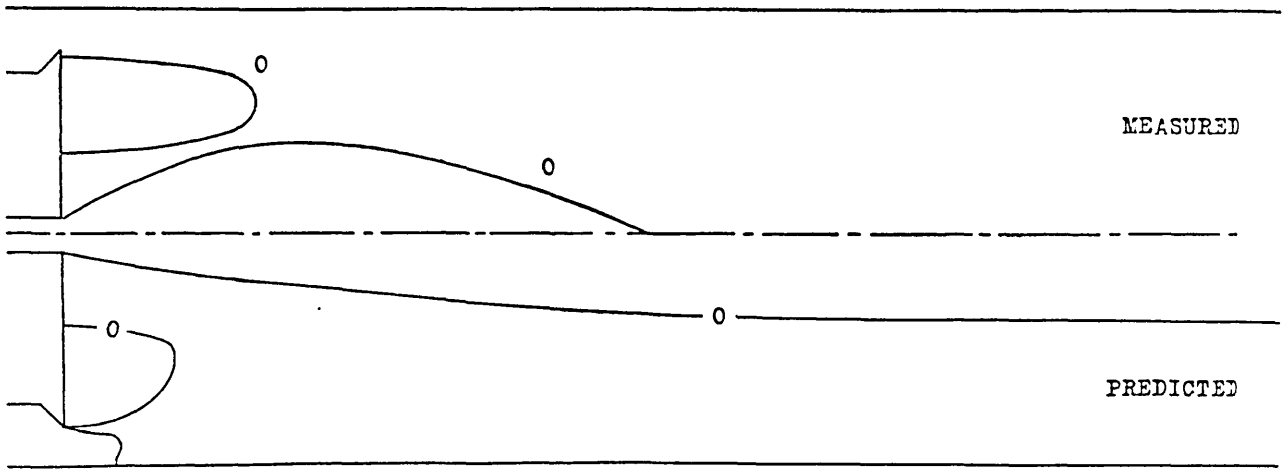


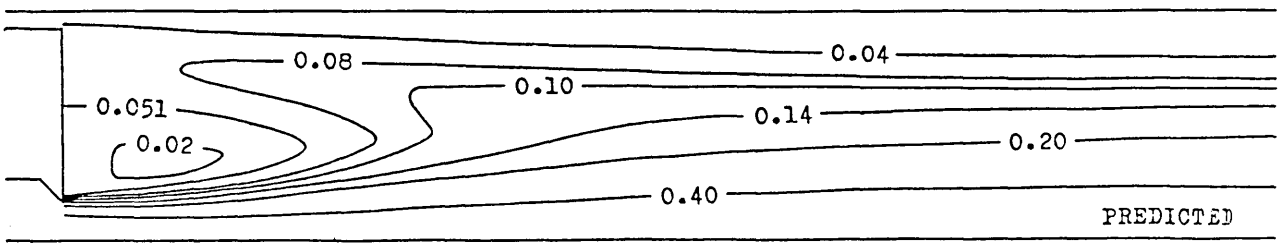
Figure 6.11 Influence of Reynolds number on the centreline mean velocity for non-reacting flow.



AXIAL VELOCITY (m/s)

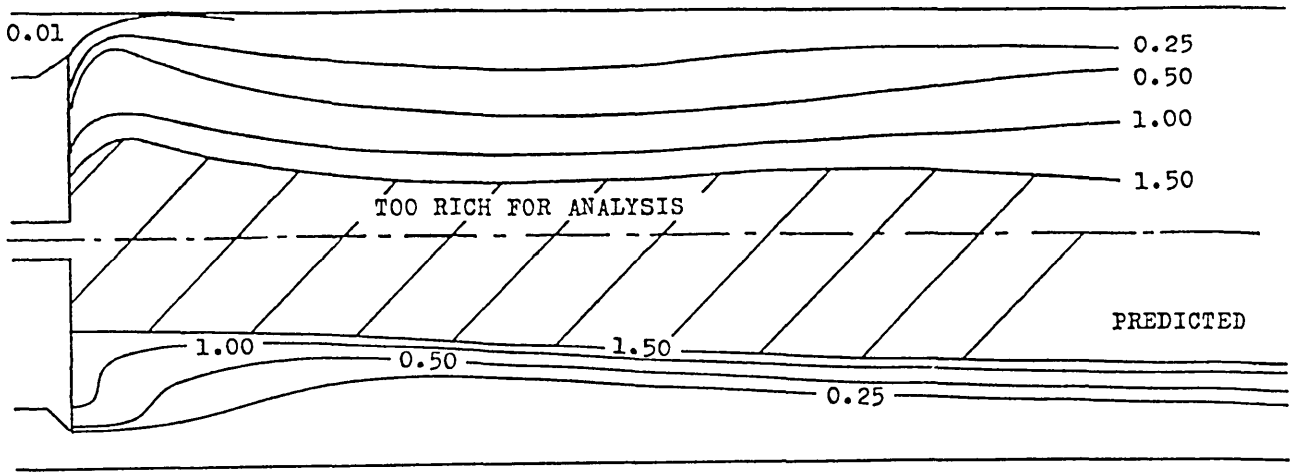


RADIAL VELOCITY (m/s)

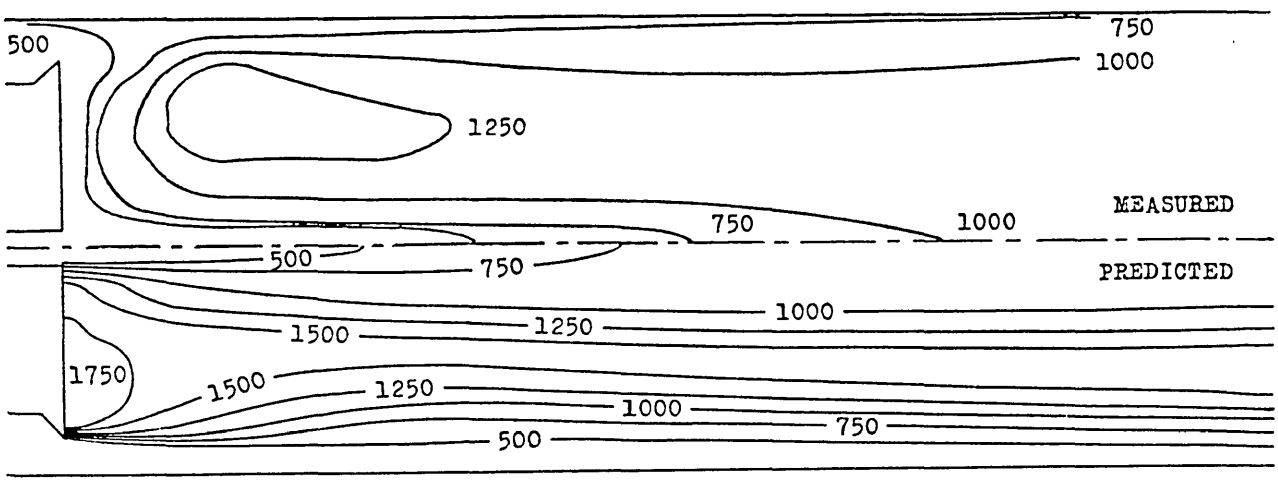


NON DIMENSIONAL STREAM FUNCTION

Figure 6.12 Contours of calculated and measured axial and radial mean velocity and non-dimensional stream function for reacting flow; condition 1.

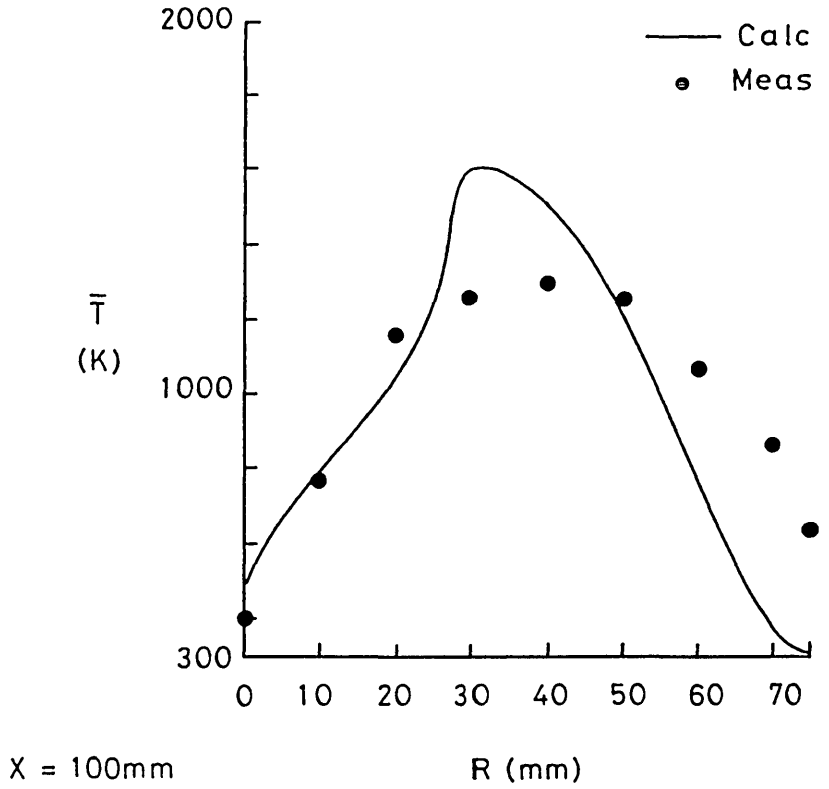


EQUIVALENCE RATIO



TEMPERATURE (K)

Figure 6.13 Contours of calculated and measured mean equivalence ratio and mean temperature for reacting flow; condition 1.



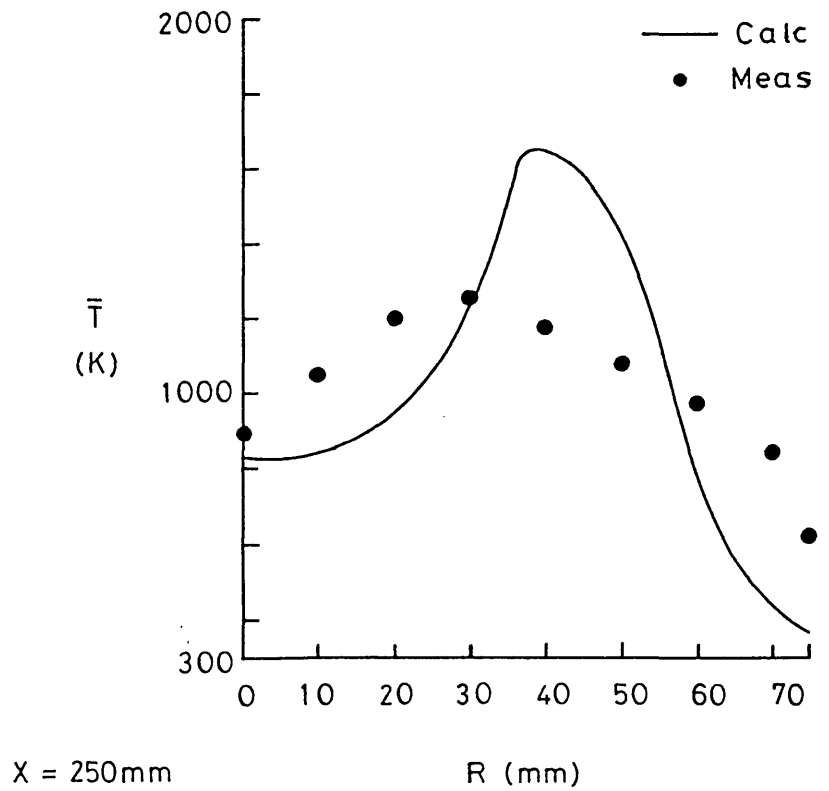
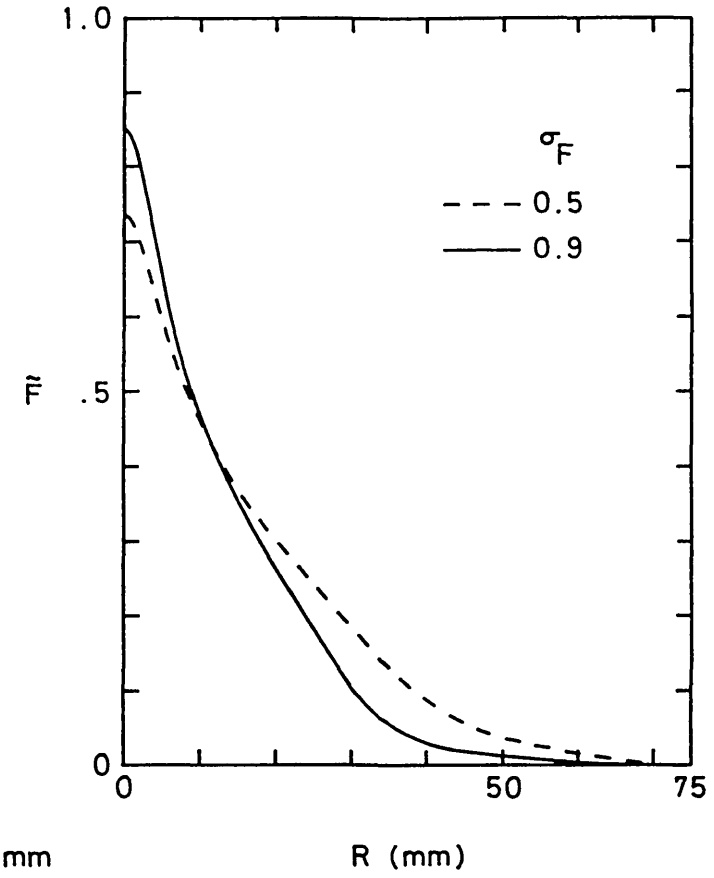


Figure 6.14 Calculated and measured radial profiles of mean temperature for reacting flow; condition 1.



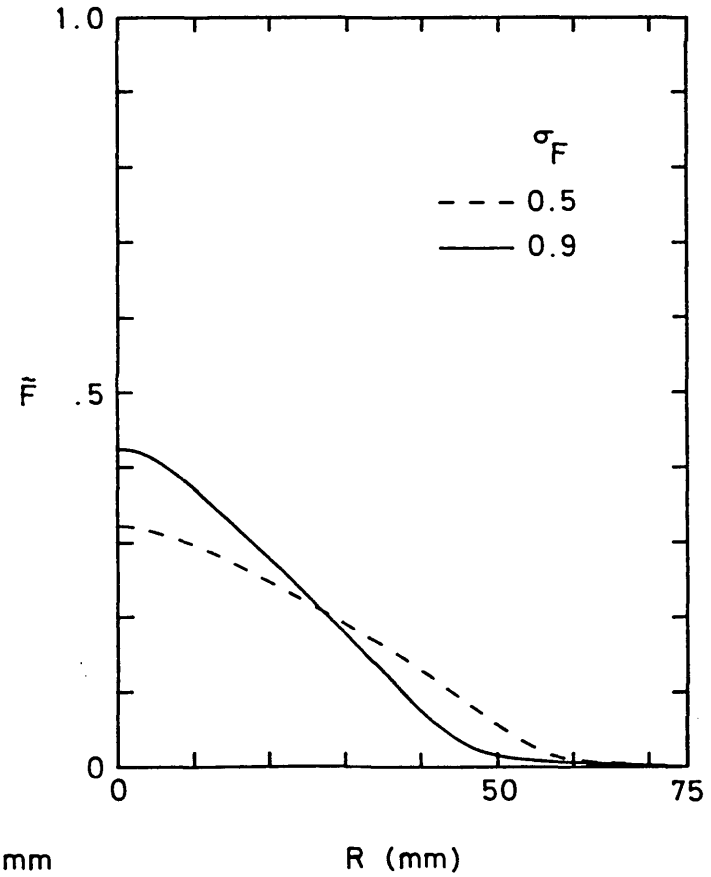
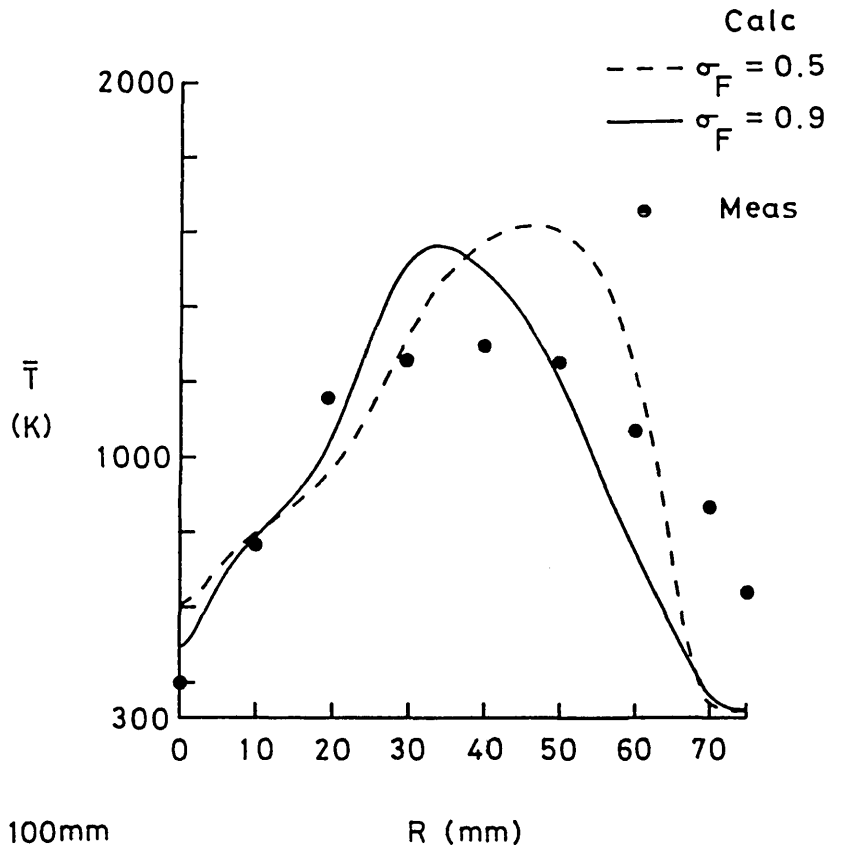


Figure 6.15 Influence of the turbulence Prandtl number σ_F on the calculated radial profiles of mean mixture fraction for reacting flow; condition 1.



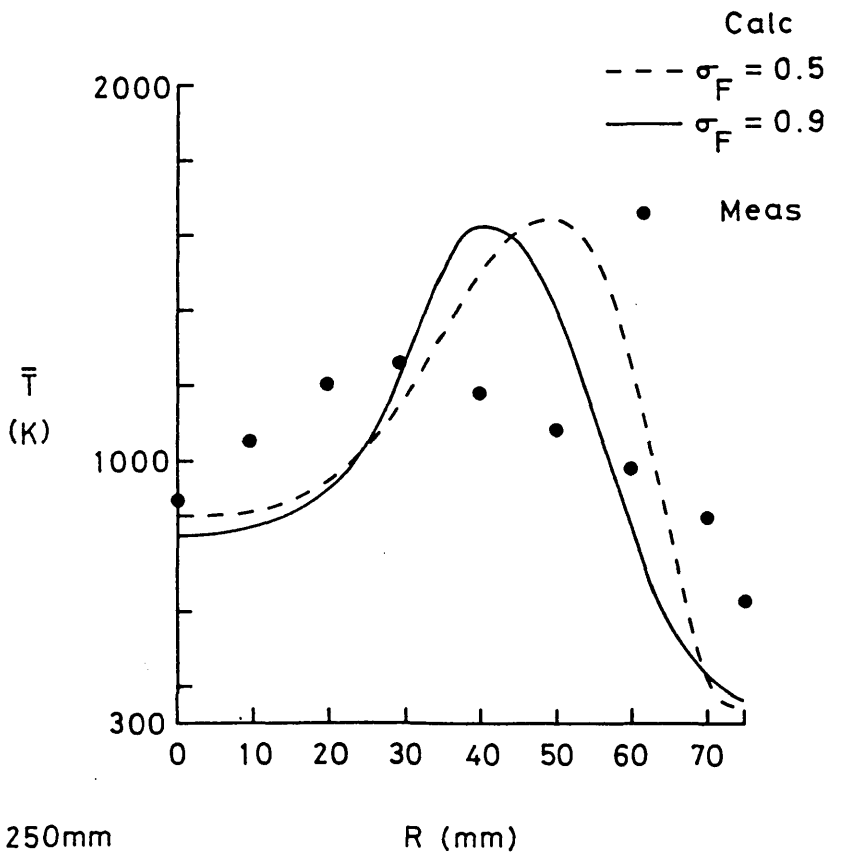
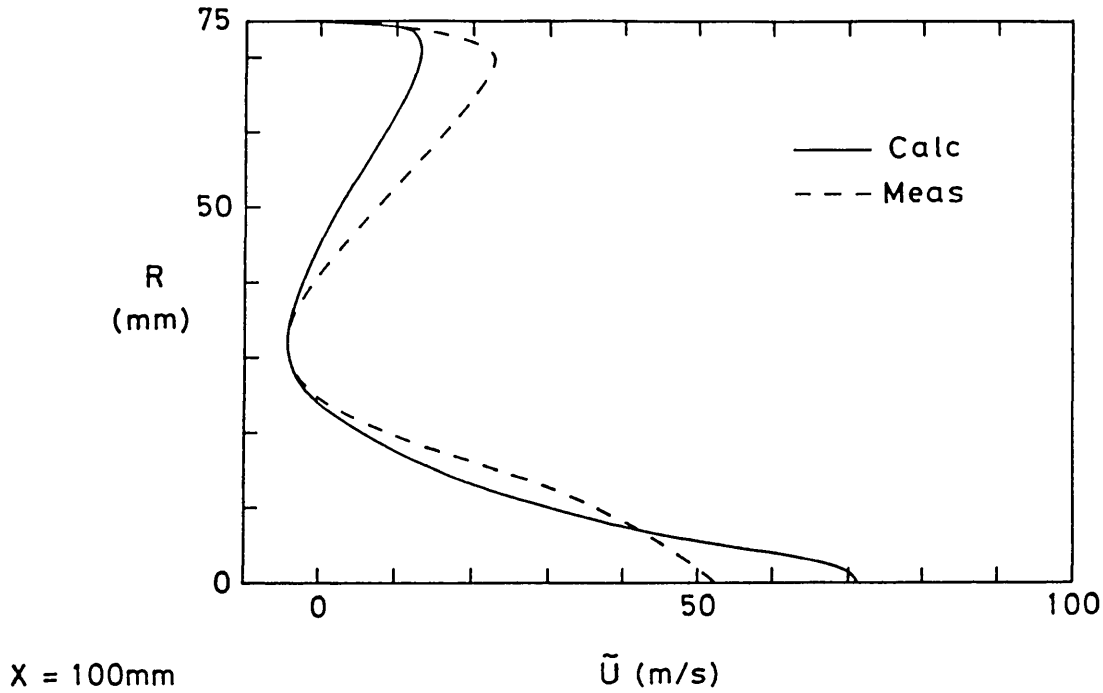


Figure 6.16 Influence of the turbulence Prandtl number σ_F on the calculated radial profiles of mean temperature for reacting flow; condition 1.



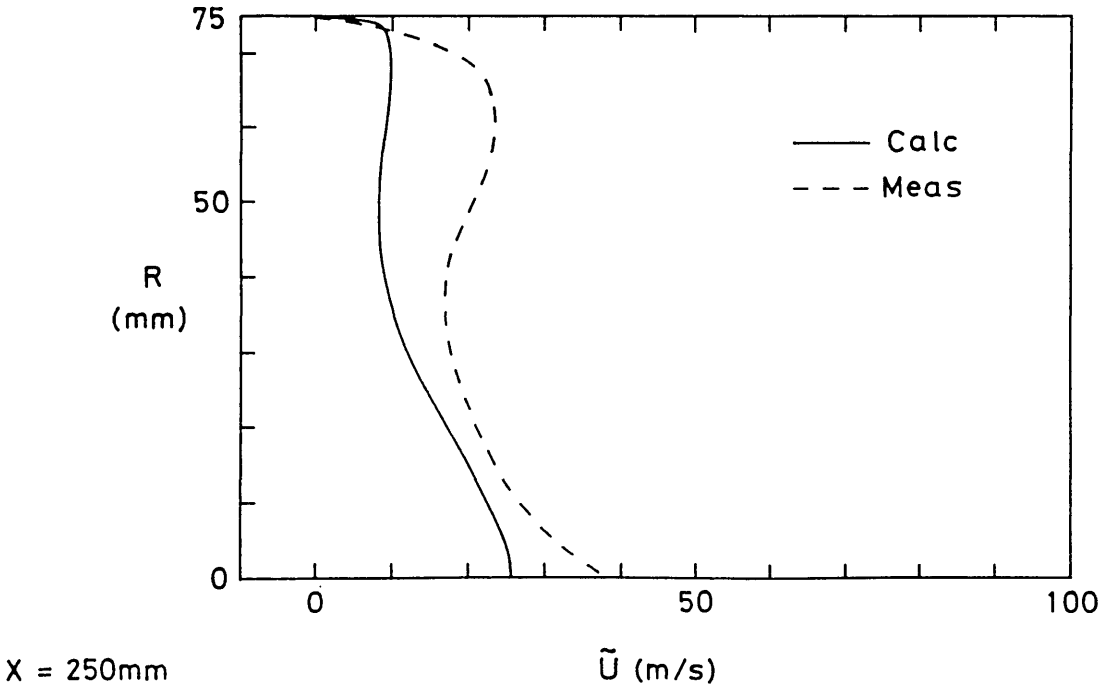
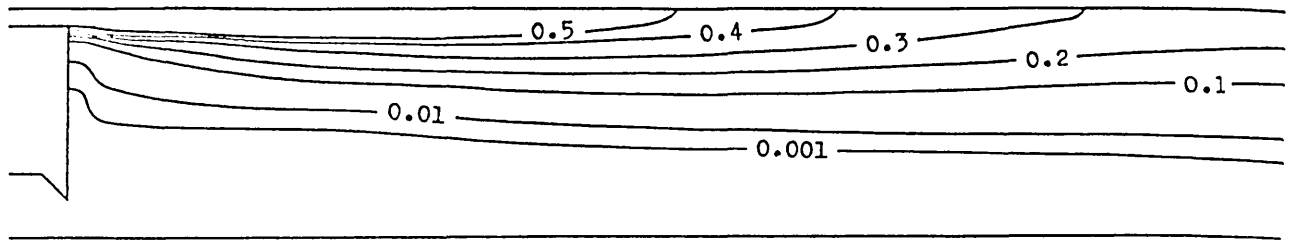
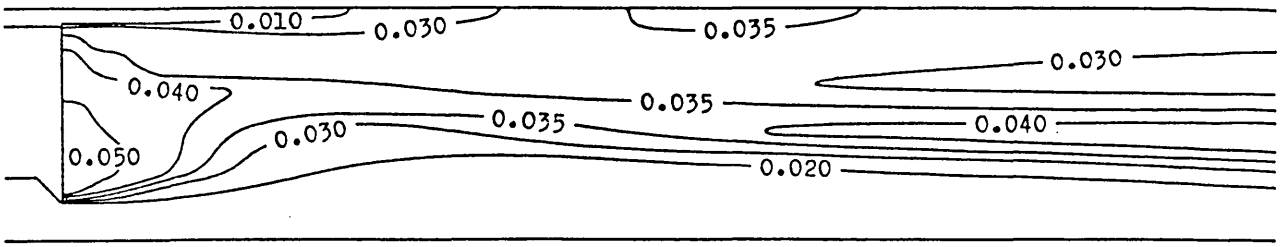


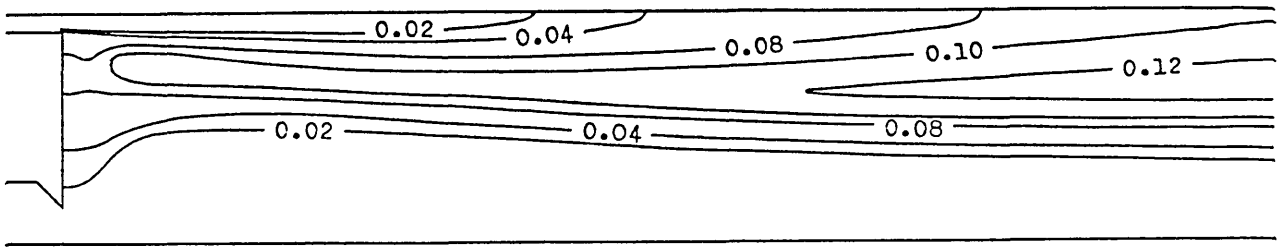
Figure 6.17 Radial profiles of calculated and measured axial mean velocity for reacting flow; condition 1.



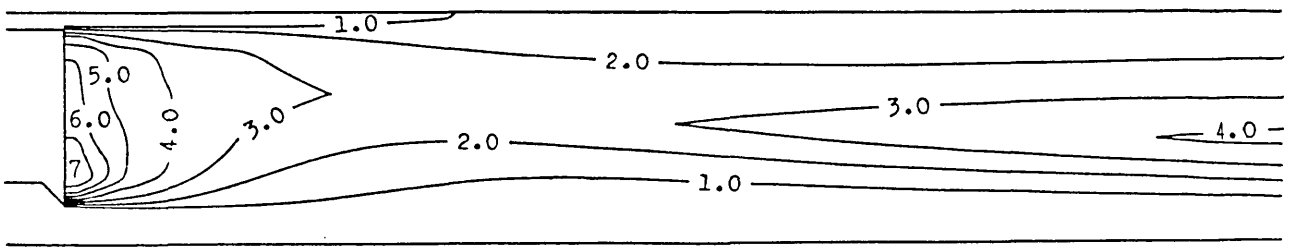
METHANE (mole fraction)



CARBON DIOXIDE (mole fraction)

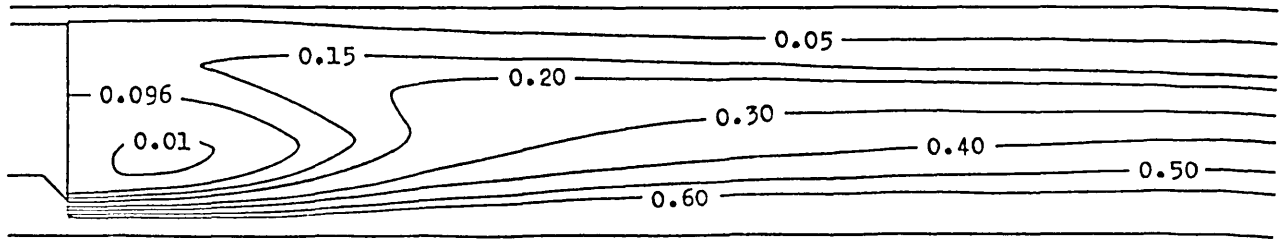


CARBON MONOXIDE (mole fraction)

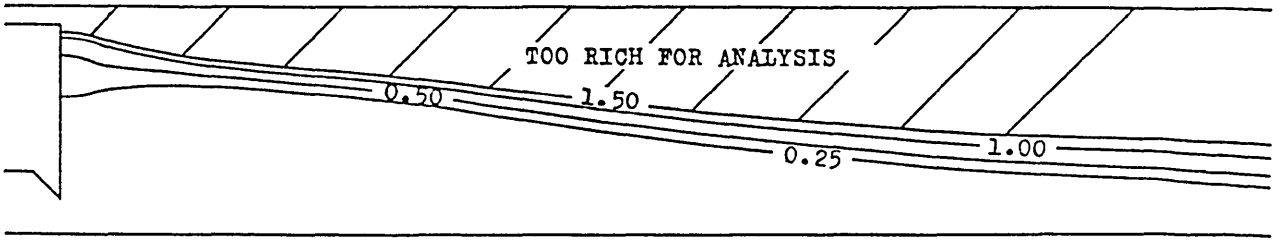


NITRIC OXIDE (P.P.M.)

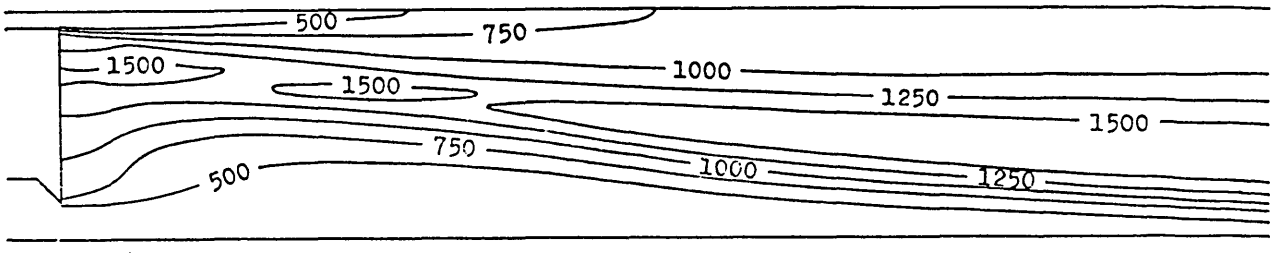
Figure 6.18 Contours of calculated and measured mean species concentrations for reacting flow; condition 1.



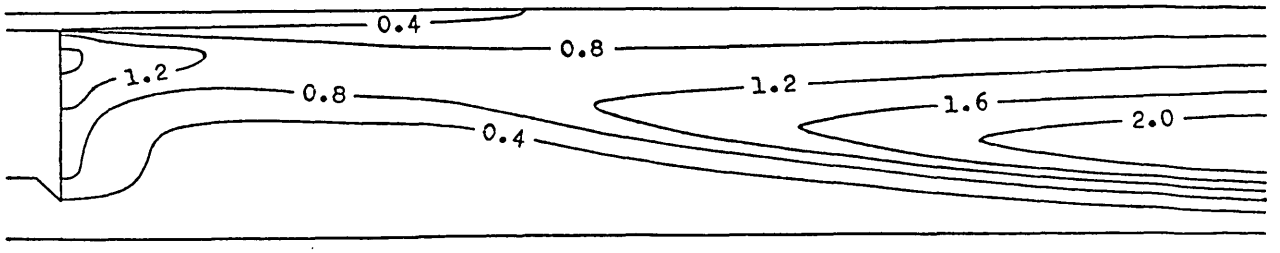
NON DIMENSIONAL STREAM FUNCTION



EQUIVALENCE RATIO

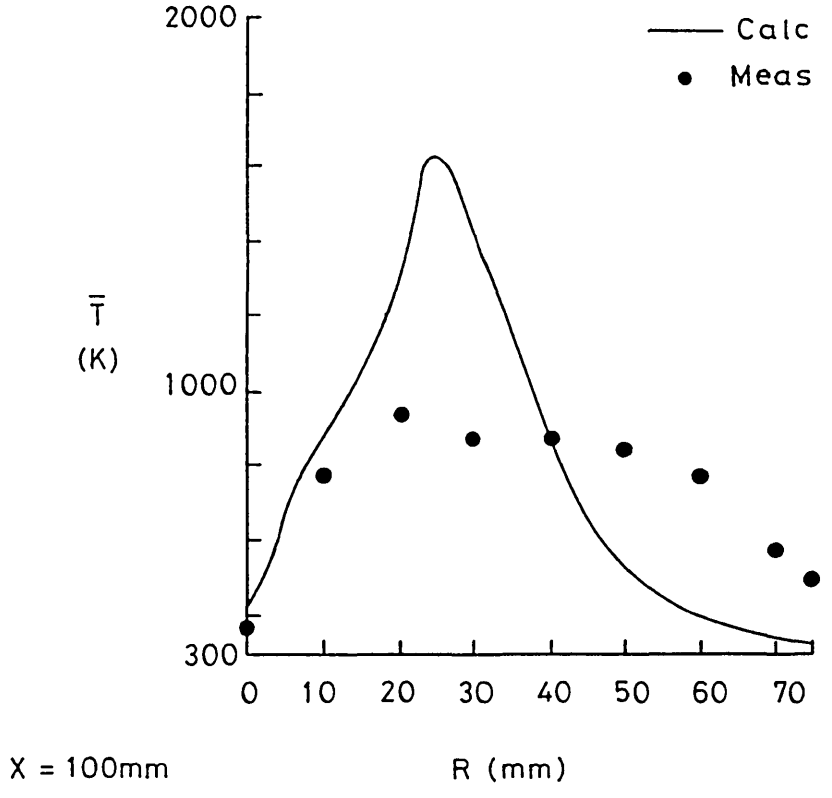


TEMPERATURE (K)



NITRIC OXIDE (P.P.M.)

Figure 6.19 Contours of calculated mean quantities for reacting flow; condition 3.



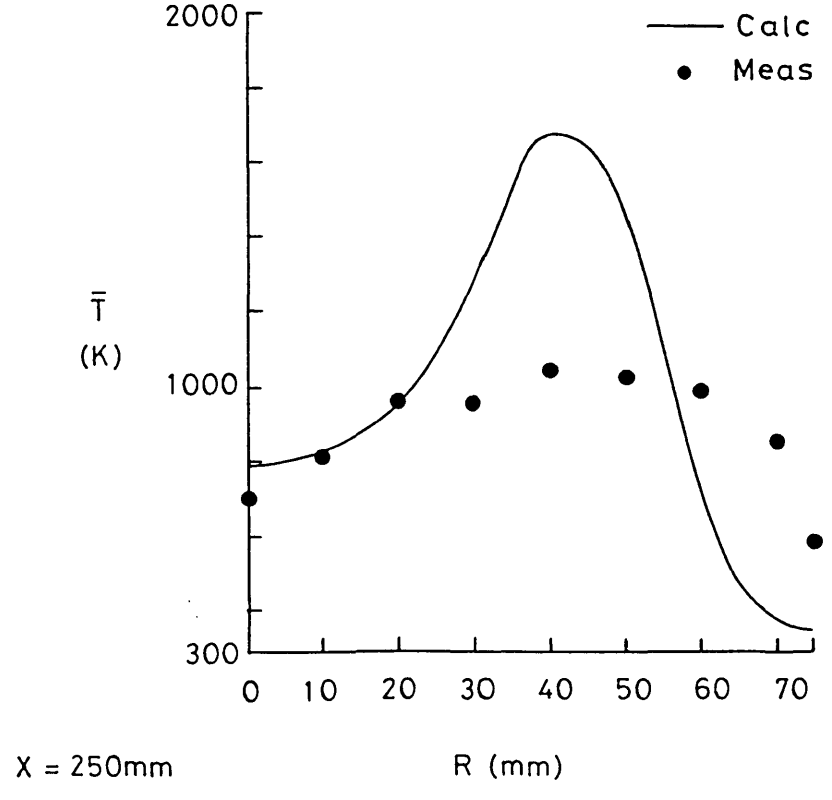
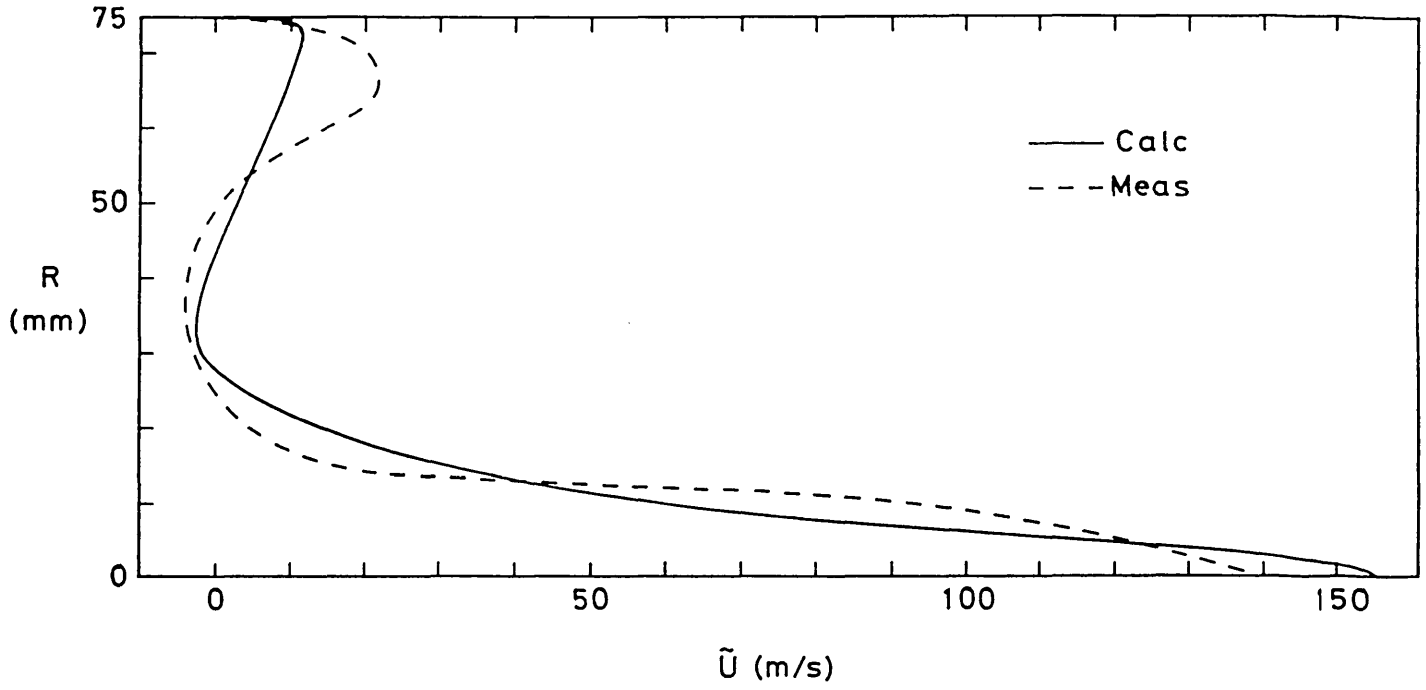


Figure 6.20 Radial profiles of calculated and measured mean temperature for reacting flow; condition 3.



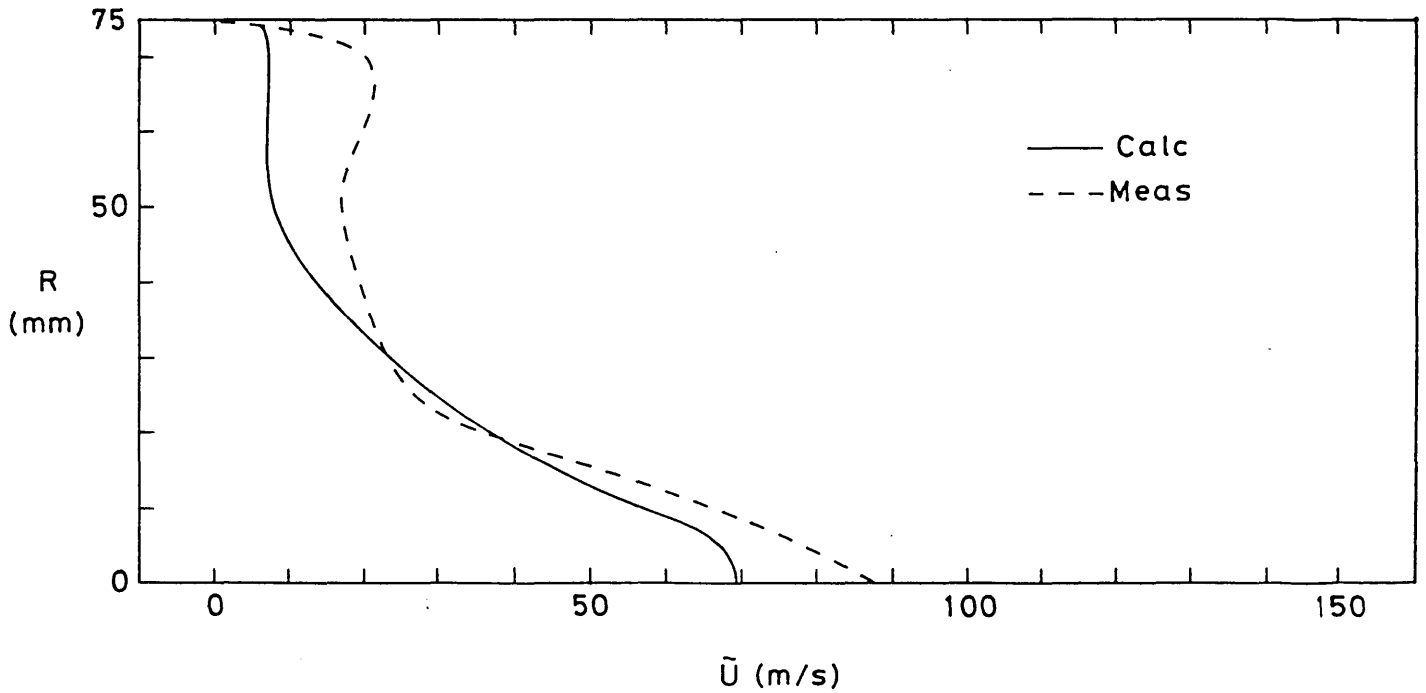


Figure 6.21 Radial profiles of calculated and measured axial mean velocity for reacting flow; condition 3.